Department of Chemistry

Electrochemical Sensing of Oxygen Gas in Ionic Liquids on Screen Printed Electrodes

Junqiao Lee

This thesis is presented for the Degree of

Doctor of Philosophy

of

Curtin University

October 2014

Declaration

To the best of my knowledge and belief, this thesis contains no material previously published by any other person except where due acknowledgement has been made. Furthermore, this thesis contains no material which has been accepted for the award of any other degree or diploma in any university.

_____

Junqiao Lee, PhD candidate

_____

Professor Damien W. M. Arrigan, supervisor

General Abstract

The work presented in this thesis aimed to investigate the potentiality of screen printed electrodes (SPEs), when used in conjunction with non-volatile room temperature ionic liquids (RTILs), for the amperometric sensing of gases. O_2 was selected as the model gas for these studies. Cyclic voltammetry (CV) and amperometry techniques were employed for these investigations. Experiments were conducted with an inert background atmosphere of N_2 gas. Four different SPE surfaces were preliminarily tested, namely, platinum (Pt), gold (Au), silver (Ag), and carbon (C). Overall, it was concluded that RTIL/SPE systems provide promising platform for the amperometric sensing of electrochemically active gases. However, these devices are limited to short-term and single-use applications for the sensing of O_2 gas, and their sensing performances are prone to degrade during continuous monitoring of O_2 gases.

Attempt was subsequently made to improve performance and extend reusability of SPEs by the investigation of various surface pre-treatment protocols on Pt-SPEs. Of all the pre-treatment protocols tested, mechanical polishing was found to be the most promising. Polishing as a pre-treatment protocol can potentially also be extended to Ag-SPEs (i.e. the RE material on Pt-SPE), and Au-SPEs. Polished Pt-SPEs were then investigated, in comparison with unpolished Pt-SPEs, for their long-term O_2 sensing performances, in two selected RTILs, namely $[C_2mim][NTf_2]$ and $[C_4mpyrr][NTf_2]$. Polishing of Pt-SPEs showed substantial improvements in the voltammetry shapes and stabilities of the CVs over prolonged repeated scanning in the presence of O_2. Polishing also was found to improve the limits of detection and sensitivity of these RTIL/Pt-SPE systems towards O_2 after continuous long-term monitoring. The improvements in performance was found to be especially significant in the mildly protic $[C_2mim][NTf_2]$. For the amperometric sensing of O_2,

responses on unpolished Pt-SPEs in both RTILs rapidly degenerated and became unstable in the presence of O_2, while remarkable improvements in amperometric response were achieved on polished Pt-SPEs. The recovery of a fouled Pt-SPE surface by polishing has also been demonstrated, and could be repeated multiple times depending on the aggressiveness and duration of each re-polishing. Standard electrochemical pre-treatment protocols in aqueous solutions were, however, found to be unsuitable for the treatment of Pt-SPEs for O_2 sensing in RTILs.

Finally, the gellification of RTILs with PMMA was investigated with the aim to improve the robustness of RTIL/Pt-SPE systems for portable gas-sensing applications. Gellification of the two selected RTILs ([C_2mim][NTf_2] and [C_4mpyrr][NTf_2]) with PMMA were characterized for their suitability as gel-polymer electrolytes (GPEs) for electrochemical O_2 sensing. Voltammetric and amperometric responses to varying O_2 concentrations for the two RTILs, doped with 150 % w/v PMMA, were investigated on polished Pt-SPE surfaces. Significant resistance of the RTIL/PMMA deposited as a thin film onto the Pt-SPE was observed in their CVs. Although non-ideal cyclic voltammograms (with significant IR-drop characteristics) were observed with both PMMA gellified RTILs, reasonable LOD values for O_2 gas were obtained from both CV and amperometry techniques. These have thus demonstrated the potential analytical utility for O_2 sensing of these new PMMA/RTIL electrolytes on polished Pt-SPEs. Better stability and response characteristics at lower O_2 concentrations suggested that the PMMA/RTIL mixtures studied may be more suited for the monitoring of lower (< 5 % vol.) range of O_2 gas concentrations. [C_2mim][NTf_2]-based GPEs gave better sensor response and overall performance compared to [C_4mpyrr][NTf_2]-based GPEs at similar PMMA doping level on polished Pt-SPEs.

“Once Submitted, Do Not Read It Anymore!”

Contents

Acknowledgements

First and foremost I would like to express my most sincere gratitude to my supervisors Dr Debbie Silvester-Dean and Professor Damien W. M. Arrigan, for their excellent guidance. Without their mentorship and encouragement, the completion of this PhD thesis would not have been possible. Most of all, I truly appreciated the excellent academic environment and freedom that they have afforded me in their (Electrochemistry & Sensors) research group; while they were always approachable and made themselves readily available to offer valuable scientific feedback and suggestions. These have allowed me to significantly grow and mature as an independent researcher.

I would also like to thank Professor Roland De Marco, for his previous mentorship during the first-half of my PhD candidacy, before he left to take up responsibility as the Pro Vice Chancellor of Research at the University of the Sunshine Coast. He had provided me with a large number of exciting research experience opportunities. This includes the numerous research experiences that I had with him at the Australian Synchrotron, working mainly at the XPS beamline, and the soft X-ray (IR) beamline, and also at the Australian Nuclear Science and Technology Organisation (ANSTO), operating the neutron reflectometry (NR) and X-ray reflectometry (XRR) beamline and instruments there. Furthermore, with his support, I was able to have the very rare opportunity to attend the CHEIRON Synchrotron School at Spring-8 in Japan in 2009, and AONSA Neutron School at the Bhabha Atomic Research Centre in Mumbai in 2010, and also receiving the AINSE PGRA for my present PhD candidacy.

I would also thank everyone in the Electrochemistry & Sensors Group (of past and present) who I consider both colleagues and friends: Eva, Krish, and Shane for the gossips, and random conversations that we shared during coffee breaks; Masniza, and Salmah, for all the lovely pastries that you've baked and shared during group presentations and meetings; and

there's Manzar, Elaine, Mickael too; and to all the newer member of our group, Yang, Ghulam, and Bren.

I would also like to acknowledge Curtin University for the funding I received for my Curtin International Postgraduate Research Scholarship (CIPRS) during the first half of my PhD, and the Australian government for the support with my Australian Postgraduate Award (APA) after I have been granted my permanent residence status in the middle of 2012. Without which I would not have been able to pursue my passion for research. Acknowledgment also goes to Australian Institute of Nuclear Science and Engineering (AINSE) for supplementing my scholarship with a top-up, and allowing me access to their facilities over at ANSTO. This has enabled me to study the interactions of RTIL/PMMA composites as a thin-film dispersed on a Langmuir Trough, using NR and XRR techniques. The results are not presented in this thesis. However, discussions are currently under way for possible publication of this work. Thanks should also go to Dr Tom Becker for the training and support he had provided with the AFM and confocal Raman instruments; Dr Nigel Chen-Tan for his assistance with the SEM instrument; Dr Damien Carter, Professor Jingbo Wang (UWA) and Professor Ricardo Mancera for their mentorship, guidance and supervision with the *QM* and *Molecular Dynamics* computational modelling aspects while I was carrying out my initial PhD thesis research with Professor Roland De Marco.

Last but not least, I would like to thank my mom and dad, for their unconditional love, acceptance, and support. My partner for lending me the strength to pull through any difficulties that I encounter, with determination and strength; and my god-parents, sister, close relatives; friends who are still with me, from my previous metal band, and from secondary school. I miss you all!

Glossary

Symbolic representations

Symbol	Definition	Unit
[*PMMA*:*RTIL*]	percentage mass (kg) of PMMA per volume (L) of RTIL.	% w/v
a	activity	-
A_a	active surface area	mm^2
A_g	geometric surface area	mm^2
A_m	topographic/microscopic surface areas	mm^2
D	diffusion coefficient	$m^2 \cdot s^{-1}$
E_1	start potential	V
E_2	end potential	V
E_{eq}	equilibrium potential	V
E_f^0	formal potential	V
$E^{Ø}$	standard potential	V
F	Faraday constant (= 96485)	$s \cdot A \cdot mol^{-1}$
I	current	A
I_p	cyclic voltammetric peak current	A
M_n	number average molecular weight	$g \cdot mol^{-1}$
m_{PMMA}	mass of p	kg
m_{Total}	total mass	kg
M_w	weight average molecular weight	$g \cdot mol^{-1}$
n	number of electrons transferred	-
Q	reaction quotient	-
Q_H	total charge associated with adsorbed hydrogen	C
R	universal gas constant (= 8.314)	$J \cdot mol^{-1} \cdot K^{-1}$
s	solubility	mM
T	temperature	K, °C
t	time	s, mins, hr
T_e	DSC extrapolated end- temperature (T_g analysis)	°C
T_f	DSC extrapolated onset temperature (T_g analysis)	°C
T_g	glass transition temperature	°C
T_i	DSC inflection temperature (T_g analysis)	°C
T_m	DSC midpoint temperature (T_g analysis)	°C

$T_{m,f}$	DSC onset temperature of PMMA melting point	°C
v	CV scan rate	$mV \cdot s^{-1}$, $V \cdot s^{-1}$
V_{RTIL}	volume of RTIL	L
$\Delta E_{p\text{-}p}$	CV peak-to-peak separation of a redox couple.	mV
η	viscosity	cP
ρ	rugosity, A_m/A_g	-
ρ_a	ratios of the active surface areas (obtained from hydrogen adsorption and redox experiments) to the geometric area of the working electrode, A_a/A_g	-
Φ_M	electrostatic potential of the electrode (metal)	V
Φ_{OHP}	electrostatic potential at the OHP	V
Φ_S	electrostatic potential of the solution	V

Commonly used units

Unit	Definition
% w/v	percentage mass per volume ($kg \cdot L^{-1}$)
°C	degree Celsius
A	ampere
cP	centipoise
hr	hour
Hz	Hertz
K	Kelvin
m	metre
M	molar
min	minute
mM	millimolar
ppm	parts per million
s	second
sccm	standard cubic centimetre per minute ($cm^3 \cdot min$)
wt. %	mass fraction

Prefixes of units

Prefix	Definition
k	kilo-
m	milli-
c	centi-
μ	micro-
n	nano-

Commonly used Abbreviations

Abbreviations	**Definition**
Ag	silver
AGS	amperometric gas sensors
Au	gold
C	carbon
CA	chronoamperometry
CE	counter electrode
CV	cyclic voltammetry
EIS	electrochemical impedance spectroscopy
GPE	gel-polymer electrolyte
LOD	limit of detection
OHP	outer Helmholtz plan
PMMA	poly(methyl methacrylate)
Pt	platinum
RE	reference electrode
RTIL	room temperature ionic liquid
SPE	screen-printed electrode
WE	working electrode

1. General Background

1.1. Introduction to Electrochemistry

Electrochemistry is a branch of physical chemistry pertaining to the study of charges and their behaviour at the interface of an electrical conductor (referred to as an *electrode*) and an ionic conductor (referred to as an *electrolyte*). The field of electrochemistry encompasses a huge array of different phenomena and deals substantially with the study of chemical changes associated with the passage of an electric current and the production of electrical energy by chemical reactions. [1] It is used in a wide range of applications such as electrophoresis and corrosion monitoring to practical devices (which include electrochromic displays, electroanalytical sensors, batteries, and fuel cells), and technologies such as electroplating, and refinement and production of raw materials and chemicals.

There are two distinct categories of electrochemistry, namely equilibrium electrochemistry and dynamic electrochemistry. As its name implies, equilibrium electrochemistry is concerned with equilibrium states of an electrochemical system where a steady-state zero-net-current is established at the electrode. The potential difference established between the electrode and electrolyte at equilibrium is described by the Nernst equation [2]:

$$E_{\text{eq}} = E^{\emptyset} + \frac{RT}{nF}\ln Q \qquad \textbf{(1.1)}$$

where E_{eq} is the equilibrium potential of the electrode dependant on the standard potential, $E^{\emptyset}$, temperature, T, number of electrons transferred, n, the gas constant, R, the Faraday constant, F, and the reaction quotient, Q, which is defined by the multiplication of all the relative activities, a, or fugacities, f, (for gases) raised to the power, v, equal to its

stoichiometric number, i.e. [2]:

$$Q = \prod_J a_J^{\nu_J} \quad \textbf{(1.2)}$$

A wealth of thermodynamic information can be readily obtained from the study of an electrochemical system's equilibrium electrochemistry, such as reaction free energies, entropies and enthalpies, equilibrium constants, activities and solution pHs. [3] However, fast (electrochemically reversible) electrode kinetics is necessary for establishment of a true electrochemical equilibrium at the electrode, and measurements are made with respect to a reference electrode. [4]

Obtaining information on the kinetics of the electron transfer process in addition to thermodynamic quantities of a wide range of electrochemical systems would require dynamic electrochemistry. [3] A three electrode system involving a counter (or auxiliary) electrode (to close the current circuit), in addition to the working and reference electrodes is generally necessary for dynamic electrochemistry studies.[4] Electron transfer between the electrode and solution phase occurs within a quantum mechanical tunnelling distance of between 10-20 Å.[4] Thus for poorly conducting media, an electrochemically inert supporting (or background) electrolyte is generally added. This also compresses the electric double layer, a layer where a potential difference exists between the electrode, Φ_M, (i.e. at the electrode surface) and the bulk solution, Φ_S, to a thickness within 10-20 Å, with supporting electrolyte concentrations at $> 10^{-1}$ M. [4] Other than typical solid electrodes, electrochemistry on dropping mercury (liquid) electrodes [3, 4], and at the interface between two immiscible electrolyte solutions (ITIES) [5-9] is also possible.

The work presented in this thesis is focused on the dynamic electrochemical processes for the study of reactions occurring between a solid electrode and a liquid electrolyte solution. Two relevant techniques are employed, namely voltammetry and amperometry. Their

essential concepts will be introduced in the later sections of this chapter. The following sections will first introduce some fundamental and essential concepts of electrochemistry related to this work. More in depth accounts of electrochemistry concepts can be found in standard Electrochemistry textbooks such as [1-4].

1.1.1. Structure of the Electrode-Electrolyte Interface

An electrode can act as either a source or sink of electrons. Most surfaces establish an electrical charge when immersed in a polar medium due to charge separation resulting from mechanisms such as ionisation, ion-adsorption and ion-dissolution.[10] The ions in the immediate vicinity of the electrode surface re-orientate in response a change in electrode polarisation to maintain electro-neutrality and to achieve energetic stability of the system. Ions of charge opposite to the surface-charge, termed the 'counter-ions', are attracted towards the surface, while the ions of the same charge, termed 'co-ions', are repelled from the surface. This tendency, aided by temperature induced Brownian motion within the polar fluid medium, leads to the formation of an 'electric double layer', setting up an effective electric field gradient extending out towards the bulk solution from the charged surface.

A simple model for the electric double layer was proposed by Helmholtz in 1879 [11] which consisted of two rigid equally and oppositely charged layers setting up at the two sides of the electrode-electrolyte interface. This is akin to the two separated layers of opposing charges setup in a parallel plate capacitor. A uniformly distributed sheet of counter-ion charges setting up on the oppositely charged electrode surface forms the 'outer Helmholtz plane' (OHP), which disregards thermal effects that tend to disrupt, break apart and disperse this wall of charge.[2] Gouy (1910) [12] and Chapman (1913) [13] then later refined Helmholtz's model, by more realistically treating the ions as point charges which form a 'diffuse layer' of

charge. Within the diffuse layer, the magnitude of the potential exponentially drops and eventually settles to a 'bulk solution' level. This local variation of ion concentrations approaching the electrode surface from that of the bulk also meant that activity coefficients characteristic of the bulk are not representative of that at the electrode surface. [2] Consequently, in dynamic electrochemistry studies, a large excess of supporting (background) electrolyte (e.g. > 0.1 M of an inert salt, acid or base) is added to the solution to overwhelm the effects of charges at the electrode surface. This effectively compresses the electric double layer, enabling the activity coefficients close to the electrode surface to remain practically constant. [4]

Finally, Stern in 1924 [14] proposed a model which combines both the OHP (of Helmholtz's model) with the diffuse double layer (from Gouy's and Chapman's model) in the manner illustrated in Figure 1.1. The potential drops linearly (characteristic of the potential within in a uniformly charged solid medium) from an initial potential, Φ_E, between the electrode-electrolyte interface to that at the OHP, Φ_{OHP}, before decreasing exponentially towards the bulk solution value, Φ_{Bulk}. A more sophiscated model was later introduced by Grahame (1947) [15], which takes into account the impact from uncharged species and solvent effects. An additional 'inner Helmholtz plane' (IHP) comprising of more tightly bounded adsorbed species of ions stripped of their solvation shells (referred to as 'specifically adsorbed ions'), together with the solvent molecules and any other possible adsorbed species was introduced. Bockris et al. (1963) [16] proposed a more sophisticated model (known as the BDM model, named after the authors of that paper: Bockris, Devanathan, and Muller) where orientations and actions of attached solvent molecules on the polarised electrode surface and impact on the IHP and OHP were considered. Although the BDM model is now commonly used, Stern's model is considered generally adequate for describing the diffuse double layer. In the work presented in this thesis, instead of conventional solvents, a material known as room

temperature ionic liquids, or RTILs, were used as the electrolyte for the experiments (see Section 1.3.2). In RTILs, the double layer is believed to be much more complicated compared to conventional aqueous and organic solvents. [17-19]

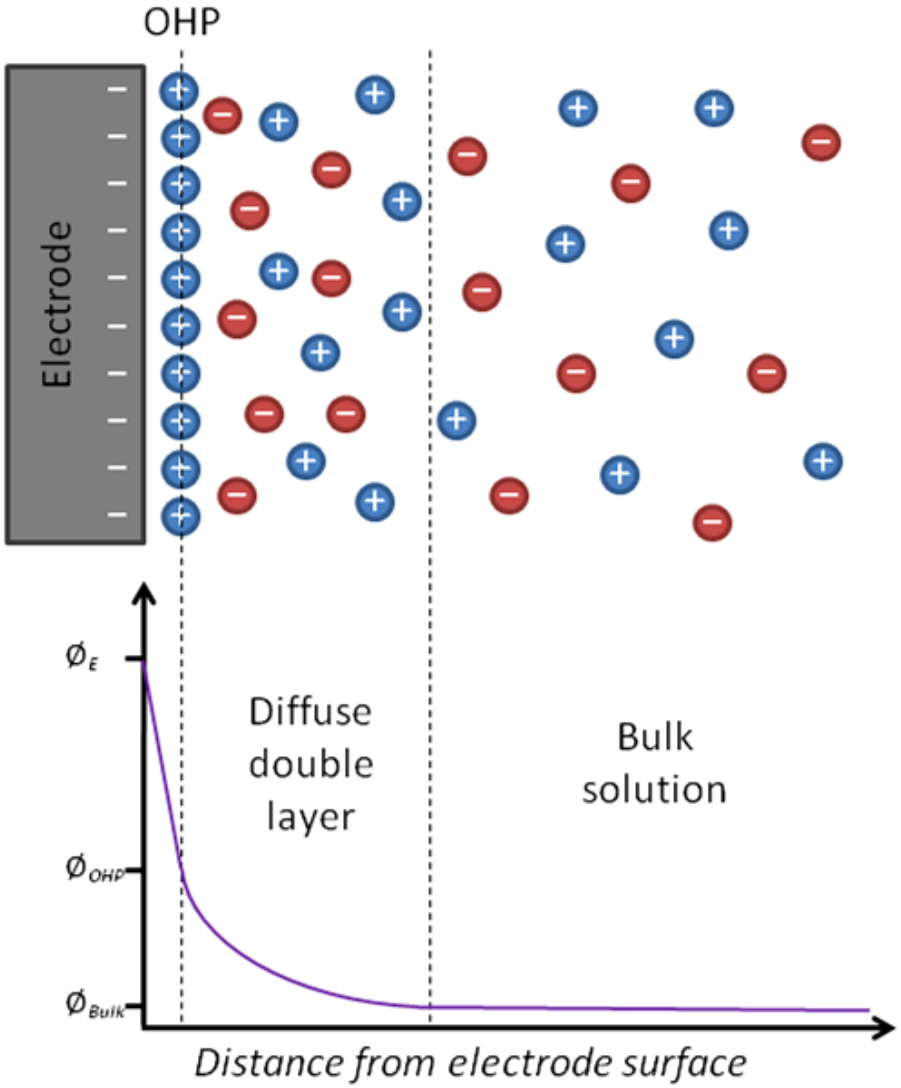

Figure 1.1. Schematic representation of the structure of the electric double layer according to Stern's theory and variation of the electrical potential vs. distance from the electrode surface.

1.1.2. Faradaic and non-Faradaic processes

Polarizing of an electrode could shift its Fermi level. [3, 20] Depending on the molecular orbital levels (either LUMO or HOMO) of species at the electrode's surface relative to the biasing potential, cathodic reduction or anodic oxidation can occur. This potential induced reaction of electrochemically active species on an electrode forms the basis of amperometry at the electrode-electrolyte interface. Electrochemical reduction-oxidation reactions (abbreviated as redox) are governed by Faraday's law of electrolysis [20, 21],

$$Q = \int_0^t i dt = n N_j F \qquad \textbf{(1.3)}$$

where Q is the charge, i is the Faradaic current, n is the number of electrons transferred in the reaction, and N_j is the number of moles of species j in the system. Electron transfers between the electrode and species within the electrolyte at the interface are known as Faradaic processes. Besides Faradaic processes, non-Faradaic processes resulting from simple electrode-electrolyte interactions (as discussed in Section 1.1.1), charging current in response to electrode-polarisations, and adsorption/desorption processes, can also exist, and result in a background current during amperometric measurements, or the setting up of an open-circuit electric potential that is monitored in potentiometric measurements.

Fundamental to the kinetics of redox reactions at the electrode-electrolyte interface is a widely accepted model proposed by Butler and Volmer [2, 3, 20], which attempts to rationalize the rate of heterogeneous electron transfer. For the simple one-electron reduction of a species, O, to its reduced form, R,

$$O + e^- \underset{k_\mathrm{b}}{\overset{k_\mathrm{f}}{\rightleftharpoons}} R \qquad \textbf{(1.4)}$$

The Butler-Volmer equation is summarized as follows [2, 3, 20],

$$i = FAk_0\left[[R]_0 \exp\left(\frac{(1-\alpha)F(E-E^{0\prime})}{RT}\right) - [O]_0 \exp\left(-\frac{\alpha F(E-E^{0\prime})}{RT}\right)\right] \qquad \textbf{(1.5)}$$

where i is the net electrolytic current, F is Faraday's constant, A is the electrode's surface area, $[R]_0$ and $[O]_0$ are the activities of species R and O at the electrode surface, R is the universal gas constant, T is the temperature of the system, α is a measure of the symmetry of the energy barrier for electron transfer, known as the 'transfer coefficient' (and often experimentally found to be 0.5 [2] via a Tafel analysis [3]), k_0 is the standard electrochemical rate constant and $\left(E - E^{0\prime}\right)$ is the overpotential (i.e. defined as the difference between the polarising potential, E, and the formal potential, $E^{0\prime}$). The current response to an applied potential can be described by combining the Butler-Volmer equation describing the reaction at the electrode-electrolyte interface, with the equations describing mass transport in the electrolyte phase (which shall be briefly covered in the following section).

The electron transfer kinetics of a redox couple can be classified as 'reversible', 'quasi-reversible' or 'irreversible'. For an electrochemically reversible system, the electron transfer is adequately fast to achieve equilibrium within a short timescale with minimal overpotential, and while electrode-potential is varied at reasonable sweep rates. For processes where equilibrium cannot be obtained within practically short timescales, a significant overpotential is required to drive the reaction. And finally, systems with intermediate electrode kinetics are described as 'quasi-reversible'.

1.1.3. Mass Transport

Three main types of mass transport processes can exist within an electrolyte solution, namely diffusion, migration and convection. Such processes ensure fresh continuous supply of electroactive species from the bulk, as they are consumed at the electrode-electrolyte interface. In electrochemical experiments (with the assumption of an infinite planar electrode), mass transport is formally defined as the total flux, $J_i(x)$, of the electro-active species, *i*, from the bulk towards the electrode-electrolyte interface, according to the Nernst-Plank equation [20, 21],

$$\underbrace{J_i(x)}_{\text{Total Flux}} = \underbrace{-D_i \frac{\partial C_i(x)}{\partial x}}_{\text{Diffusion}} \underbrace{- \frac{z_i F}{RT} D_i C_i \frac{\partial \phi(x)}{\partial x}}_{\text{Migration}} + \underbrace{C_i \upsilon(x)}_{\text{Convection}} \qquad \textbf{(1.6)}$$

where *x* is the distance from the surface of the electrode, and for species, *i*, D_i is the diffusion coefficient, z_i is the charge, C_i is the concentration, $\frac{\partial C_i(x)}{\partial x}$ is the concentration gradient at distance *x*, while $\frac{\partial \phi(x)}{\partial x}$ is the potential gradient, and *v(x)* is the convection velocity.

Generally to simplify the analysis of the current-response, contributions from migration and convection are kept negligible, while diffusion due to presence of a concentration gradient is the sole contributor to the mass transport, and equation (1.6) is simplified to Fick's first law of diffusion. Migration influences, due to electric field induced migration of ions, can be suppressed to negligible levels by addition of an inert supporting electrolyte in large excess (e.g. at least 2 orders of magnitude greater) over the electro-active species. Possible contributors to convection transportation such as stirring, vibrations, or hydrodynamic transport, are avoided, while time scales of measurements are kept to a minimum such that natural convection processes do not have a significant impact.

1.1.4. Dynamic Electrochemical Techniques

A range of dynamic electrochemical techniques exists for the study of redox reactions through current-potential relationships. Voltammetry, which measures the current produced in response to an applied potential at the electrode, is generally used for electro-analysis. The following sub-sections introduce two different and widely used voltammetric approaches that are relevant to experiments reported in this thesis. The first of which, referred to as amperometry, monitors current flow as a function of time for a fixed electrode potential. The second approach generates a current-potential profile, referred to as a voltammogram, while linearly varying the potential at the electrode. These techniques are discussed in terms of a working electrode within a quiescent environment, operating in strictly linear diffusion only condition, and in the presence of an electrochemically reversible species.

1.1.4.1. Amperometry and chronoamperometry

Single potential amperometry (also referred simply to as 'amperometry') is a simple and straightforward means of monitoring dynamic electrochemical processes at the electrode-electrolyte interface. For sensing purpose, the electrode is continuously held at a fixed potential with respect to a reference electrode, while fluctuations in the analyte concentration induces changes in current in response. Commonly, in many experiments where the concentration of an electro-active analyte is not expected to change, various parameters of the system can be analysed from conducting a 'potential step chronoamperometry' experiment (commonly referred simply to as 'chronoamperometry'). This is carried out by instantaneously stepping the potential from an initial value at E_1 at which either no Faradaic process is taking place to a final value at E_2 where electron transfer occurs at a sufficiently

high overpotential (see inset of Figure 1.2). A large current which steadily decays in magnitude over time due to depletion of the analyte species at the electrode surface is recorded. For electrodes where linear diffusion dominates, the diffusion limited current i_d, over practical timescales is reasonably approximated by the Cottrell equation (introduced in 1903) [22],

$$i_d = \frac{nFAD^{\frac{1}{2}}c}{\pi^{\frac{1}{2}}t^{\frac{1}{2}}} \quad \textbf{(1.7)}$$

where n is the number of electrons transferred per molecule, F is Faraday's constant, A is the area of the electrode, D is the diffusion coefficient, t is the corresponding time with respect to the current measured, and c is the concentration of the redox species in the solution used. An example of an i_d vs. t plot obtained from chronoamperometry measurement on a macrodisk electrode is as show in Figure 1.2.

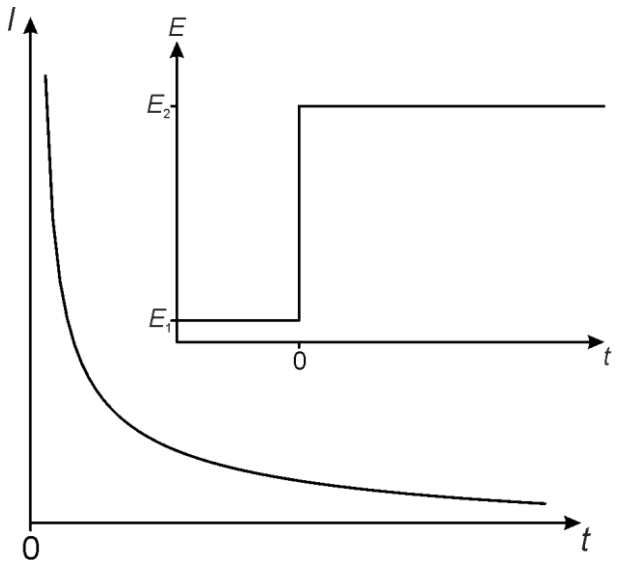

Figure 1.2. Chronoamperometry output signal obtained on a macrodisk electrode (obeying Cottrell equation), following the input potential step waveform applied (shown in the inset).

Cottrell's equation is only valid in systems (a) with a sufficiently thick bulk electrolyte layer [4] (such that the effective diffusion layer thickness during measurement is confined within the electrolyte volume), (b) the kinetics of the reaction is sufficiently fast such that the analyte species at the electrode-electrolyte interface is immediately depleted, (c) only one electrochemically active species is undergoing reduction or oxidation at the instance of the potential-step (from E_1 to E_2). From equation (1.7), assuming that all the other parameters are known, it is obvious that a plot of i_d vs. $t^{-½}$ should result in a linear line with a zero intercept, where the concentration of the electroactive species can be derived from its slope. Typically, only the currents past an initial time value (depending on the RC time constant of the cell) are considered, since the initial currents would constitute non-Faradaic contributions as the electric double-layer at the electrode-electrolyte interface readjusts in response to the potential change.

1.1.4.2. Linear sweep and cyclic voltammetry

In linear sweep voltammetry, the potential is linearly swept at a fixed scan rate, v, between E_1 and E_2, while the current in response to the changing electrode polarisation is recorded (see inset of Figure 1.3). The redox process of interest occurs between E_1 and E_2, and an appropriate electrolyte and solvent has to be selected to ensure that it is electrochemically stable within the desired potential range. Cyclic voltammetry is similar except for an additional reverse sweep from E_2 back to E_1 at the same scan rate, carried on immediately after the initial linear sweep. A plot of current, i, with respect to the instantaneous potentials, E, during a voltammetric sweep produces a 'voltammogram', where the shape and position of the voltammogram, and changes dependant on parameters such as the varying of sweep rates, analyte concentrations, electrodes (material, geometries), in the presence of other chemical

species, manner of scanning, etc. can provide a wealth of information on various aspects of the electrochemical system, including electron transfer kinetics, mechanisms, mass transport characteristics, effective electrochemically active surface area of the electrode or deposited materials, chemical and electrochemical reversibility, electron-transfer/oxidation states, and the formal potential. As such, linear sweep and cyclic voltammetry are powerful and highly versatile electrochemical techniques. For planar electrodes, the peak current generated by the reversible oxidation or reduction of an electrochemically active species is described by the Randles-Sevčik equation, [23, 24]

$$i_{\mathrm{p}} = (2.69 \times 10^5) n^{\frac{3}{2}} A D^{\frac{1}{2}} v^{\frac{1}{2}} c \qquad \textbf{(1.8)}$$

for irreversible processes, where the electron transfer is significantly slow, leading to a broader voltammetric wave and a smaller peak current than predicted by equation (1.8), viz.:

$$i_{\mathrm{p}} = (2.99 \times 10^5) n (\alpha n_{\mathrm{rd}})^{\frac{1}{2}} A D^{\frac{1}{2}} v^{\frac{1}{2}} c \qquad \textbf{(1.9)}$$

where n_{rd} is the number of electrons transferred in the rate determining step, α is the charge transfer coefficient, and v is the scan rate. The cyclic voltammograms produced for three categories of electron transfer rates (namely reversible, quasi-reversible, and irreversible) collected at the same formal potential, E_{f}^{0}, on a macrodisk electrode (where planar diffusion dominates) are represented in Figure 1.3. The absence of a voltammetric reverse reduction peak shown in the example of an irreversible reaction case could alternatively be the result of a rapid chemical (C) reaction step occurring right after the electrochemical (E) step (i.e. an EC mechanism).

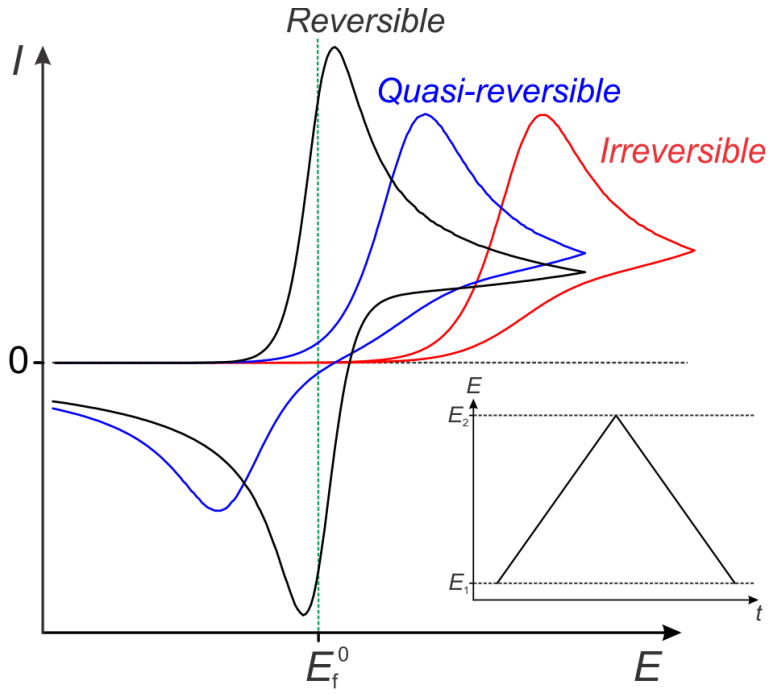

Figure 1.3. A comparison of cyclic voltammetric wave-shapes for reversible, quasi-reversible, and irreversible electron transfer process with the same formal potential, E_f^0, on a macrodisk electrode (where planar diffusion dominates). The inset shows the triangular potential 'ramp' applied to the working electrode during measurements.

1.2. Gas Sensors

Sensors are technological devices that typically convert physical or chemical conditions and properties into quantifiable electrical or electronic signals via appropriate devices and instrumentation. [25] Gas sensors are a subclass of chemical sensors, which play a crucial role in industrial safety, medical and hygiene applications, and environmental monitoring [26-29] by measuring the concentration(s) of particular gas(es) in the immediate vicinity of the sensor via a signal transduction probe (e.g. an electrode). Various non-electrochemical techniques for gas detection are available. However, for some of these techniques, the needs for bulky and costly instruments, and preparation of samples prior to analysis, may limit wide implementation for commercial and most practical use (beyond analytical laboratory work), where miniaturization (crucial for portability, and potential for sensor array

implementations), ease and cost of manufacturing, and fast response time are vital.[29] For instance, flame-[30] or photo-ionization[31] detection with gas chromatography have been employed for the detection of gas contents within samples, but these require large and expensive gas chromatographs, coupled with very slow analytical response times, rendering them impractical for many uses.

Similarly, optical gas sensors which detect concentrations of gases via changes in light absorbance of a probing medium require the use of optical spectrometers that are difficult to miniaturize.[32, 33] Ultrasonic (acoustic) gas sensors based on time of flight (TOF) measurements (which also requires bulky instrumentation) have been used for detection of a specific gas in binary non-chemically interacting mixtures (i.e. of H_2, He and CO_2) in air[34], and notably have shown high selectivity and sensitivity to inert gas molecules such as helium. The quartz crystal microbalance (QCM), which monitors the frequency shift of quartz oscillations in response to adsorbed molecules, has shown promise for the sensing of humidity[35] and various volatile organic compounds[36] using calixarene coatings to imbue sensitivity and selectivity. Surface-plasmon resonance on electrodeposited conductive polymer and gold nanoparticles-oligothiophene films for the sensing of alcohol vapours (methanol and ethanol) has also been investigated.[37]

However, electrochemical gas sensors have remained one of the most widely commercialized types of gas sensors, and can be divided into three main classes according to their operating principles, namely amperometric, potentiometric, and conductometric sensors.[25-27, 38] The work presented in this thesis focuses on the amperometric class of electrochemical gas sensors which will be discussed in greater detail under Section 1.2.1.3.

1.2.1. Electrochemical Sensors

The key advantages of electrochemical sensing over other sensing techniques are, in general, high sensitivity, durability, direct transduction into electrical signal, continuous monitoring capability, low manufacturing and instrumentation costs and ease of miniturization. [25-28] Table 1.1 summarises the typical operational response behaviour and fundamental principles behind the three classes of electrochemical gas and general chemical sensors (amperometric, potentiometric, and conductometric) mentioned under Section 1.2. The ability to miniturize the sensing probe allows the establishment of a sensor array system (also widely referred to as electronic nose or tongues dependent on the type of targeted analytes) to allow simultaneous discrimination of a particular or multiple chemical species within a complex mixture via chemometrics analysis of response signals. [29, 39-46]

1.2.1.1. Conductometric sensors

The name 'conductometric sensor' is frequently used as a synonym with the name 'impedimetric sensor', where the processes occurring at the electrode surface and/or the bulk can be represented by equivalent resistances. For sensors based on ionic conduction within an electrolyte medium, all the partial resistances in an electrochemical cell (contributed from the bulk solution as well as from the electrode interface) can be combined to form a complex resistance quantity called impedance. [25] Changes in the impedance of the overall system are monitored as a response for sensing. The four-point probes method, which uses separate pairs of voltage-sensing and current-carrying probes, is one way which eliminates the contribution from the contact resistance and wiring and is referred to as Kelvin sensing [47, 48] (named after its inventor) to improve sensitivity. It is commonly use for the determination of the sheet

resistance of thin-films. More sophisticated techniques such as EIS (electrochemical impedance spectroscopy) could be used to deconvolute the various impedance components. This allows greater sensitivity, and enables concomitant monitoring of the capacitance and inductance, on top of resistance of a given system. It typically operates in low AC polarization amplitude (typically at ca. 5 to 10 mA) to minimize electrochemical perturbation of the system during measurement, and generate impedance data (i.e. Nyquist plots and Bode plots) by scanning across a wide order of magnitude of AC voltage frequencies (e.g. from 0.1 mHz up to 10 MHz). The data generated from an EIS measurement can be modelled with equivalent circuits, representing the various impedance elements within the system.

Thin-film resistor (TFR) or thin-film transistor (TFT) gas sensors based on semiconducting metal-oxides (e.g. SnO_2, TiO_2, ZnO, and WO_3) [49-52] and of organic thin-film transistors (O-TFTs) using conductive polymers [42, 53-57], also known as chemiresistors, and carbon nanotubes or semiconducting nanowires (single or in an array) [43, 58, 59], generate a response by modification of the work-function of the sensing material in response to (selectively) reversibly adsorbed species of gases or vapours. Breakage or recovery of conduction percolation channels of polymer nanocomposite materials due to swelling, in response to absorbed chemical species, have also lead to versatile conductometric sensing material with high sensitivity. [60-62] Capacitance based sensors is another subgroup of impedimetric sensors where only the capacitance of the probing material provides a significant sensing signal, and with a predetermined resistance insensitive to the analyte species. [25] Conductometric sensors, based on semiconducting materials (such as tin oxide) are said to be the most widely used in gas-phased chemical sensing applications – owing largely to their long shelf lives, low deterioration during use, and solid state composition. [26] However, these types of gas sensors

are limited by general low selectivity and sensitivity, coupled with high electrical power consumption as the result of their high-operating temperatures. [26]

1.2.1.2. Potentiometric sensors

Potentiometric electrochemical sensors operate by monitoring the open-circuit potential (with input resistance typically in the mega to giga-ohm range [25]) that is established between two electrodes, one as the reference and the other as the working (or indicator) electrode. [27] Reference electrodes in general are effectively stable potentiometric class probes; and are commonly solid state metal/metal-salt electrodes (e.g. Ag/AgCl) [1, 2, 25] immersed in a solution containing the counter-ion of the sparingly soluble salt species of the participating metal (e.g. KCl), together with the analyte. This may be segmented by a glass frit from the solution medium being monitored by the working electrode. [2, 25] One key advantage of many potentiometric sensors is their high selectivity, in which the activities of species at the electrode-electrolyte interface are monitored. [25] Analyte concentrations over a very wide range (often more than 10 decades) can typically be measured due to the logarithmic (Nernstian) nature of potentiometric sensors' response. However, this also leads to poor sensitivity over a narrower range of concentrations, rendering them generally unsuitable for applications such as oxygen sensors in lean burn engines [63]. Potentiometric sensors operate with the assumption that during operation, all relevant chemical and diffusional processes contributing to the measured response are at equilibrium. [27] One notable example of a potentiometric gas sensor widely used today in various industrial applications and in internal combustion engines at high operating temperatures (also known as the 'lambda sensor') with a working temperature of ca. 500 °C, is based on zirconia solid electrolytes (typically yttrium stabilized zirconia, or YSZ) [26, 63, 64], which consists of two platinum electrodes (a reference

and a working electrode) printed and sintered on the opposites sides of a gas-tight zirconia ceramic electrolyte, with one side as the reference sealed with a fixed partial pressure of O_2 as follows [25, 26, 64],

$$O_2\left(P_{O_2}, RE\right), Pt|Zirconia|Pt, O_2\left(P_{O_2}, WE\right) \quad \textbf{(1.10)}$$

An e.m.f., *E*, is developed according to the Nernstian equation [25, 63, 64],

$$E = C + \frac{RT}{4F}\ln\frac{p(O_2)_{\mathrm{WE}}}{p(O_2)_{\mathrm{RE}}} \quad \textbf{(1.11)}$$

where *C* is a constant related to the thermal junctions in the probe, and mismatch of pressure and temperature at the RE/WE sides; and the rest of the terms are as commonly understood for a Nernstian electrochemical cell [1-4, 63, 64]. The lambda sensor was first introduced by Peters and Möbius [65] and Weissbart and Ruka [66] in 1961. It is now found in all modern motor vehicles to control oxygen content in combustion gas and regulate the combustion process so as to maximize fuel combustion efficiency and thus minimize the generation of carbon monoxide. [25, 26, 38] However, the principle governing the lambda probe cannot be readily extended to other applications, and displays rather narrow dynamic ranges while requiring high temperatures to operate. [26, 67]

1.2.1.3. Amperometric sensors

Amperometric sensors operate by the measurement of the electrolysis current at a polarized working electrode surface held at or varied within predetermined potential(s). [25] The thermodynamic potential response that is established in potentiometric sensors is an intensive property [2] characteristic of charge separations and organisations at interfaces within an electrochemical system [25] as discussed under Section 1.2.1.2. In contrast, amperometric

sensor current response is an extensive property [2] that scales with respect to the electroactive surface area of the working electrode via current-limiting transduction [25]. This could be taken advantage of by the use of meso- or nano-structured electrode materials to greatly enhance the sensitivity of a sensor (by increasing current densities for micro/nano-sized solid electrodes, or the electrode's surface area for porous electrodes) [27, 68-70], and even imparting selectivity via size exclusion [69] or resulting in synergistic electrocatalytic effect of the nanocomposite material [71]. Further, in contrast with potentiometric sensors, which require chemical and diffusional equilibrium to provide a thermodynamically accurate response signal, the response of an amperometric sensor is governed by Faraday's law [25, 27] and Fick's Laws of diffusion [4, 38], where the electric current measured is an expression of the reaction rate [25] and stoichiometry of electroactive species present. The steady-state current signal of dynamic reaction processes are induced at the working electrode by a predetermined fixed or varying bias, referred respectively to as constant-potential amperometry or variable-potential amperometry. [27]

Figure 1.4 illustrates the basic idea of an amperometric sensor setup, consisting of a working electrode (WE), a counter electrode (CE), and a reference electrode (RE) immersed in an electrolyte containing the dissolved analyte to be sensed. When a potential is applied between the WE and the CE, with the CE held at the same potential as that registered and monitored at the RE, an electro-reduction reaction of the active species is induced at the cathode,

$$O_{\mathrm{c}} + ne = R_{\mathrm{c}} \qquad \textbf{(1.12a)}$$

while an electro-oxidation reaction concomitantly occurs at the anode,

$$R_{\mathrm{a}} = O_{\mathrm{a}} + me \qquad \textbf{(1.12b)}$$

where *O* is the oxidized species, *R* is the reduced species, and *n* and *m* are the stoichiometric numbers of electrons, *e*, involved in the reactions with accordance to Faraday's law [27], where *n* and *m* at the two electrodes must be equal to maintain charge neutrality of the electrochemical cell. The potential on the WE is maintained, with a potentiostat, to that measured on the RE, by inducing an appropriate counter-flow of electric current at the CE [72] in response to: (a) electrochemical-redox-transitions induced electron transfer at the solid electrode-electrolyte interface [73] and/or (b) ionic-charges across other interfaces such as at the interface between two immiscible electrolyte solutions (ITIES) – typically for sensing of charged species that may not be suitable for redox-based sensing: such as proteins, electrochemically inactive salts [5-9], and perhaps species whose electrogenerated-products may irreversibly foul the working electrode surface.

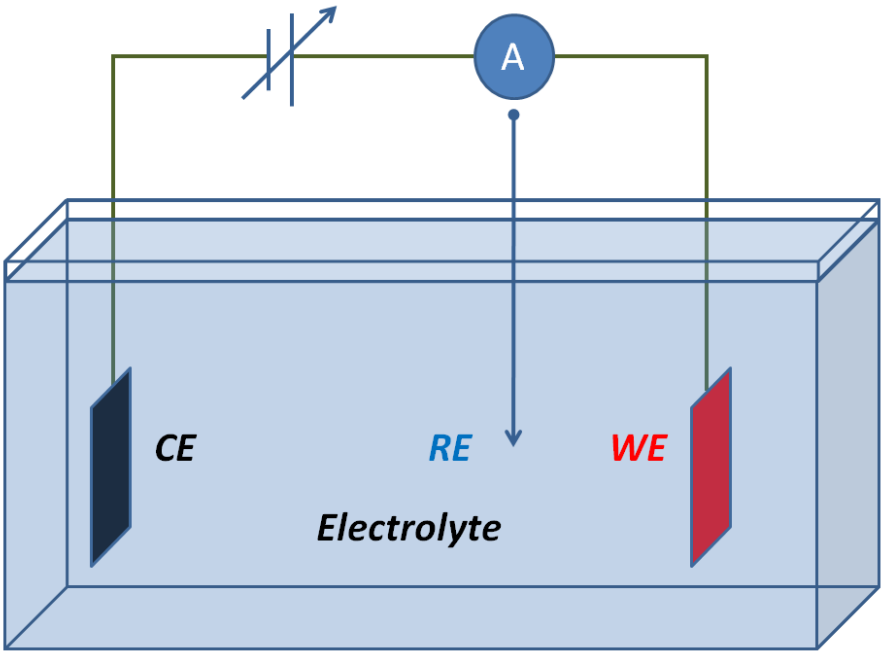

Figure 1.4. Simplified illustration (adapted from [27]) of an amperometric sensor, consisting of a working electrode (WE), a counter electrode (CE), and a reference electrode (RE) isolated from the circuit by a very high impedance, immersed in a solution (of high concentration supporting electrolyte) containing the dissolved analyte to be sensed.

Table 1.1. Comparison of the three classes of electrochemical sensors.

Electrochemical Class	Measured quantity	Sensor behaviour in response. *	Principle	General Limitations	Applications (in terms of O_2 sensing)
Amperometric (and coulometric) [4, 25, 27, 38, 63, 73]	Current (low impedance), I	$I = kP$	Kinetic, Fick's Law, Faraday's Law	Complexity in barrier control, packaging and design. **	Provides wide range of O_2 sensors.
Potentiometric [2, 25, 27, 38, 63, 74]	Potential (high impedance), E	$E = k_0 + k \ln\|P\|$	Thermodynamic, Nernst Equation	Logarithmic response ‡	λ-sensors † for high temperature operations; in automobiles and combustion monitoring in industrial boilers, etc., ion-selective electrodes.
Conductometric (or impedimetric) [25, 38, 52, 57, 63]	Resistance (i.e. reciprocal of conductance), R	$R = R_0 \, k \, P^{1/n}$	Ohm's Law and Circuit theory, Electronic Band Theory	Drift in base resistance over time	λ-sensors † in automobiles

* *P is the partial gas pressure of the analyte (i.e. O_2 gas) that is being monitored by the sensor.*
** *Due to the common use of liquid electrolytes to enable fast diffusion of the analyte gas (critical for quick sensing response time).*
† *λ-sensors (i.e. lambda sensors) will be briefly described in Section 1.2.1.2*
‡ *Sensitivity significantly decreases towards higher analyte concentration and poor sensitivity over a narrower range of concentrations.*

1.2.1.3.1. Amperometric gas sensors

Amperometric gas sensors (AGSs) are part of a large and important class of chemical sensors which play an ever-increasing role in environmental monitoring, mining, food and agriculture, home and industry safety, security, surveillance, and a wide range of medical and health applications, in robotics, and in the automotive industry. [26-29] They are also less commonly referred to in the literature by diverse and sometimes inappropriate and potentially confusing names such as: voltammetric, electrolytic, fuel cell or micro-fuel cell, polarographic, amperostatic, potentiostat, limiting current, sensors. [27, 28, 75] AGSs for an extensive number of gases and wide range of operating temperatures (from below 0 °C to over 1000 °C) are available, with a wide variety of designs and configurations dependant

significantly upon the intended application and the materials used. [25, 27, 67] Solid electrolyte materials are used primarily in automotive exhaust and stack gas process monitoring applications, while the wider and more general applications of room temperature AGSs (which is relevant to the work in this thesis) typically uses liquid electrolyte solutions and are thus not as robust [26, 27] and more difficult to construct [67]. To improve the robustness of the AGSs, polymer and polymer-gellified-electrolytes have been used, which will be reviewed in Section 1.4. AGSs generally have higher selectivity and sensitivity [26], and wider linear ranges [21, 67] compared to gas sensors based on resistive semiconductors. Their low operating power consumption coupled with ease of miniturization is especially critical for portable implementation. [25-28, 75]

1.2.1.3.2. The Clark cell and diffusion electrode designs

One of the earliest successful and most important gas-sensing probes to-date is the Clark cell, developed by Clark et al. in 1953 [76], based on amperometric detection of gases on a membrane-covered WE. [27] [21] It was originally introduced for the measurement of oxygen content in blood samples. A cellophane coating was used to filter out interfering species such as red blood cells, ions and other electroactive gases, while allowing oxygen to permeate through to the Pt-WE surface. [27, 76] This effectively imparted selectivity to the traditionally used bare Pt-WE for oxygen sensing, at the expense of an increase response time [27] due to an added diffusion layer. Soon after, the design of the Clark-cell was adapted by Sawyer et al. in 1958 [77] to investigate the amperometric response to a wide range of gases, with polyethylene and poly(tetrafluoroethylene) (PTFE, or Teflon®) as the membrane material. The group found suitable amperometric response characteristics for oxygen, chlorine, bromine, sulphur dioxide, nitrogen dioxide, and hydrogen cyanide gases. The Clark-cell

design has since been extended to a wide range of other gases. [21, 26-28, 75] Modern Clark-cells uses gas-permeable micro-porous PTFE material (with typical pore diameter of 10 μm) instead of cellophane, due to the added advantage of its high hydrophobicity preventing wetting by the aqueous solution. [26] Ultra-thin solid Teflon® films and silicone membranes are also used. [27] Figure 1.5 shows an example of a commercial AGS sold by one of the leading AGS manufacturers, City Technology Ltd. Two options for the gas selectivity mechanisms are available, (a) using a solid membrane to monitor the partial pressure of a given gas (i.e. relative concentration) and (b) using a capillary to measure its absolute concentration. [78]

Figure 1.5. Amperometric gas sensors manufactured by City Technology Ltd. [78] (Image obtained from the manufacturer's website, URL: http://www.citytech.com/, on the 12th Jun 2014) [*Used with Permission*].

A schematic representation of the basic internal components and setup of traditional AGSs is presented in Figure 1.6 (a). It consists of working, counter and reference electrodes encapsulated within a reservoir of liquid electrolyte and diffusion barrier(s) to aid selectivity of the AGS while preventing electrolyte loss due to leakage. The working electrode is typically made from a noble metal such as platinum, gold or glassy carbon, which can withstand the required polarizing potentials without corroding. [27, 79] Electrode reactions typically involve multiple steps, which can include the adsorption of the analyte species onto the working electrode surface, followed by electroreaction and subsequent desorption of products. [27, 28, 75] Platinum is also the material of choice for the counter electrode, which performs the complementary half-cell reaction to the analyte reaction. This similarly requires stability during operation in the electrolyte. [27, 79] In aqueous solutions, an Ag/AgCl electrode is typically used in the presence of Cl-based electrolytes (e.g. KCl) due to its good reversibility and stability to maintain a constant electrochemical potential during sensor-operation. [27] The Pt/air electrode [27, 80, 81] or metallic silver electrode [79, 82-85] are also popular choices for a reference electrode in an AGSs, referred to as a quasi- or pseudo-reference electrode. Pseudo-reference electrodes form unstable potentials, and must be calibrated with a redox couple of known potential since its potential is not established by a thermodynamically defined reaction. [27]

Certain AGS designs are implemented as a two electrode system, where a single electrode of inert metal such as Pt functions as both the CE and pseudo-RE. [27, 78] Instead of a solid WE positioned at a distance below the electrolyte-gas interface (separated by a hydrophobic porous membrane), many modern AGSs now use a porous WE, referred to as *diffusion electrodes*, which were originally made of a sintered Teflon-Pt catalyst composite material, positioned directly below the hydrophobic membrane layer. [26, 27, 29] It was first introduced in 1962 by Niedrach [86], and shows drastically improved sensor performances over the original

Clark-cell design. The internal layout of this modern AGS design is illustrated in Figure 1.6 (b). Firstly the use of a porous WE drastically enhances sensitivity due to (several orders of magnitude) higher current response, allowing poor electroactive species due to slow kinetics (such as oxidations of hydrocarbons and carbon monoxide), to generate measurable currents. [27] The *back-side* WE configuration of the metallised porous membranes results in drastically improved response times, due to much faster diffusion of gas through the thin membrane layers rather than through bulk RTIL [29, 67]. Better stability is maintained since the working electrode is always in direct contact with the electrolyte. In contrast, the layer of liquid electrolyte thickness above the WE in a traditional Clark-cell may vary, as the result of perturbations during gas-monitoring, and also faster gradual evaporation of the (typically) aqueous electrolyte. [26, 27, 29, 67]

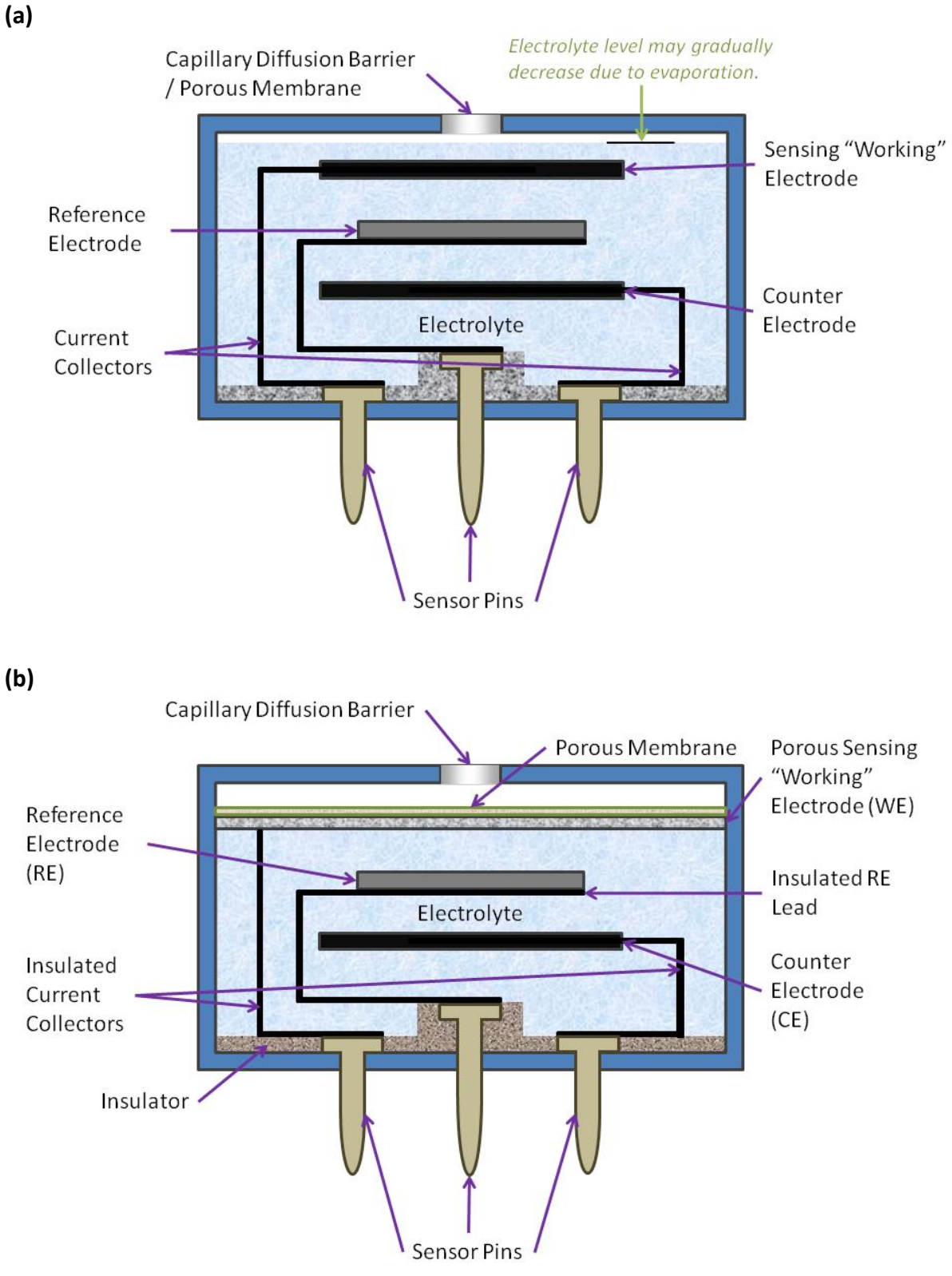

Figure 1.6. Schematic diagrams (adapted from [27, 28, 78]) of a three electrode configuration consisting of a working electrode, counter electrode and reference electrode, for **(a)** traditional amperometric gas sensors (AGSs) with the electrodes simply immersed within an enclosed reservoir of electrolyte solution and the WE positioned at the top where the analyte gas permeates through the analyte gas-selective layer, and **(b)** modern commercial AGS system using a back-side porous membrane as a diffusion WE instead.

1.2.1.3.3. Use of microelectrodes in emerging AGSs for enhanced sensing response, and device miniturization.

Advances in fabrication technologies have recently advanced the use of microelectrodes as materials for AGSs. [27] On a microelectrode, the edge effects on analyte diffusion become significant, and Cottrell's equation as shown in equation (1.7) fails to fit experimental observations, due to deviation from the linear diffusion characteristic. [4] Shoup and Szabo in 1982 [87], following on from the work by Aoki and Osteryoung the previous year [88], developed a theoretical expression to successfully describe the transient current behaviour on a microdisk electrode. This was accomplished by solving Fick's 2nd Law of diffusion in spherical coordinates, taking into account the 2D geometry of the electrode. [4, 88] The expression derived by Shoup and Szabo is given as [4],

$$I = 4nFcDr_e f(\tau) \qquad \textbf{(1.13)}$$

where, $f(\tau) \approx 0.7854 + 0.8862\tau^{-½} + 0.2146\exp(-0.7823\tau^{-½})$ and $\tau = 4Dt/r_e^2$. r_e is the radius of the microdisk electrode, while the other terms are defined in equation (1.8), and which the Cottrell's equation is simply a special case at very short time. Voltammetry on a microelectrode leads to limiting (or steady-state) currents instead of decaying towards zero. [4] Due to the very small electrode surface area and significant convergent diffusion characteristics, microelectrodes have large current densities, low non-Faradaic/capacitive background currents and fast response times compared to larger electrodes. [4] A two electrode setup (i.e. with a working and auxiliary electrode) is possible due to the comparatively much smaller surface area of the WE and lower IR-drop, and thus further enabling more compact fabrication. Microelectrode sensors in general also require only small amounts of samples, and can be easily fabricated as microelectrode arrays for membrane-free amperometric gas-sensing. [45] More recent significant studies of the amperometric behaviours of various gases

(including oxygen) on microelectrodes of various materials (such as Pt, Au and Glassy Carbon) have been conducted by the Compton group in ionic liquids [45, 83-85, 89, 90], showing considerable promises as emerging and novel AGS systems.

1.2.2. Oxygen-reduction AGSs

Oxygen (O_2) is one of the most abundant elemental molecules on Earth, and the O_2 reduction reaction (ORR) is vital for biological aerobic respiration and metabolism, and in fuel cells. [91] The cathodic monitoring of O_2 gas is crucial in many industrial processes and technological applications, ranging from high concentrations and under high temperatures (such as in combustion or steel-making processes), down to parts-per-million (ppm) levels under low pressure (such as in food packaging). [67] Potentiometric semiconductor sensors are mainly adopted for oxygen detection due to its many advantages (e.g. low cost, robustness, compact sizes), however their narrow dynamic ranges and high operation temperature requirements severely limit their applications. [79, 92] Thin-film luminescent oxygen sensors offer promising but limited trace-concentrations detection. [93] As a result, AGSs evolved from the classic Clark-cell design, due the wider linear response range which they offer, are still relevant to this day. [67, 79] For oxygen sensing, platinum is widely regarded as the most active electrode material for the electrochemical reduction of oxygen [91, 94] due to it acting as an electrocatalyst [91, 95-97] for the gas.

The reduction mechanism of oxygen on Pt is dependent on the choice of solvent and electrolyte, and is summarised in Table 1.2. In protic environments, oxygen typically undergoes a 4 electron reduction mechanism, consuming protons in the process to produce water. [27, 28] In aqueous environments, in the absence of protic electrolytes and dissolved

species, oxygen similarly undergoes a 4-electron reduction leading to the formation of hydroxide ions. [75] Although multiple electron processes would give better sensitivity, the irreversible generation of electro-reduction products could accumulate and lead to drift in the sensor response over time. For instance, the change in pH of the electrolyte solution could lead to a drift in the reference electrode potential. Further, the production of water within a protic medium could lead to undesirable accumulative contamination of non-aqueous electrolytes. These problems may become significant in minituralized sensor designs, incorporating microlitre volumes of electrolyte solution.

Within aprotic non-aqueous solvents (such as many aprotic room temperature ionic liquids) on the other hand, oxygen generally undergoes reduction to the superoxide radical via a one electron reaction as shown in Table 1.2. [4, 67, 83, 91, 98-101] The reduction is chemically reversible provided that the mildly basic superoxide species [102] is chemically stable in the presence of the electrolyte solvent or any other chemical species that may be present. [67] Frequently, absorption of ambient moisture (especially in hygroscopic or ionic solvents such as RTILs) or the presence of impurities could act as proton source(s), leading to chemical irreversibility in the electrochemical reduction of oxygen and instability of the sensor signal due to marked shift in the formal reduction potential of O_2. [67, 85, 103] This is caused by a much faster kinetics of the electrogenerated superoxide-protons reaction, which is followed by the primary one electron transfer from the negatively polarised electrode. [67] The use of stable electrocatalytic enhancing compounds to significantly lower the reduction potential of oxygen has been successfully exploited for the development of membrane-free AGSs for oxygen. [67, 91]

Table 1.2. Reduction of oxygen in various solvents/electrolyte types on inert metal electrode surfaces.

Electrolyte	Examples	Working Electrode Reaction	Standard thermodynamic electrode potentials, vs. S.H.E.† / V	References
Aqueous aprotic solvents	KCl(aq), KOH(aq)	$O_2 + 2H_2O + 4e^- \longrightarrow 4OH^-$	0.401	75, 91
		$O_2 + H_2O + 2e^- \longrightarrow HO_2^- + OH^-$	-0.065	
		$HO_2^- + 2H_2O + 2e^- \longrightarrow 3OH^-$	0.867	
Protic solvents	H_2SO_4(aq), HCl(aq), Alcohols, Protic RTILs	$O_2 + 4H^+ + 4e^- \longrightarrow 2H_2O$	1.229	27, 28, 91, 104, 105
		$O_2 + 2H^+ + 2e^- \longrightarrow H_2O_2$	0.70	
		$O_2 + 4H^+ + 4e^- \longrightarrow 2H_2O$	1.76	
Non-aqueous aprotic solvents	Tetrabutylammonium Perchlorate (TBAP) in Acetonitrile/Propylene Carbonate, Aprotic RTILs	$O_2 + e^- \rightleftharpoons O_2^{\bullet -}$	Variable, strongly dependent on solvent used	4, 67, 83, 91, 98-101, 106-110
		$O_2^{\bullet -} + e^- \rightleftharpoons O_2^{2-}$		

† *Standard hydrogen electrode.*

1.3. Background of Materials Used

1.3.1. Screen Printed Electrodes (SPEs)

Screen printing ("thick film") technology is a well-established, versatile and adaptable technique for the fabrication of disposable chemical sensors and biosensors with significant commercial applications.[111] Screen printed electrodes (SPEs) are highly cost-effective, compact, thick-film electrodes[98, 112] (with film thicknesses in the range of 20 to 100 μm, controllable by the mesh and stencil design)[111] that have been used in a multitude of electrochemical sensing studies, from bio-sensing applications (detection of proteins, glucose, microorganisms, nucleic acids, etc.)[44, 113-118], and even glucose-oxygen fuel cells[119], to the detection and monitoring of toxic heavy metals[116, 117, 120, 121]. They are conventionally used in

aqueous solutions. Screen-printing technology was touted as a promising route for the affordable mass production of miniaturized sensing platforms, due to the small amounts of materials needed and the ease with which production of these integrated devices could be scaled up. [112, 118] The cheaply manufactured integrated electrode configurations of these devices enables very small volumes of electrolyte solutions (typically in the microlitre range) to be used for gas-sensing, improving response times, and opening up the potential for further miniaturization and implementation as sensor arrays (such as electronic noses or tongues). Various companies and sources, such as Alderon, DropSens, University of Florence, Kanichi and Zensor have recently made available a wide selection of SPEs with different electrode materials and configurations for research and development. The performances of these SPEs have been characterized and compared by various groups [122-125]. Among the various commercial brands studied, it has been generally reported in the literature that DropSens SPEs tend to give the best overall electrochemical performances (in terms of background currents, peak shapes, and electron transfer kinetics) in aqueous solutions. [123, 124]

The process of the fabrication of an SPE is depicted in Figure 1.7, and involves the patterned transfer of a thixotropic fluid [111, 119, 123] (referred to as the screen printing paste or ink) through a mesh screen and a patterning mask acting as the negative of the desired shapes of the design. [119, 123] Sheer thinning induced by the laterally moving squeegee blade allows the highly viscous screen printing paste preparation (of 3-10 Pa·s at sheer rate of 230 s^{-1}) to penetrate through the screen mesh, and returns to its viscous state upon contact with the substrate (typically made of a ceramic, glass, or plastic material). [111] The process can be repeated on the same substrate to allow layer-by-layer deposition in the implementation of complex designs.

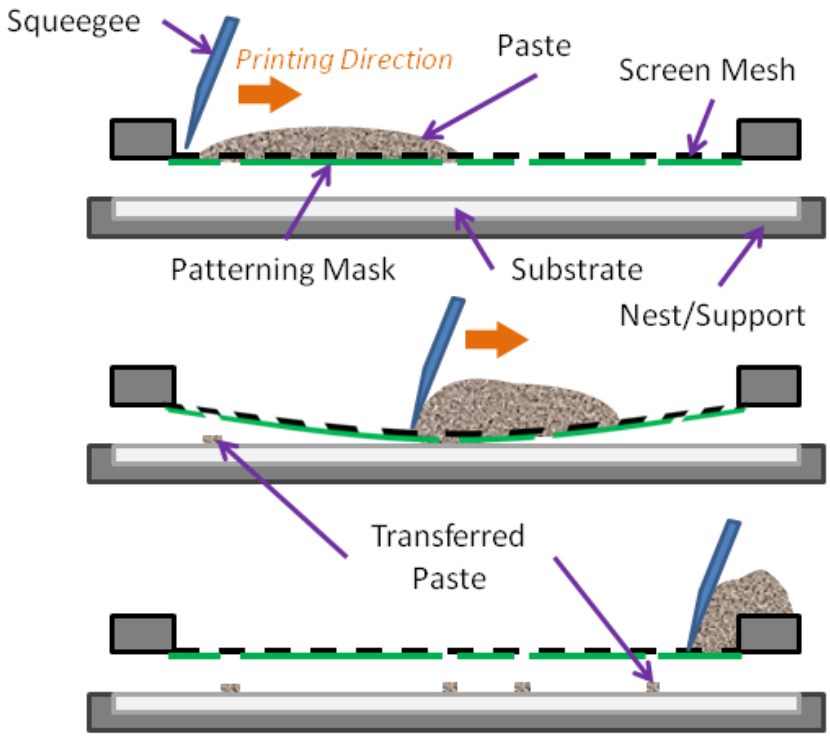

Figure 1.7. Cross-sectional side view illustration (adapted from [111]) of the screen printing process outline (from top to bottom chronologically) in the fabrication of a screen printed device supported by a substrate (such as e.g., ceramic, Pyrex, plastics).

Most SPEs currently reported in the literature are large surface area (e.g. 4 mm diameter) carbon materials. This has likely to do with the comparatively low cost of the carbon material compared to noble metals such as gold and platinum. Although manufacturers often do not disclose information on the formulation of the printing inks, they are generally thought to be comprised of synthetic grade graphite or metal particles (the conductive material), vinyl or epoxy-based polymeric binders (to enhance the adhesion properties of the ink to the substrate) and solvents (to improve the viscosity of the ink for the printing process). [119, 122, 123] Carbon-based SPEs usually perform well in aqueous solvents and show similar electrode kinetics to those observed on conventional disk-electrodes. [122, 123, 125] Gold [126, 127] and platinum [128, 129] SPEs have also been used, but much more rarely.

1.3.2. Room temperature Ionic Liquids

Room temperature ionic liquids (RTILs) are liquid solvents (at 298 K) made entirely of ions, which can be effectively described as an "electrolyte-solvent". Often regarded as "green solvents" [130], they are highly attractive solvents of choice for a multitude of electrochemical based applications [73], such as in fuel cells [131, 132], photovoltaics [133-135], light-emitting diodes (LEDs) [136], organic thin-film transistors (o-TFTs) [137, 138], ion [139] and gas [29, 90, 140-142] monitors/sensors. Their high appeal as solvents for electrochemical applications is due to several properties such as intrinsic high conductivity due to their ionic nature, high thermal stability, high polarity, wide electrochemical windows, low volatility, high viscosity and good solvating properties. [67, 83, 143-146] In particular, for the sensing of gases, their negligible volatility is crucial for microlitre aliquots of thin electrolyte layers to be used, which allows microlitre quantities of the RTIL to be simply drop-casted directly from a bottle of commercially available solvent, with no need for the user to prepare solutions of a solvent containing supporting electrolyte. The electrochemical potential windows of various RTILs at two different arbitrary chosen cut-off current values of 1 and 5 $mA \cdot cm^{-2}$ were characterized by O'Mahony et al. as summarized in Table 1.3.

Table 1.3. Electrochemical potential windows of various vacuum dried ionic liquids characterized on a platinum electrode at 295 K. [147]

Ionic Liquids	*Electrochemical Potential Window* / V	
	(1 mA·cm^{-2} cut-off)	(5 mA·cm^{-2} cut-off)
$[P_{14,6,6,6}][NTf_2]$	5.2	5.4
$[C_4mpyrr][NTf_2]$	4.2	5.2
$[C_4mim][NTf_2]$	4.3	5.0
$[C_4dmim][NTf_2]$	4.7	5.2
$[N_{6,2,2,2}][NTf_2]$	4.7	5.4
$[C_4mim][PF_6]$	4.8	5.0
$[C_2mim][NTf_2]$	4.2	4.6
$[C_4mim][BF_4]$	4.6	5.1
$[C_6mim][FAP]$	4.6	4.8
$[C_4mim][OTf]$	4.2	5.1
$[C_4mim][I]$	2.0	2.2
$[C_6mim][Cl]$	3.0	3.3

1.3.2.1. RTILs as electrolytes for gas-sensing purposes

SPEs in combination with microliter volumes of RTILs have recently been shown to be suitable for gas-sensing purposes [73, 148], since the RTIL will not evaporate, even under a fast flowing gas stream or degassing under ultra-high vacuum; Microlitre volumes of other solvents (e.g. water or acetonitrile), on the other hand, may only survive for a limited amount of time under such conditions (even at room temperature) and will therefore shorten the lifetime of any sensing device. Even with the use of porous electrodes supported on moist ion-exchange membranes acting as insoluble solid polymer electrolytes, to improve response time (by elimination of the gas permeation step) and to inhibit solvent evaporation, these AGS designs are still prone to drying out, albeit at a reduced rate (thus improving their

lifetime) [67], which also makes them unsuitable for applications under more extreme environments (e.g. low pressure or high temperature). The replacement of conventional volatile solvents with RTILs could conceivably circumvent these limitations. Moving away from experiments in aqueous-based solvents, very large background currents were discovered for carbon SPEs compared to Pt and Au SPEs when room temperature ionic liquid (RTIL) solvents were employed. [149] This could be due to the high viscosity and lower "wettability" capabilities of RTILs at carbon surfaces, compared to aqueous solvents. Alternatively, there could be an interaction of the carbon materials with ionic liquids that is causing the screen printed film to swell or dissolve. This observation should be considered when employing RTILs as solvents in sensing applications using carbon SPEs.

1.3.2.2. Amperometric O_2 sensing in RTILs

Investigations of the reduction of oxygen have been extensively and thoroughly conducted in a variety of RTILs on various electrode surfaces of macrodisk [79, 150-153] and microdisk [45, 83-85, 89, 90] electrodes. Wang et al. in 2011 reported oxygen detection limit as low as 0.05 % vol. with good selectivity, linear range, full chemical reversibility, and long-term stability (where they have tested up to 3 months and found no fouling of the electrode surface) in their simple Clark-type AGS design. [153] They used Pt-gauze working electrode with various RTILs consisting of the bis(trifluoromethylsulfonyl)imide $[NTF_2]^-$ anion (instead of the standard aqueous based supporting electrolytes). A membrane free RTIL based AGS for O_2 sensing based on a microelectrode array was successfully implemented by Huang, et al. in 2010 [45], investigating for RTIL films thicknesses between 6-125 μm, and O_2 concentrations of between 2-13 % vol. with the hydrophilic RTIL, tris(n-hexyl)tetradecylphosphonium trifluorotris(pentafluoroethyl)phosphate $[P_{14,6,6,6}][FAP]$. More recently, Li et al. in 2013

achieved limits of detection down to 0.01 % vol. in amperometric monitoring, and 0.06 % vol. using impedance monitoring, employed in a sensor array configuration for real time monitoring of O_2 in mines using [C_4mpyrr][NTf_2] RTIL. [29] In that same year, Baltes, et al. achieved a limit of detection in the ppm range (30 down to 5 ppm) using sub-mm thick films of various RTILs. [103] Portable, wearable and flexible AGS using porous electrodes and porous PTFE substrate (also using the [C_4mpyrr][NTf_2] RTIL) was found to achieve limit of detection of 0.08 % vol. O_2 with a linear range (with R^2 of 0.997 %) between 0-21 % vol. [140] Finally, in particular relevance to the work presented in this thesis, RTILs have also been recently investigated, on screen printed electrodes, by only two other groups (to the best of my knowledge) for the voltammetric characterization and sensing of oxygen gas [98, 154] on carbon and gold surfaces (as is mentioned briefly in the introduction of Chapter 3).

1.3.2.3. Oxygen electrochemical reduction mechanism within RTILs

It was reported that in aprotic RTILs in the absence of impurities [106], oxygen undergoes a reversible one electron reduction to superoxide, as listed in Table 1.2, which is found to be stable in many RTILs such as those with the imidazolium-cationic group [109]. Due to the ionic nature of the viscous RTIL, serving as both the ion-conductor and the solvent, a significant difference in diffusion rates (with diffusion coefficient differences of one order of magnitude [109]) is expected between the neutral oxygen and its negatively charged superoxide electroreduction product. This results in a significantly smaller superoxide oxidation back-peak than the oxygen reduction peak [84, 90, 103, 107, 109, 155], and results in both steady-state (radial diffusion-controlled oxygen reduction) and a peak-shaped (linear-diffusion controlled superoxide oxidation) voltammetric behaviour in the same CV on micro-electrodes [85]. This is especially apparent in RTILs with strongly charge-localized cationic groups [109] such as

imidazolium-based RTILs [103], due to strong ion-pairing of the imidazolium cations with negatively charge electrogenerated superoxides. Significant differences in the solvation structures of the neutral O_2 compared to the charged $O_2^{\bullet-}$ by the various RTILs also results in wider peak-to-peak separations in the CVs. [84, 90, 103, 107, 109, 155] The peak-to-peak separations of the $O_2/O_2^{\bullet-}$ redox couple is summarized in Table 1.4.

Table 1.4. Viscosity, diffusion coefficients, and solubilities of O_2, and peak-to-peak separations of the ($O_2/O_2^{\bullet-}$) redox couple obtained with Pt and Au microdisk working electrodes in various RTILs measured at 298 K from the literature. [84, 90, 147, 156]

Ionic Liquids	Viscosity, η (at 293 K) / cP	Diffusion Coefficient, D / $\times 10^{-10}$ $m^2 \cdot s^{-1}$	Solubility, s / mM	$\Delta E_{p\text{-}p}(O_2/O_2^{\bullet-})$ on Pt / Au microdisk WE / mV
$[P_{14,6,6,6}][FAP]$	464†	6.10	7.8	-
$[C_4mpyrr][NTf_2]$	89	5.49	3.6	563 / 332
$[C_4mim][NTf_2]$	52	8.76	3.1	-
$[C_4dmim][NTf_2]$	105	5.05-5.10	3.6	491 / 275
$[N_{6,2,2,2}][NTf_2]$	252	4.55-4.60	3.9	590 / 270
$[C_4mim][PF_6]$	201	2.50	3.0	470 / 405
$[C_2mim][NTf_2]$	34	9.30	3.9	-
$[C_4mim][BF_4]$	112	1.79	4.1	-

† *Measured at 298 K.*

1.3.2.4. Behaviour of the $O_2/O_2^{\bullet-}$ redox couple in RTILs and in the presence of impurities.

Certain impurities present can significantly reduce the electrochemical potential windows of RTILs. [147, 157, 158] One of the most common sources of impurities in RTILs is absorbed water from ambient moisture [89, 159-161], due to the polar environment within RTILs to some extent dependent on the molecular hydrophobicity of the ions. This may also modify ion-diffusion rates within the media. [158] Trace impurities (especially water) can result in irreversible reactions of RTILs at the electrode surface, leading to appearances of additional peaks and shoulders in the CV, and deposition of films of the RTIL-decomposition product(s) on the electrode surface. [103] It is thus desirable to remove moisture from the RTIL before commencing experiments, and to isolate the electrolyte of RTIL-based AGSs from ambient moisture, while ensuring the potentials applied are confined within the potential window of the RTIL to avoid electrode poisoning reactions. Residual species and by-products (such as halide) from the synthesis of the RTILs are also commonly present in trace concentration. [89] For experiments involving the reduction of oxygen, the presence of trace impurities [83, 106] such as electrochemical or thermal decomposition products [162] or water [103] may also lead to irreversibility of the $O_2/O_2^{\bullet-}$ redox couple and irreproducible results during sensing measurements. Degradation mechanisms of different RTILs are summarized in a recently published review paper by De Vos et al. [163] In imidazolium-based RTILs for instance, ring opening degradation of the cation can occur in the presence of sufficiently basic species to form β-aminoformamides. [163] Imidazolium-cations could also react with superoxide, leading to the neutrally charged imidazolone (deposited as a brownish film on the electrode surface) [103], which is a highly useful compound with applications such as polymer synthesis intermediates, herbicides, and pharmaceutical compounds [110, 164-167] but its formation is undesirable during AGS-operation. It is thus crucial to consider the hygroscopicity and water

retention tendency when choosing RTILs as an electrolyte for AGS of oxygen or other gases in general. Water contents within RTILs (summarized in Table 1.5) were measured using the Karl Fischer Titration method by O'Mahony et al. [8] for air-equilibrated and vacuum dried selected ionic liquids.

Table 1.5. Water contents of selected commonly used RTILs, obtained by Karl Fischer titration method for air equilibrated and vacuum dried (for 24 hrs at 333 K) samples, reported by O'Mahony et al. [8]

Ionic Liquids	Water contents in air equilibrated RTILs / ppm	Water contents in vacuum dried RTILs / ppm
$[P_{14,6,6,6}][FAP]$	328	-
$[C_4mpyrr][NTf_2]$	406	133
$[C_6mim][FAP]$	417	203
$[C_4mim][NTf_2]$	491	144
$[C_4dmim][NTf_2]$	504	295
$[N_{6,2,2,2}][NTf_2]$	1,150	167
$[C_4mim][PF_6]$	2,119	268
$[C_2mim][NTf_2]$	3,385	105
$[C_4mim][BF_4]$	5,083	119
$[C_4mim]I$	11,349	1,050
$[C_4mim][OTf]$	15,227	250
$[C_6mim]Cl$	61,049	2,231

1.3.2.5. Deviation from classical diffusional behaviour of species in RTILs

A major drawback of using RTILs as an electrolyte for electrochemical measurements is their high viscosity, which can be one to three orders of magnitude greater than conventional solvents. The viscosity is strongly correlated with the nature of its anion, being lowest for RTILs with the large $[NTf_2]^-$ anion, and higher for those with anions of non-planar symmetry, such as the $[PF_6]^-$ anion, for instance. [109] This has significant impact upon the diffusion coefficients of species within RTILs. Diffusion of species within a classical fluid medium is generally predicted by the Stokes-Einstein equation, [2]

$$D = \frac{k_B T}{6\pi\eta\alpha} \qquad \textbf{(1.14)}$$

where the diffusion coefficient, D, of a given species is inversely proportional to the viscosity, η, of the solvent and k_B is the Boltzmann constant, T is the temperature, and α is the hydrodynamic radius of the species modelled as a sphere. Deviation from classical Stokes-Einstein (SE) and Stoke-Einstein-Debye (SED) models for the self-diffusion of the ionic liquid $[C_2mim][NTf_2]$ have been found in computational molecular dynamics simulations. [168] Recent theoretical analysis, by Vorotyntsev et al. in 2010, of the transport of 'inert' species (such as neutrally charged gases) which do not exhibit strong interactions within highly viscous media (such as RTILs and any highly viscous fluids in general) was also found to be better described by a 'perfectly sliding sphere model' (instead of a 'sticky sphere model'), which is a limiting case of the Sutherland theory for the mathematical description of the transportation of colloidal particles. [169] For oxygen in RTILs, the diffusion coefficients were only found to be approximately described by Stokes-Einstein diffusional behaviour. [84] Viscosity, diffusion coefficient and solubility values of oxygen, and also the peak-to-peak separation of the $O_2/O_2^{\bullet-}$ redox couple (discussed under Section 1.3.2.3) in some RTILs at

room temperature (298 K) are consolidated in Table 1.4. While diffusion coefficients of oxygen within the RTILs are significantly affected by temperature, solubilities of oxygen in various RTILs are reported to be essentially independent of temperatures (measured between 293-318 K), in a study conducted by Huang et al. [84]

1.4. Gel-polymer electrolytes

To enable portable applications of AGSs, the electrolyte layer is typically contained within a reservoir enclosed by a gas-permeable membrane in conventional gas-sensing devices [73, 153]. Electrochemically active gases, after partitioning into and diffusing through the bulk of the RTIL, can be detected on the working electrode surface. [73] Due to low gas diffusion coefficients in the more viscous RTILs compared to conventional solvents [29, 45, 153, 170] (see also Table 1.4), response rates of conventional gas-sensor designs incorporating RTIL-electrolytes tend to be poor. It is thus crucial for the RTIL layer thickness to be minimized to ensure a practical response-time.

A modified novel RTIL-based oxygen gas sensor configuration which uses a gas-permeable membrane placed directly on top of porous electrodes, and with a 200 μm-thick reservoir of the RTIL electrolyte on the under-side [29] have circumvented the problem of slow diffusion within RTILs. Although, like with conventional commercial gas-sensors, requirement of a reservoir of liquid RTIL still limits the extent, cost-effectiveness and ease to which these devices could be built more compactly for further miniaturization. [171] It is thus desirable to be able to simply apply a mechanically stable thin film of electrolyte directly onto the integrated electrode surfaces. However firstly, not all RTILs have good wetting property on the electrodes surfaces to allow for casting of thinner films (i.e. < 50 μm), which causes

instability with the tendency to gather into small discontinuous droplets over time [154]. This have been attributed to a change in surface tension of the RTIL as the result of gradual uptake of ambient moisture [154] and is likely due to the polar nature of the water reducing the RTIL's hydrophobicity. Consequently, exposure to other polar gases such as ammonia, carbon monoxide, or alcohols, may also compromise the structural integrity of thinly cast RTIL films connecting the electrodes of an AGS.

For AGSs based on thin-electrolyte films, choices of RTILs are thus generally limited to those that possess extreme hydrophobicity, such as $[P_{14,6,6,6}][FAP]$. [45, 73] Baltes et al. recently published a work (in 2013) where they entrapped thin layer of various less hydrophobic (but higher conductivity) imidazolium RTILs, between two ceramic membranes of nanometre thickness, held with a sub-millimetre gap between them. [103] A significantly simpler way to overcome the casting of thinner RTIL films with less hydrophobic RTILs is by doping it with a polymer which the RTIL is soluble with to achieve gelification. These polymer-electrolyte blend materials are known as gel-polymer electrolyte (or GPE) and are typically composed of a polymer, an organic solvent as a plasticizer and an electrolyte salt. [172, 173] The earlier published work on GPEs was in 1973 by Wright et al. [174, 175] Research on GPEs has predominantly been focussed on lithium-salt-based GPEs, for applications in lithium ion batteries. [172, 176-187] GPEs have also found applications in devices such as electrochromic cells [82, 188, 189], dye sensitized solar cells [133, 190], fuel cells [131, 132, 191], supercapacitors [192, 193], ion sensors [139, 194] and gas-sensors [171, 195-199]. For gas-sensing applications, the intrinsic ion-conducting poly-electrolyte, Nafion®, has been widely investigated for the sensing of gases such as SO_2 [195], NO_2 [196, 197], NO [199] and O_2 [198]. However, Nafion® based gas-sensors and electronic devices in general suffer sensitivity to humidity due to its strong hydrophilic nature. [171]

Gelification of RTILs into GPEs would facilitate adhesion and immobilisation of the electrolyte onto the integrated electrode surfaces, enabling a much thinner and stable film to be drop or spin casted for improved sensor response time – in spite of a likely slower diffusion rate within the polymer-RTIL blend. From a GPE perspective, the use of a non-volatile, wide electrochemical window and electrochemically stable RTIL is an advantage over the use of (frequently hazardous) organic solvents in traditional GPEs. [171, 173, 193, 200, 201] The RTIL in this case acts as both a plasticizer and a charge carrier [139, 172, 202-204]. Using of an immobilized solid-gel (rather than liquid) electrolyte for gas-sensing would also further avoid problems such as leakage [75] from the reservoir onto the electronics of the device (leading to short circuiting and corrosion), and instability due to movement during portable use or installed in vehicles, fighter-jets or space-rockets (while experiencing significant acceleration and deceleration), etc. Being able to select a wider range of RTILs (to be properly casted onto different substrates and electrode surfaces) by polymer gelification would also enable greater flexibility with the tuning of physical and chemical properties specific to the desired application, such as control of the pH within the GPE medium (protic/aprotic RTILs) or its water permeability (i.e. humidity sensors), and chemical stability in the presence of certain highly reactive analytes or products, catalytic properties, and porosity (i.e. microscopic surface area), etc. Microscopic material morphologies (such as porosity and surface roughness) could also be significantly impacted by the type of polymer and RTIL used or other additives incorporated and their relative concentrations. These have previously been reported in studies of GPEs with [173, 205] and without [206-208] RTIL, and incorporation of nanomaterials into a RTIL-based GPE [205, 208].

A comparison of various host polymers for GPEs that have received much attention due to their practical significance in lithium-ion batteries, namely poly(ethylene oxide) (PEO), poly(acrylonitrile) (PAN), poly(vinylidene fluoride) (PVdF), and poly(methyl methacrylate)

(PMMA), was summarized in a 1999 review paper by Song, et al. [176] An amorphous polymer such as PMMA, which does not form rigid crystalline phases within the material, is desirable. This is to ensure higher levels of ionic-conductivity that is crucial for electrochemical based sensing, due to fluidity of the PMMA molecules. [201]

1.4.1. Poly(methyl methacrylate) in traditional gel-polymer electrolytes

PMMA was first studied as the host polymer in GPEs for lithium batteries by Iijima et al. in 1985 [181] and later by Bohnke et al. in 1992 [189] (incorporating $LiClO_4$ as the salt electrolyte and propylene carbonate as the plasticiser) and Appetecchi et al. in 1995 [177] (using propylene-/ethylene-carbonate blend as the plasticiser, and various Li-based salts). Using high molecular weight PMMA was shown by Bohnke's group to yield GPEs of very high macroscopic viscosity (~335 Pa·s) while the conductivity of the gel remained very close to that of a liquid electrolyte (i.e. 10^{-3} S·cm^{-1} at 25 °C with up to 20 wt. % PMMA). [189] The group proposed that the high conductivity observed was due to PMMA acting primarily as a stiffener while the presence of a continuous conduction path of propylene carbonate molecules within the matrix enabled fast ion transport. [189] But this was later ruled out in 1995 by Stallworth et al. based on differential scanning calorimetry (DSC) and ^{7}Li-NMR studies which revealed a relatively homogeneous material, and absence of microscopic liquid regions within the gel. [182] Bohnke et al. in 1993 [178, 179] also reported that for higher (between ca. 30-35 wt. % and up to 50 wt. %) PMMA concentrations, the ionic conductivity of their lithium-ion based GPE systems dropped (ranging between 5×10^{-3} to 5×10^{-5} S·cm^{-1}). They also reported widely varying GPE viscosities (8×10^{-3} Pa·s to 6×10^{-6} Pa·s) for their lithium-ion based GPE systems.

To improve the mechanical properties of GPEs, a blend of PVC and PMMA was investigated in 1997 by Rhoo, et al. (with ethylene carbonate and propylene carbonate as plasticizers and $LiCF_3SO_3$ as the lithium salt) [206], and further investigated by Stephan et al. in 2000 (with $LiCF_3SO_3$ or $LiBF_4$ salts) [183, 207]. They reported a significantly enhanced mechanical property by the incorporation of PVC, but with a decrease in ionic conductivity with increasing PVC concentration in the PMMA/PVC polymer blend. Pure PMMA based GPEs, however, were said to possess poor (gel-like) mechanical property and did not form a free-standing film at higher plasticizer content [201, 206], which is needed for certain applications that require a free-standing membrane (such as in fuel cells, batteries, capacitors and some chemical sensors) but not critical if utilized as an electrolyte layer to be casted over an integrated electrode platform (e.g. SPEs), which is the focus of the work in this thesis.

1.4.2. Polymer-gelified-RTIL gel-polymer electrolytes

Interest in GPEs occurs predominantly due to their application in lithium ion batteries as already discussed. However traditional electrolytes in lithium-ion based GPEs poses various safety hazards which limit the range of their application [184, 185]. Due to their thermal stability and non-volatility [184] and low toxicity [187], RTILs (especially imidazolium [184, 185] and pyrrolidinium [184, 186, 187, 209] based RTILs) blended with the bis(trifluoromethylsulfonyl)imide anion ($[NTf_2]^-$), are considered to be the most promising [184] as GPE materials for lithium battery applications. For RTIL-based GPE systems for various applications, imidazolium-based RTILs appear to be the most widely reported. [137, 171-173, 184, 185, 190, 192, 193, 201, 202, 205, 210-216] Polyvinylideneflouride-co-hexafluoropropylene (PVdF-HFP) [184, 191-193, 200, 205, 212, 213, 215, 216] have been the most commonly investigated host polymer for RTIL-based GPEs since it was first reported by Fuller et al. [215, 216] in 1997. RTIL-(PVdF-HFP) based GPEs give flexible

and freestanding films with excellent mechanical strength [192, 193] with high thermal stability [200] and good ionic-conductivity. These studies were largely focused on these mentioned properties for applications mainly in batteries and supercapacitors. The 2,3-dimethyl-1-octylimidazolium ($DMOIm^+$) cation with different anions (BF_4^-, PF_6^-, $CF_3SO_3^-$, $N(CF_3SO_2)_2^-$) blended with the PVdF-HFP has been investigated by Singh et al. in 2005, who found that polymer electrodes containing PVdF-HFP in $DMOImCF_3SO_3$ gave high ionic-conductivity (up to ~10^{-2} $S \cdot cm^{-1}$) at temperatures above 50 ºC. [212]

A study of a pyrrolidinium based RTIL, namely *N*-butyl-*N*-ethylpyrrolidinium bis(trifluoromethylsulfonyl)imide-lithium bis(trifluoromethylsulfonyl)imide at 110 ºC by Sirisopanaporn et al. in 2009 [184, 192], and also of 2-methyl-1-pyrroline, 1-methylpyrazol and imidazole based protic RTILs at 140 °C [191, 192] in PVdF-HFP gave similar stable and high ionic-conductivity at elevated temperatures without decomposition of the membranes. A nano-tubular titania nano-composite imidazolium-RTIL-based GPE, using 1-methyl-3-hexylimidazolium imide (HxMImTFSI)-(PVdF-HFP) was also studied for its electrical, thermal and morphological properties by Missan et al. in 2010 [205], showing improvement in the micro-structural morphology of the material with the addition of nano-tubular titania by inhibiting the crystallization of the rigid vinylidene fluoride unit [208].

Selected ammonium, imidazolium and phosphonium cation based RTILs have also been reported as suitable plasticizers for poly(vinyl chloride) with a focus on applications in automotive and medical industries, using up to 50 wt. % concentration of the RTIL plasticizer in studies by Rahman et al. in 2005. [217] A PMMA/PVC polymer blend based GPE, plasticised with 1-butyl-3-methylimidazolium bis(trifluoromethylsulfonyl)imide ($[C_4mim][NTf_2]$) RTIL, and with addition of lithium bis(trifluoromethylsulfonyl)imide ($LiNTf_2$) salt was also recently investigated. [173, 201] The study reported ionic conductivity of up to 1.64×10^{-4} $S \cdot cm^{-1}$ at RTIL concentrations of 60 wt. %, increased from a value of 1.11×10^{-6} $S \cdot cm^{-1}$ at 0 wt. % of RTIL

(i.e. a maximum increment of 2 orders of magnitude) in the lithium ion membrane. At higher RTIL concentrations (i.e. 90 wt. %) the ionic conductivity was found to decrease (where it was measured at 4.99×10^{-5} $S\cdot cm^{-1}$). This appears to be due to a lower concentration of lithium ions present in the material, since the $LiNTf_2$ concentration was not kept constant, but was coupled with varying PMMA-PVC concentrations. The group, however, attributed this to be primarily due to agglomeration of mobile ions or formation of neutral ion pairs (citing a study based on 1-methyl 3-propyl imidazolium iodide (PMImI)-poly(ethylene oxide) (PEO) blend) for use as a GPE in dye-sensitized solar cell application. [190] ATR-FTIR data [201] further supports the presence of complexation between the polymer, $LiNTf_2$ and $[C_2mim][NTf_2]$.

Polymerizable RTILs [214, 218, 219] by Ohno et al. in 2004, poly(vinyl alcohol) doped with 1-methyl-3-n-decylimidazolium bromide ionic liquid by Ayesh et al. in 2012 [210], and poly(styrene-block-ethylene oxide-block-styrene) (SOS) triblock copolymer in 1-butyl-3-methylimidazolium hexafluorophosphate ($[C_4mim][PF_6]$) by Lee et al. in 2007 [137] have been recently studied. In-situ polymerizations of vinyl monomers in 1-ethyl-3-methylimidazolium tetrafluoroborate ($[C_2mim][BF_4]$) and 1-butylpyridinium tetrafluoroborate ($[C_4py][BF_4]$) RTILs by Noda et al. in 2000 [202] and Singh et al. in 2005, [212] of methyl methacrylate (MMA) monomers in 1-butyl-3-methylimidazolium hexafluorophosphate ($[C_4mim][PF_6]$) by Li et al. in 2006 [172] and 1-butyl-1-methyl pyrrolidinium bis(trifluoromethylsulfonyl)imide ($[C_4mpyrr][NTf_2]$) [188] by Sydam et al. in 2012, have been investigated. The ($[C_4mim][PF_6]$)-PMMA GPE (prepared with one-to-one mass ratio of MMA to RTIL) investigated by Li et al. [172] gave an ionic-conductivity of 0.15×10^{-3} $S\cdot cm^{-1}$ at 25°C with excellent thermal stability over 260°C. The group also found evidence of a hydrogen-bonded interaction between $[C_4mim][PF_6]$ and PMMA from FT-IR spectra of the material.

Notably, the $[C_4mpyrr][NTf_2]$-PMMA based GPE investigated by Sydam et al. [188], specifically for application in electrochromic devices, is also presently studied in this thesis

as one of two potential GPE materials for oxygen sensing applications. Sydam's group prepared the in situ polymerized PMMA GPE with 30 wt. % MMA added to the $[C_4mpyrr][NTf_2]$ RTIL and using 1 wt. % benzoyl peroxide (relative to MMA) as the initiator, and sample of $[C_4mpyrr][NTf_2]$-PMMA (at 15-25 wt. % MMA) directly blended by continuous stirring at 50 to 60 °C for eight to ten hours. For their sample prepared by in situ polymerization, the group reported ionic-conductivity of 1.6×10^{-4} S·cm^{-1}, while ionic-conductivity of 4.2×10^{-5} S·cm^{-1} was reported for the directly blended GPE sample. The group found that in situ polymerization of the MMA on the (PEDOT or WO_3) electrodes surfaces showed significantly lower charge transfer resistance (R_{ct}) values compared to the directly blended GPE applied onto the same electrode surfaces, in a semi-solid state. They proposed that this was the result of the formation of a more intimate contact of the in situ polymerized GPE with the electrode surfaces as the monomer-RTIL mixture was initially introduced in a liquid state; however, the group did not consider the difference in PMMA concentrations between the two samples, the impact of the unknown degree of polymerization, and the molecular weight and its distribution of the in-situ polymerized PMMA, when making the comparison.

Only one RTIL-based GPE gas-sensor paper has been found thus far, recently published by Nádherná et al. [171] They used $[C_4mim][PF_6]$ blended with poly(ethylene glycol) methyl ether methacrylate (PEGMEMA), for the detection of NO_2 gas. [171] It is interesting to note that one of the GPEs studied in the work presented in this thesis is also an imidazolium-methacrylate based GPE (i.e. $[C_2mim][NTf_2]$-PMMA blend). For the GPE studied, Nádherná's group reported an ionic conductivity of 1.6×10^{-4} S·cm^{-1} at 20 °C at 57 % mol. $[C_4mim][PF_6]$ to PEGMEMA ratio, which gave a reproducible linear response between concentrations of 0.3 to 1.1 ppm NO_2 gas, with good long-term stability.

1.5. Aims of the work reported in this thesis

The overall work presented in this thesis is focused upon assessing the viability of low-cost and commercially available integrated electrodes manufactured via the screen printing process coupled with room temperature ionic liquids as potential systems for the sensing of oxygen gas (and gases in general). Methods to improve the performance and robustness of these systems in AGS application are explored. Oxygen is selected as the model gas for these studies mainly as it has already been widely and thoroughly studied on conventional electrodes, and also for its simple electrochemical redox mechanism. The chemically unstable superoxide species that is produced during amperometric monitoring of oxygen in the aprotic RTILs would also provide an assessment of the robustness of these non-ideal disposable electrodes.

As a preliminary survey, four different SPEs of standard electrode materials (namely platinum, gold, silver and carbon) purchased from DropSens [220] are studied with eight different ionic liquids as AGS electrolytes to select suitable SPE/RTIL systems as the basis for the work presented in subsequent chapters. A number of different pre-treatment methods are then investigated as possible protocols for the improvement of the performance of these sensors and to extend reusability of these disposable devices. The most promising pre-treatment protocol was subsequently implemented for testing with two selected RTILs for comparison with untreated specimens. Finally, gellification of the two RTIL electrolytes with a polymer additive is characterized for their long-term electrochemical stability, in an attempt to improve the robustness of these SPE/RTIL systems for portable amperometric oxygen sensing. This may also open up potential for further work to improve the response characteristics of these devices, amongst other possibilities as discussed. Primarily, the intent

is for the subsequent investigations of much thinner spin-cast and physically long-term stable electrolyte films on SPEs for enhanced AGS response times.

2. General Experimental Methods

This chapter details the general chemicals, materials, and experimental methods and techniques employed throughout the work presented in this thesis. The other chemicals, materials, and experimental methods and techniques specific to a particular investigation are presented in the relevant chapters.

2.1. Chemicals and Materials

2.1.1. General solvents and room temperature ionic liquids (RTILs)

Ethanol (EtOH 99 %, Sigma-Aldrich Pty Ltd., NSW, Australia), Milli-Q grade water with a resistance of 18.2 MΩ·cm prepared by a Milli-Q laboratory water purification system (Millipore Pty Ltd., North Ryde, NSW, Australia) and acetonitrile (MeCN 99.8 %, Sigma-Aldrich Pty Ltd., NSW, Australia) solvents were used for rinsing the macrodisk and screen printed electrodes before and after their use with RTILs. Tetrahydrofuran (THF > 99 %, Sigma-Aldrich Pty Ltd., NSW, Australia) was used to remove the blue polymer mask of the Pt-SPEs prior to polishing. N,N-Dimethylformamide (DMF 99.8 %, Sigma-Aldrich Pty Ltd., NSW, Australia), Sodium hydroxide (≥ 98 %, Sigma-Aldrich Pty Ltd., NSW, Australia), sulfuric acid (95-98 wt. %, Ajax Finechem, WA, Australia), and potassium chloride (> 99.5 %, Fluka, Buchs, Switzerland) were used for the pre-treatment of Pt-SPEs in Chapter 4. 1.10 mM hexaammineruthenium(III) chloride (98 %, Sigma-Aldrich Pty Ltd., NSW, Australia), and 1.00 M potassium hexacyanoferrate(III) (potassium ferricyanide 99+ %, STREM CHEMICALS, Massachusetts, USA) were used to characterize the

respective active surface area of the Pt-SPEs in Chapter 4. Ferrocene (Fc, 98%, Sigma-Aldrich Pty Ltd., NSW, Australia) was added to an ionic liquid ($[C_2mim][NTf_2]$) to act as an internal redox couple potential reference. High-purity nitrogen gas (99.99 %) was purchased from BOC gases (North Ryde, NSW, Australia). All reagents and solvents used throughout this thesis are listed under Table 2.1.

The RTILs 1-ethyl-3-methylimidazolium bis(trifluoromethylsulfonyl)imide ($[C_2mim][NTf_2]$), 1-butyl-3-methylimidazolium bis(trifluoromethylsulfonyl)imide ($[C_4mim][NTf_2]$), *N*-butyl-*N*-methylpyrrolidinium bis(trifluoromethylsulfonyl)imide ($[C_4mpyrr][NTf_2]$) and trihexyltetradecylphosphonium bis(trifluoromethylsulfonyl)imide ($[P_{14,6,6,6}][NTf_2]$) were synthesized according to standard literature procedures [143, 221] and kindly donated by the group of Professor Christopher Hardacre at Queens University, Belfast. The RTILs 1-hexyl-3-methylimidazolium trifluorotris(pentafluoroethyl)phosphate ($[C_6mim][FAP]$), 1-butyl-3-methylimidazolium hexafluorophosphate ($[C_4mim][PF_6]$), 1-butyl-3-methylimidazolium tetrafluroborate ($[C_4mim][BF_4]$) and trihexyltetradecylphosphonium trifluorotris(pentafluoroethyl)phosphate ($[P_{14,6,6,6}][FAP]$), were purchased from Merck KGaA (Kilsyth, Victoria, Australia) at ultra-high purity electrochemical grade (halide content less than 100 ppm). All RTILs were used as received. The chemical structure of the RTIL anions and cations employed in this work are shown in Figure 2.1. All RTILs used throughout this thesis are listed under Table 2.2.

Table 2.1. All purchased reagents and solvents used in experiments reported within this thesis. Abbreviations/formulas which they were referred to in this thesis and along with their purity and commercial sources were also respectively listed.

Name	Referred Formular / Abbreviation	Supplier	Purity
Ethanol	EtOH	Aldrich	99 %
Methanol	MeOH	Mallinckrodt	99.9 % (anhydrous)
Acetone	-	Aldrich	≥ 99.9%
Acetonitrile	MeCN	Aldrich	99.8 %
Ferrocene	Fc	Aldrich	98%
Tetrahydrofuran	THF	Aldrich	> 99 % (anhydrous)
N,N-Dimethylformamide	DMF	Aldrich	99.8 %
Sodium hydroxide	NaOH	Aldrich	≥ 98 %
Sulfuric acid	H_2SO_4	Ajax Finechem	95-98 wt. %
Potassium chloride	KCl	Fluka	> 99.5 %
Hexaammineruthenium(III) chloride	$Ru(III)(NH_3)_6Cl$	Aldrich	98 %
Potassium hexacyanoferrate(III) (potassium ferricyanide)	$K_3Fe(CN)_6$	Strem Chemicals	99+ %
Methyl methacrylate	MMA	Aldrich	99 %
2,2′-Azobis(2-methylpropionitrile)	AIBN	Aldrich	98%
1,4-Dioxacyclohexane	Dioxane	Aldrich	99.8% (anhydrous)
Poly(vinyl chloride)	PVC	Aldrich	-
Ethyl Acetate	EtOAc	Aldrich	≥ 99.5%
Sodium chloride	NaCl	Aldrich	≥ 99%
Sodium sulfate	Na_2SO_4	Aldrich	≥ 99.0% (anhydrous)
Oxygen	$O_2(g)$	BOC gases	> 99.5 %
Nitrogen	$N_2(g)$	BOC gases	99.99 %
Liquid nitrogen	$N_2(l)$	BOC gases	-

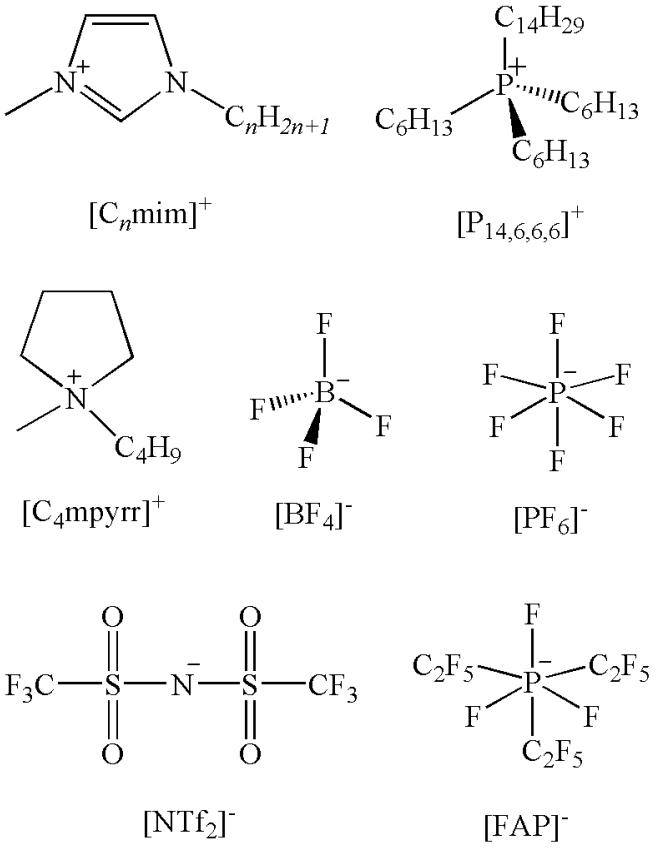

Figure 2.1. Chemical structures and abbreviations for the RTIL anions and cations employed in this work. Their full names are listed in Table 2.2.

Table 2.2. Room temperature ionic liquids used in this thesis and references to literature procedure employed in their respective synthesis.

Name	Referred Formular / Abbreviation	Source/Reference
1-ethyl-3-methylimidazolium bis(trifluoromethylsulfonyl)imide	$[C_2mim][NTf_2]$	*Donated by the group of Professor Christopher Hardacre at Queens University, Belfast; synthesized according to standard literature procedures.* [143, 221]
1-butyl-3-methylimidazolium bis(trifluoromethylsulfonyl)imide	$[C_4mim][NTf_2]$	
N-butyl-*N*-methylpyrrolidinium bis(trifluoromethylsulfonyl)imide	$[C_4mpyrr][NTf_2]$	
Trihexyltetradecylphosphonium bis(trifluoromethylsulfonyl)imide	$[P_{14,6,6,6}][NTf_2]$	
1-hexyl-3-methylimidazolium trifluorotris(pentafluoroethyl)phosphate	$[C_6mim][FAP]$	*Purchased from Merck KGaA (Kilsyth, Victoria, Australia*)
1-butyl-3-methylimidazolium hexafluorophosphate	$[C_4mim][PF_6]$	
1-butyl-3-methylimidazolium tetrafluroborate	$[C_4mim][BF_4]$	
Trihexyltetradecylphosphonium trifluorotris(pentafluoroethyl)phosphate	$[P_{14,6,6,6}][FAP]$	

2.1.2. Screen Printed Electrodes

SPEs were purchased from DropSens (Oviedo, Spain), consisting of a C, Pt, Au or Ag working electrode, Ag quasi-reference electrode and Pt/C counter electrode, as detailed in Table 2.3. DropSens SPEs were selected for the experiments since various authors have reported better electrochemical performance and reproducibility compared to SPEs purchased from other sources. [122, 123, 141] Additionally, the electrodes of DropSens are screen printed on a ceramic substrate that is compatible with RTILs and organic solvents (e.g. acetonitrile), whereas various other commercially available SPEs employ substrates that are only suitable for use in aqueous-based systems. [141] The blue material on DropSens SPEs which masks the underlying silver traces comprises of a proprietary synthetic polymeric dielectric material, which the manufacturer was unwilling to disclose. However the polymer masks are not generally stable when exposed to harsh solvents such as tetrahydrofuran (THF) or chloroform but is not attacked by acetonitrile and alcohols, according to the manufacturer.

Table 2.3. Technical parameters including the nature of working, counter and reference electrodes employed in the SPEs used in this study (according to the DropSens Co. database).

Supplier	Code	WE material	WE diameter	CE material	RE material
DropSens	DRP-110	Carbon (C)	4 mm	Carbon	Silver
DropSens	DRP-250AT	Gold (Au)	4 mm	Platinum	Silver
DropSens	DRP-550	Platinum (Pt)	4 mm	Platinum	Silver
DropSens	DRP-C013	Silver (Ag)	1.6 mm	Carbon	Silver

2.2. General electrochemical measurement setup and parameters

All voltammetric experiments were performed using a μ-Autolab Type III potentiostat (Eco-Chemie, Netherlands) interfaced to a PC with NOVA 1.8 software, recorded with a step potential of 3 mV. All experiments were carried out with the electrodes positioned inside a custom made aluminium Faraday cage (see Figure 2.2) to reduce ambient electromagnetic interferences, and internal temperatures were monitored to be within 293 ± 2 K. The waiting time between repeated scans (typically > 8 mins at a fixed concentration of O_2) was set based upon the duration necessary for the sufficient stabilization of the open circuit potential monitored on the electrode surface – which was assumed to be indicative of the stabilization of the surface conditions of the working electrodes. This would be more than sufficient for the replenishment of depleted O_2 after the previous CV scan. The starting potential used for each CV scan was typically set at (or close to, ± 0.1 V) 0 V vs. RE.

2.3. General gas-mixing set-up

The general experimental setup for the gas-sensing work is illustrated in Figure 2.2. In order to control the concentrations of oxygen gas the sensor is exposed to, the oxygen line was diluted with a nitrogen carrier gas using a gas mixing system (as shown in Figure 2.2). This consists of two separate digital flow controller-meter systems (labelled F1 and F2, from John Morris Scientific, NSW, Australia) connected via a Swagelok T-joint (Swagelok, Kardinya, WA, Australia). High purity oxygen (> 99.5 %) and high purity nitrogen (99.99 %) gas cylinders were purchased from BOC gases (North Ryde, NSW, Australia). To ensure proper mixing of the gases before it enters the T-cell, a flow-constriction *gas-mixing*

segment (see enlargement at the top-left in Figure 2.2) was improvised and added after the T-joint of the gas-mixing line. It consists of two opposing tapered glass needles inserted into a short piece of PTFE tubing for support, and inserted along the gas-mixing line via Swagelok straight fittings. The flow of mixed gases is then forced through the *gas-mixing segment* (see enlargement at the top-left in Figure 2.2), which increases gas turbulence and enhances mixing of the two gases. The relative flow rates (as monitored by the digital flow meters) of the O_2 analyte gases and the inert N_2 carrier gas were used to calculate the % vol. value of O_2 introduced into the cell. An outlet gas line was led from the other arm of the custom-made glass T-cell into a fume cupboard, to prevent build up of high concentrations of oxygen within the Faraday cage.

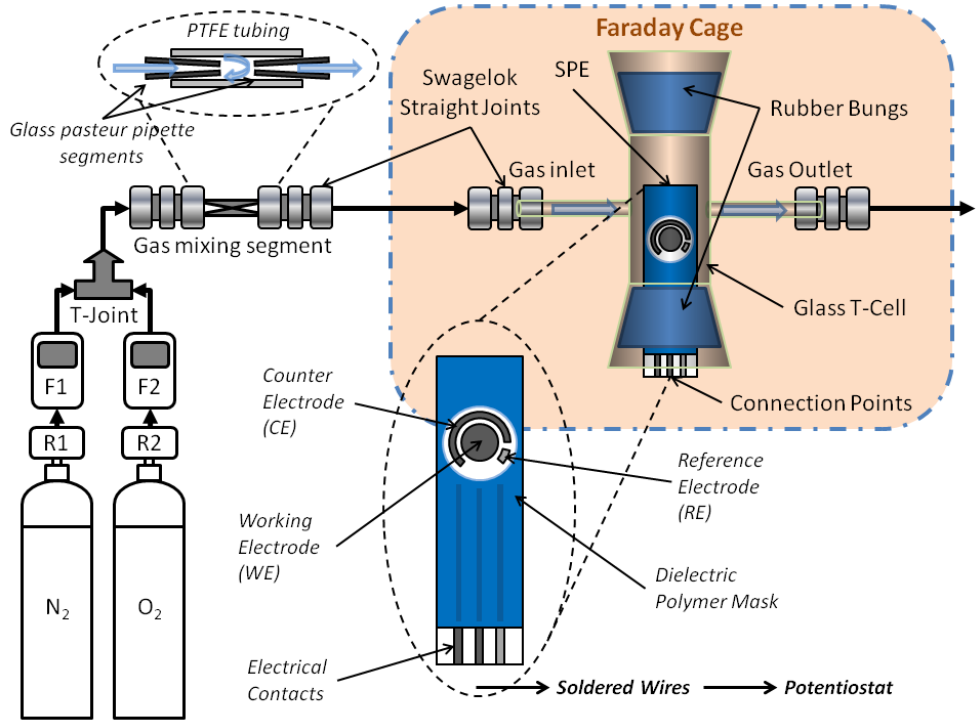

Figure 2.2. Schematic of the gas mixing system and glass cell used for voltammetric measurements on screen printed electrodes (where F1 and F2 are digital flow meters/controllers, and R1 and R2 are the pressure regulators). The glass T-cell is situated within an aluminium Faraday cage.

2.3.1. Experimental setup of SPE-RTIL systems

For experiments using SPEs, the different commercially available SPEs were inserted into a specially designed glass cell, shown in the (top) of Figure 2.3 (and as illustrated in Figure 2.2), which is based on the modification of a previously reported T-cell designed for use with microelectrodes under controlled atmospheres.[222, 223] A microlitre aliquot of RTIL was introduced via micropipette onto the SPE and spread over the three electrodes, which were connected directly to the potentiostat via soldered wires. The small microlitre volume of the RTIL used enables a rapid response time without requiring stirring. The SPE was held in place by insertion through a modified rubber bung so that the working, counter and reference electrodes were inside the T-cell (with the connections outside) and the electrodes could be placed under a controlled atmosphere of either oxygen, nitrogen or a mixture of these. The rubber-bung supported SPE was then installed into the T-cell as shown in Figure 2.2. A glass stopper was inserted into the second tapered joint (which could accommodate a second SPE). A modified version of the T-cell was later introduced, shown in the (bottom) of Figure 2.3, to allow for multiple (and up to 8) rubber-bung supported SPEs to be subjected to the same controlled atmosphere. Measurements could then be consecutively taken by a single potentiostat for each SPEs, or be concurrently acquired using multiple potentiostats.

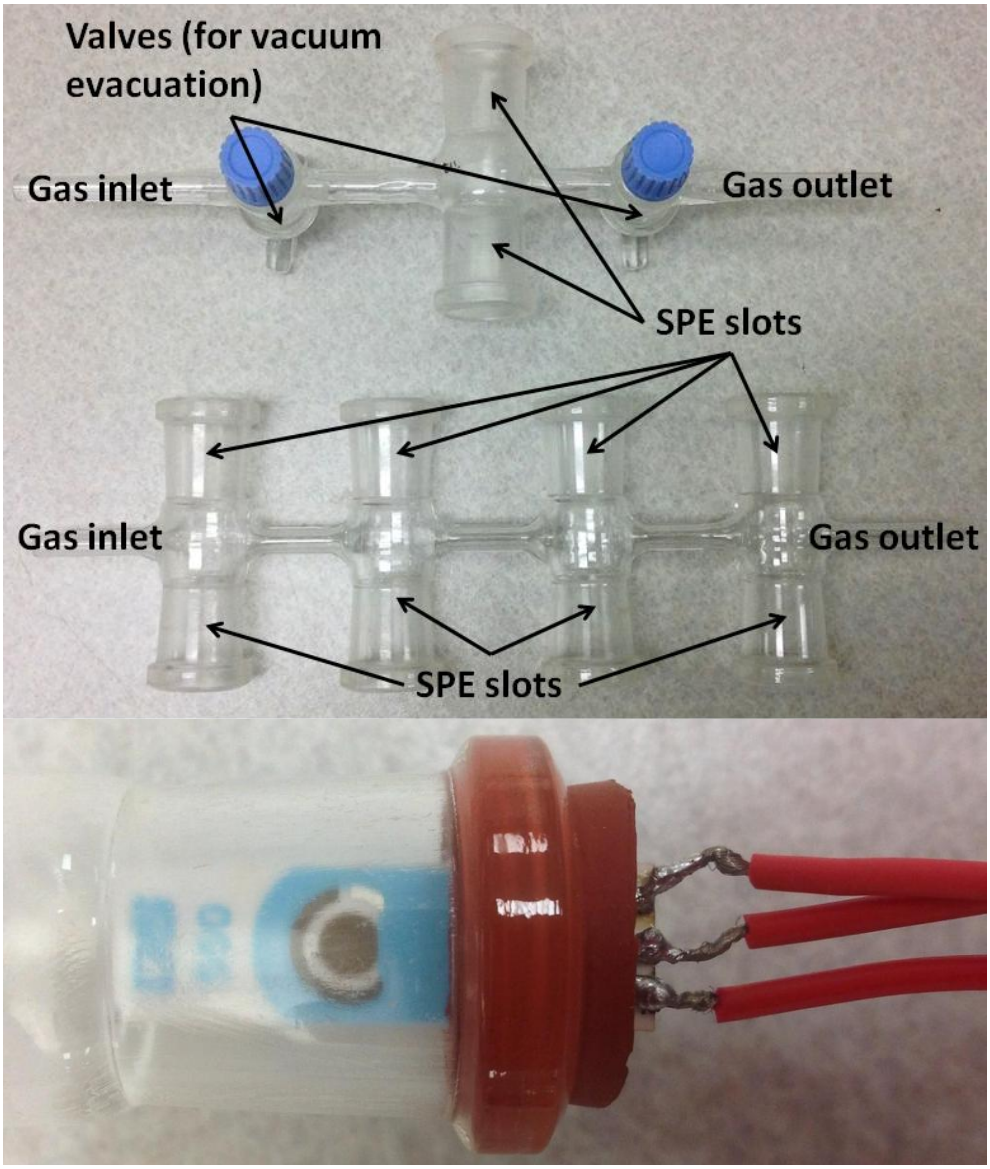

Figure 2.3. Photograph of the glass T-cells used in this work. The T-cell at the **(top)** is as illustrated in Figure 2.2, and consists of an inlet and an outlet, with a set of valves to allow the cell to be vacuum evacuated. The **(middle)** glass-cell is a modification of the above standard single T-cell, to accommodate for up to 8 rubber-bung supported SPEs to be concurrently subjected to the same controlled atmosphere. Valves were omitted for this design since vacuum evacuation of the cells was unnecessary for the work with SPEs presented in this thesis. The **(Bottom)** picture shows a Pt-SPE with wires soldered onto its leads, inserted into the T-cell, supported by a rubber bung.

Before commencement of experiments, the T-cell was purged with dry inert N_2 gas (for more than 30 mins) to not just remove any oxygen and other interfering gases present, but also to ensure that any moisture within the freshly deposited RTIL was sufficiently

eliminated since these impurities may significantly impact upon the potential window of the cyclic voltammetry (CV) scans. [89] CV measurements can then be taken to verify the 'blank' condition of the RTIL-SPE system. A side-view illustration of a droplet of RTIL deposited onto a SPE is shown in Figure 2.4. The microlitre volume of RTILs used prevents the aggressive bubbling of gas directly into the electrolyte, and makes stirring unfeasible. The RTILs were also not exposed to a vacuum line (commonly employed for experiments using RTILs on micro-disk electrodes) [156] since the RTIL would tend to bubble violently. This may potentially lead to partial loss of the aliquot of electrolyte, resulting in insufficient volume to cover and connect the three electrodes. Instead for this work, the flowing gas is allowed time to displace the atmosphere within the T-cell before partitioning into the RTIL (at the gas-RTIL interface). By merely exposing the RTIL to a nitrogen gas stream, the experimental set-up would also more closely resemble what is available in a field application for a sensing device. Once the baseline was stable after pre-conditioning in the RTIL by repeated CV scanning (until stable consecutive voltammograms are obtained), experiments with O_2 gas were then undertaken.

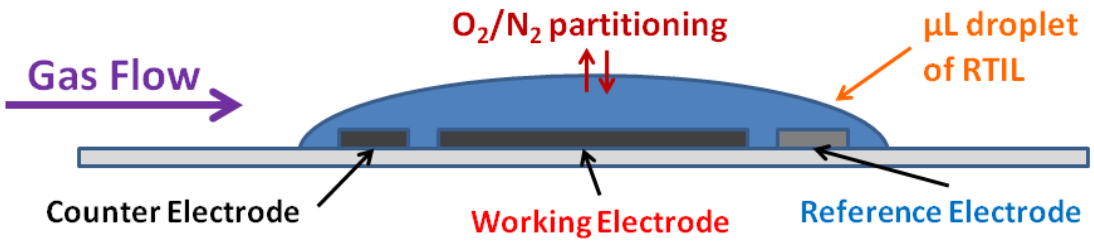

Figure 2.4. An illustration of the side-view of an SPE with a microlitre droplet of RTIL deposited onto its surface. The RTIL covers the working, counter and reference electrodes of the SPE, and is positioned within the T-cell (see Figure 2.2 and 2.3). The gas-mixture flows through the T-cell, and the gases (O_2 and N_2) are partitioned at the gas-RTIL interface into the RTIL. The partitioned gases then diffuse into the bulk of the RTIL, down the concentration gradient. The electrochemically active analyte-gas (O_2) is then electrochemically detected at the working electrode-RTIL interface.

Sufficient time was allowed for the introduced gas-mixture to partition across the gas-RTIL interface and diffuse into the RTIL until concentration equilibrium was reached. This was determined by first initially running repeated CV scans at fixed time-intervals (starting at ~30 mins) on a sample. The time-interval was gradually reduced once the voltammogram has stabilized in response to the introduced 100 % vol. O_2 concentration. The minimum duration between scans, necessary for the depleted oxygen at the working electrode (during a typical CV scan) to replenish from the bulk, was thus determined by noting a decrease in oxygen-reduction currents. Once the necessary O_2-replenishing time is determined, the time-interval scans were set slightly higher for subsequent scans. Consecutive scans were then conducted to estimate the time necessary for a N_2-purged aliquot of a given RTIL to be saturated with oxygen (i.e. flowing at 100 % vol.), and similarly the time necessary for the saturated aliquot of RTIL to be completely purged of oxygen (with 100 % vol. N_2 flow).

For plain (un-doped) RTILs, the O_2-saturation and N_2-purging duration necessary were determined to be similar, which could vary dependent on the volume and spread of the RTIL aliquot introduced to the SPE surface (which, in turn, determines the effective electrolyte film thickness). Thus, for the determination of these *gas-concentration equilibration* times, care was taken to ensure minimum spread of the RTIL (i.e. just sufficient to cover the three integrated electrode screen printed electrode surfaces) for a fixed volume aliquot of the RTILs. Small and large flow rates, from 10 to 1000 standard-cubic-centimetre-per-minute (sccm), were tested in the initial experiments with the T-cell, and a flow rate of as little as 10 sccm was found to be sufficient and did not observably impact upon the peak currents measured (provided that no significant leakages are present). A higher than the necessary flow rate was set to ensure fast displacement of pre-existing gases within the T-cell while avoiding depleting the cylinder too rapidly.

2.3.2. Macrodisk working electrodes preparation

For experiments on the macrodisk electrode, a 1.6 mm diameter platinum electrode (BASi, West Lafayette, Indiana, USA) was hand polished in a "figure-8" motion on soft lapping pads (Buehler, Illinois) with decreasing particle size of alumina (3 μm, 1 μm and 0.25 μm) using milli-Q water as the lubricant prior to each experiment. The electrode was sonicated first in milli-Q water for 15 mins, and followed by ethanol for 15 mins to remove any alumina particles, and finally washed with acetonitrile and dried under a nitrogen gas stream. The working electrode was employed in a conventional 3-electrode arrangement – with a 0.5 mm diameter Ag wire quasi-reference electrode (Sigma-Aldrich Pty Ltd., NSW, Australia) for non-aqueous experiments, and Ag|AgCl|KCl (1.0 M) (BASi, Indiana, USA) for aqueous experiments with 0.1 M KCl as supporting electrolyte, and with a 0.5 mm diameter platinum coil wire counter electrode (Goodfellow Cambridge Ltd., UK), inserted into a small home-made glass pot designed to hold up to 3 mL of solvent.

Electrolyte of ~1 mL was placed in the cell and purged with nitrogen gas by bubbling for 30 mins (to obtain a "blank" voltammogram) prior to the introduction of oxygen gas. Oxygen gas (99.5 %) was then bubbled directly into the electrolyte with stirring through a glass Pasteur pipette. A minimum of 10 mins of gas bubbling and stirring was allowed before commencement of measurements, which was observed to be more than sufficient to produce stable peak currents. The aggressive stirring action induces tiny bubbles (especially in the more viscous RTILs), which thus extends the effective area of the electrolyte in contact with the bubbling gas. This allows the gas concentrations within the electrolyte to reach equilibrium much quicker than would have been if the gas mixture were simply flowed directly above the surface of the electrolyte.

2.4. Scanning electron microscopy imaging

Scanning electron microscopy (SEM) was performed on the working electrode surfaces of SPEs. The images were obtained using a Zeiss Evo 40XVP model SEM instrument. The SEM images were collected at 2000x magnification, with an accelerating voltage of 10-15 kV, working distance of 8.5 mm and aperture spot size of 350.

3. Oxygen reduction voltammetric behaviour on platinum macrodisk and screen printed electrodes in room temperature ionic liquids.

In this chapter, viability of the screen printed electrode surfaces was investigated for their application in the sensing of oxygen gas in room temperature ionic liquids. The voltammetric shapes and peak-to-peak separations for the $O_2/O_2^{\bullet-}$ redox couple on a conventional Pt macrodisk working electrode in a bulk RTIL volume were compared to that for Pt-SPEs covered with a microlitre droplet of RTIL. Eight RTILs have been employed, and two RTILs have been chosen for further analytical characterisation on four different SPE surfaces (carbon, gold, platinum and silver). The results obtained reveal the suitability of four types of commercially available SPEs for oxygen gas-sensing in these RTILs. This work has been recently published in a peer-reviewed scientific journal, Electrochimica Acta. [141]

3.1. Introduction

Screen printed electrodes (SPEs) are widely investigated as simple, three-electrode planar surfaces for electrochemical sensing applications, and may be ideal for gas-sensing purposes when combined with non-volatile room temperature ionic liquids (RTILs). [142] However, despite their wide use, there is still relatively little fundamental understanding of analyte redox behaviour at these surfaces. Voltammetry for ammonia oxidation on three SPE surfaces (carbon, platinum and gold) from DropSens was recently reported by our research group [149]. No obvious peaks were observed on carbon SPEs, but it was found that the voltammetry on both Au and Pt-SPEs was similar to that observed on Pt microelectrodes in RTILs, suggesting

that the electrochemical reaction mechanisms were the same. Stable and reproducible peak currents were observed at different concentrations and a limit of detection of 50 ppm for ammonia on non-modified Pt-SPEs was obtained, demonstrating good analytical utility for ammonia sensing. [149] Voltammetric reduction currents for oxygen on carbon SPEs in RTILs–Au-nanomaterial composites were reported [154], showing linear current responses over a concentration range of 20-100 % vol. O_2. Gębicki et al., in the same year [98] also published their results of RTIL film thicknesses dependent response time of imidazolium-based RTILs with DropSens Au-SPE. Chemically irreversible voltammetry for O_2 reduction was reported in the three chosen imidazolium-based RTILs on Au SPEs, but their analytical utilities and reaction mechanism were however not investigated. Our group had also previously tested Zensor SPEs with various RTILs, and we have found that the electrode surfaces were unstable and disintegrate when used with RTILs. Despite of the obvious advantages of using non-volatile RTILs with low-cost SPEs for gas-sensing applications, there has been relatively little work done on fundamental gas behaviour and gas-sensing using the RTIL/SPE platform. This chapter aims to explore the potential of four different SPEs of standard electrode materials (namely platinum, gold, silver and carbon) purchased from Dropsens with eight different ionic liquids to compare their viability as oxygen AGSs. Their analytical utilities with two selected RTILs will also be investigated. This would allow selection of the best SPE for subsequent O_2 sensing experiments with RTIL-electrolytes in the following chapters.

3.2. Experimental

The eight different RTILs used in this chapter were listed under Table 2.2 (in Section 2.1.1), while details of the four different SPEs (C, Au, Pt, Ag) were specified under Table 2.3 in Section 2.1.2. The experimental setup with the macrodisk WE and the SPEs were as detailed according to Section 2.3. No attempts were made to mechanically polish the SPEs, nor to electrochemically "activate" or pre-treat their surfaces using widely-used methods in aqueous solvents [123]. Instead, repeated CV scans were conducted, first with a N_2-purged (blank) RTIL, followed by an O_2-saturated RTIL for 12 times each (with 10 mins intervals between scans) to "pre-condition" the surface before commencing with the collection of O_2 concentration calibration data. The impact that these standard activation protocols have on the Pt-SPE for O_2 sensing in RTILs has been investigated and will later be discussed in Section 5.4.1. It was found that the standard activation protocols for SPEs were in fact unsuitable pre-treatment protocols for the sensing of O_2 in RTILs. Approximately eight repeated CV scans were found to be initially needed in the presence of 100 % vol. O_2 to acquire a sufficiently stable signal. A total flow rate of 250 sccm was used consistently for all experiments on the SPEs reported in this chapter. From there on, typically 15 mins were allowed before the voltammetry was recorded after each change of O_2 gas concentration. The total time required for the equilibration of the gas-concentration in the flow-cell, and the partitioning of the gas-mixture into the RTIL electrolyte, was determined to be much shorter (and can be as low as 4 mins; depending on the spread of the RTIL) in separate amperometric experiments for the 7 μL aliquot used. The waiting time between repeated scans, of 10 mins at a fixed concentration of O_2, was typically used (see Section 2.2). This would be more than sufficient for the replenishment of depleted O_2 after the previous CV scan.

The minimum equilibration times for the partitioning and diffusion of the gases were dependent on the surface area to volume ratios, and is thus dependent upon the volume and spread of the RTILs applied. Care was taken to ensure that the RTILs were consistently spread, confined at the blue polymer dielectric mask surrounding the screen printed electrodes (see the zoomed in representation of an SPE in Figure 2.2) for all samples. The microlitre volume of RTILs used prevents bubbling of oxygen gas directly into the solvent, and makes stirring unfeasible. Instead, in this setup, the flowing gases had to displace the atmosphere within the flow-cell before partitioning into the RTIL. From amperometric experiments results, the current response was found to start visibly changing within ca. 30 s after switching to a different oxygen concentration; this is dependent on the volume of the cavity within the T-cell, coupled with the gas flow rate used, and thickness of the drop-casted RTIL aliquot above the SPE working electrode surface. Some differences in equilibration times were noticed between the eight studied RTILs, as would be expected given their different viscosities (and hence diffusion coefficients of gases) as summarized in Table 3.1. However, 15 mins was found to be more than sufficient to achieve stable CV responses in all RTILs and was uniformly used for the sake of consistency in all experiments. Background/baseline subtractions were performed by respectively subtracting the current measured from the blank CV (i.e. for 0 % vol. O_2) from the measured peak currents, I_p, at the same potential. The surface of a Pt macrodisk electrode was modified with small amounts of particles from a Pt-SPE. This was accomplished by first scraping off the screen printed Pt material from the WE of a *fresh-out-of-the-box* Pt-SPE into a vial. The material was then further crushed with a glass stirring rod and sonicated in 10 μL of acetonitrile, before it was drop-casted onto a Pt macrodisk electrode.

3.3. Results and discussion

To investigate the suitability of SPE/RTIL systems for oxygen gas monitoring and sensing, cyclic voltammetry (CV) for O_2 reduction was recorded on Pt-SPEs in eight aprotic RTILs with wide electrochemical windows, namely $[C_2mim][NTf_2]$, $[C_4mim][NTf_2]$, $[C_6mim][FAP]$, $[C_4mpyrr][NTf_2]$, $[C_4mim][BF_4]$, $[C_4mim][PF_6]$, $[P_{14,6,6,6}][NTf_2]$ and $[P_{14,6,6,6}][FAP]$ (see Figure 2.1 for ion structures). Voltammetric responses for oxygen reduction in the same eight RTILs were also measured first on polished conventional Pt macrodisk working electrode to enable an accurate comparison to be made. Finally the analytical utility of four different non-ideal screen printed surfaces (Pt, Au, Ag, C) was assessed by analysing the oxygen concentration calibration data in two of the eight RTILs tested.

3.3.1. Oxygen reduction on a Pt macroelectrode in 8 RTILs

Figure 3.1 shows the typical oxygen reduction CV collected for eight different O_2-saturated RTILs, conducted on a polished Pt macrodisk electrode at a scan rate of 100 $mV \cdot s^{-1}$. The blank CVs (i.e. in the absence of oxygen) are shown in Figure 3.1 as dotted lines. Quasi-reversible O_2 reduction was observed in all eight RTILs. This was believed to be due to a simple one-electron reduction mechanism that has been commonly reported in aprotic RTILs and organic solvents (see Table 1.2), specifically:

$$O_2 + e^- \rightleftharpoons O_2^{\bullet -} \qquad \textbf{(3.1)}$$

Voltammetry for O_2 reduction has been widely reported in several of these RTILs on: glassy carbon (GC)/Au/Pt macro-,[99, 224, 225] Pt/Au/GC micro-[100, 148, 226, 227] and Au

micro-array [228] electrodes. Voltammetric wave shapes reported in those papers were similar to those observed here (in Figure 3.1). Peak-to-peak separations for the $O_2/O_2^{\bullet-}$ redox couple, $\Delta E_{p\text{-}p}$, presented in Figure 3.1 are listed in Table 3.1. In RTILs containing imidazolium and pyrrolidinium cations, the $\Delta E_{p\text{-}p}$ values vary extensively in different ionic liquids, and typically fall in the range from 280 to 520 mV. However, significantly greater $\Delta E_{p\text{-}p}$ values were observed for the two tetraalkylphosphonium cation ($[P_{14,6,6,6}]^+$) based RTILs – with more than a 1 V separation in $[P_{14,6,6,6}][NTf_2]$ and more than 2 V in $[P_{14,6,6,6}]$[FAP]. The unusually wide peak-to-peak separation for $O_2/O_2^{\bullet-}$ has been observed previously on Pt microelectrodes in the same two RTILs with tetraalkylphosphonium cations. [226] Previously, it was suggested that the phosphonium cation acts as a weak acid, giving rise to an ECE reaction. [103, 226]

The peak-to-peak separations given in Table 3.1 show no obvious dependence on solvent viscosity, suggesting that other physical properties of the RTIL anions and cations contribute to the different kinetics of the $O_2/O_2^{\bullet-}$ redox couple. It is also to be noted that the $\Delta E_{p\text{-}p}$ value (at 284 mV) for $[C_4mpyrr][NTf_2]$ on Pt macrodisk electrode is substantially better than the corresponding literature value (at 563 mV) [84] obtained with a Pt microdisk electrode listed (Table 1.4). Generally, the data presented in Figure 3.1 and Table 3.1 correspond well to that reported at conventional solid electrodes and can serve as a comparison standard to voltammetry that is observed on SPEs, as discussed in the next section.

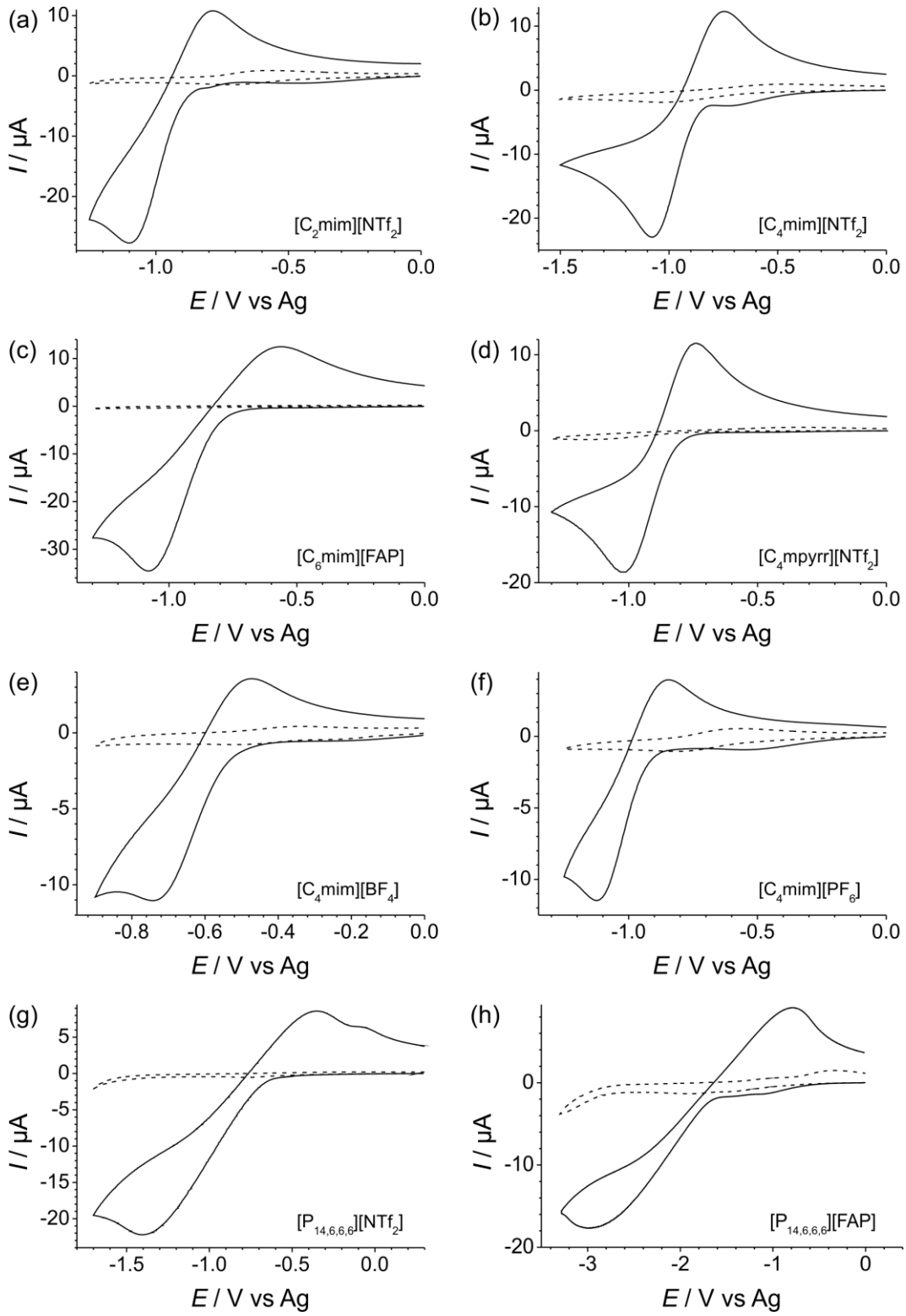

Figure 3.1. Cyclic voltammograms on a conventional platinum macrodisk electrode (diameter 1.6 mm) at a scan rate 100 mVs^{-1} for the reduction of 100 % vol. O_2 in eight RTILs: **(a)** [C_2mim][NTf_2], **(b)** [C_4mim][NTf_2], **(c)** [C_6mim][FAP], **(d)** [C_4mpyrr][NTf_2], **(e)** [C_4mim][BF_4], **(f)** [C_4mim][PF_6], **(g)** [$P_{14,6,6,6}$][NTf_2] and **(h)** [$P_{14,6,6,6}$][FAP]. The dotted line is the response in absence of O_2.

Table 3.1. Peak-to-peak separations for the $O_2/O_2^{\bullet-}$ redox couple, $\Delta E_{p\text{-}p}(O_2/O_2^{\bullet-})$, obtained on a Pt macrodisk electrode (Figure 3.1) and on a Pt-SPE (Figure 3.2) in eight RTILs, in order of increasing solvent viscosity.

RTIL	Viscosity at 293 K / cP [84, 147, 156]	$\Delta E_{p\text{-}p}(O_2/O_2^{\bullet-})$ on Pt macrodisk / mV	$\Delta E_{p\text{-}p}(O_2/O_2^{\bullet-})$ on Pt-SPE / mV
$[C_2mim][NTf_2]$	34	314	-
$[C_4mim][NTf_2]$	52	462	-
$[C_6mim][FAP]$	74	518	-
$[C_4mpyrr][NTf_2]$	89	284	355
$[C_4mim][BF_4]$	112	269	-
$[C_4mim][PF_6]$	201	278	-
$[P_{14,6,6,6}][NTf_2]$	450	1051	No reduction peak
$[P_{14,6,6,6}][FAP]$	464†	2197	No reduction peak

† *Measured at 298 K.*

3.3.2. Oxygen reduction on Pt screen printed electrodes in 8 RTILs

Figure 3.2 shows typical oxygen reduction CV collected for eight different O_2-saturated RTILs, conducted on DropSens Pt-SPEs at a scan rate of 100 $mV \cdot s^{-1}$. Both the first (dot dashed line) and second (solid line) voltammetric scans are presented, along with the response in the absence of oxygen (dotted line). It was observed that the first scans were, in general, substantially different (with respect to shapes, peak potentials and peak currents). The CVs from the second and subsequent scans tends to be more stable, but requiring up to eight repeat scans for O_2 (at 100 % vol.) peak currents and positions to sufficiently stabilize.

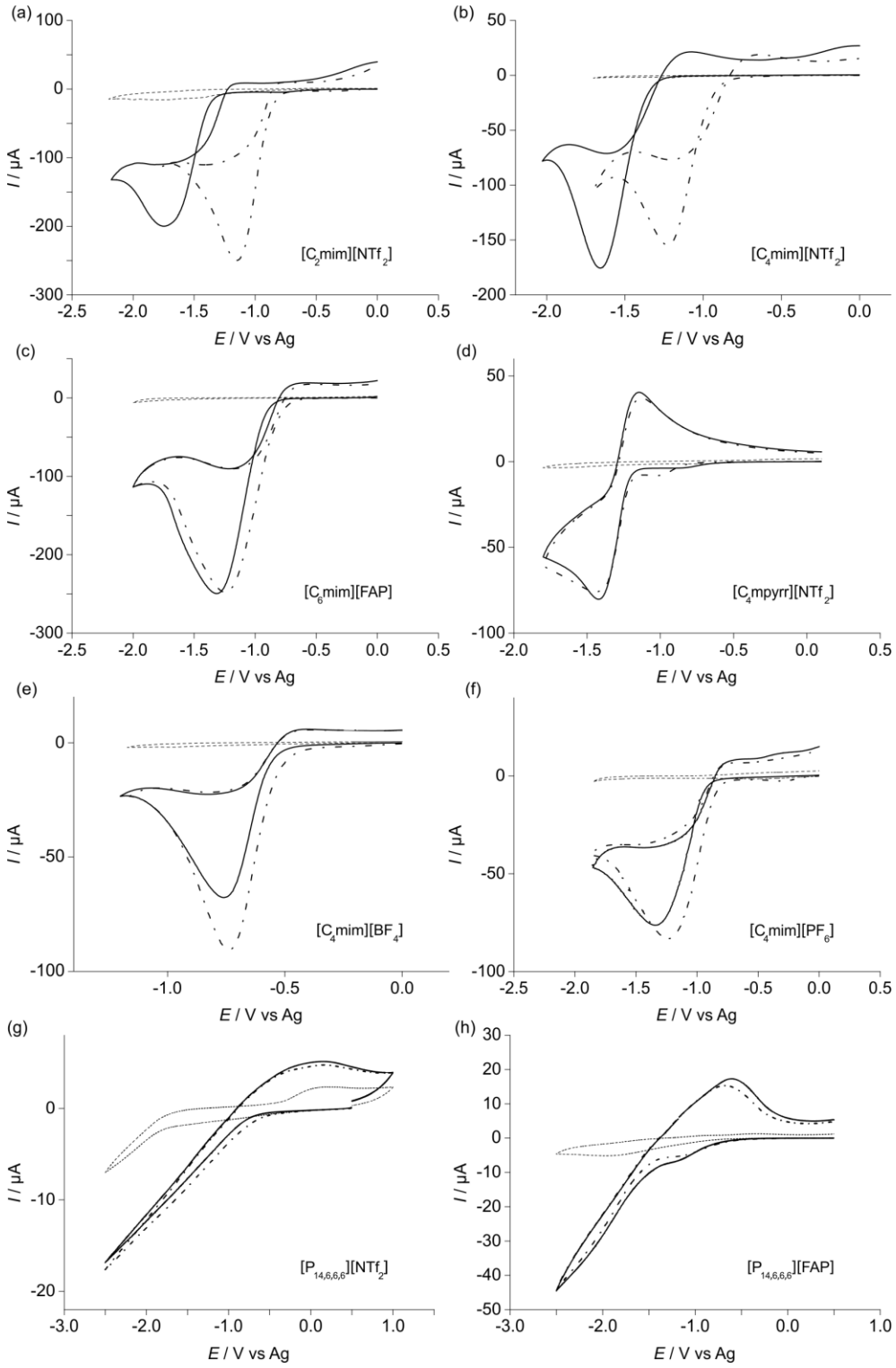

Figure 3.2. Cyclic voltammograms on a screen printed DropSens platinum electrode (diameter 4.0 mm) at a scan rate 100 mVs^{-1} for the reduction of 100 % vol. O_2 in eight RTILs: **(a)** $[C_2mim][NTf_2]$, **(b)** $[C_4mim][NTf_2]$, **(c)** $[C_6mim][FAP]$, **(d)** $[C_4mpyrr][NTf_2]$, **(e)** $[C_4mim][BF_4]$, **(f)** $[C_4mim][PF_6]$, **(g)** $[P_{14,6,6,6}][NTf_2]$ and **(h)** $[P_{14,6,6,6}][FAP]$. Dot dashed line is the first scan, solid line is the second scan and dotted line is the response in absence of oxygen.

It is clearly evident from this figure that the voltammetric wave shapes are drastically different on the SPEs compared to that for the macrodisk electrode (as shown in Figure 3.1). In particular, in the five imidazolium cation based RTILs tested, significant closeness or "cross-over" between the cathodic and anodic scans were observed in the voltammetry. This suggests that the surface has somehow been modified or changed as a result of the oxygen reduction reaction. The lack of an anodic reverse peak in these five RTILs also indicates that there is a follow-up chemical reaction occurring, thus removing the electrogenerated superoxide from the working electrode surface.

3.3.2.1. Cross-over characteristic in CVs of oxygen reduction in imidazolium-based RTILs on SPEs.

The cause of the cross-over voltammetry is suspected to be due to chemical reactions of the electrogenerated superoxide with one or more of the compounds present in the paste of the SPE working electrode. In order to test this hypothesis, the surface of a Pt macrodisk WE was modified with Pt-SPE material following the procedure at the end of Section 3.2. The modified electrode was then immersed in O_2-saturated [C_2mim][NTf_2]. This RTIL was chosen because it is one of the imidazolium-based RTILs where cross-over CV was observed. The resulting oxygen CV (in Figure 3.3) shows cross-over identifiably similar to that obtained with the Pt-SPE as reported in Figure 3.2 (a), but which was absent from the voltammetry collected with an un-modified Pt macrodisk electrode (in Figure 3.3). This experiment ruled out the possibility that the altered CV is caused by other factors, such as: reactions with the ceramic substrate or the surrounding dielectric polymer mask, reference or counter electrodes, or impurities in the RTIL. Chemically irreversible CV for oxygen reduction on gold SPEs in three imidazolium ionic liquids has also been reported by

Gebicki et al., [127] but the cause of the irreversible voltammetry was unknown. It is highly possible that a similar reaction also occurred between superoxide and the ink/pastes in the Au SPEs previously reported.

It should be noted that in a previous work on ammonia gas oxidation on C, Pt and Au SPEs in $[C_2mim][NTf_2]$, [149] no unusual voltammetry or change in reaction mechanism was observed on SPEs (compared to that obtained with conventional solid electrodes). This suggests that the reaction with material(s) present in the screen printing pastes of SPEs only occurs when highly reactive species such as superoxide are present. The subsequent desorption of the product(s) from the WE surfaces during the reverse scan of the CV could lead to the cross-over characteristic that is observed.

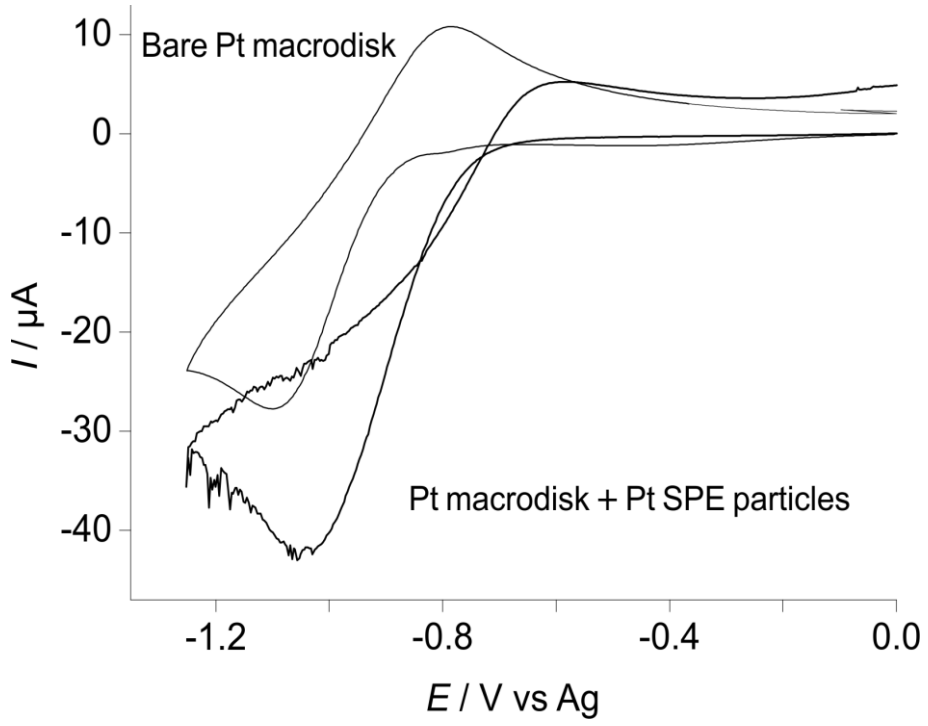

Figure 3.3. Cyclic voltammetry for 100 % vol. O_2 in $[C_2mim][NTf_2]$ at a scan rate of 100 mVs^{-1}. Thin line represents response on a bare Pt macrodisk electrode (of 1.6 mm diameter) and thicker line represents response on the same electrode covered with Pt-SPE particles.

Another plausible explanation considered for the unusual voltammetry observed was that products from the SPE counter electrode are reaching the working electrode within the timescale of the experiment. Using the equation:

$$t = \frac{d^2}{D} \qquad \textbf{(3.2)}$$

where *t* is the time, *d* is the maximum distance the product could travel within *t*, and *D* is the diffusion coefficient. By taking *t* to be at 50 s (which is equivalent to two consecutive CVs conducted over 5 V at 100 mVs^{-1}) while using a generous value for *D* (for the counter electrode reaction products) at the value of 10×10^{-10} $m^2 \cdot s^{-1}$, the products of the counter electrode process could only travel a distance, *d*, of ~0.22 mm. Since the working and counter electrode are separated by 1 mm, this implies that the closely-positioned working and counter electrode are not likely to cross-contaminate one another in the ionic liquid during the scan (which may a possibility in an aqueous sample), and is thus ruled out as a possible cause of the cross-over characteristic seen on Pt-SPEs with imidazolium based RTILs.

For the two RTILs that contain the $[P_{14,6,6,6}]^+$ cation (in Figure 3.2 (g) and (f)), there was no well-defined O_2 reduction peak on the SPE surface but only a gradual increase in reduction current until the edge of the available electrochemical window. This indicates that these two RTILs are not suitable for oxygen sensing on Pt-SPEs. Interestingly, it was found that in one out of the eight RTILs studied ($[C_4mpyrr][NTf_2]$, Figure 3.2(d)), the shape of the voltammetry on Pt-SPE was relatively similar to that observed on a conventional macrodisk electrode. The clear existence of an oxidation peak on the reverse sweep in Figure 3.2 (d) indicates that the electrogenerated superoxide is stable and re-oxidised back to oxygen at ca. -0.9 V vs. Ag. The peak-to-peak separation for the $O_2/O_2^{\bullet-}$ redox couple in $[C_4mpyrr][NTf_2]$ on Pt-SPEs (355 mV) was found to be only slightly larger than what was observed on the Pt

macroelectrode (331 mV). This suggests that the two surfaces give rise to similar kinetics. It is unclear as to why the reaction is chemically reversible in only this particular RTIL on the SPEs (Figure 3.2).

It was postulated that this may be due to the more chemically and electrochemically inert pyrrolidinium cation (as previously demonstrated by Compton and Wibowo, who have shown that only this RTIL and two other tetraalkylammonium based RTILs were capable of supporting alkali metal deposition [229]). Further, in the literature, it has been suggested that both imidazolium and phosphonium cations are weakly acidic [103, 105, 143, 163, 226, 230] and may partake in an acid-base reaction in the presence of mildly basic species such as superoxide [102, 105]. It appears that although this acid-base reaction is not observed for O_2 reduction on conventional solid electrodes (e.g. Figure 3.1 and also Figure 3.7), the combination of superoxide with compounds in the pastes of SPEs may give rise to very basic species which may subsequently react with the weakly acidic RTIL cations. On the other hand, the pyrrolidinium cation ($[C_4mpyrr]^+$) does not have an acidic proton and consequently, electrogenerated superoxide would be stable at the screen printed surface. As mentioned under Section 1.3.2.4, the reaction of freshly generated superoxide with trace impurities may lead to chemical and electrochemical irreversibility of the $O_2/O_2^{\bullet-}$ redox couple. [103] Since the unusual voltammetric behaviour was not observed on conventional solid electrodes, this source of impurity is likely from within the SPE material rather than from the RTIL. Neutrally charged products may weakly adsorb onto the WE surface during the forward cathodic scan, while it's desorption during the reverse anodic scan could lead to the voltammetric cross-over characteristic seen (e.g. Figure 3.2) due to the resultant shifting WE surface energy.

To further verify these, an experiment was carried out to determine the approximate volume ratio of $[C_4mpyrr][NTf_2]$:$[C_2mim][NTf_2]$ RTIL mixtures on Pt-SPEs at which the reversibility

of the $O_2/O_2^{\bullet-}$ redox reaction changes. The results of four RTILs mixtures of different volume ratios are presented in Figure 3.4 plotted with the same axes scales. A larger reduction peak current is observed in $[C_2mim][NTf_2]$ compared to $[C_4mpyrr][NTf_2]$ as shown respectively in Figure 3.4 (d) and (a). This has likely to do with their different solvent viscosities and oxygen partitioning coefficients. The voltammetries of the mixtures presented in Figure 3.4 (b) and (c) reveals that cross-over is sensitive to the composition of the RTIL medium. At a $[C_4mpyrr][NTf_2]$:$[C_2mim][NTf_2]$ volume ratios of 50:50, the voltammetry exhibits this cross-over characteristic; however, when 60 % vol. or more of $[C_4mpyrr][NTf_2]$ is present, the cross-over is absent. It was additionally noted that the relative height of the superoxide oxidation peak increases with increasing ratio of $[C_4mpyrr][NTf_2]$ in the mixture. This is an extremely interesting observation and highlights that the choice of RTIL is very important for electrochemical reactions where highly reactive species are present.

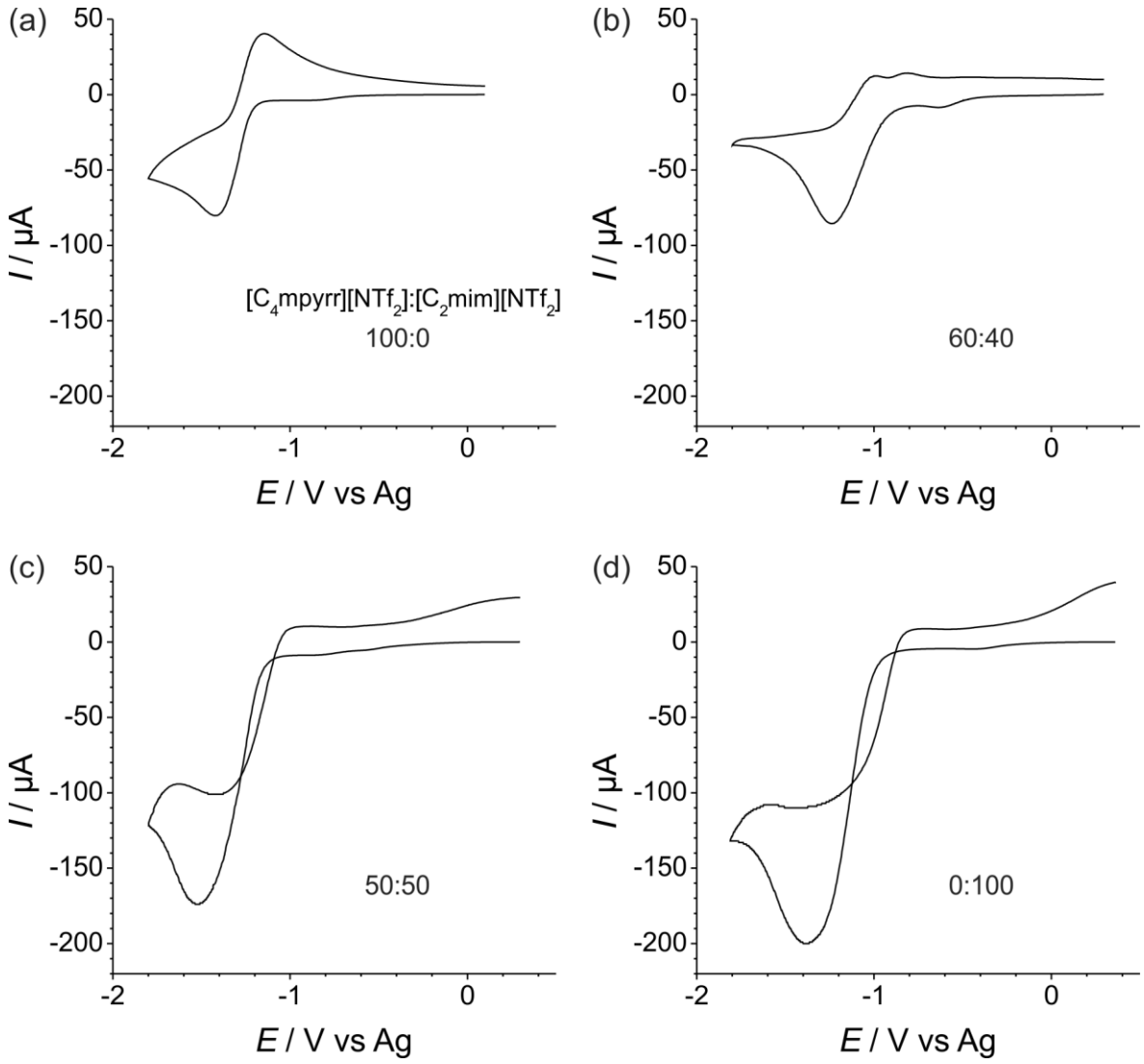

Figure 3.4. Cyclic voltammetry for 100 % vol. O_2 on a DropSens Pt electrode at a scan rate of 100 mVs^{-1} in electrolytes with different $[C_4mpyrr][NTf_2]$:$[C_2mim][NTf_2]$ mixing-ratios as labeled for each voltammograms. The voltammograms were all plotted with the same x-axis and y-axis scales.

3.3.3. Oxygen reduction on four different SPE surfaces in RTILs

Since we have shown that the voltammetry for O_2 reduction on a Pt-SPE is significantly different to that on a macrodisk electrode in seven of the eight RTILs, it is useful to also study other SPE surfaces to see if similar behaviour occurs, and ultimately to see if this affects the analytical utility of the surface for oxygen sensing. Four common working electrode surfaces (carbon, gold, platinum and silver) were employed for this study, and CVs

were recorded at various concentrations of O_2. Two RTILs have been chosen for this study, one where no obvious cross-over voltammetry is observed on SPEs ($[C_4mpyrr][NTf_2]$) and one where obvious cross-over occurs ($[C_2mim][NTf_2]$). It is also useful to look at the structure of the DropSens SPE surfaces using imaging techniques to see if this can be related to the observed voltammetry.

3.3.3.1. Surface structure of four different screen printed working electrodes

Scanning electron microscopy (SEM) images of the four DropSens working electrode surfaces were recorded (with the parameters specified in Section 2.4) to investigate and compare their topography and structure. Figure 3.5 shows the SEM images obtained for C-, Au-, Pt- and Ag-SPE surfaces. The images show that the carbon surface has flake-like particles and cracks indicating that the particles may not be held together strongly. On the gold surface tiny *islands* of gold scattered over the surface are present. It can also be seen that the platinum surface is more porous compared to silver and gold surfaces, and the general appearance of the silver SPE is smoother than the other three surfaces. It is clear from these images that the porosity and roughness of the SPE surfaces are significantly different depending on the material used for the working electrode, and this in turn may affect the measured voltammetry using these screen printed surfaces.

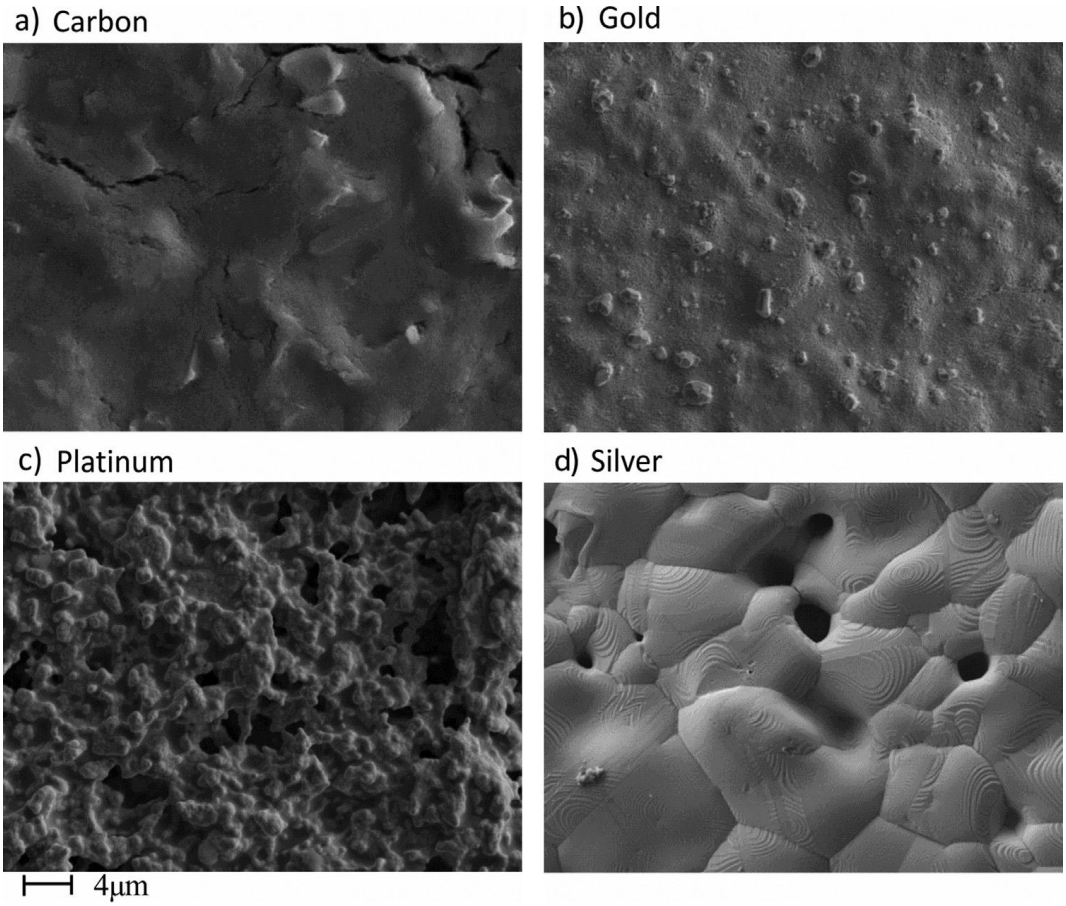

Figure 3.5. Scanning electron micrographs (taken by Krishnan Murugappan) of fresh-out-of-the-box DropSens SPEs for screen printed **(a)** carbon, **(b)** gold, **(c)** platinum and **(d)** silver electrodes.

3.3.3.2. Analytical utility for oxygen reduction on four different SPEs in [C_4mpyrr][NTf_2]

Figure 3.6 shows the reduction of oxygen at different concentrations (0, 10, 20, 40, 60, 80 and 100 % vol. by volume, nitrogen fill) in the RTIL [C_4mpyrr][NTf_2] on four SPE surfaces (C, Au, Pt and Ag). The measurements were performed when the voltammetry had stabilized after initial cycles. On all surfaces, chemically reversible reduction waves are seen and the peak currents increase with increasing O_2 concentration (as previously reported on Au microelectrodes, [100] Pt macroelectrodes [224] and carbon SPEs [154] in RTILs). On the carbon

SPE (Figure 3.6 (a)), a very high background current is observed in RTILs (as previously reported by our research group when studying ammonia oxidation on SPEs). [149] There are also some small impurity peaks present (e.g. oxidation peak at ~-0.5 V on C, ~-1.0 V on Au, and reduction peak at ~-0.8 V on Ag), which are also present in the blank scans (dotted lines). Contributing factors to these peaks may include the fact that the surfaces were not polished or cleaned before experiments, the presence of intrinsic electrochemically active materials in the SPE pastes, or the fact that the RTIL was not evacuated in vacuum prior to experiments (as explained in Section 3.2). However, these peaks do not interfere with the measurements of peak currents due to oxygen reduction since background subtraction was employed.

The relative magnitude of the peak current varies between the carbon, gold and platinum surfaces, despite the screen printed working-electrode surfaces having the same manufacturer specified nominal diameter of 4.0 mm, as listed in Table 2.3. Assuming that the transport of oxygen to the electrode is fully diffusion controlled, this suggests that the electrochemically active area varies between the three surfaces, and is unsurprising considering the different surface structures observed in the SEM images as shown in Figure 3.5. In Figure 3.6, the reduction peak on carbon is roughly twice as large as on Au, while the peak on Pt is approximately two thirds that of Au. The diameter of the screen printed silver surface is significantly smaller (at 1.6 mm) compared to the C, Au and Pt (4 mm) SPEs; and as a result, the current Ag-SPEs is approximately $1/5^{th}$ compared to that on the Pt- and Au-SPE. However, the current density of the Ag-SPE was calculated to be ca. 30 % greater than that of Pt/Au-SPE. This is even though the Ag-SPE surface appears to be much smoother than the other two SPEs, while Pt is well known to have the highest activity for oxygen reduction reaction (ORR) in fuel cells. [231] A plausible explanation could be that significantly more of the metal particles are exposed on the surface on the Ag-SPE compared to Pt- and Au-SPEs,

perhaps due to differences in ratios of metal to binding material required for their preparation during manufacturing.

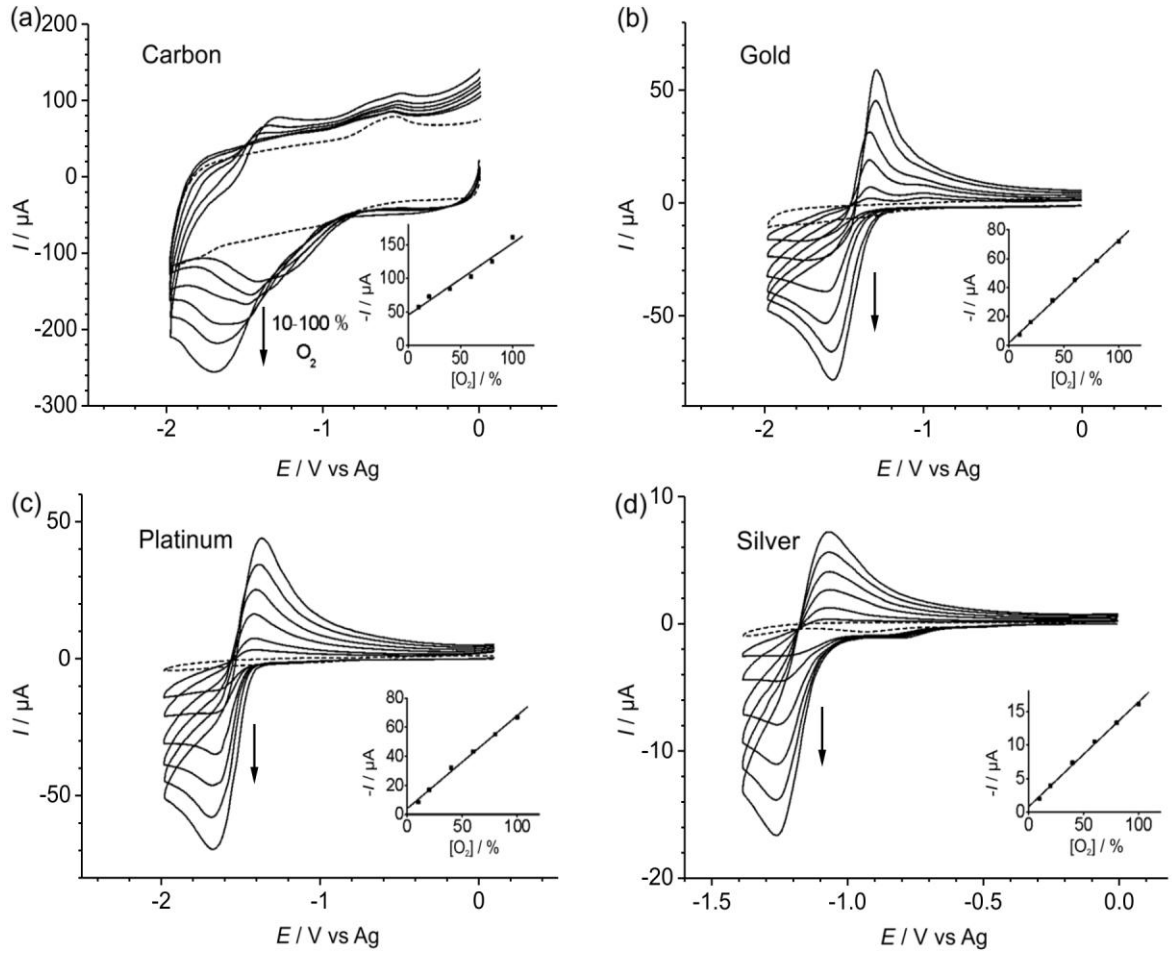

Figure 3.6. Cyclic voltammetry for O_2 reduction in $[C_4mpyrr][NTf_2]$ on **(a)** C, **(b)** Au, **(c)** Pt and **(d)** Ag SPEs at 10, 20, 40, 60, 80 and 100 % vol. O_2 at a scan rate of 100 mVs^{-1}. The dotted line is the response in the absence of oxygen. The insets are the corresponding calibration plots of background subtracted reduction peak current vs. % vol. O_2 and the line of best-fit.

A very important observation to note is that after experiments using C-SPEs for O_2 sensing, the RTIL solvent became brownish/black, probably due to materials from the C-SPE leaching from the electrode into the RTIL. This is supported by the observation that after removing the RTIL from the surface, the surface looked faded in comparison to a fresh C-SPE. This was

only found to happen when a potential is applied and did not occur when the surface is simply covered with the RTIL for extended periods of time. However, despite the obvious degradation of the carbon surface, CV can still be recorded at different concentrations and reasonable calibration graphs could be extracted.

The insets to Figure 3.6 show the corresponding plots of (baseline corrected) peak current versus % vol. O_2 and the best-fit straight-line. The equations for the calibration curves and their linear regression coefficient, R^2, values are given in the top half of Table 3.2. The LOD values, derived with equation (D.1) in the appendix, were found to be within a moderate percentage range between 4 to 20 % vol. For a real oxygen sensor, the ability to measure between ~5 to 20 % vol. O_2 in the atmosphere is sufficient, since in most real-world conditions, the concentration of O_2 lies near 20 % vol. Anything less than this requires investigation, so a sensor with a linear response from a few % vol. up to 20 % vol. concentrations is optimal. All SPEs satisfy this requirement, with the exception of carbon, possibly due to the degradation of the surface during potential cycling in RTILs (discussed earlier). However, in spite of the excellent R^2 values reported in Table 3.2, the calibration responses were observed to vary between experiments and were dependent upon the pre-conditioning steps taken (see Section 3.2) and the duration of their use. It is also noted that the voltammetry can shift on the potential axis, probably due to the unstable screen printed silver quasi-reference electrode.

3.3.3.3. Analytical utility for oxygen reduction on four different SPEs in $[C_2mim][NTf_2]$

Since significant cross-over of the voltammetry was observed on screen printed Pt surfaces with $[C_2mim][NTf_2]$ RTIL electrolyte as shown in Figure 3.2 (a), it is of interest to see if this occurs at other surfaces in this RTIL, and ultimately if this affects the sensing ability of the surface. Figure 3.7 shows the reduction of oxygen at different concentrations (0, 10, 20, 40, 60, 80 and 100 % vol.) in $[C_2mim][NTf_2]$ on four SPEs, namely C, Au, Pt and Ag. The measurements were performed when the voltammetry had stabilized after initial cycles in the presence of 100 % vol. O_2. On carbon, there is again a large background charging current, but the reduction peak for O_2 can be clearly distinguished at different concentrations. However, there is no obvious superoxide oxidation peak, suggesting that the product may have reacted with compounds in the C-SPE paste in this RTIL. It can be seen from Figure 3.7 that the cathodic and anodic scans on Au and Ag surfaces also are very close together, although this effect is not as dramatic as on Pt surfaces, where the scans crossed over. There is a much smaller superoxide oxidation peak on Au and Ag in $[C_2mim][NTf_2]$ compared to $[C_4mpyrr][NTf_2]$, suggesting that the Au and Ag surfaces may also have been changed/modified as the result of reaction products of the superoxide/paste/RTIL interaction. There are also additional oxidation peaks between -0.5 and 0 V on all four surfaces, which may be oxidations of these reduction products at the SPEs. However, despite the unusual wave shapes on the four surfaces, the baseline corrected reduction peak currents are seen to increase linearly with concentration of O_2, as shown in the insets to Figure 3.7. Again, for the Ag-SPE, its O_2 reduction peak current is significantly lower due to its smaller WE area compared to the other SPEs (Table 2.3).

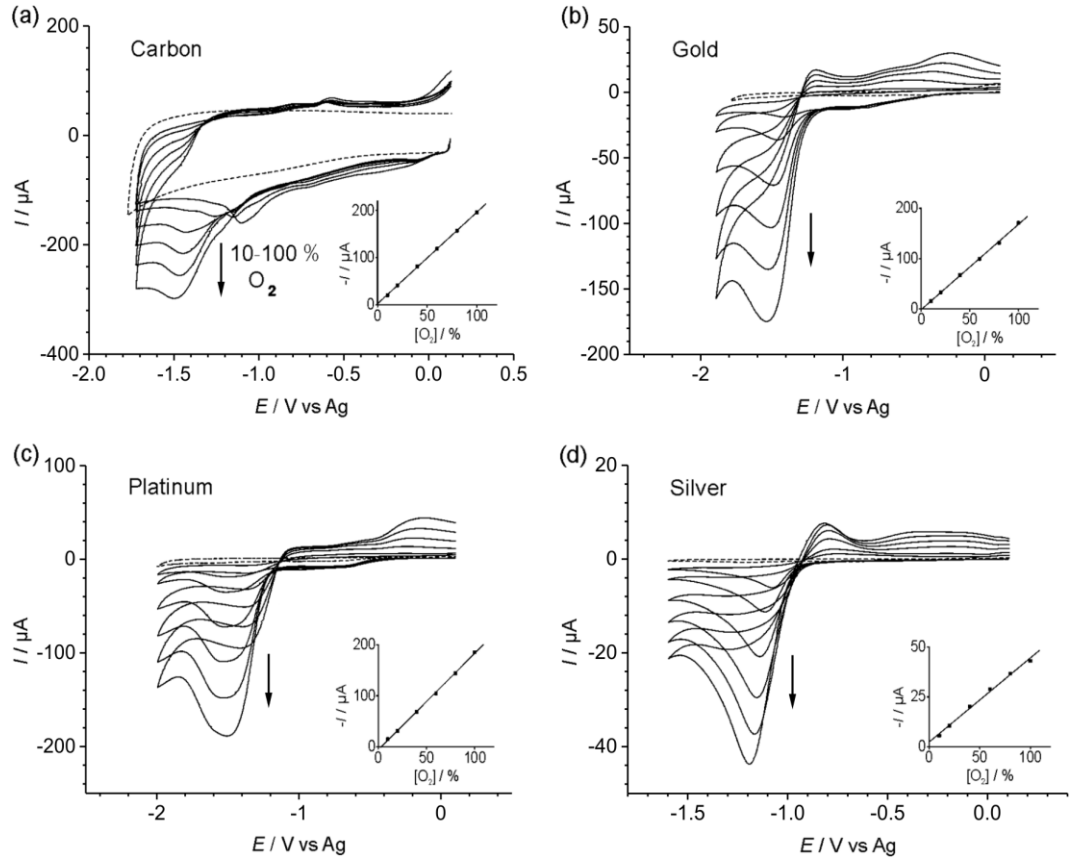

Figure 3.7. Cyclic voltammetry for O_2 reduction in $[C_2mim][NTf_2]$ on **(a)** C, **(b)** Au, **(c)** Pt and **(d)** Ag SPEs at 10, 20, 40, 60, 80 and 100 % vol. O_2 at a scan rate of 100 mVs^{-1}. The dotted line is the response in the absence of oxygen. The insets are the corresponding calibration plots of background subtracted reduction peak current vs. % vol. O_2 and the line of best-fit.

The equations for the best-fit straight-lines are given in the bottom half of Table 3.2, together with their R^2 value. Excellent linearity is observed with $R^2 > 0.99$ on all four SPEs, and C, Au and Pt were very similar with regards to sensitivity of ~2 µA $[\%O_2]^{-1}$. Similar limits of detection of a few % vol. were obtained in this RTIL, as in $[C_4mpyrr][NTf_2]$, however more pre-conditioning scans were found to be necessary before the voltammetry stabilizes. Additionally, the signals were found to degrade more quickly over prolonged use in this RTIL, possibly due to a build-up of the reaction product from the superoxide/SPE paste/RTIL reaction. In both RTILs, the silver surface gave rise to the most reproducible voltammetry and was also the easiest surface in which to regain a reliable blank signal (under

a nitrogen atmosphere) after experiments. It was impossible to regain a featureless blank signal on the other three surfaces after substantial further scanning in the RTIL in the presence of oxygen, suggesting that long-term monitoring of oxygen may not be possible on C, Au and Pt-SPEs in this RTIL. However, it was also noted that the Ag-SPE surface tends to tarnish over time in presence of moisture and air, and may thus not be robust enough to be employed for long-term sensing applications.

Table 3.2. Equations for the linear best-fit for the calibration graphs presented in Figures 3.6 and 3.7, and the corresponding limits of detection (LODs) values based on 3 standard deviations from the regression fittings.

RTIL	**SPE surface**	**Equation of calibration graph** I **/ A,** $[O_2]$ **/ % vol.**	R^2	**LOD / % vol.**
$[C_4mpyrr][NTf_2]$	C	$-I = 1.07\times10^{-6}\,[O_2] + 4.54\times10^{-5}$	0.985	20.7
	Au	$-I = 7.13\times10^{-7}\,[O_2] + 1.58\times10^{-6}$	0.999	4.5
	Pt	$-I = 6.40\times10^{-7}\,[O_2] + 4.02\times10^{-6}$	0.998	7.9
	Ag	$-I = 1.56\times10^{-7}\,[O_2] + 7.94\times10^{-7}$	0.998	6.4
$[C_2mim][NTf_2]$	C	$-I = 1.93\times10^{-6}\,[O_2] + 2.71\times10^{-6}$	0.999	1.5
	Au	$-I = 1.79\times10^{-6}\,[O_2] + 1.38\times10^{-6}$	0.999	4.0
	Pt	$-I = 1.88\times10^{-6}\,[O_2] - 5.93\times10^{-6}$	0.999	3.3
	Ag	$-I = 4.20\times10^{-7}\,[O_2] + 2.45\times10^{-6}$	0.997	8.9

3.4. Conclusion

Cyclic voltammetry for oxygen reduction in eight RTILs was examined on Pt macrodisk electrodes and Pt-SPEs, with significantly different voltammetric wave shapes observed on the two types of surface. An obvious cross-over of the voltammetry on SPEs with the use of imidazolium-based RTILs indicates that the surface has been modified, possibly as the result of the mildly basic electrogenerated superoxide [102] reacting with compounds in the Pt-SPE ink/paste which subsequently reacts with the slightly protic imidazolium cations. In contrast, this characteristic is not observed in $[C_4mpyrr][NTf_2]$, suggesting there may be a stabilizing effect from the less acidic and more chemically stable pyrrolidinium cation (compared to imidazolium and phosphonium). [163] Despite the obvious change in voltammetry and reaction mechanism, plots of peak current vs. % vol. concentration O_2 were linear in both $[C_4mpyrr][NTf_2]$ and $[C_2mim][NTf_2]$, suggesting that SPEs with RTILs may indeed be viable sensing surfaces for oxygen – with silver being the best surface in terms of reproducibility. However, significantly more pre-conditioning of the SPE surfaces were required compared to the conventional ideal surfaces of solid micro- or macro- electrodes before measurements can commence to yield reasonably reproducible response to partitioned oxygen concentrations. Additionally, the signals were found to degenerate much more rapidly on SPEs – especially in RTILs where the cross-over characteristic was observed. This suggests that these cheaply made and commercially available SPEs may only be a "single-use" sensing surface for oxygen detection in RTILs.

One pre-treatment protocol of the Pt-SPE surface was found to drastically improve the performance and robustness of SPEs for the sensing of O_2 (and other gases) with RTILs electrolytes (Chapter 5). To identify a potential pre-treatment protocol that may accomplish this, a number of pre-treatment protocols were applied on Pt-SPEs. The treated Pt-SPEs were

then electrochemically characterized with well-known redox couples, hydrogen adsorption/desorption, and other techniques (i.e. confocal Raman mapping, electrochemical impedance spectroscopy). The results of these studies will be discussed in the next chapter.

4. Survey and characterization of various pre-treatment protocols for the platinum screen printed electrode.

Results from the investigation of eight different ionic liquids on four different SPE surfaces for amperometric sensing of oxygen gas were presented and discussed in Chapter 3. It was discovered that the highly reactive superoxide radical produced from the electrochemical reduction of oxygen at these non-ideal SPE working electrode surfaces tends to lead to atypical voltammetry (compared to what is expected on respective ideal macrodisk electrode surfaces). This chapter aims to compare the viability of five different pre-treatment protocols on the Pt-SPE, with four of these based on existing methods that were reported to be ideal for carbon SPEs (namely, polishing [114], plasma cleaning [232], soaking in DMF [112], and soaking and anodizing in aqueous NaOH solution [233]) and in addition, ultrasonication in THF.

4.1. Introduction

Although various commercial brands of screen printed electrodes are now available for purchase, the specific composition of the commercial screen printed electrode materials are however not disclosed by the manufacturers. As introduced in Section 1.3.1, typical formulations of the screen-printing inks comprise of a blend of conductive material (such as synthetic grade graphite or metal particles), mixed with vinyl or epoxy-based polymeric binders (for adhesion between the conductive materials, and onto the supporting substrate) and solvents (to optimize the viscosity of the ink for the screen printing process). [122, 233] These generally electrochemically-inert binding materials could potentially block the

electrochemically active surfaces, and consequently increase the electron transfer resistance resulting in slower kinetics of heterogeneous reactions. [123, 233] As a result, the development of surface treatment methods to enhance the electrochemical properties of SPEs has been of great interest. [233]

The suitability of room temperature ionic liquids (RTILs) with various (Pt, Au, Ag and C) commercial DropSens SPEs has previously been investigated for the sensing of ammonia [142], and oxygen gases (Chapter 3). It was discovered that SPEs gave a poorer response for oxygen reduction, and the appearance of a "cross-over" characteristic, in imidazolium based RTILs. [141] It was proposed that this was due to a chemical reaction of the highly reactive superoxide product of oxygen reduction with the binding materials present on these non-ideal surfaces. [141] This demonstrates that the binding materials in SPEs could in fact undesirably interfere with the electrochemistry of certain target species.

Investigations into pre-treatment methods for SPEs have been largely focused on carbon based SPEs [112, 114, 123, 232, 233], likely due to their comparatively low cost and wide use in a range of sensing strategies. However results from Chapter 3 have shown that carbon SPEs may not perform as well compared with other available SPEs for applications that utilize certain non-aqueous solvents such as RTILs. This has motivated the pursual of alternative pre-treatment protocols for the platinum SPE in order to improve their long-term stability (specifically for gas-sensing applications in this PhD thesis). This chapter aims to compare the viability of five different pre-treatment protocols. Four of the methods were based upon existing protocols that were reported to be ideal for carbon SPEs (namely, polishing [114], UV-ozone cleaning [232], soaking in DMF [112], and soaking followed by anodizing in aqueous NaOH solution [233]) and one (ultrasonication in THF) served as a control to the specific polishing procedure investigated in this study. Here, UV-ozone cleaning (a comparable surface cleaning technique [234, 235]) was used instead of plasma cleaning due to the

unavailability of a plasma cleaner. The goal was to assess their viability as pre-treatment protocols for Pt-SPEs for the improvement of their performance, for use with RTILs for amperometric O_2 sensing.

4.2. Experimental

4.2.1. Chemical reagents

The suppliers and sources for all the chemicals used in this chapter are summarized under Table 2.1. Milli-Q grade water and ethanol were used as solvents to rinse the Pt-SPEs before and after experiments. Tetrahydrofuran and N,N-Dimethylformamide were used as received without purification. 0.5 M and 3 M Sodium hydroxide (NaOH(aq)), 0.5 M sulfuric acid (H_2SO_4(aq)), and 0.1 M potassium chloride (KCl(aq)) solutions were prepared in Milli-Q grade water. An assumption of 96.5 wt. % of sulfuric acid was made based on its hygroscopic nature and the manufacture supplied assay purity (where the predominant impurity is absorbed water). 1.10 mM hexaammineruthenium(III) chloride, and 1.00 potassium hexacyanoferrate(III) solutions were used to characterize the respective redox active surface areas of the Pt-SPEs.

4.2.2. Electrode Preparation

4.2.2.1. Mechanical polishing of Pt-SPEs

As mentioned under Section 2.1.2, DropSens SPEs are coated with a blue polymer mask to cover the underlying silver traces. This is a proprietary synthetic polymeric dielectric material, which the manufacture was unwilling to disclose. But it is known to be soluble in tetrahydrofuran (THF) according to the manufacturer. DropSens Pt-SPEs (DRP-550) were chosen for this study as a continuation of the work presented in Chapter 3.

Before the Pt-SPEs were polished, the blue polymer coating was stripped off by sonication in THF in a small glass vial for 15 mins. The Pt-SPEs were further sonicated in fresh THF to remove any trace of residual polymer material before aggressively polished with a mechanical polisher (Dap-V, Struers, Copenhagen, Denmark) at its maximum rotation speed of 600 rpm, using 1 μm alumina powder (Kemet Australia Pty Ltd, Marayong, NSW) on a soft lapping pad (Buehler, Illionis, USA) until a glossy finish was obtained.

The polished Pt-SPEs were then sonicated in Milli-Q water followed by THF, and finally EtOH, for 15 mins each, before drying in a stream of nitrogen gas. Wires were then soldered onto the connection points of the Pt-SPEs and attached to the potentiostat via crocodile clips. The exposed screen printed silver electrical-traces of the THF-sonicated Pt-SPEs were re-masked with SELLEYS® Silicone Sealant (100% Silicone, purchased from local hardware store) and allowed to set for a minimum of 48 hrs, before rinsing with Milli-Q water followed by EtOH, and finally drying under nitrogen gas. Photographs of unpolished and silicone-masked polished Pt-SPE samples with connecting wires soldered on are shown in Figure 4.1. During the application of silicone onto polished Pt-SPEs, care was taken to ensure that the geometric surface area of the exposed working electrode did not significantly differ for polished Pt-SPEs compared to unpolished Pt-SPEs.

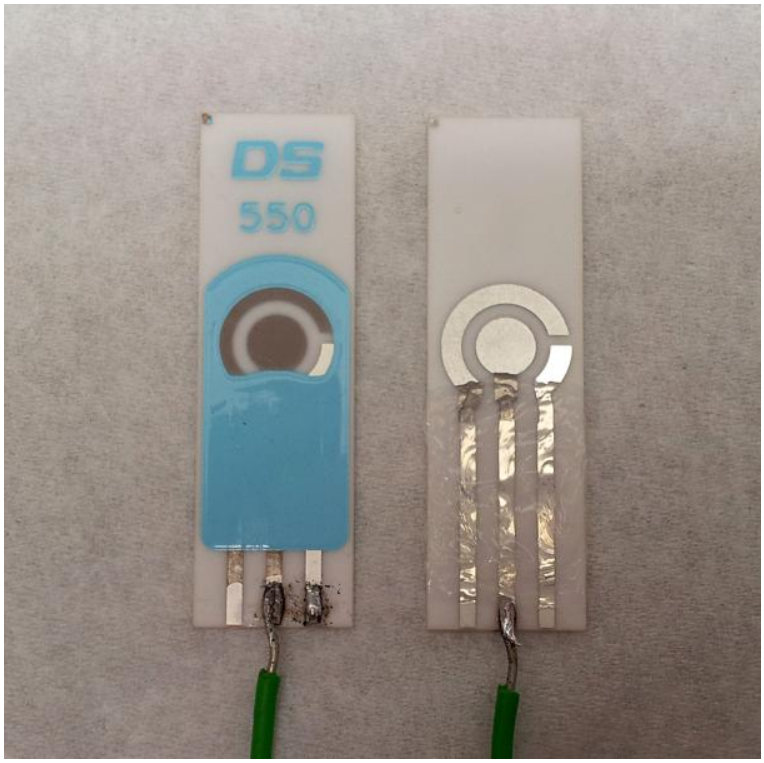

Figure 4.1. (Left) Fresh-out-of-the-box (untreated), and **(right)** mechanically polished Pt-SPEs. A layer of silicone mask was implemented to cover the exposed screen printed silver traces, and wires were soldered to connect the working electrode with the potentiostat.

4.2.2.2. THF sonication pre-treatment of Pt-SPEs

Samples designated as 'THF treated' were subjected to the same pre-cleaning and post-cleaning protocols (by sonication in THF and other solvents) as polished samples, but with the mechanical polishing step omitted. The THF treated sample serves as a control for the polished samples, and also to explore its viability as a "stand-alone" alternative pre-treatment protocol for Pt-SPEs.

4.2.2.3. UV-Ozone pre-treatment of Pt-SPEs

For the plasma cleaning pre-treatment protocol investigated by Wang et al. in 2009 [232] for carbon SPEs (C-SPEs), optimal conditions for treating C-SPEs were found to be with an oxygen plasma generation power of 100 W and an exposure time of 20 mins. The paper also reported that over treated samples may lead to over etching and degradation of the stability of the screen printed device. In this work with Pt-SPEs, due to the unavailability of a plasma cleaner, a ~50 W UV-ozone cleaner (BIOFORCE Nanosciences, Inc., Model: UV.TC.220 USA) was used instead, and Pt-SPEs were subjected to a conservative exposure duration of 30 min as a preliminary investigation of the impact which ozone may have on Pt-SPEs manufactured by DropSens. Both plasma (which includes ozone, amongst other highly energetic oxygen species) and the comparatively less aggressive UV-generated ozone treatments were common procedures for the cleaning of silicon surfaces in the manufacturing of electronic devices, while showing comparable cleaning performance for exposed surfaces. [234, 235]

4.2.2.4. NaOH pre-treatment of Pt-SPEs

NaOH treated samples were prepared based on the protocol suggested for C-SPEs [233]. Following the recommended pre-treatment conditions specified in that paper, the Pt-SPEs in this work were soaked in 3 M NaOH(aq) for 1 hr, followed by anodizing at 1.2 V vs. Ag/AgCl RE in 0.5 NaOH(aq) for 20 s. The NaOH treated Pt-SPEs were then thoroughly rinsed in Milli-Q water, and dried under a stream of nitrogen gas.

4.2.2.5. DMF pre-treatment of Pt-SPEs

The DMF treated samples were prepared based on the pre-treatment protocol suggested for C-SPEs [112]. Pt-SPEs were briefly soaked in N,N-dimethylformamide (DMF) in a small glass vial for 5 mins, before curing in an oven for 20 mins at 100 °C in a covered glass Petri dish.

4.2.3. Electrochemical experiments

The experiments were set up as according to Section 2.3.2. The counter and reference electrodes built into the SPE were not used. The use of an external reference (Ag|AgCl|KCl (1.0 M)) (BASi, Indiana, USA), and counter electrodes was to ensure that any differences observed in the voltammetric response were purely attributed to differences in the condition of the working electrodes. Unless otherwise noted, all potentials are reported with respect to this reference electrode. The platinum wire counter electrode (Goodfellow Cambridge Ltd., UK) was cleaned by rinsing in EtOH, flaming in a Bunsen burner, sonicating in EtOH and then in Milli-Q water. Before commencement of measurements, the solutions were purged with nitrogen gas by bubbling for 15 mins, and stirring using a magnetic stirrer. Cyclic voltammograms (CVs) were collected with scan rates of 100 $mV \cdot s^{-1}$ or 1 $V \cdot s^{-1}$. For the ruthenium(III/II)hexamine and hexacyanoferrate(III/II) redox experiments, background-corrections of the peak currents, I_p, were performed by subtracting from I_p a baseline value of the current taken at the same potential along a linearly extrapolated line from the non-Faradaic part of the CV right before onset of the peak. Once the relevant peak potentials were established from the CVs, chronoamperometric (CA) measurements were then performed for 20 s (with 60 s pre-biasing at 0 V) with suitable over-potentials to ensure fast kinetics for convergence to a Cottrellian type response. A CA measurement, conducted in 0.1 M KCl(aq), was also performed to allow for background-subtraction of the CA data.

Finally, electrochemical impedance spectroscopy (EIS) of the unpolished and polished Pt-SPE samples were conducted in 0.1 M KCl(aq) electrolyte solution. EIS data was measured in the frequency range between 1 mHz – 1.5 MHz, operating in the single-sine-wave mode, with an RMS AC voltage of 5 mV oscillating about the open-circuit-potential (OCP), which indicates the equilibrium potential of the system. To ensure that the reference electrode (RE) was as close to the working electrode as possible for the EIS measurements, the Ag-RE on the integrated Pt-SPE device was used. A coil of platinum wire was employed as the counter electrode.

4.2.4. Atomic Force Microscopy imaging of surfaces

Tapping mode atomic force microscope (TM-AFM) surface mapping was performed using the Bruker Fastscan instrument in the scanning probe microscopy facility at Curtin University. Due to the high roughness of the unpolished Pt-SPE surface, AFM mapping was only performed on a polished Pt-SPE.

4.2.5. 3D confocal optical and Raman microscopy

The 3D confocal optical images and Raman spectra mappings were collected with a WITec (alpha300 series) confocal Raman microscope. The unpolished and polished Pt-SPEs were left overnight in a vacuum desiccator to remove any adsorbed volatile contaminants. Screen printed platinum surfaces were too rough for atomic force microscopy characterization of their topographical surfaces. However, quantification of surface roughness of materials from confocal microscopy images has been previously reported. [236]

4.2.5.1. 3D confocal optical imaging

3D confocal optical stacked images were taken in a fixed scan region of 120 × 120 μm with a lateral resolution of ~4.3 pixels·μm^{-1} (i.e. image pixel dimension of 512 × 512 pixels), and an effective z-thickness (focusing depth) of 250 nm for each of the stack-slices scanned. To estimate the topographical surface areas of the Pt-SPEs, 3D confocal optical stacked images were first exported with the proprietary software, WITec Project (v2.10), as individual image files and loaded into the ImageJ (1.47v) software. The image stacks were processed with ImageJ's *despeckle* filter. A height-map was constructed (with the *Easy* mode, with maximum level of *Quality*, and medium level of smoothing) using the EDF (v11.07.2011, plugin for ImageJ) [237] based on the complex wavelet transformation of the signals [238]. The generated height-maps were then exported and loaded into Gwyddion (v2.31). Finally, values of the topographic surface area were extracted using the *Statistical Quantities* tool in the Gwyddion software package. The rugosity, ρ, is defined as the ratio of the topographic (microscopic) surface area (A_m) to the geometric area (A_g), i.e. A_m/A_g [236, 239]. ρ was derived for the electrode surfaces by dividing the estimated topographic surface area (from the confocal data) by the projected area of the sample analysed. Similarly, ratios of the active surface areas (obtained from hydrogen adsorption and redox experiments) to the geometric area of the working electrode, ρ_a, were derived. The ratio, ρ_a/ρ (which is equivalent to A_a/A_m), thus provides a measure of the active sites with respect to the topographic surface area, and would theoretically be at unity for a 100 % topographically active surface.

4.2.5.2. Raman mapping of contaminants present on screen printed platinum surfaces

For 3D confocal Raman stacked mappings of the samples, lateral resolution of ~3.3 pixels·μm^{-1} were used, with an effective z-thickness of 1 μm for each of the stack-slices scanned. The slices were then analysed for the presence of contaminant signals in the spectra. Corresponding maps were then generated with the *sum filter* for each stacked layer before they were collapsed into a single image by integrating each corresponding pixel along the stack. The brightest intensities corresponding to the individual contaminant signals were then overlaid onto its corresponding optical image. False colours were assigned to provide a qualitative idea of the distribution of contaminants present.

4.3. Results and Discussion

To investigate the effectiveness of the five different pre-treatment protocols, namely sonication in THF, polishing, UV-ozone cleaning, NaOH treating, and DMF soaking of Pt-SPEs, both hydrogen adsorption/desorption voltammetry, and cyclic voltammetry of the hexacyanoferrate(III/II) and hexaammineruthenium(III/II) redox couples was performed. Topographical surface areas of unpolished and polished SPEs were also estimated from their 3D confocal optical stacked images. The following sections provide a qualitative comparison of the efficacy of each of the pre-treatment protocols studied.

4.3.1. Voltammetry in 0.5 M H_2SO_4(aq)

Hydrogen adsorption/desorption voltammetry is commonly used for the activation of Pt surfaces as well as the estimation of the electrochemically active surface area. [240-244] Adsorption/desorption of hydrogen on platinum surfaces is described by the following equation [240]:

$$H^+(aq) + e^- \rightleftharpoons H_{adsorbed} \qquad \textbf{(4.1)}$$

CV experiments on six Pt-SPEs (one untreated and 5 subject to different pre-treatment protocols) were conducted by repeated cycling between +1.25 V and -0.3 V in 0.5 M H_2SO_4(aq), with the starting potential set at the OCP value. Figure 4.2 compares the voltammograms of the 25th and 150th consecutive scans. The redox process at ca. 1 V in the oxidative scan, and at 0.46 V in the reduction scan corresponds to the oxidation and reduction of platinum via the formation of quasi-3D platinum oxide lattices. [241, 245, 246] Broad contaminant shoulders between 0.6 V and 0.9 V on the oxidative scans appeared to vary

between samples. A large contaminant peak at 0.42 V on the oxidative scan (which grows with progressive CV cycles) was present in all CVs with the exception of NaOH treated samples. This peak was also substantially decreased in the polished SPE. The hydrogen adsorption and desorption peaks (at ca. -0.1 V) were considerably larger for both polished and NaOH treated Pt-SPEs compared to unpolished Pt-SPEs. A pair of reversible contaminant peaks, at 0 V for reduction, and 0.23 V for oxidation (which diminished with progressive CV cycles) appeared more significant for the untreated and polished samples. These contaminant peaks observed are believed to be primarily due to the presence of polymer binders exposed on the screen printed surfaces. [112, 114, 232, 233]

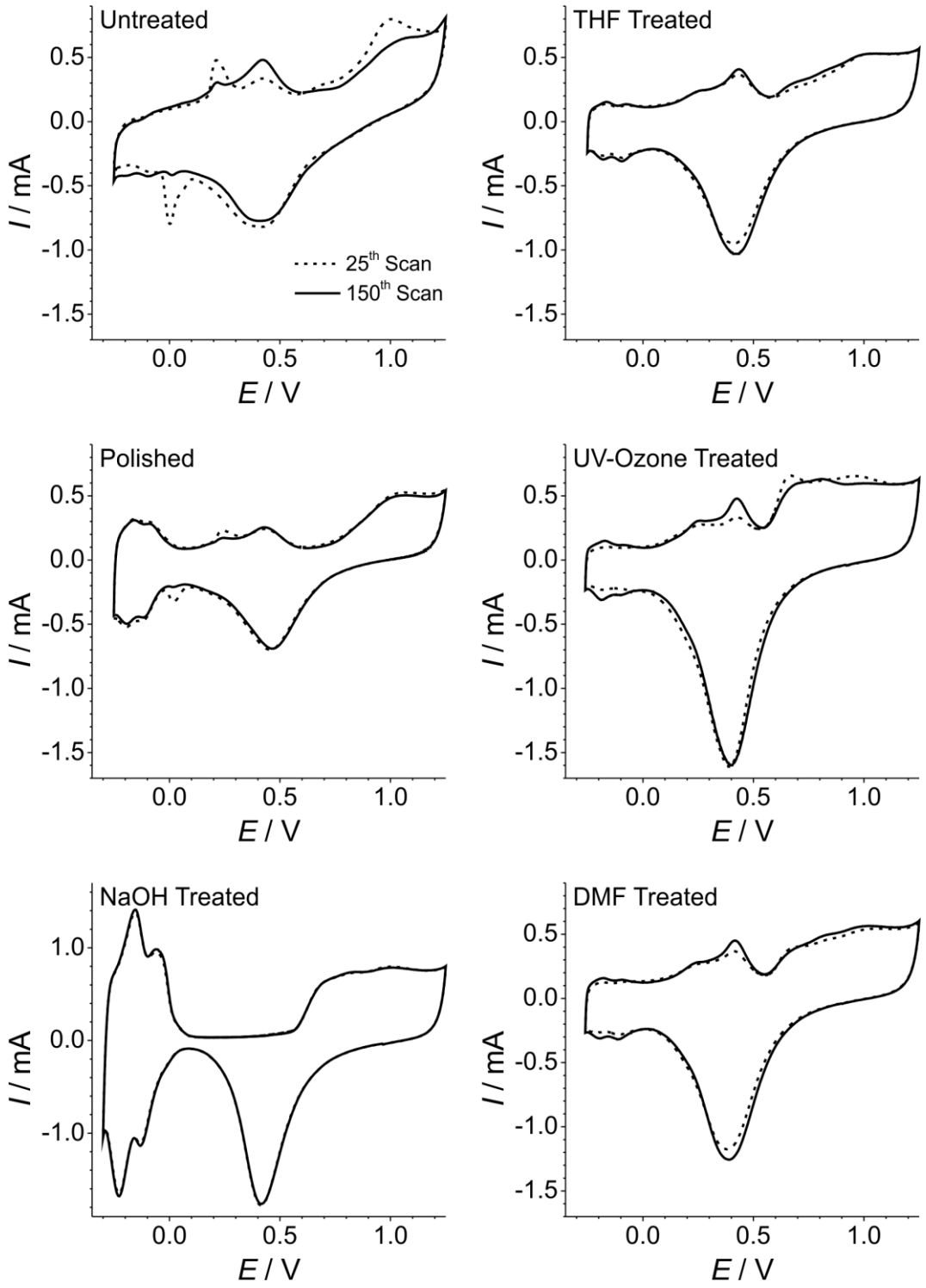

Figure 4.2. The 25th (- -) and 150th (–) cyclic voltammetric cycles of 0.5 M H_2SO_4(aq), scanned between 1.25 V and -0.3 V vs. Ag/AgCl at 1 V·s^{-1} (with starting potential set as the OCP) on untreated and the various treated Pt-SPEs. All the voltammograms were plotted on the same scale to allow for direct comparison, except for the NaOH treated sample due to its substantially larger H^+(aq) desorption waves. The solid line overlays the dashed line exactly where the latter is not visible.

Peaks relating to the oxidation and reduction of platinum stabilized within the first 10-15 cycles for all Pt-SPE samples, while characteristic hydrogen adsorption and desorption peaks gradually become more distinct as the consecutive CV cycles progressed. This can plausibly be attributed to the gradual desorption of passivating contaminants (e.g. SPE binding material) with each consecutive oxidation/reduction cycling of surface-platinum, leading to an increase in active sites for hydrogen adsorption. The characteristic waves associated with hydrogen desorption for unpolished Pt-SPEs, between 0 V and -0.3 V, remain vaguely visible and distinct, even after more than 200 cycles at a reasonably high scan rate of 1 $V \cdot s^{-1}$. However, after more than 500 consecutive cycles, the hydrogen desorption currents of unpolished Pt-SPEs gradually grew and eventually become comparable to those of the THF/UV-ozone/DMF treated Pt-SPE samples (as presented in the right-hand-side of Figure 4.2). Continuing past 500 cycles did not further increase hydrogen adsorption/desorption currents for any of the samples. Polished and NaOH treated Pt-SPEs showed a substantial increase in the hydrogen desorption peak currents compared to the other treated samples, and stability was generally achieved within 25-30 cycles. These results revealed that the repeated CVs in 0.5 M H_2SO_4(aq) procedure for untreated Pt-SPE was ineffective in removing the passivating layer of surface contaminant that was clearly present, whereas, polishing and the NaOH treatment appeared to be highly effective. However hexaammineruthenium(III/II) as well as hexacyanoferrate(III/II) voltammetry studies discussed in the next section, and physical signs of degradation of the materials (see Section 4.3.6) raise doubts on the suitability of NaOH treatment for screen printed surfaces.

4.3.2. Cyclic voltammetry of hexaammineruthenium(III) and hexacyanoferrate(III) on Pt-SPEs

Untreated and treated Pt-SPEs were characterized in aqueous hexaammineruthenium(III) chloride and potassium hexacyanoferrate(III) solutions with both CV and CA. CVs for 1.10 mM hexaammineruthenium(III) chloride and 1.00 mM potassium hexacyanoferrate(III) in 0.1 M KCl(aq) are presented in Figure 4.3 and Figure 4.4, respectively. $\Delta E_{\text{p-p}}$ values obtained from the CV of hexaammineruthenium(III/II) and hexacyanoferrate(III/II) redox are presented in Table 4.3. The redox reaction of the hexaammineruthenium(III/II) redox couple is [247]

$$[Ru(NH_3)_6]^{3+} + e^- \rightleftharpoons [Ru(NH_3)_6]^{2+} \quad \textbf{(4.2)}$$

while for the hexacyanoferrate(III/II) redox couple, the reaction is

$$[Fe(CN)_6]^{3-} + e^- \rightleftharpoons [Fe(CN)_6]^{4-} \quad \textbf{(4.3)}$$

For the hexaammineruthenium(III/II) experiments, the peak-to-peak separations, $\Delta E_{\text{p-p}}$, for this redox process at the untreated, polished, NaOH and UV-ozone treated Pt-SPE samples were all 76 mV, while the DMF treated sample shows a significant improvement in electron transfer kinetics with a $\Delta E_{\text{p-p}}$ of 64 mV. The THF treated sample was slightly wider at 79 mV, and the voltammetry exhibited signs of surface contamination, or passivation of the working electrode surfaces. This suggests that the dissolved blue dielectric polymer mask may have left behind a stubborn thin residual layer on the working electrode surface that even further aggressive sonication in THF solvent was unable to completely remove. For the voltammetry of hexacyanoferrate(III), the THF treated samples also showed slower redox kinetics (higher $\Delta E_{\text{p-p}}$) compared to untreated samples. However the shape of the voltammetry appears to remain unaffected.

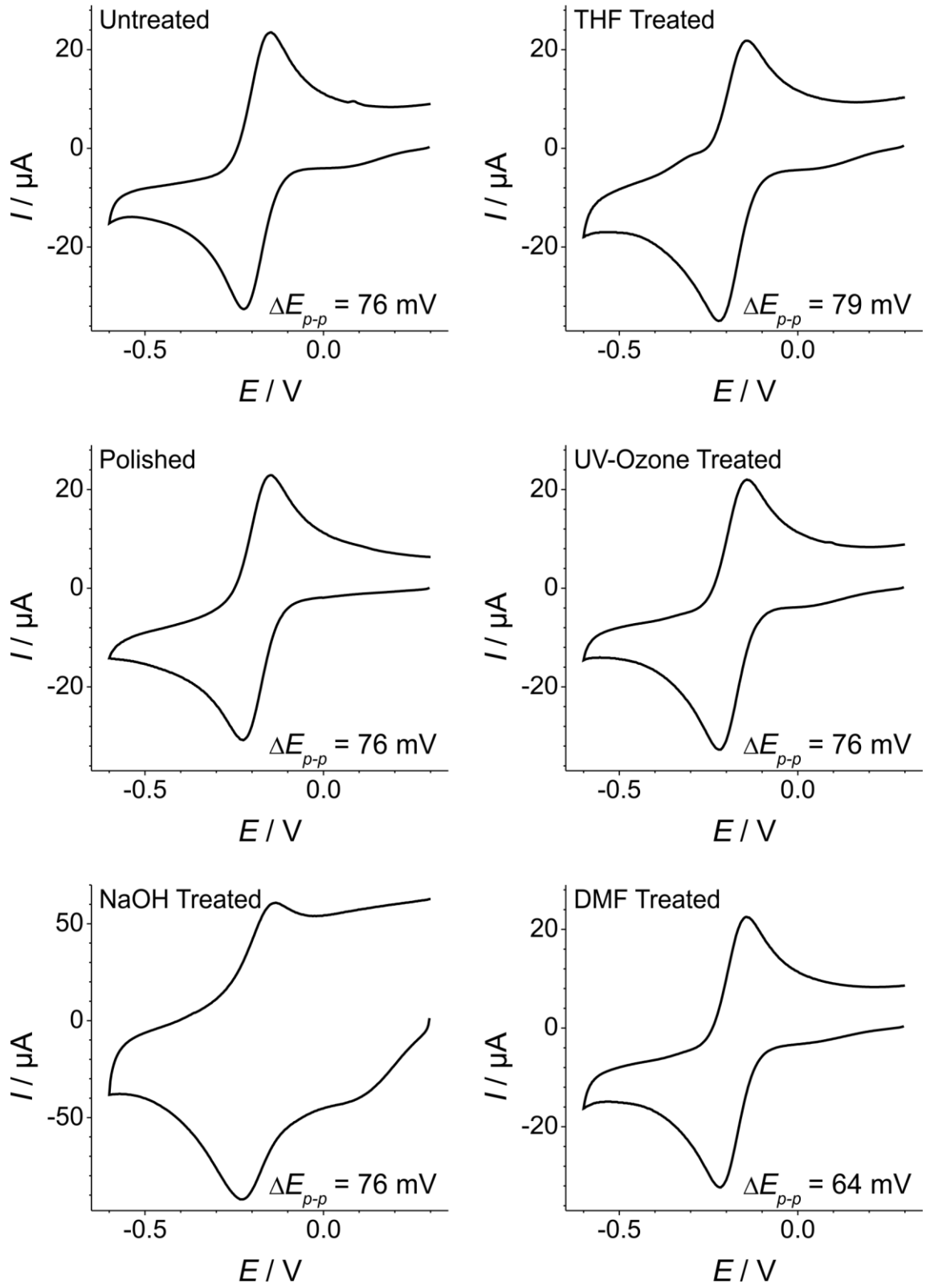

Figure 4.3. Cyclic voltammetry of 1.10 mM of hexaammineruthenium(III) chloride in 0.1 M KCl(aq) supporting electrolyte, scanned between 0.2 V and -0.6 V vs. Ag/AgCl at 100 $mV \cdot s^{-1}$, on untreated and the various treated Pt-SPEs. All the voltammograms were plotted on the same scale to allow for direct comparison, except for the NaOH treated sample due to its substantially larger currents.

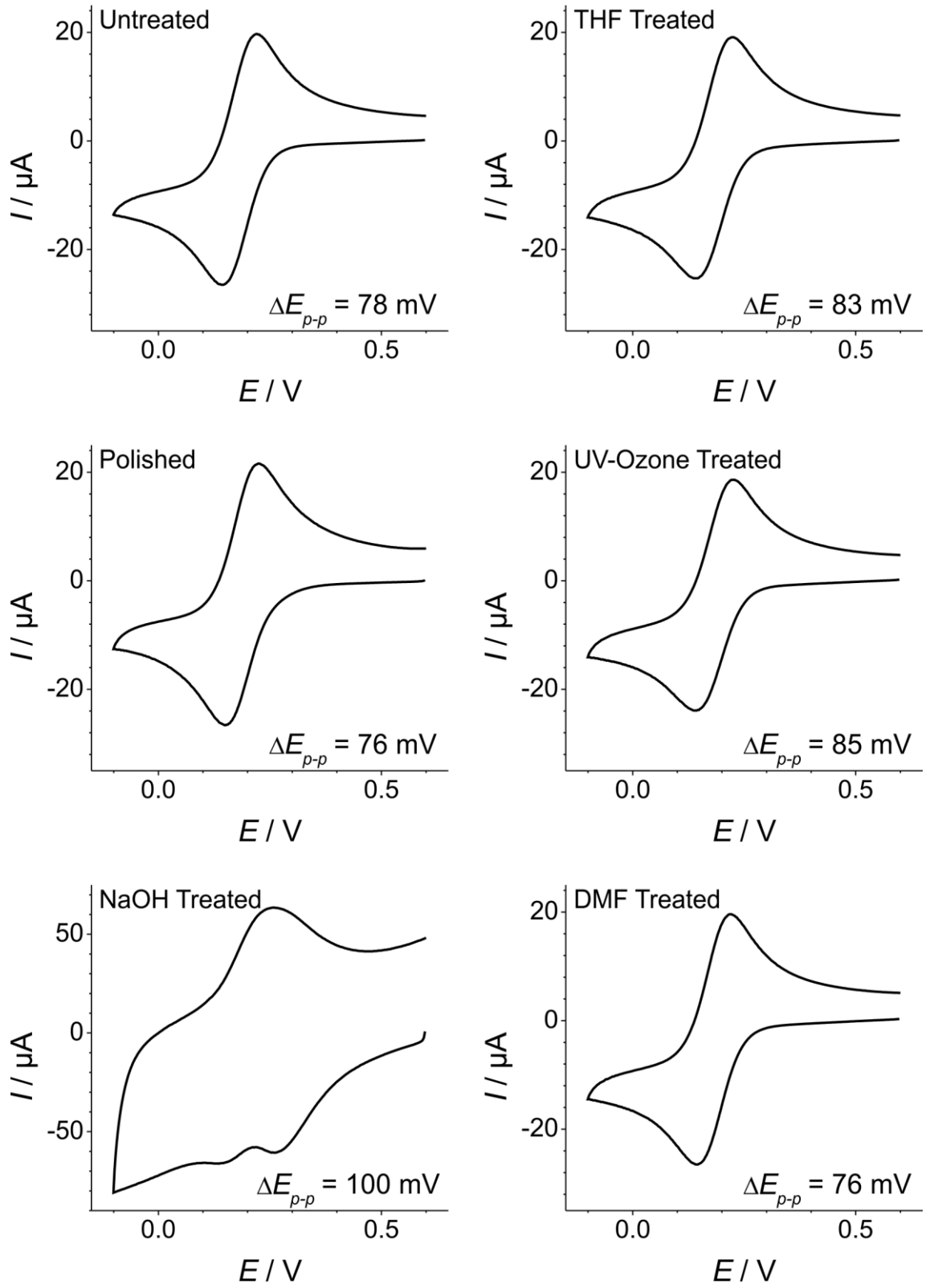

Figure 4.4. Cyclic voltammetry of 1.00 mM of potassium hexacyanoferrate(III) in 0.1 M KCl(aq) supporting electrolyte, scanned between 0.6 V and -0.1 V vs. Ag/AgCl at 100 $mV \cdot s^{-1}$, on untreated and the various treated Pt-SPEs. All the voltammograms were plotted on the same scale to allow for direct comparison, except for the NaOH treated sample due to its substantially larger currents.

Hexacyanoferrate(III) is known to possess a weak innersphere electron transfer character [248], and can be catalysed by the platinum electrode surface to deposit a passivating layer of prussian blue ($KFe(II)[Fe(III)(CN)_6]$) [249]. A larger variability in $\Delta E_{p\text{-}p}$ for hexacyanoferrate(III/II) experiments was observed, compared to hexaammineruthenium(III/II) experiments. Comparison of their values indicated that while the pre-treatment protocols studied generally do not affect the kinetics of purely outer shell electron transfer reactions (such as the electrochemical redox of hexaammineruthenium(III/II)), hexacyanoferrate(III/II) CV appears to be comparatively more sensitive to differences in conditioning of the electrode surfaces. For instance, although the $\Delta E_{p\text{-}p}$ values from hexaammineruthenium(III/II) CV on the UV-ozone treated Pt-SPE samples were the same as that of the untreated Pt-SPEs (at 76 mV), the hexacyanoferrate(III) CVs show significantly wider $\Delta E_{p\text{-}p}$ of 85 mV on both samples. For the NaOH treated sample, two reduction peaks were present. The cathodic peak at ca. -150 mV was attributed to the reduction of ruthenium(III)hexamine, due to it occurring at the potential lower with respected to the ruthenium(II)hexamine oxidation peak during the anodic scan. The cause of the appearance of the other peak at -261 mV after the NaOH pre-treatment is unclear at this point. Larger background currents developed on NaOH treated samples in both the hexaammineruthenium(III/II) and hexacyanoferrate(III/II) experiments. However, the hexaammineruthenium(III/II) $\Delta E_{p\text{-}p}$ for the NaOH treated samples appeared to be unaffected (compared with the untreated sample), while a much wider $\Delta E_{p\text{-}p}$ value was observed with hexacyanoferrate(III/II).

4.3.3. Estimating the topographical surface areas of unpolished and polished Pt-SPEs

SEM micrographs of typical unpolished and polished working electrodes of Pt-SPE samples are presented in Figure 4.5. The SEM images show that untreated platinum SPE surface is extremely rough and porous, while the topographical features are significantly flattened after polishing. The expected reduction in topographical surface areas of polished Pt-SPE was characterized with 3D confocal optical imaging. Some of the topographical features were expected to be inaccessible or hidden to 3D confocal optical imaging due to the porous nature of the surfaces; and thus, the topographical surface areas (and consequently, the values of ρ) derived are expected to be systematically underestimated.

The working electrode diameter of Pt-SPEs is 4.0 mm, as given in Table 2.3. Estimations from 3D-stacked confocal optical images of the duplicate unpolished and polished samples gave rugosity values (as defined in Section 4.2.5.1), ρ, of about 2.42 and 2.72 for unpolished Pt-SPE surface, and 1.77 and 2.09 for polished Pt-SPE surface. The values of ρ estimated for the respective duplicate samples show good agreement between one another – with the variability of the duplicate measurements from their common mean at 5.8 % for the unpolished samples, and 8.3 % for the polished samples. Also, the wider difference noted between the polished samples could be explained by expected inconsistencies with their preparations (i.e. force applied, position of the sample on the rotating polishing pad, etc.) even if they were to be subjected to similar duration of mechanical polishing. The results are summarized in Table 4.1, and their derivations are detailed under Section 4.2.5.1. The averaged values from the duplicate measurements for A_m and ρ will be used for the normalization of the electrochemically active surface areas of the untreated and treated Pt-SPEs.

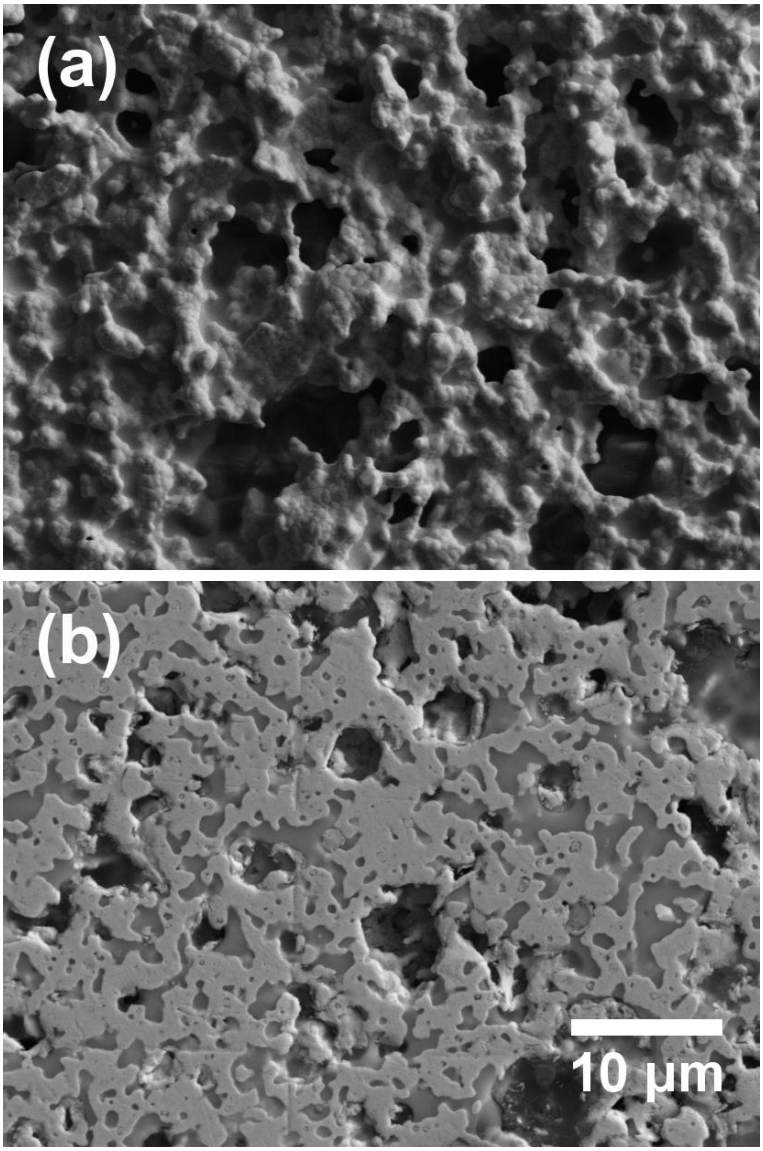

Figure 4.5. SEM images of representative **(a)** unpolished and **(b)** polished Pt-SPE samples. The Pt-SPE was mechanical polished on a rotating mechanical polisher with 1 µm alumina powder. Pt-SPEs were sonicated in THF to remove the blue dielectric polymer mask before commencing the polishing, and further sonicated after in Milli-Q water, followed by THF and finally EtOH as detailed under the experimental Section 4.2.2.1.

Figure 4.6 shows the tapping mode atomic force microscope topographic and phase images collected on a polished Pt-SPE surface. The phase image on the right of Figure 4.6 clearly shows that Pt-SPE surfaces, on the µm level, are comprised of particles (e.g. Pt) that are tightly held together (i.e. by binding materials).

Table 4.1. Topographic surface areas, A_m, and rugosity, ρ, values estimated from *two* independently measured 3D confocal optical stacked images of unpolished and polished platinum screen printed electrodes (Pt-SPEs). The independently obtained A_m and ρ values for unpolished and polished Pt-SPEs were separated by a comma. The average of the two values for A_m and ρ were presented in the accompanying brackets.

Treatment	Surface Area, A_m	ρ
	mm^2	
Untreated	30.4, 34.2 (32.3)	2.42, 2.72 (2.57)
Polished	22.2, 26.2 (24.2)	1.77, 2.09 (1.93)

Details of how A_m were estimated from the 3D confocal optical stacked images was summarised under Section 4.2.5.1. Variability of the two values from the average of the duplicate measurements was 5.8 % for the unpolished Pt-SPE, and 8.3 % for the polished Pt-SPE.

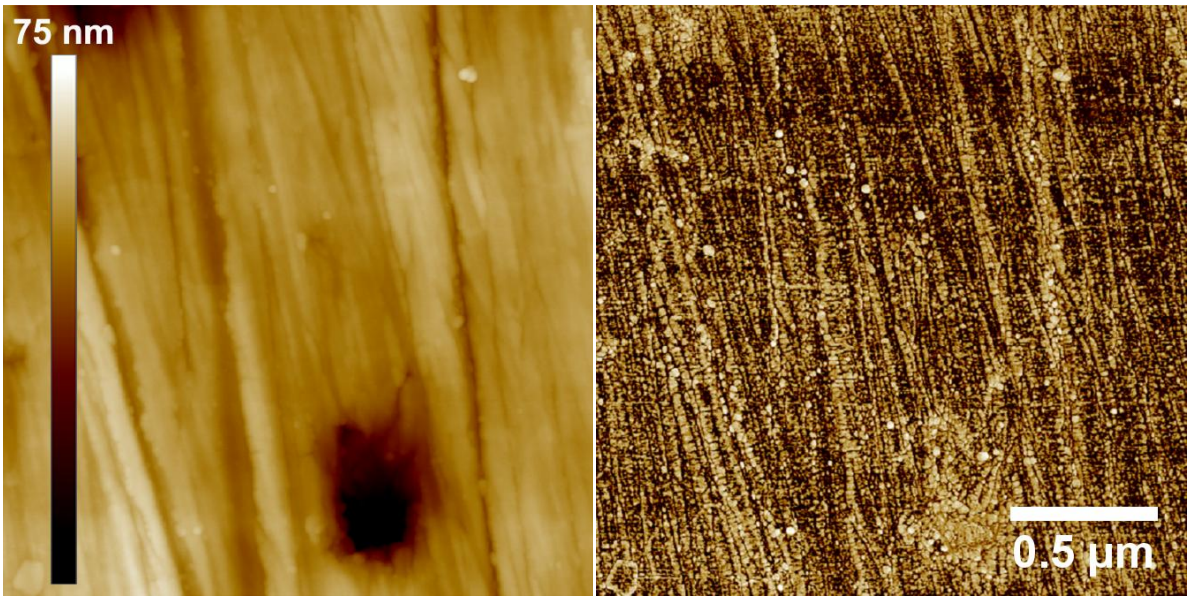

Figure 4.6. Tapping Mode AFM mapping of a polished screen printed platinum surface collected on a 2 µm by 2 µm area. The left image shows the topographic image with the vertical scale bar embedded. The right image is the phase mapping showing microscopic features of the surface consisting of particles of platinum embedded in the binder. Unpolished Pt-SPE surfaces were too rough (ca. 10 µm features) for AFM measurements to be conducted (see Figure 4.5).

4.3.4. Comparison of active surface areas of Pt-SPEs with respect to their topographical surface areas.

For adsorption of a hydrogen monolayer on Pt, the total electrical charge per unit surface area was reported to be 210 $\mu C \cdot cm^{-2}$. [240, 250] The hydrogen adsorption surface area was estimated by dividing the total charge associated with adsorbed hydrogen, Q_H, for each Pt-SPE with this value. Q_H was calculated for each Pt-SPE by integrating the area under their hydrogen desorption current peaks (between -0.3 V and ca. -0.05 V) after first subtracting contributions from background currents, and finally dividing by the scan rate. [240] Results from hydrogen adsorption/desorption experiments are summarized in Table 4.2. The magnitude of the platinum oxide reduction peak currents, $|I_{Pt\text{-}Red}|$, are also presented and can be related to the microscopic surface areas of the Pt-SPE materials that were accessible to oxidation (i.e. not blocked by contaminants). The hydrogen desorption peak of the untreated Pt-SPE sample (as shown in Figure 4.2) could not be reliably analysed and was thus omitted. Polished Pt-SPEs show an order of magnitude increase in surface area accessible for hydrogen adsorption (i.e. the hydrogen adsorption active surface area) compared to the THF-treated Pt-SPE that merely had its polymer mask stripped. The 33 % decrease of $|I_{Pt\text{-}Red}|$ from untreated to polished Pt-SPE matches reasonably well to the 25 % decrease in ρ due to polishing (Table 4.1). The lower value of $|I_{Pt\text{-}Red}|$ of the untreated Pt-SPE may be due to the presence of thicker layer of passivating contaminants blocking the platinum surfaces from undergoing oxidation, and may also explain the more "rounded" peak shape of the reduction peak.

ρ_a/ρ ratios provides a measure of the active sites with respect to the topographic surface area (see Section 4.2.5.1). THF-sonicated Pt-SPEs will be used as the reference sample as no clear hydrogen desorption peaks were present in the hydrogen desorption voltammetry for the

untreated Pt-SPE to allow derivation of ρ_a/ρ for comparison. Further, sonication of Pt-SPEs in THF was considered to be comparatively milder than the others pre-treatment protocols. ρ_a/ρ ratios of the UV-ozone and DMF treated Pt-SPE samples did not show any significant improvements compared to the THF-treated Pt-SPE. However, the appreciable increase in their $|I_{Pt\text{-}Red}|$ values suggested a significant decrease or thinning of surface contaminant, as has been observed in studies conducted on carbon SPEs [112, 232]. The relatively suppressed value of $|I_{Pt\text{-}Red}|$ of untreated samples could relate to thicker surface contaminant films which passivate a larger total area of the screen printed platinum working electrode surfaces. The hydrogen adsorption active surface area of the NaOH treated Pt-SPE showed an even more substantial increase (at two orders of magnitude) compared to the THF-treated Pt-SPE. However, the ρ_a/ρ value at 4.06 is well over the theoretical maximum of unity. This is probably due to substantial over-etching by the 3 M NaOH(aq) solution, as illustrated in Figure 4.7. The weakening of the supporting polymeric binders holding the conductive platinum particles together (see also Figure 4.6) compromised the structural integrity of the screen printed material (as mentioned in Section 4.3.6), and could also substantially increase its capacitance (as observed in Figure 4.3 and Figure 4.4, and discussed in Section 4.3.2) as the result of severe degradation in the quality of the electrical contacts along the electrical percolation channels.

Table 4.2. ρ_a/ρ values (see Section 4.2.5.1), and the peak current magnitudes from platinum reduction, $|I_{Pt\text{-}Red}|$, obtained from hydrogen desorption voltammetries conducted in 0.5 M H_2SO_4(aq), as presented in Figure 4.2. Consecutive CVs were collected at a scan rate of 1 $V \cdot s^{-1}$, and consistently analysed on the 150th cycle, with Ag/AgCl as the reference electrode.

Treatment	Surface Area, A_a *	ρ_a/ρ †	$\lvert I_{Pt\text{-}Red} \rvert$
	mm^2		mA
Untreated/Unpolished	N.A.	N.A.	0.77
THF-Sonication	1.89	0.06	1.03
Polished	18.2	0.75	0.69
UV-ozone	2.72	0.08	1.60
NaOH	131	4.06	1.76
DMF	1.80	0.06	1.26

* *Active surface areas, A_a, derived from the hydrogen desorption CVs were normalized with respected to the geometric surface areas of the WE, ρ_a. A_a were derived based on the assumption of a hydrogen monolayer establishing on Pt during the cathodic scan (Figure 4.2), and with a total electrical charge per unit surface area of 210 $\mu C \cdot cm^{-2}$.* [240, 250]

† *ρ_a divided by the estimated rugosity values, ρ_a/ρ, were derived to account for differences in their topographic surface areas of unpolished and polished Pt-SPEs. The rugosity values are presented in Table 4.1, and their estimation were discussed under Section 4.3.3.*

‡ *CVs were conducted at a sweep rate of 1 $V \cdot s^{-1}$.*

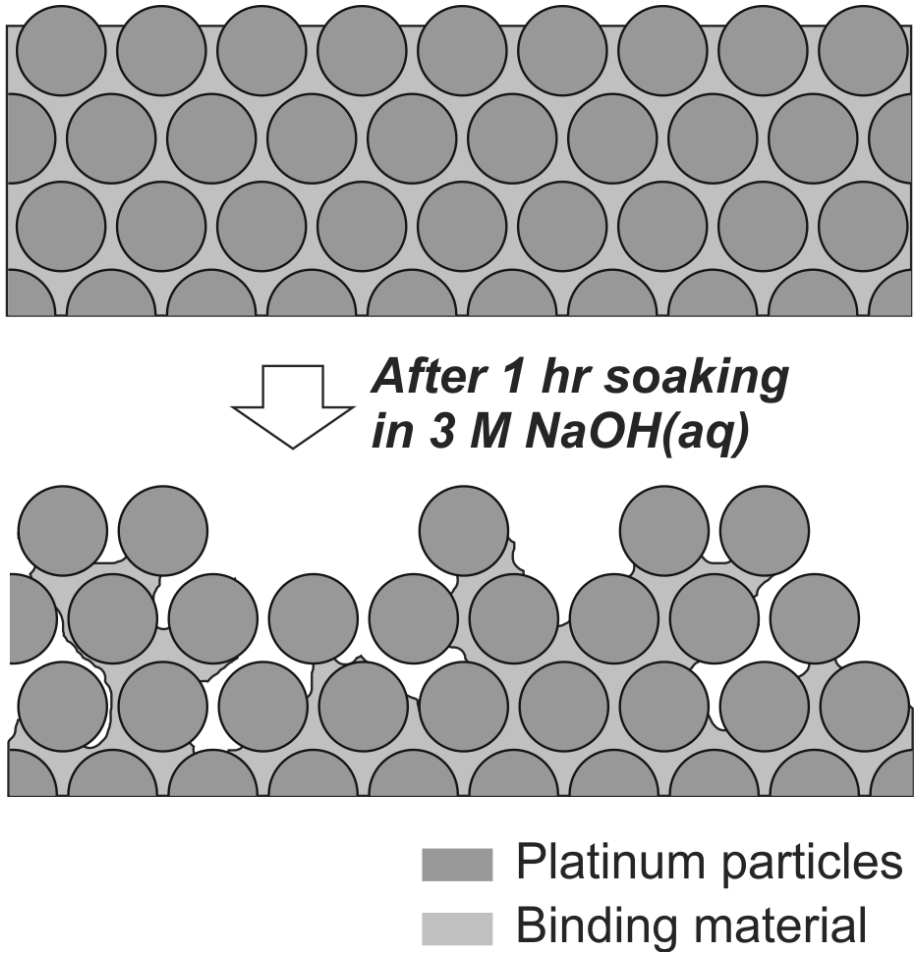

Figure 4.7. Cartoon illustrating the possible effect of the harsh NaOH treatment of platinum screen printed electrodes. The Pt-SPE devices were soaked in concentrated 3 M NaOH for 1 hr.

The electrochemically active surface areas were derived from background-corrected CV peak currents (see Section 4.2.3) for each Pt-SPE via. equation (1.8) (i.e. Randles-Sevčik equation), and from the diffusion limited currents via chronoamperometric experiments using equation (1.7) (i.e. Cottrell equation). The diffusion coefficients of hexaammineruthenium(III) and hexacyanoferrate(III) in 0.1 M KCl(aq) are reported to be 8.43 (± 0.03) × 10^{-10} $m^2 \cdot s^{-1}$ [251] and 7.20 (± 0.18) × 10^{-10} $m^2 \cdot s^{-1}$ [252], respectively. Using these values, the active surface areas of each sample were derived from CV and CA data. ρ_a values for untreated and treated Pt-SPEs were derived from analysis of hydrogen desorption peaks

on the 150th CV cycle conducted in 0.5 M H_2SO_4(aq), and for 1.10 mM hexaammineruthenium(III) chloride and 1.00 mM hexacyanoferrate(III) in 0.1 M KCl(aq).

Table 4.3 summarises the results of characterization of untreated and treated Pt-SPEs, via the redox couples of hexaammineruthenium(III/II) and hexacyanoferrate(III/II) using CV and CA. Differences between the peak-to-peak separation potentials in the CV data were discussed in Section 4.3.2. ρ_a/ρ values from these experiments are in general agreement. Firstly, it is interesting to also observe that ρ_a/ρ of the polished and NaOH treated samples did not increase as drastically as the data obtained from the hydrogen adsorption/desorption experiments. This can be explained by the fact that the ρ_a/ρ values were derived based upon markedly different electrochemical processes, namely, hydrogen adsorption/desorption vs. electrochemical reactions of hexaammineruthenium(III/II) and hexacyanoferrate(III/II) redox couples. For instance, while part of the surfaces of the other (untreated and the various treated) unpolished Pt-SPEs may remain substantially blocked by a thin coating of residual contaminants, preventing hydrogen adsorption, the outer shell electron transfer of the hexaammineruthenium(III/II) redox process [247, 253] may still remain largely unaffected by the more thinly contaminated surface regions. Furthermore, compared to hydrogen adsorption, diffusion of the larger hexaammineruthenium(III) and hexacyanoferrate(III) ions may not be able to effectively characterize the newly exposed surfaces in the microscopic gaps between the tightly packed platinum particles after the binding materials were etched away by NaOH. The reduction peak current for hexacyanoferrate(III) at the NaOH treated Pt-SPE could not be reliably analysed, and a CA measurement cannot be reliably conducted (see Figure 4.4) and have thus been omitted from Table 4.3.

Table 4.3. ρ_a/ρ values (see Section 4.2.5.1), of hexaammineruthenium(III/II) redox, obtained from CV and CA of 1.10 mM of hexaammineruthenium(III) chloride in 0.1 M KCl(aq) supporting electrolyte (as presented in Figure 4.3) and of hexacyanoferrate(III/II) redox couple, obtained from cyclic voltammetry of 1.00 mM of potassium hexacyanoferrate(III) in 0.1 M KCl supporting electrolyte (as presented in Figure 4.4), of untreated, THF-sonicated, polished, UV-ozone treated, NaOH treated and DMF treated Pt-SPEs. Peak-to-peak separations, $\Delta E_{p\text{-}p}$ values, extracted from the CVs, are also presented. The CVs were collected at a scan rate of 100 mV·s^{-1}, while CA measurements were performed for 20 s with suitable over-potentials to ensure fast diffusion controlled kinetics.

Treatment	hexaammineruthenium(III/II)			$Fe(III)(CN)_6^{3-}/Fe(II)(CN)_6^{4-}$		
	Surface Area, A_a [a]	ρ_a/ρ [d]	$\Delta E_{p\text{-}p}$	Surface Area, A_a [a]	ρ_a/ρ [d]	$\Delta E_{p\text{-}p}$
	mm^2		mV	mm^2		mV
CV [b]						
Untreated	10.3	0.32	76	11.0	0.34	78
THF-Sonication	10.9	0.34	79	10.3	0.32	83
Polished	10.1	0.42	76	11.1	0.46	76
UV-ozone	10.3	0.32	76	9.80	0.30	85
NaOH	12.7	0.39	76	N.A.	N.A.	100
DMF	10.1	0.31	64	10.9	0.34	76
CA [c]						
Untreated	11.6	0.36	N.A.	10.9	0.34	N.A.
THF-Sonication	10.5	0.33	N.A.	8.37	0.26	N.A.
Polished	11.7	0.48	N.A.	11.9	0.49	N.A.
UV-ozone	9.18	0.28	N.A.	10.4	0.32	N.A.
NaOH	15.1	0.47	N.A.	N.A.	N.A.	N.A.
DMF	11.0	0.34	N.A.	8.13	0.25	N.A.

a *Active surface areas, A_a, derived from ruthenium(III)hexamine and hexacyanoferrate(III) reduction (background corrected) CV peak currents were normalized with respected to the geometric surface areas of the WE, ρ_a. Diffusion coefficients of 8.43 (± 0.03) × 10^{-10} m^2·s^{-1} [251] and 7.20 (± 0.18) × 10^{-10} m^2·s^{-1} [252], respectively for hexaammineruthenium(III) and hexacyanoferrate(III) in 0.1 M KCl(aq), were used for the derivation of A_a.*

b *Derived from the cathodic peak currents of cyclic voltammetry measurements via Equation (1.8) (i.e. Randles-Sevčik equation).*

c *Derived from the diffusion limited currents via chronoamperometric experiments using Equation (1.7) (i.e. Cottrell equation)*

d *ρ_a divided by the estimated rugosity values, ρ_a/ρ, were derived to account for differences in their topographic surface areas of unpolished and polished Pt-SPEs. The rugosity values are presented in Table 4.1, and their estimation were discussed under Section 4.3.3.*

Significant improvements in ρ_a/ρ values were consistently observed in the results obtained from the hexaammineruthenium(III/II) chloride and hexacyanoferrate(III/II) redox voltammetries for polished Pt-SPEs (refer to Table 4.3). Polishing appears to be the only pre-treatment protocol that has shown significant increase in the hydrogen adsorption active surface area, without deterioration of the structural integrity of the screen printed material, which was seen as an increase in its electrical capacitance (in CV). Figure 4.8 illustrates the effective removal of surface contaminants (such as excess binding materials or adsorbed organic oils, etc.) by mechanical polishing, which exposes a fresh surface of screen printed platinum material (such as excess binding materials, adsorbed organic oils, etc.) during the manufacturing and packaging process of these commercial devices are removed.

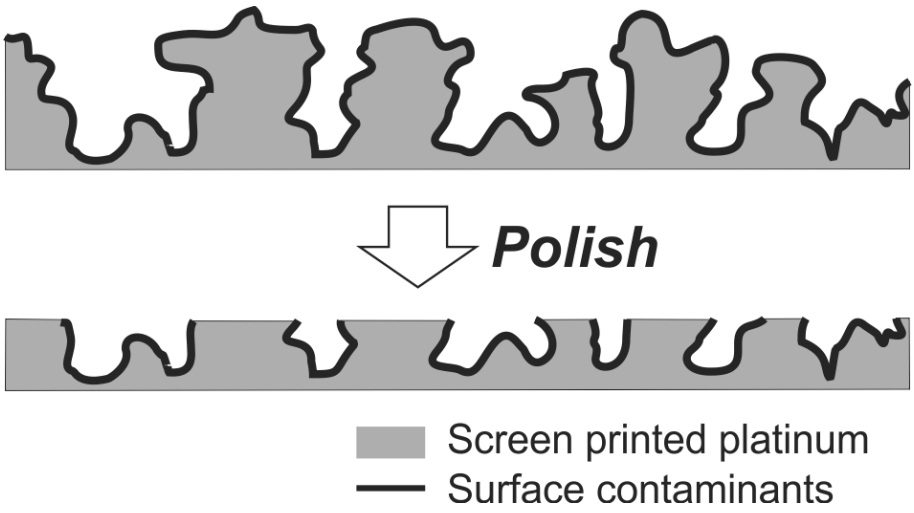

Figure 4.8. Illustration of a screen printed platinum surface before (top) and after (bottom) being subjected to mechanical polishing. Polishing exposes a fresh surface of screen printed platinum material, while contaminant residues (such as excess binding materials, adsorbed organic oils, etc.) during the manufacturing and packaging process of these commercial devices are removed.

In spite of the binding materials in Pt-SPEs being found to be susceptible to acid attack (as discussed in Section 4.3.6), it is unlikely that this improvement was due to immersion in the

0.5 M H_2SO_4(aq) solution. Firstly, the duration (< 30 mins) at which the samples were immersed in the dilute acid solution was not sufficient to cause substantial structural deterioration of the screen printed material. Furthermore, the marked increase in the active sites for hydrogen adsorption was apparent from the initial scan, and stability was typically established within the first 30 cycles. Most importantly, the other samples did not exhibit any signs of improvement, even well beyond the 150^{th} CV cycle in 0.5 M H_2SO_4(aq). Comparing the results of Pt-SPEs subjected to the various pre-treatment protocols, polishing appears to give the best improvement. Mechanical polishing of solid electrodes is a facile standard surface cleaning protocol for the preparation of surfaces for electrochemical use, which is cheap and convenient to employ, does not (necessarily) require expensive specialized instruments (such as a plasma or UV-ozone cleaner), nor the use of organic solvents such as DMF or highly corrosive concentrated NaOH(aq) solution. And most importantly, it may enable the re-utilization of "fouled" surfaces, thus extending the life of these disposable SPEs.

4.3.5. Confocal Raman mapping and electrochemical impedance spectroscopy of unpolished and polished Pt-SPE surfaces.

To verify the chemical nature of any contaminant and gain insight into the distribution of the contaminant on the surface of Pt-SPEs, confocal Raman mapping of untreated and polished Pt-SPEs was performed. Figure 4.9 presents the chemical maps superimposed onto an optical image of the same area, and the corresponding Raman spectra of a polished Pt-SPE. Fourier transform infrared spectrometry (FTIR) was also attempted but was not sensitive enough. Distinct peaks were found in the Raman spectra in the range of 1272-1634 cm^{-1} (coloured as red and yellow) indicating the presence of significant levels of

carbon based material(s) on those surfaces. The broad peak in the range of 2857-3711 cm^{-1} (coloured in green) may relate to the presence of polymeric species. These Raman peaks are likely to be associated with areas or spots with significant amount of binding material exposed at the SPE surface. This was also found to be present on the untreated samples. Areas with lower amounts of the binding material may, however, be undetectable. The Raman map of a polished Pt-SPE in Figure 4.9 shows that the surface contaminants predominantly lie within the unpolished depressions. This clearly demonstrates that polishing removes the surface contaminants that cause passivation of active sites for hydrogen adsorption, and consequently increases the active surface areas accessible for the electrochemical redox couples of hexaammineruthenium(III/II) and hexacyanoferrate(III/II).

For a qualitative verification of the impact of polishing, electrochemical impedance spectroscopy (EIS) was performed on unpolished and polished Pt-SPEs. Large and distinct time constants were observed in the Nyquist plots for the unpolished Pt-SPE samples (in Figure 4.10). Polishing, however, resulted in a substantial decrease of the time constant polarization resistance, by a factor of ca. 10. This suggests the presence of a dielectric film (e.g. binding material) present on the unpolished Pt-SPE, which was substantially reduced after polishing.

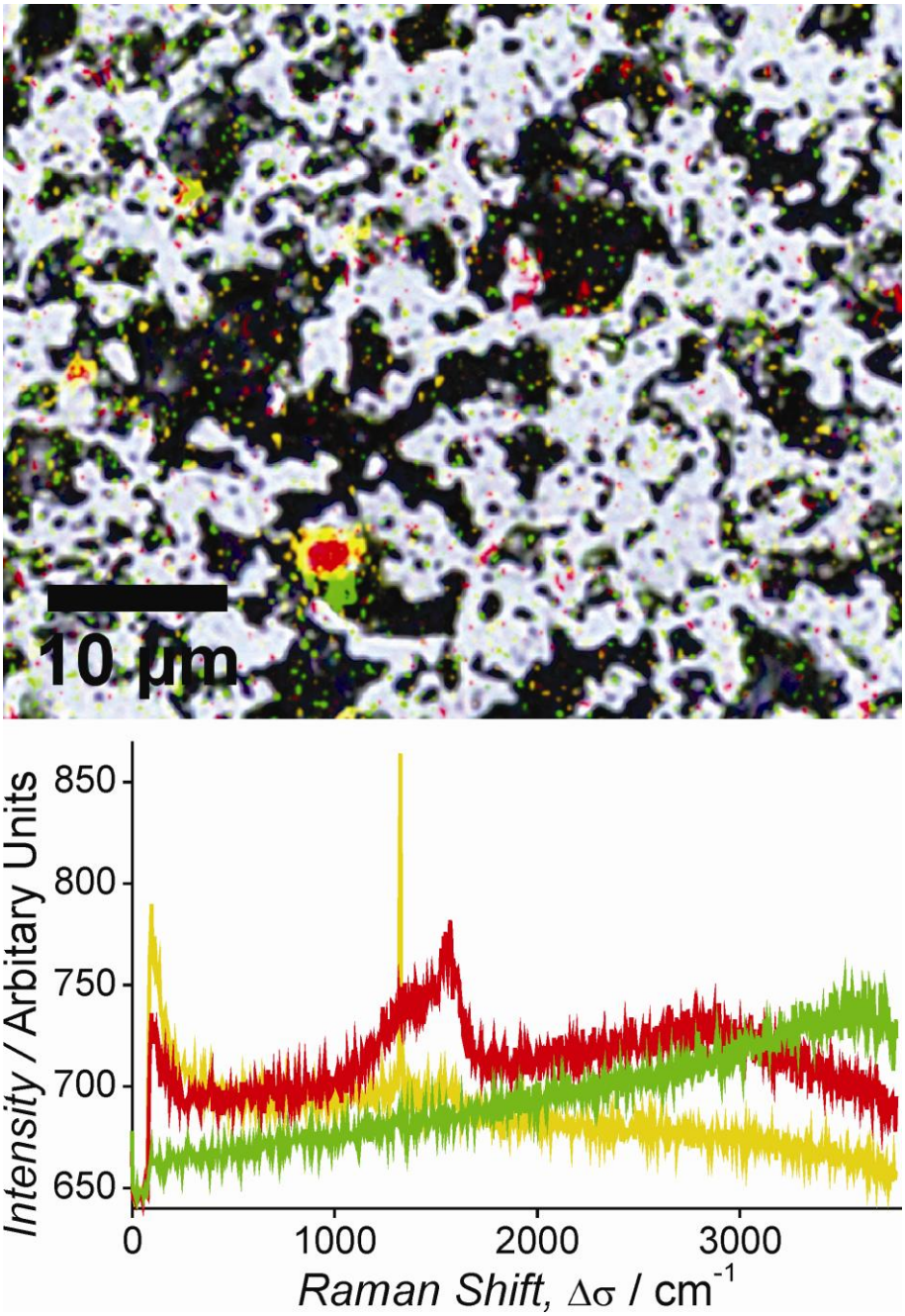

Figure 4.9. Confocal Raman mappings (in red, yellow and green) superimposed over the optical image of the same area. The three arbitrarily assigned colours of the Raman maps correspond to the Raman spectra presented below of the same colour. Each colour mapping was constructed with a band-selecting filtering applied, respectively for (red) 1272-1634 cm^{-1}, (yellow) 1317-1331 cm^{-1} and (green) 2857-3711 cm^{-1}, to Raman spectra collected at each pixel, to construct the maps.

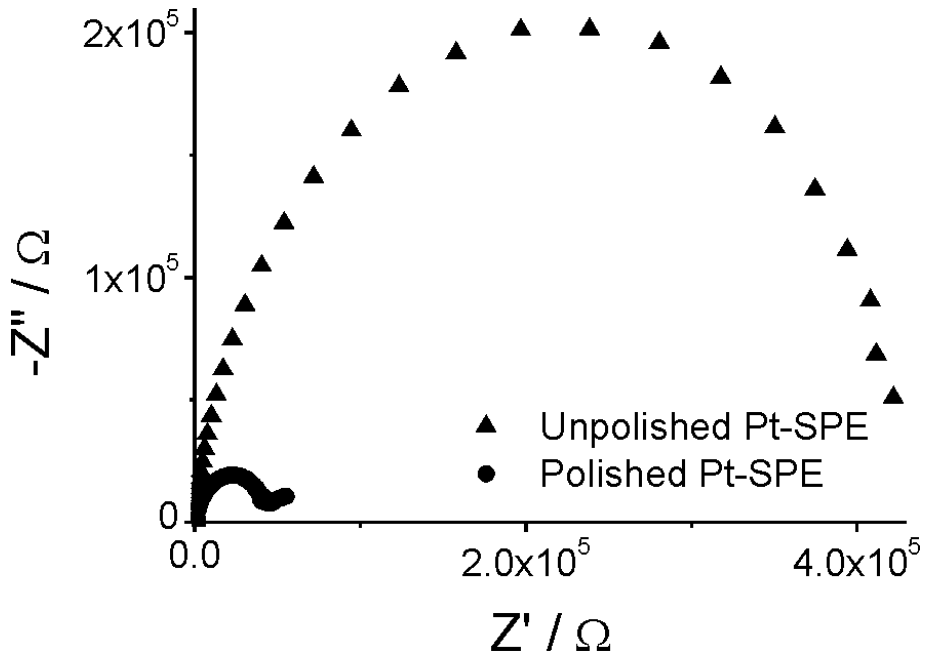

Figure 4.10. Nyquist plot of (▲) unpolished and (●) polished Pt-SPEs, collected in the frequency range of 1 mHz to 1.5 MHz (single-sine-wave mode) at RMS AC voltage of 5 mV oscillating about the pre-measured OCP, and conducted in 0.1 M KCl(aq).

4.3.6. Degradation of screen printed electrodes subjected to various treatments

Figure 4.11 (a) shows an unpolished Pt-SPE subjected to extensive CV cycling (> 1200 scans) in 0.5 M H_2SO_4(aq). The exposed working electrode considerably darkened after extensive scanning and with the screen printed silver reference electrode appearing appreciably tarnished. Similar extensive cycling in nitrogen purged 0.5 M KCl(aq) (and with fresh-out-of the-box Pt-SPEs) also was found to cause darkening of the screen printed working electrodes, which indicates that acid was not the cause. Overnight soaking of samples in 0.5 M H_2SO_4(aq) did not induce visible darkening of the working electrode as shown in Figure 4.11 (b), even though the less-inert screen printed silver surfaces were observed to tarnish. No darkening of macrodisk platinum working electrodes subjected to the same extensive electrochemical activation cycling was observed. This suggests that the

supporting materials, present in the screen printed platinum, may significantly decompose whilst the electrode is simply subjected to a relatively gentle scanning potential range (between 1.25 to -0.3 V). The binding materials of the Pt-SPEs are not perfectly inert or stable, and could also plausibly be correlated to the contaminant peaks (Figure 4.2), and the cross-over characteristics of O_2 reduction in RTILs discussed in Chapter 3 (see Section 3.3.2.1).

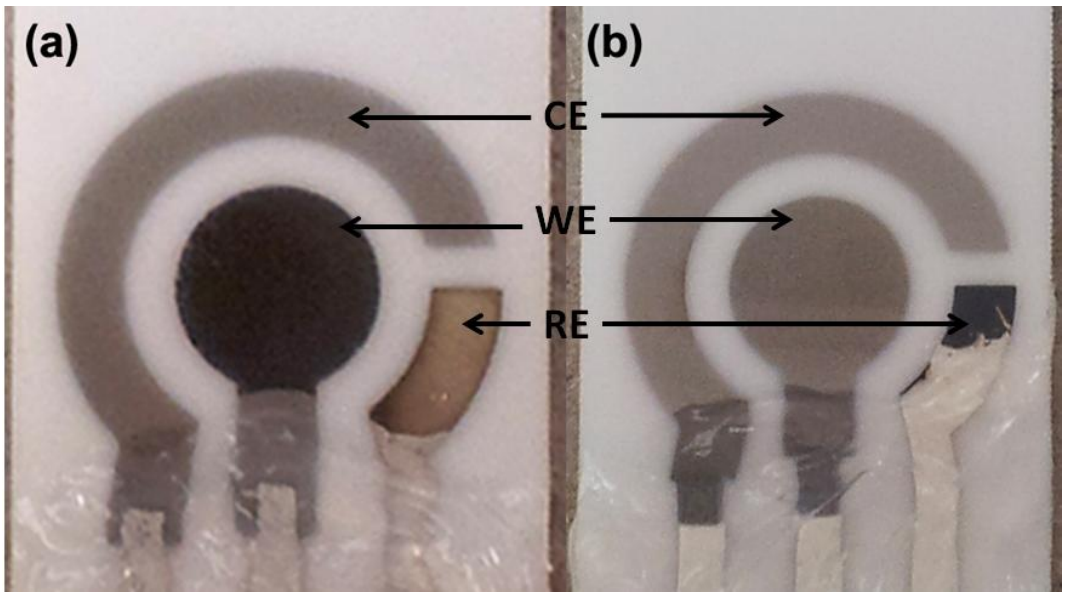

Figure 4.11. Photos of unpolished Pt-SPEs **(a)** after more than 1000 surface activation cycles in 0.5 M H_2SO_4(aq), and **(b)** after soaking in 0.5 M H_2SO_4(aq) overnight. The polymer mask was stripped by sonication in THF and the silver traces were covered with silicone.

Unpolished Pt-SPEs were soaked in 0.5 M H_2SO_4(aq) for more than three hours before they were sonicated for merely 5 mins in Milli-Q water or THF as respectively shown in Figure 4.12 (a) and (b). The images show severe structural deterioration of the screen printed materials due to exposure in 0.5 M H_2SO_4(aq). However, without the prolonged immersion in acid, the screen printed materials did not disintegrate under sonication, as was demonstrated by both the polished and unpolished THF-sonicated Pt-SPEs. Furthermore, as can be seen in

Figure 4.12 (b), the screen printed materials previously covered by the blue polymer mask remained intact after sonication since they were unexposed to acid. DropSens Ag (DRP-C013) and Au (DRP-250AT) SPEs were also subjected to similar acid treatment, and all similarly showed substantial structural deterioration. These findings suggest that the acid may have attacked the compounds within the screen printed material (e.g. the binding materials). This implies that the standard and widely used protocol for the activation of platinum electrode surfaces may not only be ineffective for the removal of passivating binding polymers/oils (as seen in the results presented in Figure 4.2), but may actually compromise the structural integrity of the screen printed materials.

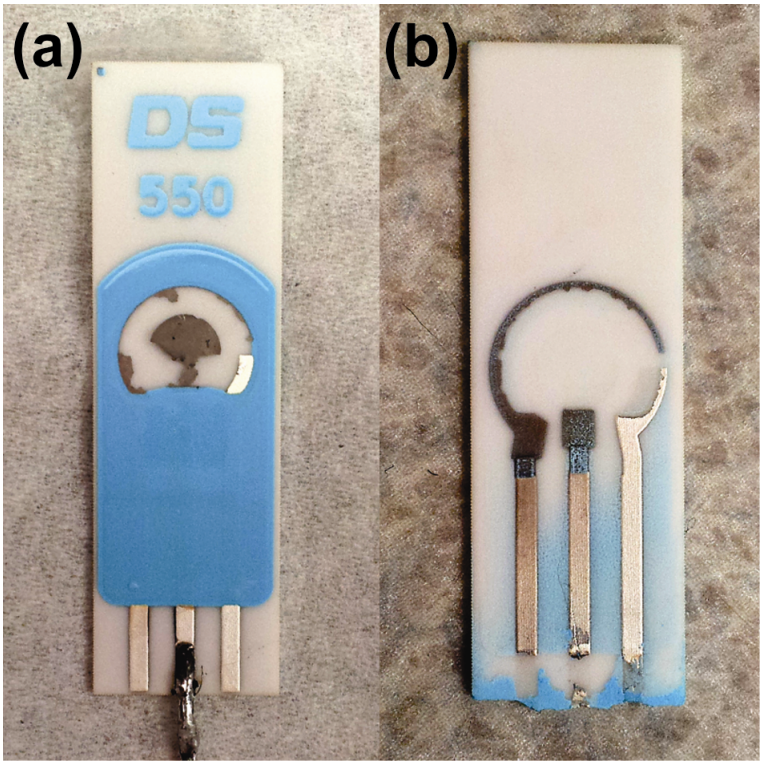

Figure 4.12. Photos of Pt-SPEs exposed to 0.5 M H_2SO_4 for more than three hours, followed by 5 mins sonication in **(a)** Milli-Q Water, and **(b)** in THF. Pt-SPEs that were not exposed to acidic or caustic solvents did not disintegrate during sonication (e.g. Figure 4.11).

NaOH treated (soaked for 1 hr in a 3 M solution) Pt, Au and Ag SPEs were also sonicated in Milli-Q water for 5 mins, and similar deterioration of the screen printed materials were observed. Soaking of Pt-SPEs in 0.5 M H_2SO_4(aq) for merely 30 mins did not show visible signs of disintegration after sonication. Regardless, these findings suggest that strong acidic or alkaline solutions may not be suitable electrolytes for use with SPEs in long-term experiments. This is because the continual etching effect of the acid/alkaline solution may potentially lead to instability in the long term; thus, a more dilute solution may be better for longer (> 1 hr) experiments.

Untreated C-SPE (DRP-110) showed significant signs of disintegration after 5 mins of sonication in water, and completely disintegrated when sonicated in THF. Exposure to the acid appears to substantially exacerbate the effect that sonication has on the screen printed carbon material in water. Furthermore, C-SPEs were unable to withstand the harsh polishing treatment described in this work. However, gentle polishing with office paper has been recommended for C-SPEs. [114] Polishing had also been successfully applied on Au-SPE w/o observable disintegration of the screen printed material. Mechanical polishing as a pre-treatment protocol can thus also potentially be extended to Ag-SPEs (i.e. the RE material on Pt-SPE), and Au-SPEs. This is provided that the CE and RE of those electrodes were not made of screen printed carbon, or materials which similarly could not withstand the harsh mechanical polishing used. Electrochemical studies of polished Au- nor Ag-SPEs with RTIL electrolytes were however not investigated. The screen printed silver of the Pt-SPE reference electrode and contact-pads was also found to visibly tarnish (to a light green colour) after being exposed to ozone. This suggests that the UV-ozone treatment protocol is not suitable for SPEs that contain silver as a SPE material.

4.4. Conclusions

Five different surface pre-treatment protocols have been explored for commercially available Pt-SPEs. Of the main surface cleaning protocols studied, electrochemical activation of Pt-SPEs in 0.5 M H_2SO_4(aq) was discovered to be ineffective for the removal of contaminants substantially passivating the screen printed surfaces for adsorption of hydrogen. NaOH treatment of Pt-SPEs showed an even more impressive enhancement in their active hydrogen adsorption surface area compared to other pre-treatments. However, large capacitive background currents in the hexaammineruthenium(III/II) chloride and hexacyanoferrate(III/II) voltammetries were observed, likely due to degradation of the screen printed material as the result of over etching. Tests conducted on different SPEs (Pt/Au/Ag/C) suggest that they are highly susceptible to degradation by strong acidic or caustic solutions, and could potentially lead to instability in the long-term due to continual etching of the binding materials. A more dilute solution is recommended if acidic/alkaline conditions are necessary. A marked improvement in the hexaammineruthenium(III/II) redox couple kinetics after DMF treatment was also seen. Mechanical polishing showed significant improvement in the hydrogen adsorption and redox active surface areas by the effective removal of the surface contaminants; this was verified by confocal Raman mapping of unpolished and polished surfaces. Mechanical polishing as a pre-treatment protocol can potentially also be extended to Ag-SPEs (i.e. the RE material on Pt-SPE), and Au-SPEs. This is provided that the CE and RE of those electrodes were not made of screen printed carbon, or materials which similarly could not withstand the harsh mechanical polishing used. The ability of SPEs to be polished would also effectively extend the reusability of these traditionally "single-use" devices. The effectiveness that polishing has on the O_2 sensing performance of Pt-SPEs in RTILs, compared to unpolished Pt-SPEs, were investigated, and will be discussed in the next chapter.

5. Performance enhancement by mechanical polishing of platinum screen printed electrodes for oxygen sensing in room temperature ionic liquids.

5.1. Introduction

As described in Chapter 3, eight different RTILs on Pt-SPEs, and four different SPEs (C, Au, Ag, Pt) with two selected RTILs were investigated for their reductive electrochemical responses to oxygen gas, and to survey their analytical utility for the sensing of oxygen gas. Results have suggested that the commercially available SPE devices may only generally be implemented as short-term or "single-use" sensing surfaces for O_2 detection in those RTILs investigated. Oxygen redox voltammetries on these SPE/RTIL systems were observed to significantly degrade after prolonged repeated CV cycling. A 'cross-over' (or narrowing) characteristic during the reverse scan of the $O_2/O_2^{\bullet-}$ redox CV was generally observed for the slightly protic imidazolium based RTILs on Ag, Au, and Pt-SPEs. In contrast, the pyrrolidinium RTIL (e.g. $[C_4mpyrr][NTf_2]$) showed CVs that are comparable to those collected on standard Pt macrodisk electrodes. For the purpose of investigating the impact of mechanical polishing on the $O_2/O_2^{\bullet-}$ redox couple on Pt-SPEs, an imidazolium RTIL (i.e. $[C_2mim][NTf_2]$) and the $[C_4mpyrr][NTf_2]$ RTIL were selected for the studies presented in this chapter. $[C_2mim][NTf_2]$ was selected since it has the highest O_2 diffusion coefficient amongst the imidazolium RTILs tested, while $[C_4mpyrr][NTf_2]$ was selected due to its highly aprotic nature [230], the high stability exhibited in the presence of $O_2^{\bullet-}$ and binding materials of the SPEs (as reported in Chapter 3).

In a follow up study (Chapter 4), five different pre-treatment protocols were tested on Pt-SPEs, and the treated SPEs were characterized for their effective active surface areas in aqueous solutions of H_2SO_4, hexaammineruthenium(III) chloride and potassium hexacyanoferrate(III) (ferricyanide). Results showed that not only could Pt-SPEs withstand significant mechanical polishing without structural disintegration, but the electrochemically active surface areas (normalized with respect to their topographical surface areas) of polished Pt-SPEs significantly increased. It was proposed that polishing results in the effective removal of residual binding material on the surface of untreated Pt-SPEs, exposing a fresh surface of active material (i.e. platinum particles) underneath. This chapter carries on from that study, and investigates the viability of polishing as a technique to extend the lifespan of these integrated screen printed devices when used for oxygen sensing with RTILs. In contrast with the previous study for O_2 sensing on RTIL/SPE systems (in Chapter 3), this chapter instead focuses on providing a further look into the longer-term performance of the platinum SPE, for its potential application in sensing and monitoring of oxygen gas concentrations in a controlled environment (with inert nitrogen as the background carrier gas). Only one other work has reported the polishing of SPE as a pre-treatment before sensing use [114] (as has been previously discussed under Section 4.3.6). That work involves using a gentler method of polishing (using office paper) for the preparation of C-SPE for the sensing of rabbit immunoglobulin in aqueous solutions. [114]

5.2. Experimental

DropSens Pt-SPEs (DRP-550, Oviedo, Spain) were chosen for this study as a continuation of the work presented in Chapter 3. The Pt-SPEs were polished and prepared according to the procedures described in Chapter 4, under Section 4.2.2.1. Pt-SPEs described as 'unpolished' were used 'as-is', i.e. straight out of the box without being subjected to any pre-treatment. The amperometric gas-sensing experimental setup was as detailed under Section 2.3. To ensure proper coverage of the 3 electrodes on the polished Pt-SPE after the blue polymer mask has been stripped, 30 μL aliquots of the respective RTILs were consistently used for each experiment presented in this chapter (in contrast with Chapter 3, where only 7 μL was used). It is standard practice before conducting amperometric measurements, for a linear sweep or cyclic voltammetry to be run, to verify the formal potential of electron transfer (especially if an unstable/pseudo-reference is used). A scan rate of 100 $mV \cdot s^{-1}$ was used to conduct the CV measurements, unless otherwise stated. Before the commencement of CV scans in 100% oxygen, repeated consecutive CV scans were performed in a nitrogen purged environment until the voltammetry stabilized (typically up to 12 cycles; see Section 3.2). For the consecutive CV scan studies, 8 mins was allowed before the commencement of the next scan to allow for depleted oxygen gas from the previous scan to replenish at the WE surface.

For amperometric experiments, the data was collected at 15 s time intervals with an overpotential of 200~300 mV, set from the O_2 reduction peak position in the CV measurements. The response was allowed to stabilize for at least 30 mins before commencing with introduction of O_2 gas. This was to allow the non-Faradaic background charging currents, and current contributions from electrochemically active contaminants to be sufficiently suppressed. A gas flow rate of 100 sccm was used for all CV experiments. To ensure faster displacement of the previous concentration of oxygen within the cell, a much

higher flow rate of 1000 sccm was used during the Amperometric experiments. Bulk electrolysis experiments were conducted on a polished platinum macrodisk working electrode (1.6 mm diameter, BASi, West Lafayette, Indiana, USA), with a Pt-wire coil as the counter electrode and a Ag wire as the pseudo reference electrode. For the electrochemical activation experiments, the setup follows what was described in Sections 2.3.2 and 4.2.3. Pt-SPEs were immersed in solutions of 0.5 M H_2SO_4(aq) and 0.5 KCl(aq) and cycled for 30 times between 1.25 V and -0.25 V (vs. Ag/AgCl reference electrode), at a scan rate of 1 $V \cdot s^{-1}$. Pt-SPEs were also simply soaked in 0.5 M H_2SO_4(aq) for an hour as a control.

5.3. Results and Discussion

5.3.1. Comparison of unpolished and polished Pt-SPE/RTIL systems for $O_2/O_2^{\bullet-}$ redox voltammetry subjected to consecutive cycling.

To compare the effect of polishing on the short- and long-term performance and stability of the Pt-SPE/RTIL systems for oxygen sensing, and to assess the susceptibility towards deterioration in response over time, polished and unpolished Pt-SPEs were subjected to numerous repeated scans in O_2 saturated RTILs (i.e. conducted under 100% O_2 flow). The higher volume of RTIL aliquot (30 μL), in contrast with Chapter 3 (where 7 μL was used), was necessary to ensure full coverage of the 3 electrodes on the polished Pt-SPE after the blue polymer mask has been stripped. Stripping of the blue polymer mask exposed previously covered electrode materials of the CE and RE. Also, the surrounding polymer-mask, which holds the spread of the RTIL at its well defined rim, was removed by polishing. This consequently resulted in a greater tendency for the spread of the RTIL thin-films (namely $[C_2mim][NTf_2]$ and $[C_4mpyrr][NTf_2]$) to recede over time, leading to gradual unwetting of parts of the electrode surfaces by the electrolyte (see also Section 1.4). 8 mins between consecutive scans was set during the CV experiments, to allow for depleted oxygen gas from the previous scan to replenish at the WE surface. Setting the waiting time to as low as 4 mins was found not to have any impact on the voltammogram of the consecutive scans. However, the background currents were observed to decrease at shorter waiting times. This was due to the depletion of the (likely) slower diffusing RTIL decomposition contaminant products (see Section 1.3.2.4) that was built up over the consecutive scans which was found to appear as a 'pre-peak' before the onset of the O_2 reduction peak.

Figure 5.1 shows the CVs of $O_2/O_2^{\bullet-}$ redox in the two selected RTILs ([C_2mim][NTf_2] and [C_4mpyrr][NTf_2]) conducted on unpolished and polished Pt-SPEs, with only the 1st, 2nd and 120th scans presented. Figure 5.1 (a) presents representative CVs of $O_2/O_2^{\bullet-}$ redox in [C_2mim][NTf_2] on unpolished Pt-SPEs. The oxygen reduction peak potential, $E_{p(O_2)}$, typically shifts significantly (~600 mV) to lower potentials with successive scans, with the development of a cross-over characteristic from the second scan (as reported in Chapter 3). This shift in O_2 reduction potential is present in both [C_2mim][NTf_2] and [C_4myprr][NTf_2] electrolytes (albeit more gradual in the latter RTIL). There are two possible reasons for this: **(1)** a shift in the potential of the reference electrode, or **(2)** an alteration of the WE surface. In order to test this, ferrocene was added as an internal reference to [C_2mim][NTf_2] on an unpolished Pt-SPE (see Figure A.1 (a)-(c) in Appendix A). The result demonstrated that the shift in $E_{p(O_2)}$ was due mainly to the unstable Ag pseudo-reference on the Pt-SPE. However, it was also observed (as discussed in Appendix A) that the presence of ferrocene as an internal reference has significant (positive) influence on the long-term behaviour of the RTIL/Pt-SPE systems. It was believed that this may be due to ferrocene being reversibly oxidized as the counter electrode reaction species (in place of the irreversible oxidation of the $[NTf_2]^-$ anion). The use of ferrocene/ferrocenium as an in-situ redox couple was avoided for all future experiments, since it was found to alter the O_2 response. Terriero, et al. [254] also reported that the diffusion transport properties of the species within the electrolyte can significantly depend on the presence/absence of ferrocene or other impurities added to the neat RTIL, and may not be ideal for analytical purposes. Hence, in this thesis, the currents and peak shapes are compared, but the absolute values of the potentials are not examined.

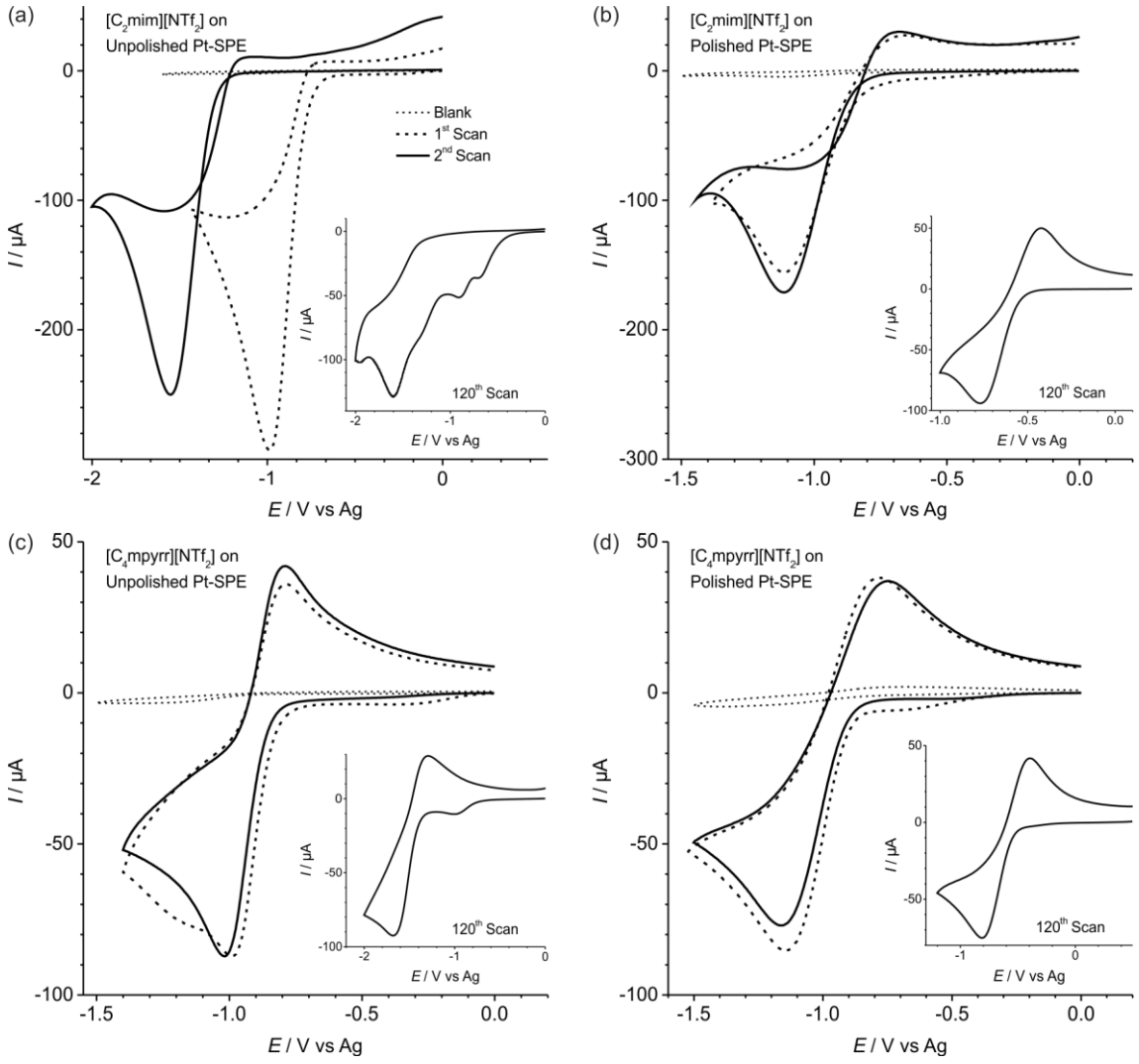

Figure 5.1. Comparison of the (**- -**) 1st, (**–**) 2nd, and (inset) 120th cyclic voltammetric scan cycles of $O_2/O_2^{\bullet-}$ redox with 100 %O_2 flow, in **(a)** [C_2mim][NTf_2] on unpolished and **(b)** polished Pt-SPEs, and **(c)** [C_4mpyrr][NTf_2] on unpolished and **(d)** [C_4mpyrr][NTf_2] on polished Pt-SPEs. The blank voltammetry performed under 100 %N_2 flow is indicated by the small dotted lines (···). The CV scans were conducted with a scan rate of 100 mV·s^{-1}, with a waiting time of 8 mins between consecutive scans (at open circuit potential).

The oxygen reduction reaction in Figure 5.1 (a) (i.e. [C_2mim][NTf_2] on an unpolished Pt-SPE) is chemically irreversible as can be seen from the absence of a reverse peak for superoxide oxidation. It was proposed in Chapter 3 that these observations were the result of electrogenerated superoxide reacting with the screen printing pastes in the presence of the mildly acidic [230] [C_2mim][NTf_2], and the subsequent desorption of the product(s) from the working electrode surfaces (see Section 3.3.2.1). The oxidation peak during the anodic cycle

near 0 V is likely to be due to oxidation of products generated from the interaction of superoxide with the screen printing pastes, and grows from the second scan onwards together with the appearance of the cross-over characteristic. This cross-over characteristic persists typically for ~35 and up to 40 scans (in the presence of 100 % O_2), and gradually disappears with the appearance of additional contaminant peaks which becomes more significant with consecutive scans (e.g. as shown for the 120th scan in the inset of Figure 5.1 (a)). Evolution of the degradation in the voltammetry slows with lower concentrations of O_2. The precise chemistry of those contaminant peaks are currently unclear, however, they are likely the result of a build-up of reaction products of the binding materials (residing on the screen printed Pt surface) and the superoxide in the presence of [C_2mim][NTf_2]. With continued scanning, the voltammetry degrades further, with growth of multiple contaminant peaks as shown in the inset of Figure 5.1 (a). Appreciable pre-peak development was observed to occur within the first 10 scans. Some of the pre-peaks that appeared may plausibly be attributed to a comparable radical transfer mechanisms, that have been observed for O_2 with polyaniline-tannic acid (PANI-TA) samples studied by Ležaić et al. [255] This radical transfer mechanism was proposed to be the major mechanism for the reaction between monophenols and $O_2^{\bullet-}$ in aprotic solvents. [102] In that work, the electrogenerated $O_2^{\bullet-}$ acts as a weak base, while the phenolic compound acts as a Brönsted acid (see paper by René et al. [102]). β-aminoformamides could also form in the presence of sufficiently basic species (i.e. products due to interactions $O_2^{\bullet-}$ and SPE binding materials) leading to ring opening degradation of the cation. [163] This may explain the appearance of multiple pre-peaks observed on the unpolished Pt-SPE after running many consecutive CV scans.

Figure 5.1 (b) presents representative CVs of $O_2/O_2^{\bullet-}$ redox in [C_2mim][NTf_2] on polished Pt-SPEs. After polishing, the oxygen reduction peak current tends to shift slowly towards less negative potentials (by ca. 340 mV) and with the disappearance of the cross-over

characteristic occurs just within the first 15 scans. This is in contrast with the oxygen reduction voltammetric behaviour for unpolished Pt-SPE discussed in Section 3.3.2. After more than 80 cycles, the CV eventually evolved into what resembles the reversible $O_2/O_2^{\bullet-}$ redox couple on a typical macrodisk Pt-electrode [141] with significant attenuation of the peak current (as was the case with unpolished Pt-SPEs). Based on this result, repeated CV cycling of a sufficient number of times (e.g. 20 scans) in the presence of oxygen (i.e. at 100 % vol.), could be implemented as a pre-conditioning step to be incorporated, as part of the pre-treatment protocol, after the Pt-SPEs are polished. With further consecutive CV scans, beyond the 120th cycle, a small O_2 reduction pre-peak develops in the cathodic scan, resembling the feature in the CVs of Figure 5.1 (c).

Figure 5.1 (c) presents representative CVs of $O_2/O_2^{\bullet-}$ redox in [C_4mpyrr][NTf_2] on unpolished Pt-SPEs. Compared to the $O_2/O_2^{\bullet-}$ redox voltammetric response in the imidazolium RTIL, [C_2mim][NTf_2], the current in the pyrrolidinium RTIL, [C_4mpyrr][NTf_2], showed substantially more stability over repeated scans (see Table 5.1) and the reaction is reversible. This could be attributed to the high aprotic character of the pyrrolidinium cation [230] compared to imidazolium cations, as discussed in Chapter 3. The O_2 reduction peak potential tends to progressively shift towards more negative potentials, by up to 500-700 mV from its initial position after the first ca. 50 cycles, and remained relatively stable thereafter. The magnitude of this shift is similar to that observed for the unpolished Pt-SPE in the RTIL, [C_2mim][NTf_2]. The more gradual shift in O_2 reduction peak potential observed in [C_4mpyrr][NTf_2] could again be due to the comparatively higher stability of binding materials from degradation by interaction with the superoxide radical in this comparatively more aprotic and stable RTIL. [163] An appreciable “pre-peak”, gradually develops over time during the consecutive scans within 50 CV scan cycles. This is possibly due to the gradual build-up of reaction products in the presence of impurities (e.g. screen-printing binders, impurities

from the RTIL synthesis, absorbed moisture, etc. as discussed under Section 1.3.2.4) within the 30 μL RTIL aliquot.

Figure 5.1 (d) presents representative CVs of $O_2/O_2^{\bullet-}$ redox in $[C_4mpyrr][NTf_2]$ on polished Pt-SPEs. The voltammetry was reversible and O_2 reduction peak current was relatively stable through the consecutive cycling. In contrast with unpolished Pt-SPEs, the O_2 reduction peak position, E_p, tends to shift to less negative potentials over time by ca. 340 mV. This value of E_p is at a similar value observed for polished Pt-SPEs with the imidazolium RTIL (see values of E_p summarized in Table 5.1). No visible pre-peak were present until more than 250 CV cycles, and the voltammetry resembles that collected on the standard platinum macrodisk working electrode even after more than 120 CV cycles. Despite of the relative stability of the $[C_4mpyrr]^+$ cation (compared to $[C_2mim]^+$), degradation of the $[C_4mpyrr]^+$ cation by reduction into N-methylpyrrolidine and the butyl radical may still be possible.[163] The degradation could be aggravated by the presence of binding material on the SPE surface interacting with the electrogenerated superoxide. This may explain the more significant appearance of a pre-peak on the unpolished SPE compared to the polished SPE.

5.3.2. Comparison of the active surface areas of unpolished and polished Pt-SPEs for O_2 reduction.

Table 5.1 summarizes the various measured parameters from the CV, and the derived active surface area, A_a, of the Pt-SPEs towards the reduction of O_2. A_a was derived from the CV peak currents using equation (1.8), with the respective solubility, *s*, and diffusion coefficient, *D*, of O_2 in the two RTILs (given in Table 1.4). Values of the topographic surface areas, A_m, for the unpolished (e.g. untreated) and polished Pt-SPE were estimated and summarized in Table 4.1, and the average values are presented in Table 5.1. The values of A_a were then

normalized with respect to the averaged topographic surface areas, A_m, of the unpolished and polished Pt-SPEs respectively (i.e. A_a/A_m) (also see Section 4.2.5.1).

Table 5.1. Averaged topographic surface areas, A_m, (from Table 4.1) estimated from 3D stacked confocal microscopy imaging in Section 4.3.3, and active surface areas, A_a, derived from oxygen reduction cyclic voltammetric experiments in the two RTILs, for unpolished and polished Pt-SPEs. A_a was then normalized with respect to A_m (i.e. A_a/A_m).

	Unpolished		**Polished**	
Topographic Surface Area, A_m / mm^2	32		24	
	[C_2mim][NTf_2]			
	1st Scan	120th Scan	1st Scan	120th Scan
O_2 reduction peak potential, E_p / V	-0.989	-1.60	-1.11	-0.773
O_2 reduction peak current, I_p / μA	-293	-129	-156	-94.0
Active surface area, A_a / mm^2	29.0	12.7	15.4	9.29
A_a/A_m	0.91	0.40	0.64	0.39
	[C_4mpyrr][NTf_2]			
	1st Scan	120th Scan	1st Scan	120th Scan
O_2 reduction peak potential, E_p / V	-0.989	-1.68	-1.15	-0.812
O_2 reduction peak current, I_p / μA	-87.2	-92.5	-85.3	-75.2
Active surface area, A_a / mm^2	12.2	12.9	11.9	10.5
A_a/A_m	0.38	0.40	0.50	0.44

Comparing the change in A_a/A_m for the 1st and 120th scans, listed in Table 5.1, on unpolished Pt-SPEs, a 56 % decrease was found in [C_2mim][NTf_2] while a 6 % increase was found in [C_4mpyrr][NTf_2]. After polishing, the change in A_a/A_m was reduced to a 40 %

decrease in $[C_2mim][NTf_2]$, whereas a 12 % decrease was noted in $[C_4mpyrr][NTf_2]$. Rather than an actual change occurring in active surface area (i.e. passivation) during the consecutive CV scans, it is hypothesised that the presence of significant binding material on the unpolished Pt-SPE in the presence of the mildly protic $[C_2mim][NTf_2]$ could have lead to an overall > 1 electron process during the reduction of O_2 (refer to Table 1.2, and also Section 1.2.2 and 1.3.2.4). This is likely the result of a radical transfer reaction between the electrogenerated superoxide with the binding material (giving rise to very basic species), which then subsequently reacts with the mildly protic $[C_2mim]^+$ cation (as discussed in Section 3.3.2.1). This may account for the larger peak currents observed for the unpolished Pt-SPE in $[C_2mim][NTf_2]$ on its initial CV scan. Depletion of surface-exposed binding materials after many consecutive CV cycles could thus explain the large attenuation of the currents after 120 CV cycles. This is further supported by the fact that current vs. voltage slopes at the onset of the O_2 reduction were appreciably steeper for unpolished Pt-SPEs in $[C_2mim][NTf_2]$.

Further, comparing A_a/A_m of only the 1st scans, a 29 % decrease was observed in $[C_2mim][NTf_2]$ after the Pt-SPE was polished. This could indicate significant removal of surface-exposed binding materials available (to contribute to the > 1 electron process as discussed) after polishing. In contrast, a 30 % increase was observed in $[C_4mpyrr][NTf_2]$ after the Pt-SPE was polished. This may perhaps be due to an actual increase in exposed active surface area after removal of passivating binders due to polishing. The significant differences observed in A_a/A_m, from the first CV scans due to polishing, cannot be explained by inconsistencies in polishing of separate Pt-SPE samples alone (assessed from duplicate measurements to be at only ca. 6 and 8 % for unpolished and polished Pt-SPEs respectively, see Table 4.1 and discussions in Section 4.3.3).

Comparing A_a/A_m for the 120th CV cycle, A_a/A_m appears to have converged to a similar value (of ca. 0.4) in [C_2mim][NTf_2], while a smaller 9 % increase was noted in [C_4mpyrr][NTf_2] after polishing. Overall A_a/A_m values obtained in all four RTIL/Pt-SPE systems appear to be significantly more similar in value to one another (at ca. 0.4) at the 120th compared to the 1st CV scan. This shows a RTIL independent convergent tendency of the O_2 reduction peak currents after sufficient consecutive CV scans (e.g. 120 cycles), and the surface area derived from the O_2 reduction peak current may thus be reflective of the actual electrochemically active surface area of Pt-SPE with a one electron O_2 reduction process on both unpolished and polished Pt-SPEs.

5.3.3. Comparison of $O_2/O_2^{\bullet-}$ redox couple peak-to-peak separations in RTILs on unpolished and polished Pt-SPEs.

Table 5.2 lists the peak-to-peak separations of $O_2/O_2^{\bullet-}$ redox, ΔE_{p-p}, in [C_2mim][NTf_2] and [C_4mpyrr][NTf_2] RTILs, on the 1st, 2nd and 120th scan cycles, for unpolished and polished Pt-SPEs. In [C_2mim][NTf_2], the superoxide oxidation peak is only visible on the polished Pt-SPE samples. In [C_4mpyrr][NTf_2], ΔE_{p-p} values for the Pt-SPEs are larger after polishing in the initial scans, and increase after multiple consecutive scanning for both unpolished and polished Pt-SPEs. After 120 cycles, ΔE_{p-p} values for unpolished and polished Pt-SPEs converge towards each other. The slower convergence of ΔE_{p-p} values observed in [C_4mpyrr][NTf_2] (compared to [C_2mim][NTf_2]) may be attributed to the slower (but present) degradation of binding-materials, exposed to superoxide in the more aprotic [C_4mpyrr][NTf_2] [141, 230]. However, trace amounts of water present in [C_4mpyrr][NTf_2] (see Figure 1.5) could act as a proton donor, as discussed under Section 1.3.2.4, despite of the aprotic nature of the RTIL.

Table 5.2. Comparison of peak-to-peak separations of $O_2/O_2^{\bullet-}$ redox voltammetry, $\Delta E_{p\text{-}p}$, in $[C_2mim][NTf_2]$ and $[C_4mpyrr][NTf_2]$, on the 1st, 2nd and 120th scan cycles, measured on unpolished and polished Pt-SPEs.

RTIL	Surface	1st / 2nd Scan	120th Scan
		$\Delta E_{p\text{-}p}$ ($O_2/O_2^{\bullet-}$) / mV	
$[C_2mim][NTf_2]$	Unpolished Pt-SPE	No oxidation peak	No oxidation peak
	Polished Pt-SPE	455 / 430	351
$[C_4mpyrr][NTf_2]$	Unpolished Pt-SPE	201 / 226	381
	Polished Pt-SPE	363 / 412	415

5.3.4. Improved limits of detection (LOD) and stability of Pt-SPEs for oxygen sensing in RTILs after polishing.

5.3.4.1. Analytical utility for oxygen gas-sensing of unpolished vs. polished Pt-SPEs in RTILs.

Figure 5.2 shows $O_2/O_2^{\bullet-}$ redox CVs at varying concentrations (0, 10, 20, 40, 60 80, 100 % vol., vs. N_2 as the inert carrier gas) in both $[C_2mim][NTf_2]$ and $[C_4mpyrr][NTf_2]$ RTILs on unpolished and polished Pt-SPEs. To assess the long term advantages of polishing, in contrast with the experiments presented in Chapter 3, acquisition of the calibration response characteristics of these systems were conducted after the respective systems had undergone 120 CV cycles in the presence of 100 % vol. O_2. The repeated CV cycling in the O_2 saturated RTILs were carried out to simulate prolonged amperometric O_2 sensing use, and each sample was carried out under identical conditions just described. As was already shown in the inset of Figure 5.1, unusual voltammetry on the unpolished Pt-SPEs is observed after prolonged scanning (especially for $[C_2mim][NTf_2]$), with the appearance of additional peaks

(as discussed in Section 5.3.1). This also leads to very significant background currents (i.e. at 100 % vol. N_2 flow) for $[C_2mim][NTf_2]$ on unpolished Pt-SPEs, which is undesirable for gas-sensing purposes. Furthermore, on the unpolished Pt-SPEs, the relative peak currents of the contaminant waves that have developed appear to vary in response to changing oxygen concentrations in both RTILs. This indicates that the accumulated electrogenerated products within the RTIL, attributed to these contaminant waves (see Section 5.3.1), interact with the electrochemical reduction of oxygen to varying degrees, for the different electrochemically active species present in $[C_2mim][NTf_2]$ on unpolished Pt-SPE. A significant but much smaller pre-peak to the O_2 reduction current peak can be seen in $[C_2mim][NTf_2]$ on a polished Pt-SPE – which does not vary in response to varying concentrations of O_2.

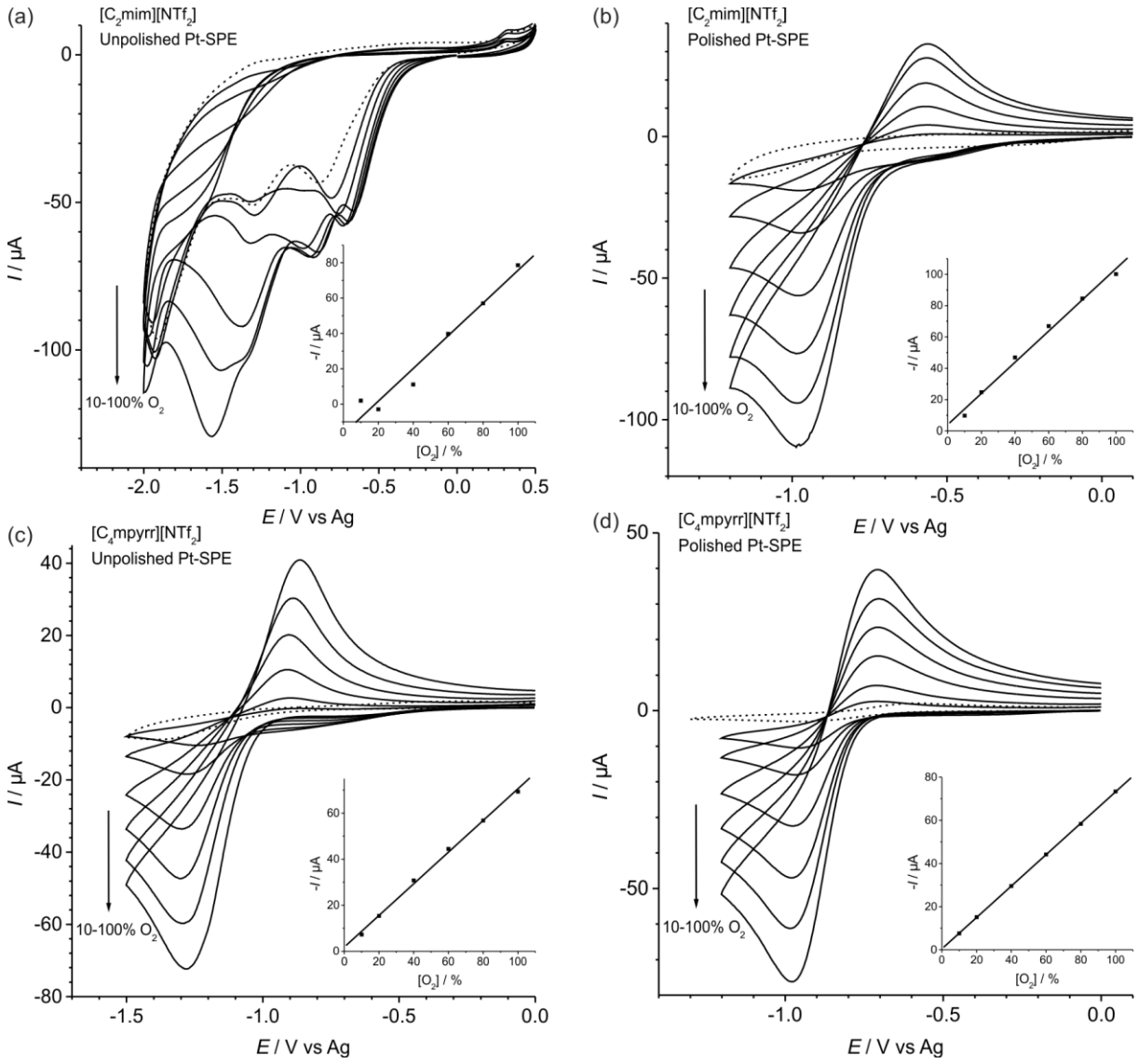

Figure 5.2. Cyclic voltammetry for O_2 reduction in $[C_2mim][NTf_2]$ carried out on **(a)** an unpolished Pt-SPE and **(b)** a polished Pt-SPE, and also in $[C_4mpyrr][NTf_2]$ on **(c)** an unpolished Pt-SPE and **(d)** a polished Pt-SPE. The votammograms were collected at a scan rate of 100 $mV{\cdot}s^{-1}$ vs. Ag-RE at 10, 20, 40, 60, 80 and 100 % vol. O_2. The dotted lines are CVs in the absence of oxygen. The insets are corresponding plots of O_2 reduction peak current vs. % vol. O_2 in the flow, and the line of best-fit.

The O_2 reduction peak currents were background subtracted by the corresponding currents on the blank CVs, and plotted with respect to varying oxygen concentrations (as shown in the insets of Figure 5.2). For $[C_2mim][NTf_2]$ on the unpolished Pt-SPE in (a), the currents of the largest peak at potentials < -1.2 V were chosen to construct the calibration data. For the unpolished Pt-SPE (and especially in $[C_2mim][NTf_2]$), despite of the presence of

electrochemically active interfering species, reasonable linear calibration plots were obtainable. Linear regression analysis was performed on the calibration plots. The equations for the linear best-fits and the corresponding LOD values (derived viz. equation (D.1)) are presented in Table 5.3.

It is to be noted that for the unpolished Pt-SPEs, the RTIL/Pt-SPE systems have been subjected to 120 consecutive CV cycles in the presence of 100 % vol. O_2, for the values presented in Table 5.3. Whereas, the values presented in Table 3.2 were for RTIL/Pt-SPE systems there were only subjected to 12 consecutive CV cycles in the presence of 100 % vol. O_2, before O_2 calibration experiments were performed. The LOD for $[C_2mim][NTf_2]$ on unpolished Pt-SPE in Table 5.3 is substantially poorer (at 23.0 % vol.) compared to the LOD presented in Table 3.2 (at 3.3 % vol.). The sensitivity, at 8.98×10^{-7} A·(% vol.)$^{-1}$, in Table 5.3 is also significantly poorer compared to that presented in Table 3.2 (1.88×10^{-6} A·(% vol.)$^{-1}$). These are likely due to the deterioration of the voltammetry, after the RTIL/Pt-SPE system have been subjected to 120 consecutive CV cycles, for Table 5.3. However, for $[C_4mpyrr][NTf_2]$ on unpolished Pt-SPEs, the LOD improved after 120 consecutive CV cycles, from 7.9 % vol. (Table 3.2) to 0.82 % vol. (Table 5.3). This may perhaps be due to the depletion of trace amounts of impurities (such as water) after 120 consecutive CV cycles in the presence of O_2. The O_2 sensitivities, before and after the RTIL/unpolished Pt-SPE systems were subjected to 120 consecutive CV cycles, were however similar, at 6.40×10^{-7} A·(% vol.)$^{-1}$ and 6.88×10^{-7} A·(% vol.)$^{-1}$ (from Table 3.2 and 5.3 respectively).

The LOD values for O_2, measured in both RTILs, were significantly better on polished Pt-SPEs, and the improvement from polishing was more remarkable in $[C_2mim][NTf_2]$, with a 46 % improvement in the estimated LOD, whereas the LOD in $[C_4mpyrr][NTf_2]$ only saw a modest 5 % improvement after polishing. The LOD value in $[C_4mpyrr][NTf_2]$ was

significantly lower than that in $[C_2mim][NTf_2]$. This was likely due to the better stability of the less protic $[C_4mpyrr][NTf_2]$ in the presence of superoxide and binding materials. Interactions of superoxide with the binding materials in $[C_2mim][NTf_2]$ (see Section 5.3.2) could lead to instability of the electrochemical response towards O_2 as binding materials are consumed in the reaction, coupled with the significant accumulation of reaction by-products within the microlitre RTIL aliquot. Furthermore, O_2 concentration sensitivities (i.e. the gradients of the linear regression lines) in both RTILs increased, while the intercepts of the calibration fit are closer to zero at 0 % vol. O_2 after polishing. This suggests a reduced presence of passivating and electrochemically active contaminants accumulated on the Pt-SPE surface and in the RTILs during consecutive scanning. These results demonstrate a significant advantage that polishing Pt-SPEs has on their performance in O_2 sensing with the two RTIL electrolytes.

Table 5.3. Equations for the linear best-fit for the calibration graphs presented in Figure 5.2, and corresponding limits of detection (LODs) based on 3 standard deviations from the regression fittings.

RTIL	Platinum SPE	Equation of calibration graph (where I / A and $[O_2]$ / % vol.)	R^2	LOD / % vol.
$[C_2mim][NTf_2]$	Unpolished	$-I = 8.98\times10^{-7}\,[O_2] + 3.63\times10^{-5}$	0.9537	23.0
	Polished	$-I = 1.00\times10^{-6}\,[O_2] + 1.33\times10^{-5}$	0.9972	12.5
$[C_4mpyrr][NTf_2]$	Unpolished	$-I = 6.88\times10^{-7}\,[O_2] + 1.81\times10^{-6}$	0.9967	0.82
	Polished	$-I = 7.27\times10^{-7}\,[O_2] + 4.64\times10^{-7}$	0.9999	0.78

5.3.4.2. Amperometry comparisons of unpolished vs. polished Pt-SPEs for oxygen sensing.

Amperometry monitoring of O_2 concentrations was also conducted for unpolished and polished Pt-SPEs in the two RTILs as presented in Figure 5.3. The amperometric measurements were conducted after the respective systems have each undergone 120 CV cycles in the presence of 100 %vol. O_2 (which shall be referred to as the 'conditioning' of the RTIL/Pt-SPE system). The O_2 concentrations were varied between 0 and 5 % vol. with respect to N_2 carrier gas in the sequence as specified in the figure legend. Before introduction of O_2, 30 mins of constant biasing under N_2 was implemented to allow background charging currents to stabilize. The cell was intermittently flushed with N_2-gas between each change of O_2-concentration, and sufficient time (up to ~50 mins) was allowed for the baseline to stabilize. This was to allow the monitoring of the stability of the baseline signal over the duration of O_2-monitoring. The slow response (Figure 5.3, estimated from 99 % of the stead state value from its baseline), of ca. 7.5 mins for $[C_2mim][NTf_2]$ and 12.5 mins for $[C_4mpyrr][NTf_2]$ was due to the large volume (30 µL) of RTIL used. As mentioned previously, this was necessary to ensure proper coverage of the exposed area of the three electrode surfaces, particularly on the polished Pt-SPEs.

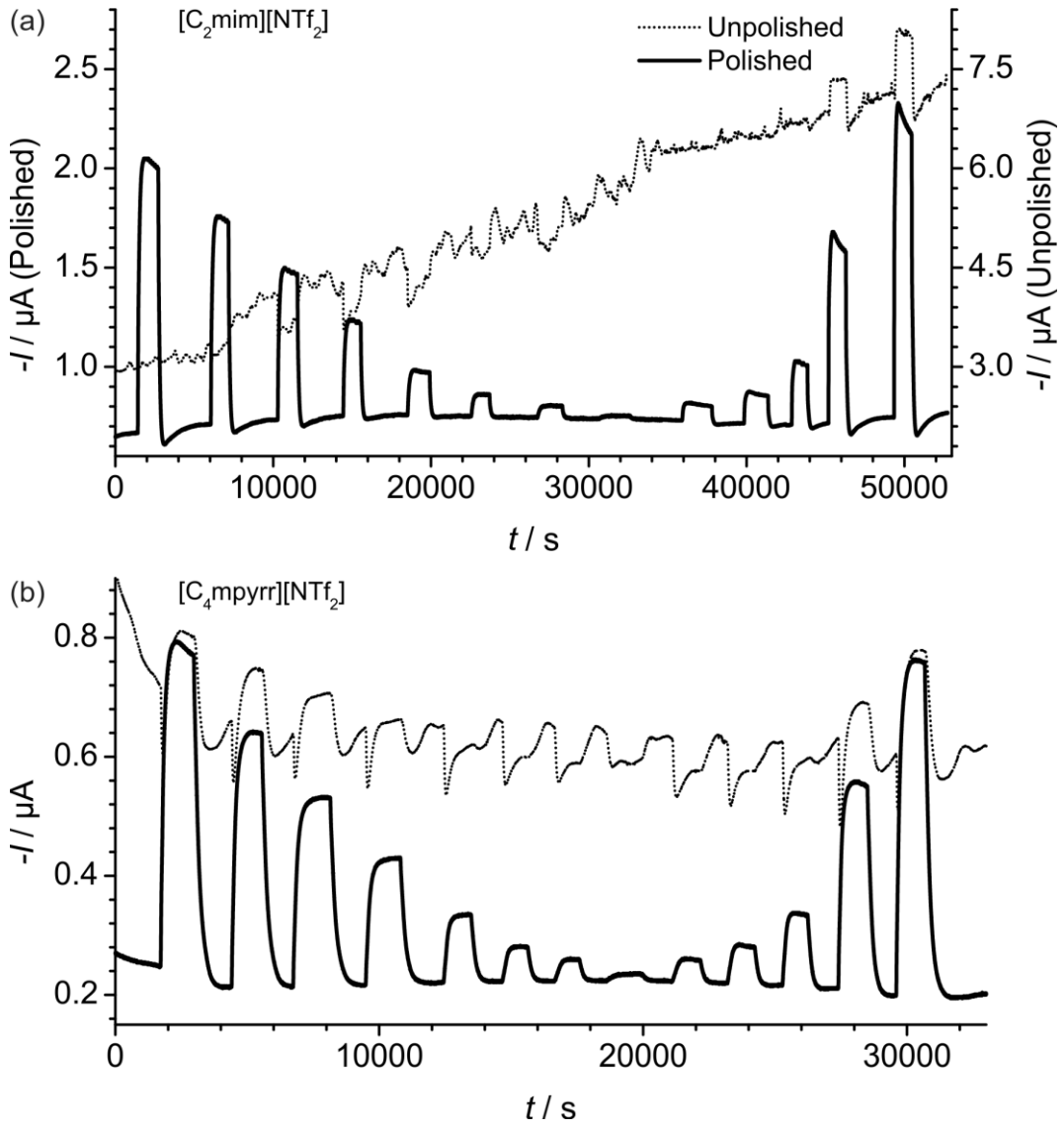

Figure 5.3. Amperometric monitoring of O_2 gas concentrations in **(a)** [C_2mim][NTf_2] and **(b)** [C_4mpyrr][NTf_2] on unpolished (dotted line) and polished (solid line) Pt-SPEs. The gas flow was alternated between N_2 and varying concentrations of O_2 in the following order: 5, 4, 3, 2, 1, 0.5, 0.3, 0.1, 0.3, 0.5, 1, 3, 5 % vol., and concurrently conducted (using the cell as shown in Figure 2.3) for unpolished and polished Pt-SPEs. The data presented were collected at 15 s time intervals with an overpotential of 200~300 mV, set from the O_2 reduction peak potential obtained from prior CV measurements. 30 mins of constant biasing under N_2 was allowed before commencing with introduction of O_2 gas to allow background charging currents to stabilize.

Substantial baseline currents were measured at 0 % vol. O_2 concentrations for all samples (Figure 5.3), and were significantly higher for measurements taken on unpolished Pt-SPEs compared to polished Pt-SPEs. This was especially true for $[C_2mim][NTf_2]$ on unpolished Pt-SPEs. The substantial baseline currents are likely due to contributions from accumulated redox active contaminants present, which can be observed as additional peaks appearing in the CVs, presented in the insets of Figure 5.2 and discussed under Section 5.3.1. The probable source of the redox active contaminants is likely to be from interactions between superoxide and the binding material occurring during the preliminary 'conditioning' CV scans, in the presence of a proton donor such as $[C_2mim]^+$ or absorbed moisture as discussed in Section 5.3.4.1. These undesired side-reactions could generate electrochemically active products which may accumulate within the μL aliquot of RTILs that were used. Hence this would also explain the markedly more significant and growing baseline currents observed in the mildly acidic $[C_2mim][NTf_2]$ on unpolished Pt-SPE (see Section 3.3.2.1) compared to the other systems investigated. This indicates the presence of much higher concentrations of accumulated redox active contaminants in the electrolyte which reduces at less negative potentials than was applied. The reduction of these progressively accumulating electrogenerated redox active contaminants would increasingly add to the baseline currents over time and introduce instability. Furthermore, $[C_2mim][NTf_2]$ on an unpolished Pt-SPE appears to be less responsive to O_2 concentrations compared to a polished Pt-SPE, while its background current was observed to be unstable. This may in turn suggests a continuous production and desorption of electrochemically passivating products at the WE/RTIL interface, as the existing contaminating species (from the preliminary 'conditioning') present in $[C_2mim][NTf_2]$ get reduced. It is also to be noted that the long-term constant biasing (during amperometric measurements) can be consider a much 'harsher' technique, compared to CV or (short-term) chronoamperometry, for amperometric O_2 sensing due to the constant generation and accumulation of superoxide at the WE.

Without first 'conditioning' the Pt-SPE/RTIL systems, the amperometric response on unpolished Pt-SPE samples was also found to rapidly achieve the response shown in Figure 5.3 in the presence of 5 % vol. O_2. Higher O_2 concentrations were observed to accelerate this degradation of amperometric response, and was more drastic in $[C_2mim][NTf_2]$. Unpolished Pt-SPE samples were subjected to similar conditions via amperometry, but placed strictly under a N_2-purged environment without the introduction of O_2, however, did not show degradation in their baseline signals. These observations suggest that the deteriorations in amperometric response (into what is observed in Figure 5.3) may indeed be the result of an accumulation of reaction products as suggested, and also indicates that polishing was capable of removing significant amounts of surface binding materials from fresh-out-of-the-box Pt-SPEs, which thus substantially reduced the generation of contaminating redox active by-products from the undesired side-reactions discussed.

An unusual response was observed in $[C_4mpyrr][NTf_2]$ on unpolished Pt-SPEs, where the current magnitude dips initially after O_2 is introduced before increasing, as shown by the dashed line in Figure 5.3 (b). This unusual response observed on the unpolished Pt-SPE could be related to the presence of an appreciable pre-peak that is sensitive to concentrations of O_2 in the CV (inset, Figure 5.2 (c), briefly discussed in Section 5.3.1), occurring before the onset of the O_2 reduction peak in the cathodic scan. This 'pre-peak' appears to be more significant during absence of O_2 while diminishing in the presence of oxygen, which indicates that the associated contaminant species may be depleted in the presence of O_2, plausibly due to reaction with the electrogenerated superoxide. To further investigate this, a follow-up experiment was conducted by monitoring the evolution of the peaks as O_2 (at 10 % vol.) was introduced into the N_2 purged $[C_4mpyrr][NTf_2]$ that was previously 'conditioned'. This was accomplished by running quick consecutive CV measurements (with 5 mins wait time between scans), as 10 % vol. O_2 was introduced into the flow cell, until the O_2 concentration

in the [C_4mpyrr][NTf_2] reached equilibrium, as shown in Figure 5.4. The O_2 reduction peak appears to have stabilized on the second scan, indicating that the oxygen concentration within the RTIL has reached equilibrium with respect to the 10 % vol. O_2. It can be clearly seen that the pre-peak current (associated with the contaminant species accumulated during preliminary 'aging') decreases, with a concomitant increase in the superoxide peak. This supports the idea proposed that the contaminant species is depleting due to reaction with superoxide after each consecutive CV cycle (i.e. not interacting with the increasing oxygen concentration entering the RTIL). The apparent diminishing oxygen reduction peak after subsequent scans could be accounted for by the suppression of the pre-peak current.

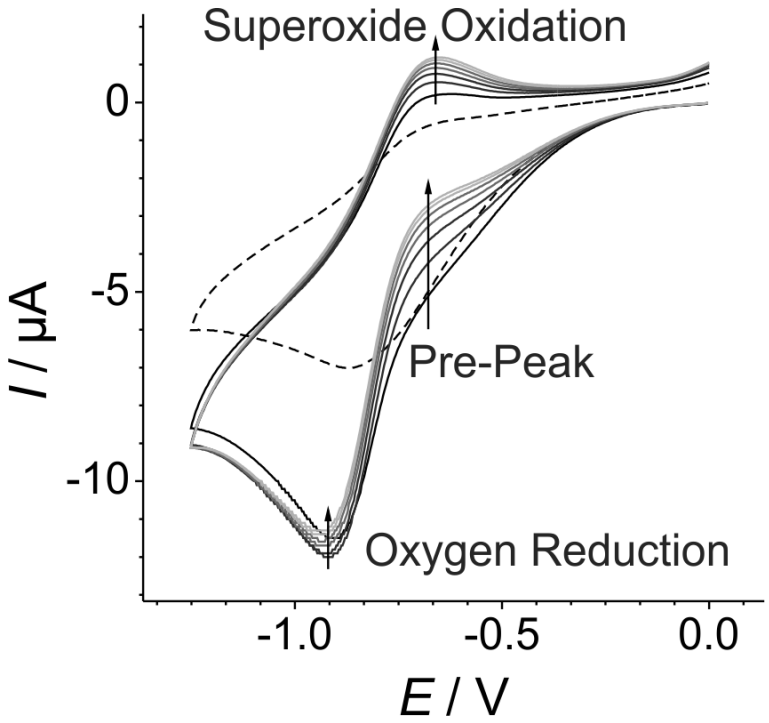

Figure 5.4. Evolution of the voltammetry in [C_4mpyrr][NTf_2] collected on unpolished Pt-SPE after it had been previously subjected to 120 CV cycles in the presence of 100 % vol. O_2. Quick consecutive CV measurements (with a 5 mins wait time between scans) were run, as the 10 % vol. O_2 was introduced into the flow cell, and continued (for a total of 7 cycles) until the O_2 concentration in the [C_4mpyrr][NTf_2] had reached equilibrium. The chronology of the CV cycles is indicated by solid lines with progressively lighter tones. The peaks are labelled, and arrows indicate the time-evolution of the respective peaks after oxygen has been introduced and was partitioning into the RTIL. The dashed line (- -) represents the blank collected from the N_2-purged [C_4mpyrr][NTf_2].

5.3.4.2.1. Analysis of O_2 concentration calibration plots from amperometric experiments

Finally, amperometric current signals presented in Figure 5.3 were analysed and background-corrected current vs. oxygen gas concentrations are plotted in Figure 5.5. Due to two distinct trends apparent in the calibration plots for each RTIL, the data was divided into two datasets (at 'descending' and 'ascending' sequence of varying oxygen gas concentrations) to be analysed. The solid lines represents the linear regression for the first 'descending' eight oxygen concentrations (5, 4, 3, 2, 1, 0.5, 0.3, 0.1 % vol.), and the short-dashed line for the last 'ascending' 6 oxygen concentrations (0.1, 0.3, 0.5, 1, 3, 5 % vol.). The linear regressions for both 'descending' and 'ascending' data sets were fitted sharing the same data point for 0.1 % vol. O_2. Each oxygen concentration response was typically taken at the current plateau Figure 5.3. However, for oxygen response that did not reach a plateau, but drops offs in amplitude upon reaching a peak, the current response was taken as the peak. Background currents corresponding to each O_2 concentration were taken to be the current measured just preceding the introduction of oxygen gas.

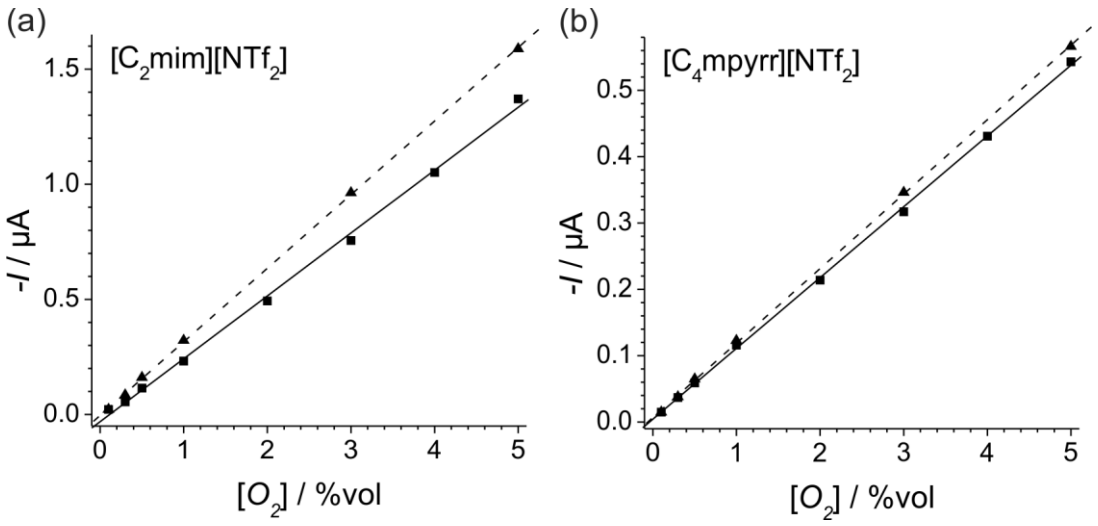

Figure 5.5. Plots of background corrected oxygen response currents vs. % vol. O_2 in the flow, and the lines of best-fit for **(a)** [C_2mim][NTf_2] and **(b)** [C_4mpyrr][NTf_2] on a polished Pt-SPE, extracted from amperometric measurements presented in Figure 5.3. The solid lines (–) represents the linear regression for the first eight oxygen concentrations response signals (5, 4, 3, 2, 1, 0.5, 0.3, 0.1 % vol.) measured with descending O_2 concentrations, and the short-dashed lines (--) for the last 6 oxygen concentrations response signals (0.1, 0.3, 0.5, 1, 3, 5 % vol.) measured with ascending O_2 concentrations (see Figure 5.3).

Reasonable LODs for O_2 gas can be obtained in both RTILs (as listed in Table 5.4). The positive shift in sensitivity of the O_2 responses for both RTILs, during 'ascending' concentrations of O_2, may be due to gradual desorption of the built-ups of passivating species from the Pt-SPE surfaces during the scans conducted at higher O_2 concentrations (during the 'descending'). This will be discussed in more detail in Section 5.3.4.2.2. This is supported by the higher LOD value for the initial 'descending' data sets compared to the 'ascending' data sets, which can be explained by an increasingly higher desorption rates vs. generation of passivating species (significantly generated during ca. 5 % vol. O_2) at the WE/RTIL interface following a sequential decrease in O_2 concentrations. The higher sensitivity in [C_2mim][NTf_2] compared to [C_4mpyrr][NTf_2] may be due to the lower viscosity of [C_2mim][NTf_2]. The impact of O_2 concentration on the stability of the amperometric response is further discussed in the following section (i.e. Section 5.3.4.2.2).

Table 5.4. Equations for the linear best-fit for the calibration graphs presented in Figure 5.5 (a) and (b) for $[C_2mim][NTf_2]$ and $[C_4mpyrr][NTf_2]$ respectively on polished Pt-SPEs, and corresponding limits of detection (LODs) based on 3 standard deviations from the regression fitting.

RTIL	Data Set	Equation of calibration graph (where I / A and $[O_2]$ / % vol.)	R^2	LOD / % vol.
$[C_2mim][NTf_2]$	Descending	$-I = 2.73\times10^{-7}\,[O_2] - 3.06\times10^{-8}$	0.9978	0.278
	Ascending	$-I = 3.20\times10^{-7}\,[O_2] - 3.78\times10^{-9}$	0.9999	0.075
$[C_4mpyrr][NTf_2]$	Descending	$-I = 1.07\times10^{-7}\,[O_2] + 4.45\times10^{-9}$	0.9954	0.127
	Ascending	$-I = 1.12\times10^{-7}\,[O_2] + 7.00\times10^{-9}$	0.9998	0.090

The LOD values reported under Table 5.4 from amperometry studies were significantly lower than that obtained from the CV measurements reported under Table 5.3. However poorer sensitivity were observed from the amperometry calibration compared to that obtained with CV. However, it is to be noted that the concentration range chosen for the two studies were substantially different (with O_2 concentrations assessed between 0.1-5 % vol. via amperometry, and between 10-100 % vol. via CV). The choices of concentration ranges for these two techniques had to do the lowest O_2 concentration that can be discriminated from the background currents via CV, and the instability of the response at higher concentrations during amperometry monitoring (which will be discussed more in Section 5.3.4.2.2). Notably, the LOD values obtained with the two RTILs were a lot more similar from amperometry (Table 5.4) compared to that obtained from CV (Table 5.3), especially from the ascending dataset in Table 5.4 (where the system has been allowed a longer time to stabilise). Due to pre-stabilization of the current contributions from accumulation of the contaminant species discussed, which may appear as peaks overlapping the oxygen reduction peak in the CVs (see Figure 5.2 and 5.4), distinguishing of O_2 concentrations down to 0.1 % vol. from the background is possible in amperometry studies. In contrast, the lowest O_2 concentrations

that could be distinguished from the background after 'conditioning' (via 120 CV cycles) were ca. 5 % vol. This continued stabilization of background contributions due to reduction of accumulate contaminant species in the amperometric measurements could explain the more similar LOD values obtainable via this technique (compared to CVs).

5.3.4.2.2. Stability of amperometric response for the reduction of O_2 in RTILs at low and high concentrations on a polished Pt-SPE.

For amperometric measurements conducted on polished Pt-SPEs, the O_2 current responses are expected to increase with increasing oxygen concentration (at the WE/RTIL interface) as O_2 is partitioning into the RTIL from the gaseous phase. The current response is expected to eventually reach a steady state as equilibrium is attained at the RTIL/gas interface. [170] However at higher O_2 concentration (e.g. > 1 % vol. for $[C_2mim][NTf_2]$, and > 4 % vol. for $[C_2mim][NTf_2]$ on polished Pt-SPE), the signal instead typically reached a peak before diminishing gradually (Figure 5.3). This was comparatively more significant with $[C_2mim][NTf_2]$ than the more stable $[C_4mpyrr][NTf_2]$ [163]. This can be observed in the amperometric responses collected on polished Pt-SPEs in Figure 5.3, by comparing the response behaviour between the two RTILs at ca. 5 % vol. O_2. This behaviour was also observed strongly with ammonia gas in $[C_2mim][NTf_2]$ on unpolished Pt-SPE surfaces studied by our group [142]. For this O_2 amperometry study, it was also noted that the higher the O_2 concentrations, the faster the rate at which the signal diminishes (typically).

With further continued constant biasing at high (i.e. 100 % vol.) O_2 concentration, the currents eventually became very unstable, particularly in $[C_2mim][NTf_2]$. An example of this is shown in Figure 5.6 for $[C_4mpyrr][NTf_2]$ being subjected to a gas flow of 100 % vol. O_2. An unstable response sets in after remaining relatively stable (only slightly diminishing over

time) for up to ca. 1 hr. This was suspected to be due to gradual build up of passivating reaction products such as neutral imidazolone (as discussed in Section 1.3.2.4) for the case of $[C_2mim][NTf_2]$. For the case of $[C_4mpyrr][NTf_2]$, persistent trace concentrations of water present could act as the main source of protic impurity which could induce an interaction of the electrogenerated superoxide with the remaining binding material (that is left over after polishing), and the breakdown of the $[C_4mpyrr]^+$ cation (see also Sections 1.3.2.4 and 5.3.3) at the negatively polarised WE.

Eventually, significant desorption of the passivating species from the WE surface (while it is constantly generated) can occur after sufficient build up of adsorbed passivating species, thus leading to the unstable current response observed at longer times. This could also explain the unstable amperometric response observed for $[C_2mim][NTf_2]$ on unpolished Pt-SPE, where the presence of significant exposed binding material on the surface could lead to substantial generation of passivating contaminant products (as discussed in Section 5.3.2).

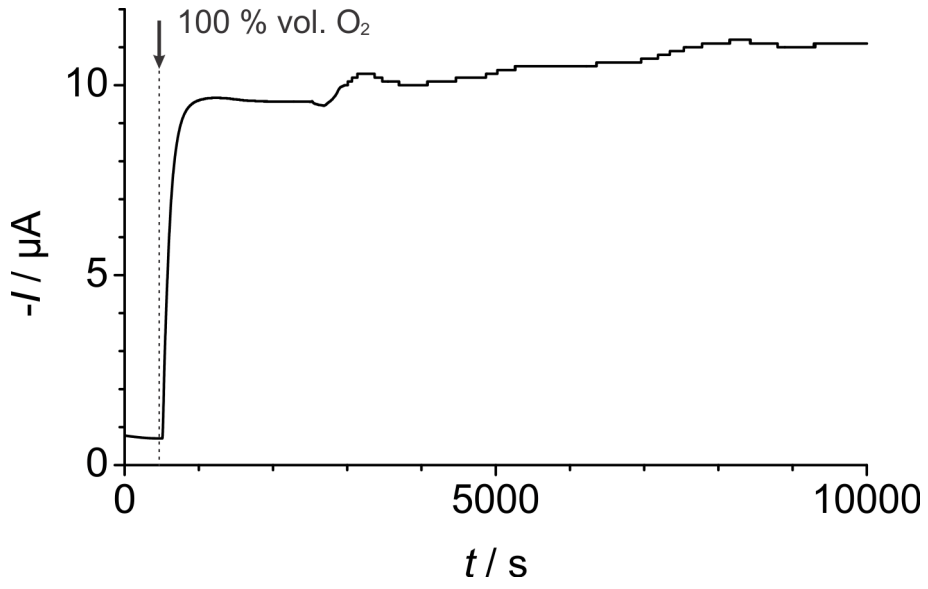

Figure 5.6. Amperometric response of O_2 reduction in [C_4mpyrr][NTf_2] on polished Pt-SPE with continued exposure for more than 2.5 hrs. The RTIL was first N_2-purged before 100 % vol. O_2 was introduced at a flow rate of 1000 sccm at the instant as indicated by the arrow.

At lower oxygen concentrations (i.e. < 1 % vol. for [C_2mim][NTf_2], and < 4 % vol. for [C_2mim][NTf_2] on a polished Pt-SPE) however, the amperometric oxygen response shows negligible diminishing current rates (Figure 5.3). This shows that perhaps these RTIL/Pt-SPE systems are better suited for the amperometric sensing of O_2 gas at those stated lower concentrations for the two respective RTILs on polished Pt-SPEs. To significantly extend the lifespan of these SPE/RTIL systems and to improve response stability for the sensing of O_2 at high concentrations, instead of a single-potential amperometry approach, a square wave potential of intermittent biasing approach (also referred to as pulsed amperometry) was used by Wang, et al. [79]. In their work, electrogenerated superoxide was periodically oxidized back into O_2, between consecutive short-term O_2 reduction chronoamperometric measurements. The concentration of O_2 could thus be obtained from diffusion limited currents by application of the Cottrell equation (Equation (1.7)). However, for the present thesis study, to enable

better assessment of the robustness and performances of Pt-SPE/RTIL systems, the harsher constant biasing amperometry approach was selected.

5.4. Long-term effect of amperometric O_2 sensing on Pt-SPE/RTIL systems.

Figure 5.7 shows deterioration of the 30 μL $[C_2mim][NTf_2]$ RTIL aliquot, after prolonged O_2 monitoring (> 250 CV cycles), to a dark brown colour with a strong smell of amine. This darkening of the RTIL was also observed with a standard macrodisk platinum working electrode in a 50 μL aliquot of $[C_2mim][NTf_2]$ after bulk electrolysis at negative potentials for > 1 hr in the presence of 100% O_2 flow. On Pt-SPEs, the degree of darkening was observed to be considerably greater on unpolished Pt-SPEs than polished Pt-SPEs. However, it can frequently be observed that the browning is concentrated around the screen printed Pt counter electrode surfaces, which can be more apparently discerned for the polished Pt-SPE sample in Figure 5.7.

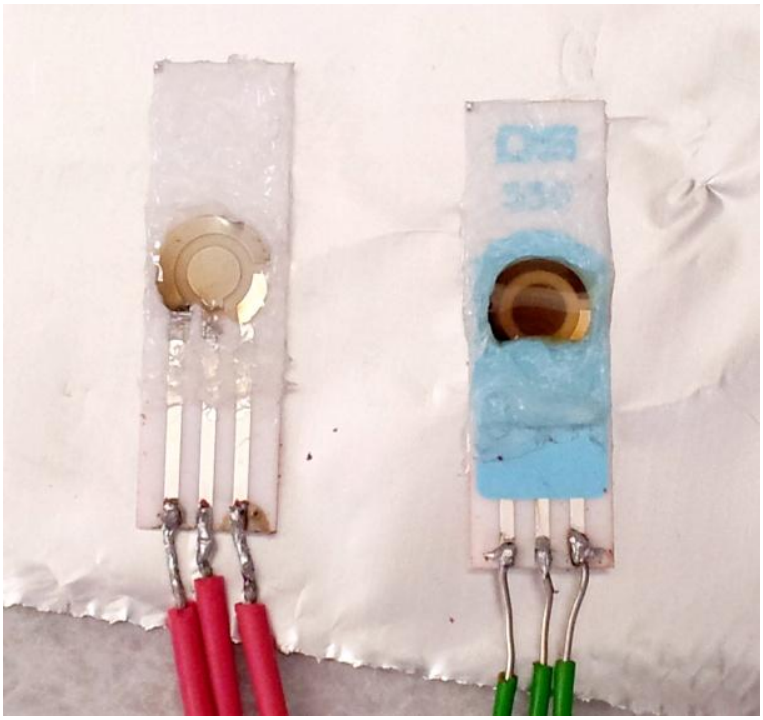

Figure 5.7. Darkening of deposited [C_2mim][NTf_2] RTIL aliquots after 120 CV cycles on **(left)** polished, and **(right)** unpolished Pt-SPE surfaces.

During the reduction of O_2 to superoxide on the negatively biased working electrode, the $[NTf_2]^-$ anion can undergo oxidation at the counter electrode, resulting in the breaking of the N-S bond, followed by a cascade of reactions that might end up with the brown liquid which smells strongly of amine observed during experiments. On the unpolished Pt-SPE, the surface is substantially covered by residual binding materials. If the presence of binding materials results in an overall > 1 electron process, then more $[NTf_2]^-$ anions would be expected to be concomitantly decomposed at the counter electrode, and thus lead to a greater extent of discolouration, as observed on the unpolished Pt-SPE. Browning of the [C_4mpyrr][NTf_2] was also observed to occur in the presence of O_2 under repeated cycling, but to a much lesser extent compared to [C_2mim][NTf_2], owing to the relative stability of the binding materials degrading during interaction with superoxide in the less protic environment of [C_4mpyrr][NTf_2] [230]. Imidazole carbenes [163] (i.e. deprotonated imidazolium cations) or

imidazolone [103] are also brown/yellow, and could also have contributed to the discolouration of the RTILs (generated at the WE). This can further be supported by observation of an intensification of a browning colouration of the RTILs after they have been subjected to multiple (> 50) cycles in the presence of oxygen and left overnight, even on polished Pt-SPEs. This is possibly due to residues of superoxide gradually deprotonating the $[C_2mim]^+$ cation into imidazole carbenes [163] over an extended period. Rinsing off the fouled RTIL revealed a stained screen printed platinum working electrode surface as shown in Figure 5.8. This staining is thus likely due to an adsorbed layer of the neutrally charged imidazolone (as discussed in Section 1.3.2.4) generated during the course of consecutive measurements which has previously been reported in the literature [103].

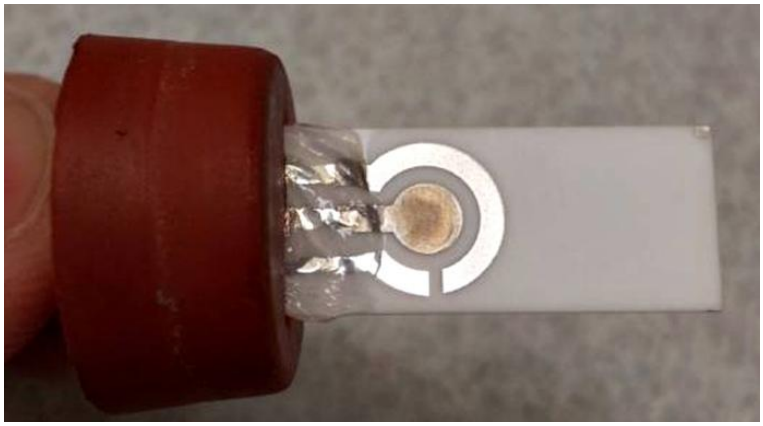

Figure 5.8. Fouling of a polished Pt-SPE WE surface after being subjected to O_2 sensing amperometric experiment in $[C_2mim][NTf_2]$. The browned RTIL was rinsed off with acetonitrile after the experiment.

5.4.1. Effect of standard electrochemical pre-treatment, and acid soaking on $O_2/O_2^{\bullet-}$ redox CVs on unpolished Pt-SPEs.

Unpolished Pt-SPEs were subjected to two standard electrochemical pre-treatment methods, namely, repeated CV cycling in H_2SO_4(aq) and KCl(aq) solutions. These pre-treatments are commonly conducted on SPEs in aqueous-solutions [123, 239-244, 250, 256] and are also recommended by the manufacturer. The treated Pt-SPEs were then implemented for O_2 sensing. The $O_2/O_2^{\bullet-}$ redox voltammograms at unpolished Pt-SPEs electrochemically pre-treated in 0.5 M H_2SO_4(aq) are presented in Figure 5.9 in the two RTILs. These pre-treatments was found to lead to non-standard $O_2/O_2^{\bullet-}$ redox voltammetries on Pt-SPEs.

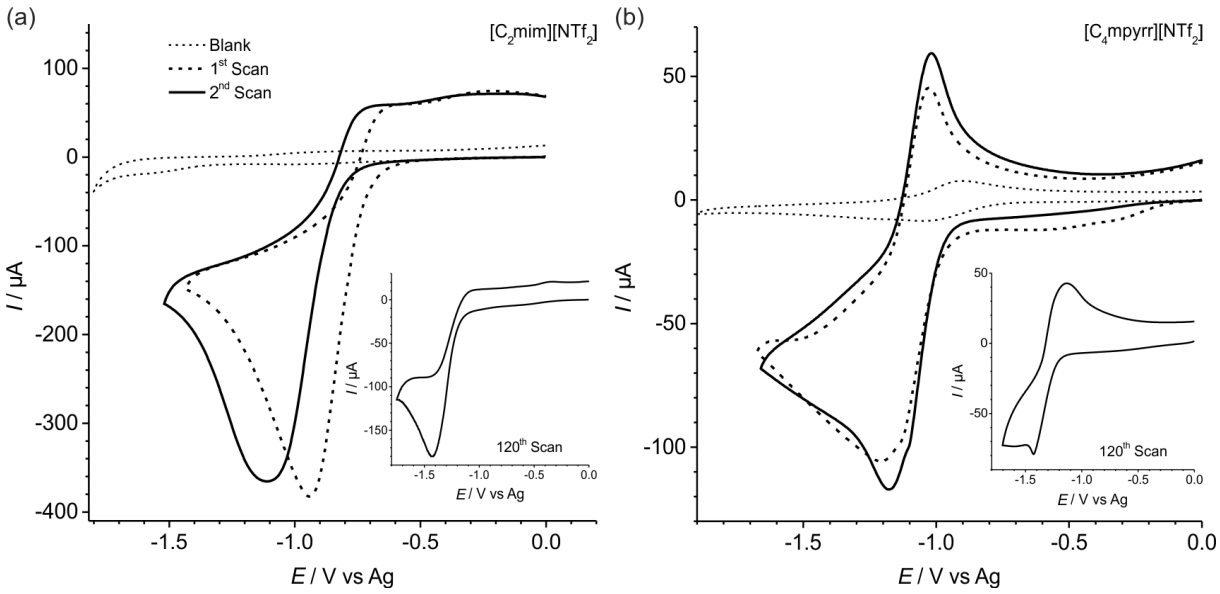

Figure 5.9. $O_2/O_2^{\bullet-}$ redox CVs in **(a)** [C_2mim][NTf_2] and **(b)** [C_4mpyrr][NTf_2] collected at scan rate of 100 $mV \cdot s^{-1}$, on Pt-SPEs electrochemically pre-treated in 0.5 M H_2SO_4(aq) vs. Ag-RE, according to procedures described under Section 5.2.

Repeating the same experiment in 0.5 M KCl(aq), and simply soaking in 0.5 M H_2SO_4(aq) for an hour similarly resulted in the unusual $O_2/O_2^{\bullet-}$ redox voltammetric behaviour in

[C_4mpyrr][NTf_2], as shown respectively in Figure 5.10 (a) and (b). In relevance to this, it was previously noted (in Section 4.3.6 and shown in Figure 4.11) that the working electrode surface of Pt-SPEs darkens after extensive cycling (> 1000 times) in both 0.5 M H_2SO_4(aq) and 0.5 M KCl(aq). Typical CV was however obtained when Pt-SPEs were merely soaked in 0.5 M KCl(aq). The cause of this unusual CV behaviour for the $O_2/O_2^{\bullet-}$ couple is unclear.

In Chapter 4, NaOH treated samples also exhibited unusual CVs for hexaammineruthenium(III/II) and hexacyanoferrate(III/II) redox couples (as shown in Figure 4.3 and Figure 4.4). As has been previously discussed in that chapter, subjecting Pt-SPEs to prolonged exposure in acidic or caustic solutions may lead to over-etching of the surface (illustrated in Figure 4.7). Firstly, this would explain the significantly higher than expected O_2 reduction peak currents measured for the acid-soaked samples. Furthermore, over-etching of the Pt-SPE surface would not only lead to more electrochemically active material becoming exposed to the electrolyte, but also result in exposure of more binding materials. Interactions of substantially more surface binding materials with the electrogenerated superoxide may partly explain the unusual voltammetry. However, this could not account for the case of the Pt-SPE electrochemically treated in 0.5 M KCl(aq). Characterization of Pt-SPE surfaces by energy dispersive electron spectroscopy (EDS) on SEM found characteristic peaks for lead, and the CV cycling in aqueous media may perhaps lead to its oxidation into lead dioxide. The presence of lead could also perhaps be due to trace impurities present in the Pt particles used for the manufacturing of Pt-SPEs. But regardless of the cause, it is obvious that these standard pre-treatment protocols recommended by the manufacturer are in fact unsuitable to prepare Pt-SPEs for use with RTILs in O_2 gas-sensing experiments.

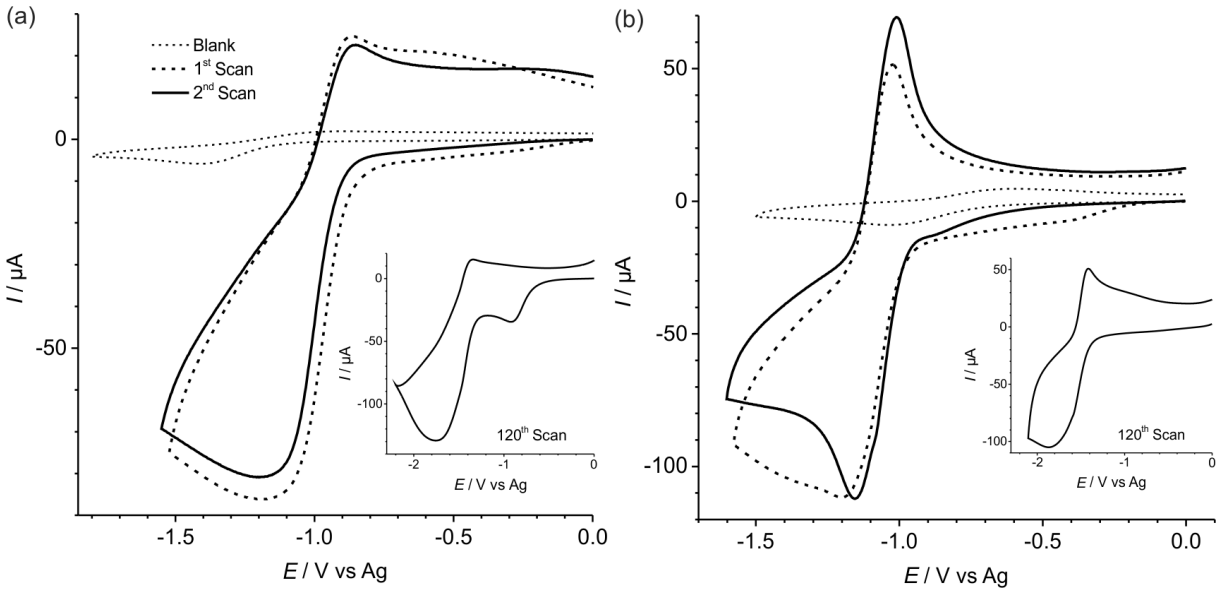

Figure 5.10. $O_2/O_2^{\bullet-}$ redox CVs in $[C_4mpyrr][NTf_2]$ collected at scan rate of 100 $mV \cdot s^{-1}$, on **(a)** Pt-SPEs electrochemically pre-treated in 0.5 M KCl(aq) vs. Ag-RE, and **(b)** on Pt-SPEs pre-soaked in 0.5 M H_2SO_4(aq) for an hour vs. Ag-RE. The pre-treatment protocols were as described under Section under Section 5.2.

5.4.2. Recovery of fouled Pt-SPE surfaces by polishing.

Similar improvements to the voltammetry discussed under Section 5.3.1 were also achieved by gentle hand-polishing of the Pt-SPEs about the working electrode surface (leaving the surrounding blue dielectric polymer mask intact) with 1 μm alumina powder on a small piece of wet soft lapping pad, before spraying with Milli-Q water and EtOH at least twice before drying under a stream of N_2 gas. This indicates that improvement to the $O_2/O_2^{\bullet-}$ redox voltammetries is not due to the sonication of Pt-SPE in THF for the removal of the blue polymer mask in the procedure (described under Section 4.2.2.1). Figure 5.11 shows the recovery of an unpolished Pt-SPE surface by polishing. After subjecting to over 120 CV cycles under 100% O_2, the initially colourless $[C_4mpyrr][NTf_2]$ RTIL became a dark brown colour as previously discussed. Replacing the RTIL with a fresh aliquot did not recover the CV, while subjecting the Pt-SPE to polishing did. Only light polishing by gently rubbing with

1 μm alumina powder with a small cut-out of soft wet lapping pad for 1~2 mins was generally enough to remove adsorbed contaminants (for instance, the screen printed platinum surface fouled with imidazole carbenes from deprotonated $[C_2mim]^+$ cation as shown in Figure 5.8).

The Pt-SPE had been successfully re-polished more than 12 times before a reasonable voltammetry in $[C_4mpyrr][NTf_2]$ is not obtainable and the screen printed platinum surface becomes visually worn out and depleted. However, the number of times that an SPE could withstand repeated re-polishing is heavily dependent on various factors such as the degree of its initial polishing, and also the pressure and duration of each surface-refreshment polishing thereafter (which is dependent on the extent of the surface fouling from the prior experiment). Additional unidentified peaks may appear after repolishing, but the voltammetry was found to quickly recover after only a few scans (i.e. < 3) in the presence of 100% O_2. Nonetheless the results show that SPEs, which are typically marketed as single used, can be reused multiple times by simply polishing the surface before it eventually wears out. The number of times before the Pt-SPE wears out would obviously depend on the extend of each repolishing that is necessary to recover a clean surface.

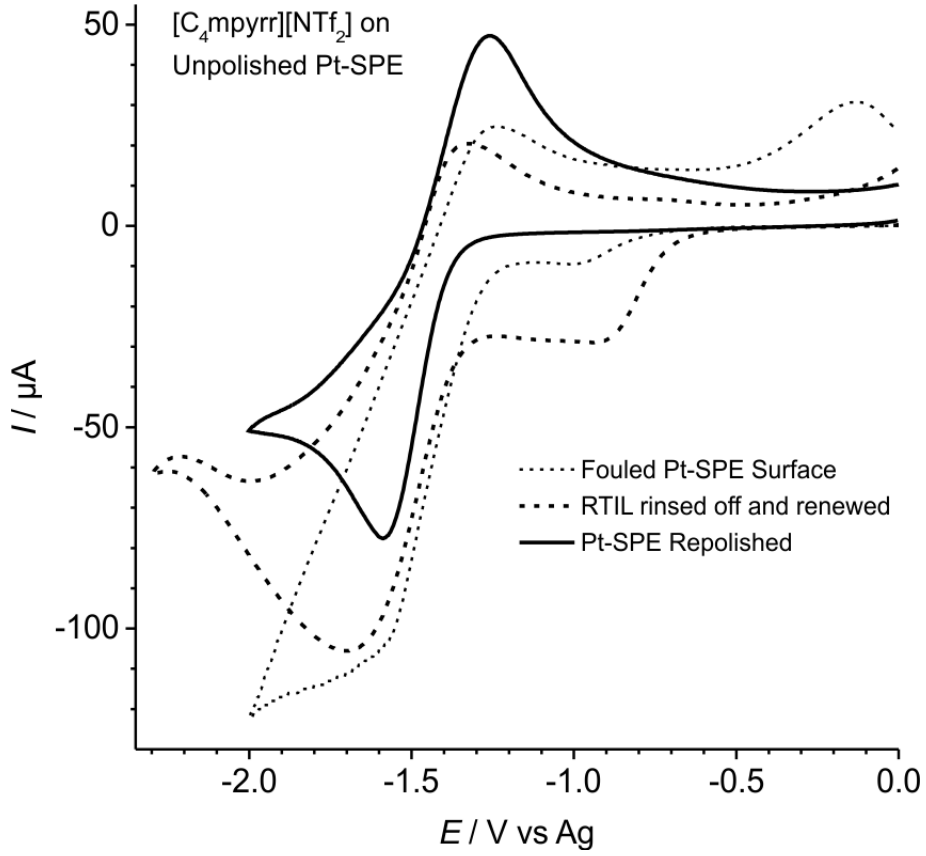

Figure 5.11. Recovery of fouled Pt-SPE surfaces after polishing. The short-dotted line (···) shows the cyclic voltammogram of $O_2/O_2^{\bullet-}$ redox couple on a Pt-SPE surface, degraded after amperometric experiments (> 8 hrs) in [C_4mpyrr][NTf_2]. The short dashed-line (--) shows the cyclic voltammogram after the fouled (browned) RTIL was rinsed off and a fresh 30 µL aliquot applied. The solid line (–) shows the cyclic voltammogram after the RTIL was rinsed off, and the surface polished before applying a fresh 30 µL aliquot of the RTIL. The CV scans were conducted with a scan rate of 100 $mV \cdot s^{-1}$.

5.5. Conclusions

The long-term performances of platinum SPEs before and after mechanical polishing, for the sensing of O_2 gas in $[C_2mim][NTf_2]$ and $[C_4mpyrr][NTf_2]$, has been compared. Polishing has been demonstrated as a highly effective pre-treatment protocol for Pt-SPEs prior to their utilisation as amperometric O_2 sensors in the two RTILs. Polishing could be repeated to recover fouled Pt-SPEs (generally regarded as one use electrodes) for multiple times. The number of times a Pt-SPE could be polished would depend on the aggressiveness of the independent polishing that was necessary to recover the electrode surface, before its surface eventually wears out. In contrast, subjecting Pt-SPEs to the standard aqueous solutions based electrochemical pre-treatment protocols resulted in unusual voltammetric behaviour for O_2 sensing in the two RTILs. Polishing of the Pt-SPE shows substantial improvement, in the voltammetry shapes and stability of the CVs, over prolonged repeated scanning. In particular for $[C_2mim][NTf_2]$, the cross-over characteristic (discussed in Section 3.3.2.1) disappeared rapidly and eventually evolved to a voltammetry that resembles one collected on a typical platinum macrodisk electrode. This is in contrast with severe degradation that was observed on unpolished Pt-SPEs. There was some improvement in the CV response for the $O_2/O_2^{\bullet-}$ redox couple in $[C_4mpyrr][NTf_2]$ on the Pt-SPE after polishing, but it was not as pronounced compared to $[C_2mim][NTf_2]$. Analytical utilities for unpolished and polished Pt-SPEs were compared from the voltammetries of different O_2 concentration collected. Calibration plots from O_2 reduction CVs peak currents on Pt-SPEs showed improved sensitivities and limits of detection after polishing in both RTILs, where the LOD was almost halved in $[C_2mim][NTf_2]$, while a more modest 5 % improvement was observed in $[C_4mpyrr][NTf_2]$. Further O_2 responses on unpolished Pt-SPEs in both RTILs were found to rapidly degenerate during amperometric monitoring of O_2, while remarkable improvements in current response

were achieved on polished Pt-SPEs, yielding reasonable LODs (down to ca. 0.1 % vol.), and O_2 sensitivities > 10^{-7} A·%$[O_2]^{-1}$.

6. Immobilization of room temperature ionic liquids on integrated electrodes by polymer gelification.

6.1. Introduction

In spite of their many advantages in gas-sensing, the fluid nature of RTILs makes them unsuitable for portable applications. Consolidating and following on from work presented in earlier chapters, this chapter aims to investigate an inexpensive [211] and facile method of immobilizing the RTIL electrolyte layer onto polished Pt-SPEs by gelification using polymer additives. It takes a preliminary look into the electrochemical mechanism of the $O_2/O_2^{\bullet-}$ redox couple within selected PMMA/RTIL electrolytes, and assesses the analytical utilities of these gel-polymer electrolyte (GPE) systems on polished Pt-SPE sensing platforms. The two RTILs $[C_2mim][NTf_2]$ and $[C_4mpyrr][NTf_2]$ will be focused on in the present study. Gelification of RTILs would not only allow a wider range of RTILs (with lower hydrophobicity and poorer surface wetting property) to be implemented for portable gas-sensing on integrated electrodes sensor platforms, but would improve their robustness for portable applications. Polymer gelification of the RTILs could further allow for significantly thinner electrolyte films (of sub-micron to nano thicknesses) to be applied onto integrated electrode platforms (i.e. by spin-casting, or Langmuir trough deposition techniques), with improved mechanical stability, to give significantly faster gas-sensing response times. It would also open up the possibility for cheap, versatile, and scalable construction of gelified RTIL-based gas-sensing devices within existing manufacturing process of SPEs, and other potential cost-efficient production methods such as inkjet [137] or aerosol [138] printing. Further, studies of these selected GPE systems focused in this chapter would also extend the palette of materials available in these relatively new [211] RTIL-based conductive polymer membrane materials. This would have

relevance for a wide range of other applications, from batteries, supercapacitors, photovoltaics and fuel cells to light-emitting diodes (LEDs), organic thin-film transistors (o-TFTs) and electrochromic devices. [131-133, 136-138, 188-190, 192]

6.2. Experimental

6.2.1. Synthesis of poly(methyl methacrylate)

Poly(methyl methacrylate) (PMMA) was synthesized from methyl methacrylate (MMA 99 %, Sigma-Aldrich Pty Ltd., NSW, Australia) following the procedures set out in [257] via the well known thermally initiated (85 °C for ca. 12 hrs) free radical solution polymerization route. The free radical initiator used was 2,2′-Azobis(2-methylpropionitrile) (AIBN 98 %, Sigma-Aldrich Pty Ltd., NSW, Australia) purified by recrystallization from warm methanol (MeOH anhydrous 99.9 %, Mallinckrodt Pty Ltd., NSW, Australia) prior to use. The synthesized polymer was purified five times by redissolving in distilled 1,4-dioxane (anhydrous 99.8 %, Sigma-Aldrich Pty Ltd., NSW, Australia) and added dropwise to 800 mL of milli-Q grade water under vigorous stirring. Finally, the white precipitate of the purified PMMA was collected and left to air dry overnight before dissolving in tetrahydrofuran (THF, anhydrous, ≥ 99.9 %, inhibitor-free Sigma-Aldrich Pty Ltd., NSW, Australia). The PMMA dissolved in THF were then drop-casted onto a polished Teflon® surface, and the thin-films of PMMA were then collected. The PMMA films were then frozen with liquid nitrogen (BOC gases, North Ryde, NSW, Australia) before crushing in a mortar with a pestle. The process was repeated until the PMMA was crushed into sufficiently fine powder to improve dissolution. Finally, the fine PMMA powder was annealed in an oven at about 60 °C for 3 hrs to remove any residual THF. The PMMA synthesized was expected to be atactic and amorphous in nature, since it was synthesized in the absence of a catalyst. For PMMA synthesized by free radical polymerization (held at < 100 °C), a tacticity ratio of ca. 0.45 : 0.14 : 0.41 (syndiotactic (*s*) : isotactic (*i*) : heterotactic (*h*)) is expected. [258] The number average molecular weight, M_n, of the synthesized PMMA was estimated to be $(9.5\pm1.0)\times10^3$,

based on the glass transition temperature, T_g, of 91.96 °C characterized via differential scanning calorimetry (DSC) (see Appendix C).

6.2.2. Polymer gelification of $[C_2mim][NTf_2]$ and $[C_4mpyrr][NTf_2]$ RTILs.

Polymer to RTIL concentration-ratios, [*PMMA*:*RTIL*], are presented as percentage weight-per-volume, abbreviated as % w/v in standard units (i.e. mass of polymer, in kg, per liquid-volume, L, of RTIL). For example, 0.1 g of PMMA added to 0.1 mL of RTIL will give 100 % w/v of [*PMMA*:*RTIL*]. GPEs were prepared by first weighing out ~150 mg of the polymer into a 2 mL glass vial before addition of 300 μL of acetone (CHROMASOLV®, for HPLC, ≥ 99.9%, Sigma-Aldrich Pty Ltd., NSW, Australia). The vial was then sonicated with regular shaking to prevent the PMMA powder from clumping together, until all the powder was dissolved. Finally, appropriate volumes of the RTILs was then added into the PMMA-acetone solution to make up the varying % w/v *PMMA*:*RTIL* concentrations. The acetone acts as the casting solvent by reducing fluid-viscosities of the GPEs (especially for higher PMMA concentration) to allow their transfer via micropipettes, and thinner films to be casted. Poly(vinyl chloride) (PVC) (Sigma-Aldrich Pty Ltd., NSW, Australia) was also tested with the RTILs as potential GPE materials, using tetrahydrofuran (THF, anhydrous, ≥ 99.9 %, inhibitor-free Sigma-Aldrich Pty Ltd., NSW, Australia) as the casting solvent. The doping concentrations of PMMA in RTIL, given in mass fraction (wt. %) and mass concentration (% w/v) values, investigated in this chapter are summarized in Table 6.1.

Table 6.1. Mixing ratios of *PMMA*:*RTIL* prepared, expressed in units of mass fractions (wt. %) for each of the two RTILs, and mass concentration (% w/v) values consistent for both RTILs.

Ratio		***Mass fraction,*** $\%(m_{PMMA}/m_{Total})$ / wt. %		***Mass concentration,*** $\%(m_{PMMA}/V_{RTIL})$ / % w/v
PMMA (*m*)	**RTIL (*V*)**	$[C_2mim][NTf_2]^{\dagger}$	$[C_4mpyrr][NTf_2]^{\ddagger}$	
0	1	0	0	0
1	10	6.13	6.67	10
3	10	16.4	17.6	30
1	2	24.6	26.3	50
1	1	39.5	41.7	100
15	10	49.5	51.7	150

† *Density of $[C_2mim][NTf_2]$ is 1.53 kg/L.*
‡ *Density of $[C_4mpyrr][NTf_2]$ is 1.40 kg/L.*

6.2.3. Electrochemistry experiments

For experiments with the polished Pt-SPEs, their experimental setup and preparations were already detailed under Sections 2.3 and 4.2.2.1 respectively. 30 µL aliquots of the PMMA-RTIL-acetone solutions were carefully drop-casted onto polished Pt-SPEs. The dissolved acetone was allowed to completely volatilize under a flow of nitrogen gas (at 1000 sccm) within the cell as shown in Figure 2.2. CV and amperometric experiments were carried out as detailed in Section 5.2. For experiments conducted with polished macrodisk Pt-WE, a setup as detailed under Section 2.3.2 could not be used for experiments with gellified-RTILs. Fluid viscosity of GPEs at high concentrations of PMMA doping prevents direct bubbling of gas into it, and sluggish diffusion rates in the media necessitate a much smaller distance (i.e. < 1 mm) between the electrolyte-gas interface and the working electrode. Consequently, these meant that the setup using a glass pot as described under Section 2.3.2 was unsuitable for experiments with GPEs. A modified electrode setup (as illustrated in Figure 6.1) was consequently improvised to accommodate the macrodisk WE in the T-cell,

which allows only a maximum of ~50 μL aliquots of electrolyte to be used. This effectively reduced the thickness of the electrolyte layer and thus resulting in more efficient diffusional transport of partitioned oxygen-nitrogen gas mixtures into the bulk media for more reasonable experimental response time. As shown in Figure 6.1, a polished platinum macrodisk working electrode (1.6 mm diameter, BASi, West Lafayette, Indiana, USA) was inserted into a rubber bung where a round cavity with diameter, just slightly smaller than that of the macrodisk electrode's poly(chlorotrifluoroethylene) (pCTFE) casing, was carved at its centre, to allow an air-tight seal around the electrode. The working electrode was repolished and sonicated (see Section 2.3.2) between measurements conducted for each PMMA/RTIL sample. A polypropylene barrier, made from a sliced segment of a 1 mL micropipette tip (Eppendorf, Australia) was fitted at the top of the working electrode to hold the electrolyte. Platinum wire coil sits at the inner rim around and close to the working electrode (resting right on top of the pCTFE surface) which serves as the counter electrode. A straight polished and flame-treated silver wire was carefully positioned at ~1 mm above the surface of the working electrode, which acts as a pseudo-reference electrode. Care was taken to avoid contact of the reference with the counter electrode, using cured silicone as a separator.

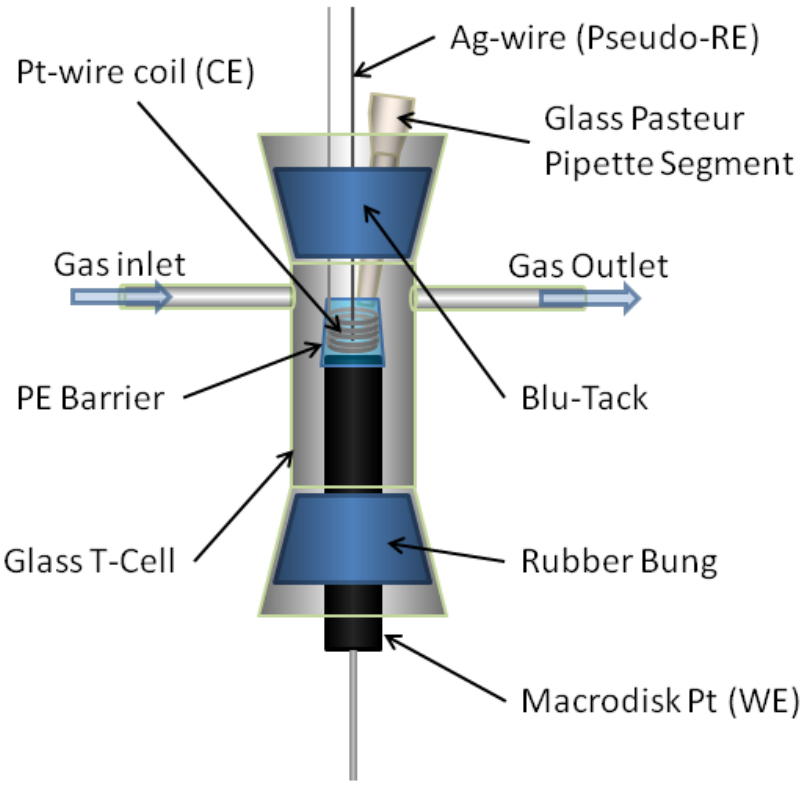

Figure 6.1. Schematic of the modified T-cell setup to accommodate commercially available macrodisk working electrodes to enable µL-volumes of electrolytes to be used.

Before introducing the PMMA-RTIL-acetone blend onto the working electrode, the mixture was placed under a gentle flowing stream of nitrogen gas to reduce its acetone content until a more viscous material was obtained. For higher levels of doping, which forms solidified GPE material (found to be somewhere between 50-100 % w/v PMMA doping), a sufficient remaining acetone would allow transfer of the GPE with a micropipette (as a viscous fluid), while reducing the duration necessary to completely volatilize the acetone and ensuring sufficient electrolyte thicknesses (for proper contact between the three electrodes) within the polypropylene barrier. 50 µL of the viscous PMMA-RTIL-acetone mixture were transferred into the polypropylene barrier, and the cell was set up as described above. A glass Pasteur pipette was carefully inserted from the top through the Blu-Tack seal (see Figure 6.1), and lowered into the polypropylene barrier just over the electrolyte surface. Blocking the gas

outlet of the T-cell with Blu-Tack would direct the flow of the gas mixture towards the GPE's surface within the cell, as it tries to exit through the opening provided by the glass pasteur pipette. This allows a gentle flow (~30 sccm) of nitrogen gas to efficiently evaporate the residual acetone within the electrolyte left overnight, and also to allow re-introduction of acetone, via the Pasteur pipette, to sufficiently soften the effectively solidified GPE (to enable the disassembling of the setup after completion of experiments). GPE film thicknesses of ca. 1.5 mm were typically set up within the barrier once all the acetone has volatilized.

CVs were recorded at 10 mins intervals upon the introduction of 100 % vol. O_2 into the cell (left under a N_2-purged environment overnight prior to experiment) to assess the time necessary to fully saturate the GPE material with oxygen. CVs were also taken at varying time-intervals to determine the minimum waiting period necessary to allow for depleted oxygen during the previous CV scan to be replenished at saturation. For amperometric studies, O_2 gas concentrations in the cell were monitored with a constant bias of -1.6 V vs. Ag-RE. The gas flow was alternated between 0 % vol. O_2 (i.e. at 100 % vol. N_2 flow) and the sequential order of concentrations that were specified in the captions of the respective figures in the results sections. Prior to the commencement of actual measurements, the devices were left N_2-purging for up to 2 hrs, and pre-conditioned by constantly biasing the WE at -1.6 V vs. Ag-RE for close to an hour, for stabilization of background currents.

6.3. Results and Discussions

PMMA (~10 % w/v) was blended with all eight RTILs (listed in Section 2.1) to investigate their viability as GPE materials for this study. All RTILs showed good miscibility characteristics (such as homogeneity, and stability from phase-separating or leaching) with the exception of $[C_4mim][BF_4]$. Poly(vinyl chloride) (PVC) (a polymer that generally produces membranes with better mechanical properties [183, 201, 206, 207]) was also explored as a potential host polymer for the gelification of the eight RTILs. However all RTILs surveyed, with the exception of the two highly hydrophobic trihexyl(tetradecyl) phosphonium $[P_{14,6,6,6}]^+$ based RTILs (namely $[P_{14,6,6,6}][NTf_2]$ and $[P_{14,6,6,6}][FAP]$) eventually visibly leached out of the composite material. This would effectively lead to instability in the GPE's conductivity, diffusional and partitioning coefficients of analyte gases over time, and thus instability in their electrochemical response, making them unsuitable for electrochemical gas-sensing purposes. A study on the miscibility of PVC and RTILs (at 20 wt. %), namely 1-butyl-3-methyl imidazolium hexafluorophosphate $[C_4mim][PF_6]$, 1-hexyl-3-methyl imidazolium dioctylsulfosuccinate $[C_6mim][doss]$, 1-hexyl-3-methyl imidazolium hexfluorophosphate $[C_6mim][PF_6]$, trihexyl(tetradccyl) phosphonium decanoate $[P_{14,6,6,6}][deca]$, trihexyl(tetradecyl) phosphonium chloride $[P_{14,6,6,6}][Cl]$, and Trihexyl(tetradecyl) phosphonium bis(trifluoromethane) sulfonylimide $[P_{14,6,6,6}][Tf_2N]$, by Rahman's group [217] reported comparable findings. This chapter consequently focuses on only PMMA-based GPEs, as a preliminary investigation of their viability in electrochemical gas-sensing. To prepare the GPEs to be investigated here, PMMA will be plasticised with the RTILs $[C_2mim][NTf_2]$ and $[C_4mpyrr][NTf_2]$, both of which were selected to be focused on in the study presented in Chapter 5.

6.3.1. Cyclic voltammetry of PMMA gelified RTILs on platinum macrodisk working electrode.

GPEs at 0, 10, 30, 50, 100, and 150 % w/v concentrations of the PMMA polymer were prepared with $[C_2mim][NTf_2]$ and $[C_4mpyrr][NTf_2]$ RTILs, and deposited onto the platinum macrodisk working electrode positioned within the glass T-cell shown in Figure 6.1. For both RTILs, at 50 % w/v PMMA concentration, the PMMA-RTIL blends became significantly more viscous, while gelification was attained with PMMA doping levels of 50-100 % w/v, with no appreciable flow of the mixture when the Pt-SPE was tilted vertically at 90 °. N_2-gas was set flowing at 100 sccm and left overnight, allowing any remaining acetone in the PMMA-RTIL blend to completely volatilise. CVs of oxygen reduction at 100 % vol. O_2 concentrations and their respective blanks (N_2-purged) at different % w/v PMMA doping of $[C_2mim][NTf_2]$ and $[C_4mpyrr][NTf_2]$ are respectively presented in Figure 6.2 and 6.3 and will be discussed in the following sub-sections in detail. The times necessary to oxygen saturate the N_2-purged PMMA/RTIL mixtures was roughly estimated to range from 1.5 to 2 hrs for $[C_2mim][NTf_2]$, and 2 to 4 hrs for $[C_4mpyrr][NTf_2]$, for PMMA doping concentrations between 10 % w/v and 150 % w/v in the ~1.5 mm thick PMMA-doped-RTIL films. The minimum time between scans required to allow for depleted oxygen at the WE's surface to recover in 100 % vol. O_2 flow was found to be shorter than 5 mins for all samples.

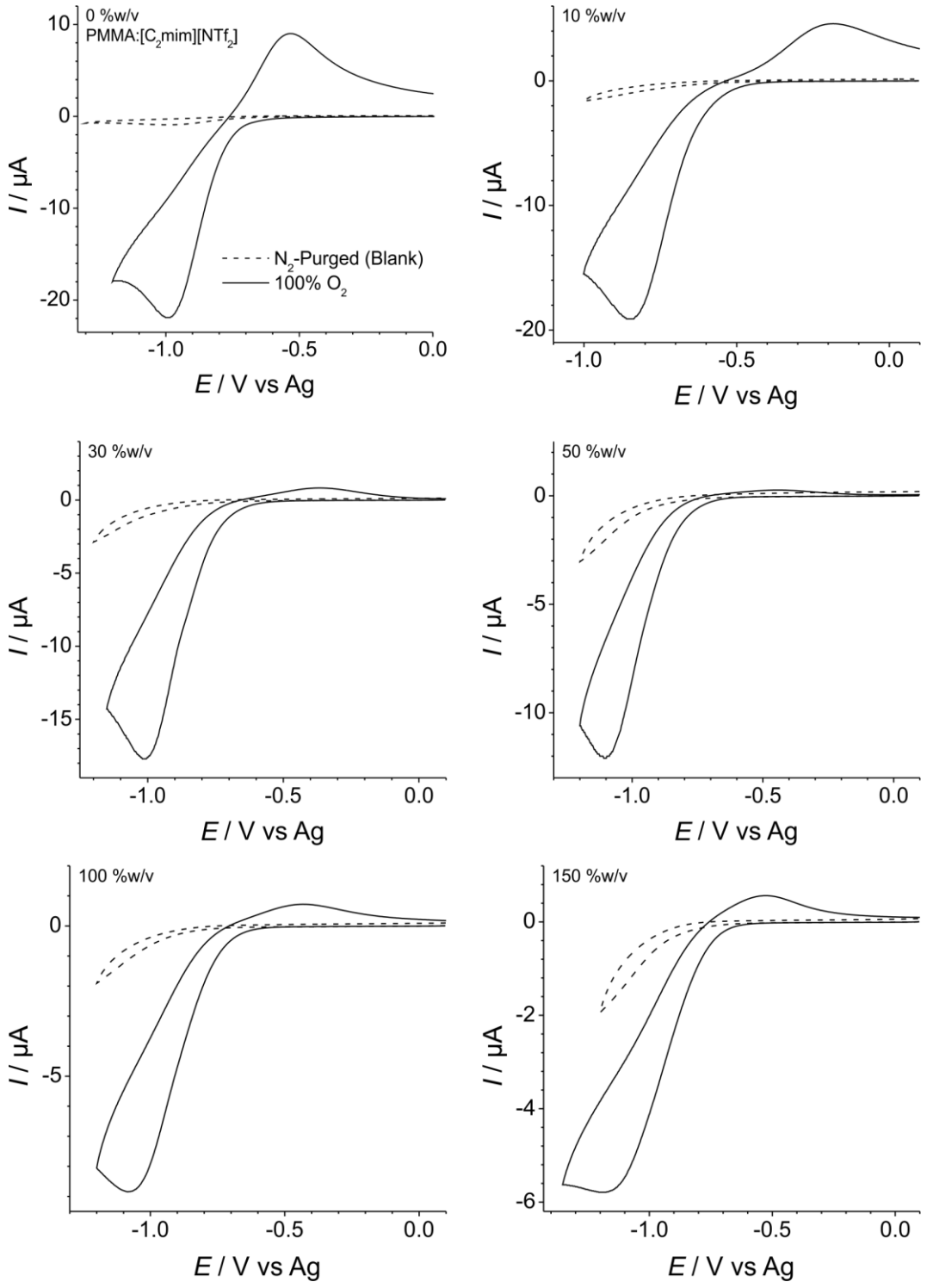

Figure 6.2. Cyclic voltammograms of the $O_2/O_2^{\bullet-}$ redox couple conducted on Pt macrodisk working electrode (vs. Ag-RE) in $[C_2mim][NTf_2]$ based GPEs at varying % w/v PMMA doping levels (solid lines) saturated with oxygen (i.e. at 100 % vol. O_2), collected at a scan rate of 100 $mV \cdot s^{-1}$. The dotted lines represent the blank CVs collected for the respective N_2-purged GPEs.

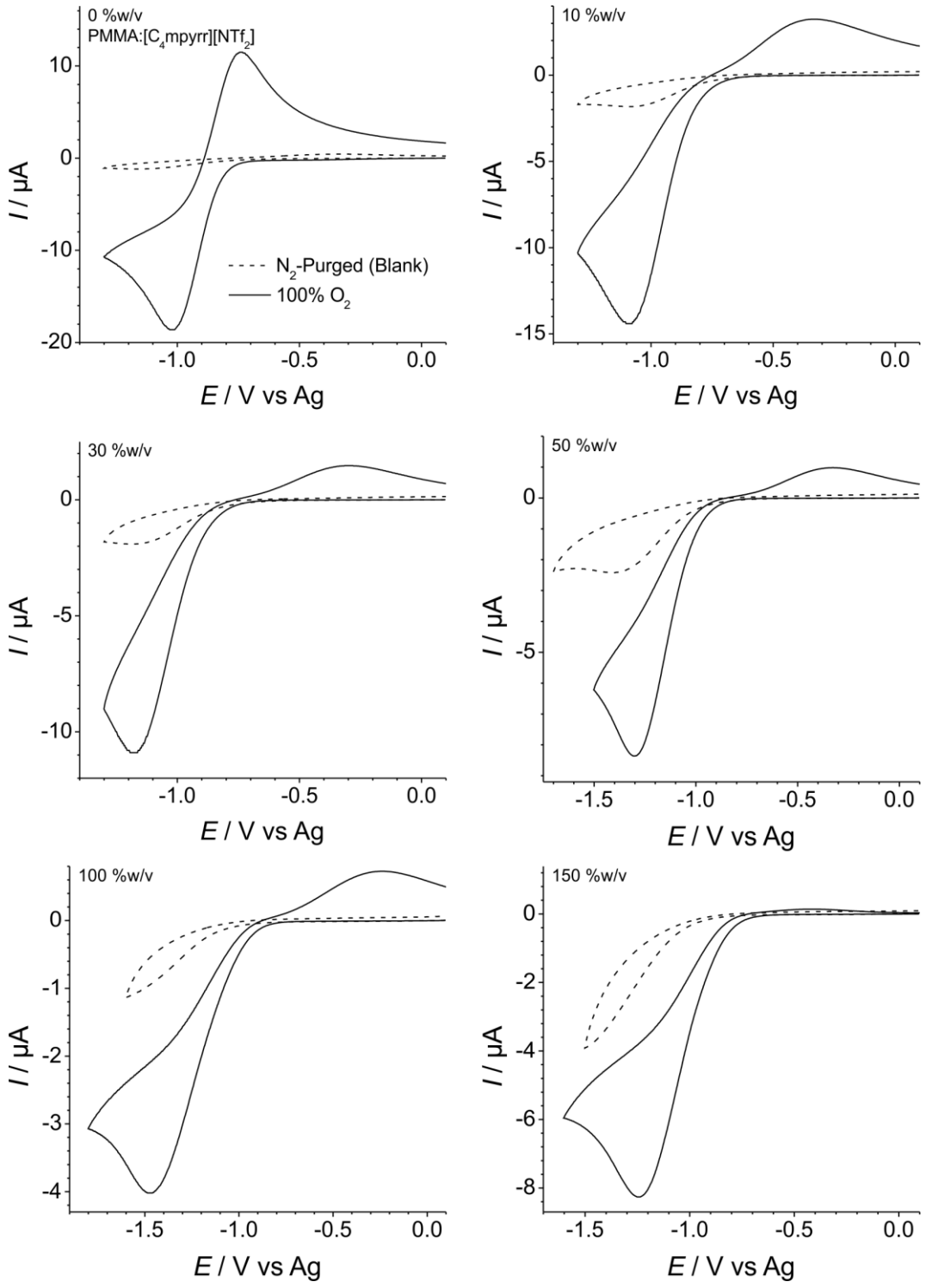

Figure 6.3. Cyclic voltammograms of the $O_2/O_2^{\bullet-}$ redox couple conducted on Pt macrodisk working electrode (vs. Ag-RE) in $[C_4mpyrr][NTf_2]$ based GPEs at varying % w/v PMMA doping levels (solid lines) saturated with oxygen (i.e. at 100 % vol. O_2), collected at a scan rate of 100 $mV \cdot s^{-1}$. The dotted lines represent the blank CVs collected for the respective N_2-purged GPEs.

6.3.1.1. Analysis of the impact of PMMA addition on $O_2/O_2^{\bullet-}$ redox couple's cyclic voltammetry peak currents.

The background subtracted oxygen reduction peak currents were extracted from CVs presented in Figure 6.2 and Figure 6.3, and plotted against their respective % w/v PMMA doping levels for the two RTILs as shown in Figure 6.4 (a) and (b). The equations and R^2 values of the linear regressions are summarized in Table 6.2 below. For the $[C_4mpyrr][NTf_2]$-based GPE, the data point at 150 % w/v PMMA doping level was omitted, and linear regression was reapplied for the remaining data points (shown in Figure 6.4 (b) by the dashed line), improving the R^2 value (from 0.5927 to 0.8751). Omitting the last two data points (at 100 and 150 % w/v) further improved the R^2 value (to 0.9338) of the linear regression (as shown by the dotted line in Figure 6.4 (b). The red dashed arrow highlights a possible mark change in signal response beyond ca. 77 % w/v PMMA doping, which has to be verified with follow-up repeat measurements.

From the linear regression fits presented in Figure 6.4 and the corresponding R^2 values for $[C_2mim][NTf_2]$ and the refitted $[C_4mpyrr][NTf_2]$ data listed in Table 6.2, it can be seen that, overall, the O_2 reduction peak current shows a linearly reducing relationship with respect to the PMMA doping levels. Decrease in either the solubilities and/or diffusion coefficients of O_2 with increasing PMMA doping in the two RTILs were plausible explanation to account for this. However, due to an expected (and visually observable) significant increase in the viscosity of the PMMA/RTIL mixture, with increasing PMMA doping (from 0-150 % w/v PMMA in RTIL), coupled with the linear behaviour of the plots of peak currents vs. PMMA doping for the two RTILs, the decrease in O_2 reduction peak currents was attributed more likely to be mainly due to a decrease in diffusion coefficient for O_2 in the PMMA/RTIL electrolyte. Decrease in the partitioning coefficient for oxygen with respect to nitrogen may

also lead to a decrease in O_2 reduction peak currents measured. However this is unlikely since both oxygen and nitrogen gas molecules are neutrally charged species, and have similar molecular sizes. Furthermore, a power relationship (rather than a linear one) would be expected between O_2 reduction peak currents vs. PMMA doping levels, if significant decrement in partitioning coefficient and/or a change in solubility (on top of diffusion coefficient) are also present, with increasing PMMA doping.

It is not clear at this point if the data points for $[C_4mpyrr][NTf_2]$, at 100 and 150 % w/v PMMA doping, was an outlier or the result of an actual transition in the property of the PMMA-RTIL composite material past a certain critical % w/v PMMA doping (occurring somewhere between 100-150 % w/v). However, referring to the equation of linear regression obtained for $[C_4mpyrr][NTf_2]$ (with the 100 and 150 % w/v data points omitted), it is interesting to note that the line intercepts the x-axis (i,e. $I = 0$ A) at 77.6 % w/v PMMA doping (i.e. between 50-150 % w/v, where the deviation from the fitted linear trend appear to occur). This rebounding of the O_2 reduction current for the measured 100 and 150 % w/v PMMA doping of $[C_4mpyrr][NTf_2]$ may perhaps be attributed to a homogeneous phase transition occurring within the composite material beyond a critical PMMA-doping level (ca. 77.6 % w/v), which could affect the diffusion of O_2. Alternatively, the formation of non-homogeneous micro- or meso-porous PMMA scaffold holding pockets of RTIL, thus setting up O_2 diffusion percolation channels within the GPE, could also be a plausible explanation. This could be investigated by small-angle X-ray scattering (SAXS) or small-angle neutron scattering (SANS) techniques, or by atomic force microscopy characterization of surfaces of drop-cast PMMA/RTIL films at different levels of PMMA doping, about ca. 112 % w/v PMMA in a follow up study.

In contrast, for the case of $[C_2mim][NTf_2]$ (where no such deviation was observed), the x-intercept cross-over point occurred at 176 % w/v, based on the linear regression fit for the

full range (of 0-150 % w/v PMMA doping levels) measured. This is significantly higher than the range of PMMA doping levels investigated for this RTIL. At least a duplicate set of data would be necessary to ascertain reliability of the data points, especially at 100 and 150 % w/v PMMA doping for [C_4mpyrr][NTf_2]. This notable divergence in behaviour was also observed in the trend of $O_2/O_2^{\bullet-}$ redox peak-to-peak separations vs. % w/v PMMA doping levels as shown in Figure 6.8.

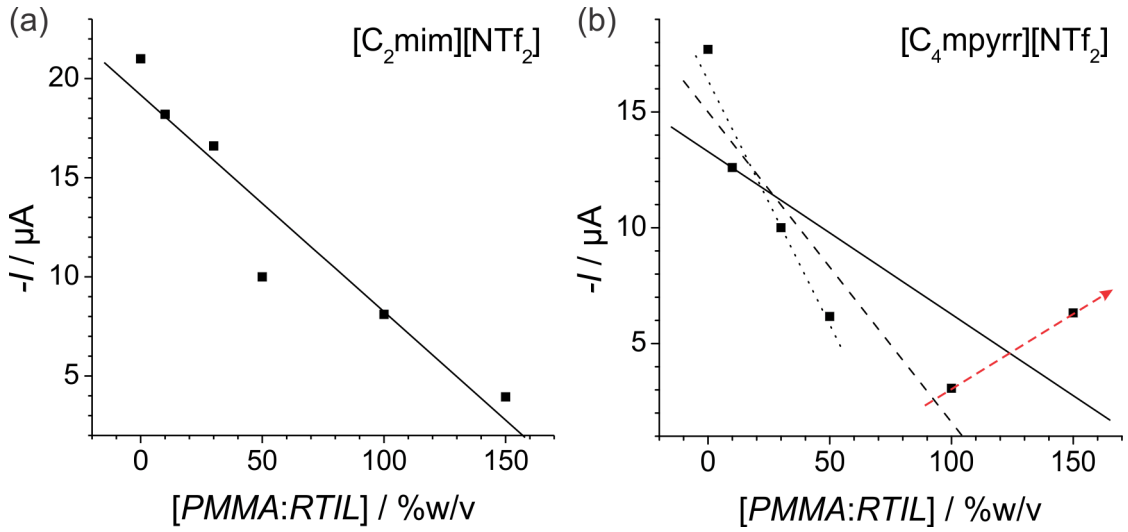

Figure 6.4. Plot of background corrected peak currents of O_2 reductions on Pt macrodisk working electrode (vs. Ag-RE), extracted from CVs presented in Figure 6.2 and Figure 6.3 and plotted against their respective % w/v PMMA doping levels for the two RTILs: **(a)** [C_2mim][NTf_2] and **(b)** [C_4mpyrr][NTf_2]. Linear lines of least squares were fitted to the data points. For [C_4mpyrr][NTf_2], the 150 % w/v data point, and also for both 100 and 150 % w/v, were omitted and re-fitted, as respectively shown by the dashed and dotted line in (b). The red dashed arrow highlights a possible mark change in signal response. Corresponding equations and R^2 values of the linear regressions shown were presented in Table 6.2 below.

Table 6.2. Equations of linear best-fits and R^2 values for the plots of background corrected peak currents of O_2 reductions on Pt macrodisk working electrode (vs. Ag-RE) in PMMA-RTIL blends vs. % w/v PMMA doping levels for the two RTILs plotted in Figure 6.4 above.

RTIL	**Equation of linear regressions (where *I* / A and [*PMMA:RTIL*] / % w/v)**	R^2
$[C_2mim][NTf_2]$	$I = 1.09\times10^{-7}$ [*PMMA:RTIL*] - 1.92×10^{-5}	0.9132
$[C_4mpyrr][NTf_2]$	$I = 7.03\times10^{-8}$ [*PMMA:RTIL*] - 1.33×10^{-5}	0.5927
$[C_4mpyrr][NTf_2]^{\dagger}$	$I = 1.34\times10^{-7}$ [*PMMA:RTIL*] - 1.50×10^{-5}	0.8751
$[C_4mpyrr][NTf_2]^{\ddagger}$	$I = 2.11\times10^{-7}$ [*PMMA:RTIL*] - 1.64×10^{-5}	0.9338

† *Fitted with the data point at 150 % w/v [PMMA:RTIL] omitted.*
‡ *Fitted with the data points at 100 and 150 % w/v [PMMA:RTIL] omitted.*

Background subtracted peak currents of superoxide oxidation were also extracted from the CVs presented in Figure 6.2 and Figure 6.3, and plotted against their respective % w/v PMMA doping levels for the two RTILs as shown in Figure 6.5 (a). The equations and R^2 values from the regressions are summarized in Table 6.3 below. A first order inverse proportionality of superoxide oxidation currents, with respect to varying PMMA doping levels, for the two RTILs were found (as shown in the inset of Figure 6.5 (a)). These were likely correlated solely to the linear decrease in O_2 reduction peak currents (hence resulting in a decrease in superoxide production during the cathodic scan) with respect to increasing PMMA concentrations as shown in Figure 6.4. Base on this consideration, a possible chemical interaction between the superoxide radical and the aprotic polymer was unlikely to be present. Chemical interaction between superoxide and PMMA was expected to result in partial chemical irreversibility and hence a higher order inverse proportionality (i.e. $I \propto x^{-n}$, where $n > 1$) than was observed.

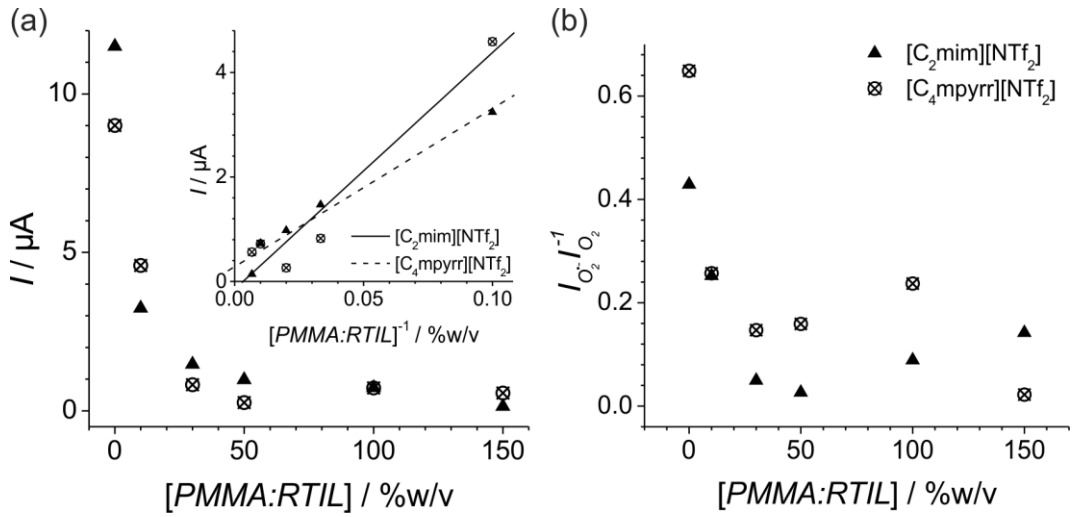

Figure 6.5. (a) Plot of background corrected peak currents of superoxide ($O_2^{\bullet-}$) oxidation on Pt macrodisk working electrode (vs. Ag-RE), extracted from CVs presented in Figure 6.2 and Figure 6.3 and plotted vs. % w/v PMMA doping levels for $[C_2mim][NTf_2]$ and $[C_4mpyrr][NTf_2]$. Corresponding equations and R^2 values of the linear regressions shown were presented in Table 6.3 below. **(b)** Normalized superoxide oxidation peak currents, $I_{O_2^{\bullet-}}$, against oxygen reduction peak currents (presented in Figure 6.4), I_{O_2}, were also plotted against their respective % w/v PMMA doping levels for the two RTILs.

Table 6.3. Equations of linear best-fits and R^2 values for the plots of background corrected peak currents of superoxide ($O_2^{\bullet-}$) oxidation, the reverse cycle of O_2 CV, on Pt macrodisk working electrode (vs. Ag-RE) in PMMA-RTIL blends vs. % w/v PMMA doping levels for the two RTILs plotted in the inset of Figure 6.5 above.

RTIL	**Equation of linear regressions (where *I* / A and [*PMMA:RTIL*]$^{-1}$ / % w/v^{-1})**	R^2
$[C_2mim][NTf_2]$	$I = 4.53\times10^{-5}\,[PMMA:RTIL]^{-1} - 1.48\times10^{-7}$	0.9291
$[C_4mpyrr][NTf_2]$	$I = 3.03\times10^{-5}\,[PMMA:RTIL]^{-1} + 2.82\times10^{-7}$	0.9670

Superoxide oxidation peak currents as shown in Figure 6.5 (a) were also normalized against their corresponding oxygen reduction peak currents (that were presented in Figure 6.4), and plotted against respective % w/v PMMA doping levels for the two RTILs as presented in Figure 6.5 (b). The normalized superoxide reduction peak currents for both PMMA gelified RTILs sharply decreased up to ca. 30 % w/v PMMA doping, and exhibited a more gradual increase after that, as shown in Figure 6.5 (b). This was likely due to a significant lowering of the mobility of the electrogenerated superoxide due to the addition of PMMA. The increased fluid-viscosities of the PMMA/RTIL electrolyte at higher levels of PMMA doping would, at the same time, effectively keep more electrogenerated superoxide from diffusing away from the WE surface, which would then be oxidised back into oxygen during the reverse anodic scan. This would result in the shape of the superoxide oxidation peak shifting from diffusion controlled type behaviour towards a more surface-confined type behaviour (i.e. a diminished presence of a diffusive tail, and a more symmetrical peak shape) with increasing PMMA doping levels, as can be seen in Figure 6.2 and 6.3. This effect became more apparent at the slower scan rate of 10 $mV \cdot s^{-1}$ (from the usual scan rate of 100 $mV \cdot s^{-1}$), as shown in Figure 6.6. Confinement of superoxide close to the surface of the electrode within the duration of the CV scans would ensure that most of the electrogenerated superoxides were oxidized back into oxygen during the reverse scan. This would consequently result in an improved long-term-stability of the sensing response, due to reduced accumulation of degradation products, resulting from the interaction of unoxidized superoxide with the RTIL (see Section 5.4).

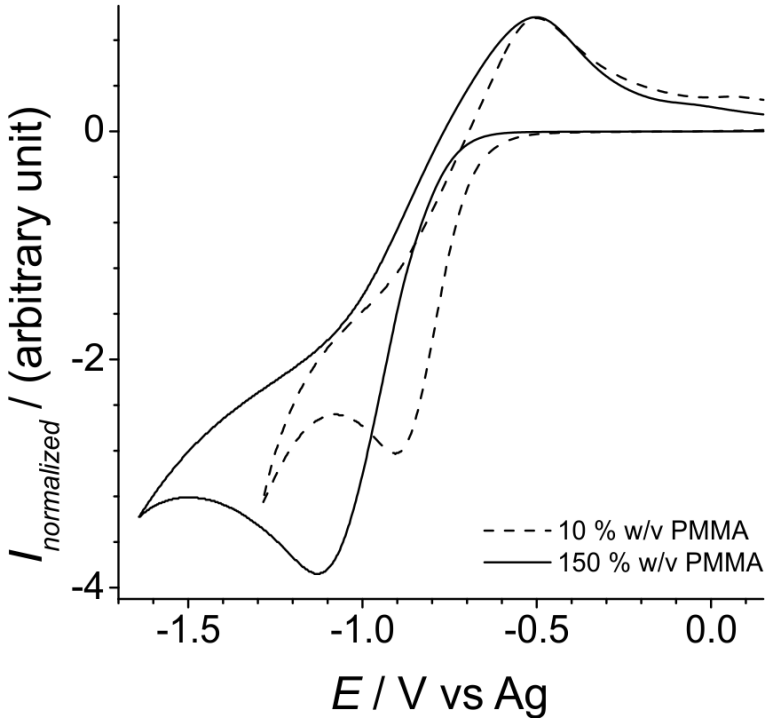

Figure 6.6. Cyclic voltammograms of the $O_2/O_2^{\bullet-}$ redox couple conducted on Pt macrodisk working electrode (vs. Ag-RE) in $[C_2mim][NTf_2]$ based GPEs at 10 and 150 % w/v PMMA doping levels saturated with oxygen, collected at a scan rate of 10 $mV \cdot s^{-1}$. The superoxide oxidation peak currents for both CVs were normalized to unity to allow for comparison of their peak shapes.

6.3.1.2. Mechanisms of $O_2/O_2^{\bullet-}$ redox couple in PMMA doped $[C_2mim][NTf_2]$ and $[C_4mpyrr][NTf_2]$

CVs at different scan rates were carried out for three O_2 saturated PMMA-doped RTIL systems (10 and 150 % w/v PMMA for $[C_2mim][NTf_2]$, and 10 % w/v PMMA for $[C_4mpyrr][NTf_2]$). Significant variations of the peak-to-peak separation potentials, $\Delta E_{p\text{-}p}$, of the $O_2/O_2^{\bullet-}$ redox couple in response to varying scan rates, v, (as shown in the inset of Figure 6.7) for 10 % w/v PMMA in the two RTILs were also present. This may be a sign of slow electron transfer kinetics or uncompensated resistance. $\Delta E_{p\text{-}p}$ was found to exhibit a strong linear correlation to v raised to the power of x (i.e. v^x) as shown in Figure 6.7 and Table 6.4, where x for $[C_2mim][NTf_2]$ increased significantly from a value of ca. 0.15 (at 10 % w/v PMMA doping) to ca. 0.20 (at 150 % w/v PMMA doping). For a perfectly reversible system, with negligible electrolyte resistance, $\Delta E_{p\text{-}p}$ is invariant with respect to scan rate (i.e. $x = 0$). Figure 6.7 suggests perhaps a change in electrode kinetics of the $O_2/O_2^{\bullet-}$ redox couple at the electrode with increasing level of PMMA doping. A significant change in the difference in solvation structures of O_2 and $O_2^{\bullet-}$ at different PMMA concentrations could perhaps explain this (see Section 1.3.2.3). The non-linear $\Delta E_{p\text{-}p}$ vs. v relationships (i.e. $x \neq 1$), and a variation in x with respect to PMMA doping levels, hints of a combination of contributing influences. It was expected that the trend would be substantially related to a significant increase in electrolyte resistance (due to slower diffusion of the RTIL ions with increasing fluid-viscosity, coupled with a reduced ionic concentration within the electrolyte) with increasing PMMA doping levels for the $[C_2mim][NTf_2]$ that was investigated in this preliminary study. These could be further investigated by modelling the voltammetry data with *Fast Implicit Finite Difference method* [259] using the commercially available software package, DigiSim® [260].

From Figure 6.7, $[C_4mpyrr][NTf_2]$ at 10 % w/v PMMA doping appears to have intermediate resistance, compared to $[C_2mim][NTf_2]$ at the two PMMA doping levels presented. This may be due to the intrinsically higher viscosity of $[C_4mpyrr][NTf_2]$ compared to $[C_2mim][NTf_2]$ (see Table 1.4). Also perhaps, a stronger interaction between $[C_4mpyrr][NTf_2]$ with PMMA exists, which would lead to a much stronger change in $\Delta E_{p\text{-}p}$ vs. v with increasing PMMA doping as compared to $[C_2mim][NTf_2]$. Evidence of this may possibly be unveiled if the change in $\Delta E_{p\text{-}p}$ vs. v behaviour is examined at a larger number of PMMA doping levels (i.e. at least 6 different PMMA concentrations between 10-150 %w/v *PMMA*:*RTIL* ratio). This was however not investigated in the present preliminary study on these PMMA/RTIL systems. Referring to Figure 6.2 and 6.3, even at the high PMMA levels (i.e. 100 – 150 % w/v) where the electrolyte essentially became a solid gel (with negligible fluid-viscosity), it is interesting to find absence of any appreciable signs of increase in background capacitive currents from the voltammetries conducted in the two PMMA doped RTIL systems.

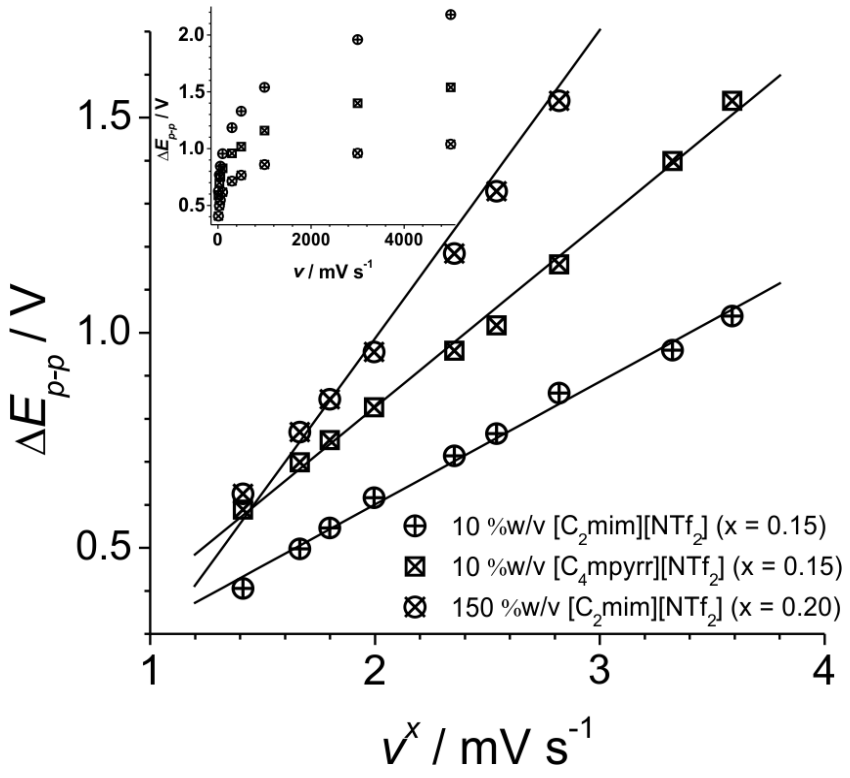

Figure 6.7. Peak-to-peak separations for the $O_2/O_2^{\bullet-}$ redox couple, $\Delta E_{p\text{-}p}$ vs. scan rates, v, for 10 % w/v PMMA in $[C_2mim][NTf_2]$ and $[C_4mpyrr][NTf_2]$, and 150 % w/v PMMA in $[C_2mim][NTf_2]$, measured on Pt macrodisk WE (vs. Ag-RE) as shown in the inset. $\Delta E_{p\text{-}p}$ was found to strongly correlate to v raised by a power of x, where x are as indicated by the linear regressions. Corresponding equations and R^2 values were presented in Table 6.4.

Table 6.4. Equations of linear best-fits and R^2 values for peak-to-peak separations for the $O_2/O_2^{\bullet-}$ redox couple, $\Delta E_{p\text{-}p}$ vs. scan rates raised to a power of x, v^x, for 10 % w/v PMMA in $[C_2mim][NTf_2]$ and $[C_4mpyrr][NTf_2]$, and 150 % w/v PMMA in $[C_2mim][NTf_2]$, measured on Pt macrodisk WE (vs. Ag-RE) and plotted for GPEs presented in Figure 6.7 above.

RTIL	***PMMA:RTIL* / % w/v**	**Equation of linear regressions (where *I* / A and [Scan Rates]^{½}, $v^{½}$ / mV^{½}·s$^{-½}$)**	R^2
$[C_2mim][NTf_2]$	10	$\Delta E_{p\text{-}p} = 2.85\times10^{-1}\, v^{0.15} + 2.99\times10^{-2}$	0.9965
$[C_4mpyrr][NTf_2]$	10	$\Delta E_{p\text{-}p} = 4.28\times10^{-1}\, v^{0.15} - 2.91\times10^{-2}$	0.9976
$[C_2mim][NTf_2]$	150	$\Delta E_{p\text{-}p} = 7.17\times10^{-1}\, v^{0.20} - 4.48\times10^{-1}$	0.9937

Plot of $\Delta E_{p\text{-}p}$ vs. % w/v PMMA doping levels (for the $O_2/O_2^{\bullet-}$ redox couple) is presented in Figure 6.8. $\Delta E_{p\text{-}p}$ for both RTILs showed a sharp jump between pure RTILs (circled in green) and 10 % w/v PMMA doping. After which, $\Delta E_{p\text{-}p}$ for $[C_2mim][NTf_2]$ remained independent of increasing PMMA doping, while $\Delta E_{p\text{-}p}$ for $[C_4mpyrr][NTf_2]$ linearly increased up to 100 % w/v PMMA doping concentration, before drastically dropping down to a value below that of 30 % w/v PMMA doping (as indicated by the dotted red arrow) at 150 % w/v PMMA doping (as circled in red). This sudden change for $[C_4mpyrr][NTf_2]$ between 100 and 150 % w/v was also observed in the trend of O_2 reduction peak currents, shown in Figure 6.4, as discussed above. This, if proved reproducible, could possibly indicate a change in PMMA morphology. This could perhaps also lead to better GPE-WE interfacing at PMMA doping concentration between 100 and 150 % w/v for $[C_4mpyrr][NTf_2]$ RTIL. However, as has been earlier discussed, repeat measurements for 150 % w/v PMMA doping in $[C_4mpyrr][NTf_2]$ is required to affirm the observed deviation from the general trend at lower % w/v doping levels.

The cause of the mark difference in behaviour of $\Delta E_{p\text{-}p}$ vs. % w/v PMMA doping for the $O_2/O_2^{\bullet-}$ redox couple (as shown in Figure 6.8) between the two RTILs is unclear at this point in time. If the change in $\Delta E_{p\text{-}p}$ values is attributed purely to resistive effect with the addition of PMMA, the plot of $\Delta E_{p\text{-}p}$ vs. % w/v PMMA doping would be expected to increase for $[C_2mim][NTf_2]$ with increasing PMMA doping level. It was suggested above that a stronger interaction between $[C_4mpyrr][NTf_2]$ and PMMA, compared to $[C_2mim][NTf_2]$, may exist which would also explain the difference in the behaviour of $\Delta E_{p\text{-}p}$ vs. PMMA doping between the two RTILs. This could be further studied by the nuclear magnetic resonance (NMR) spectroscopy technique. Another plausible explanation for the linearly increasing $\Delta E_{p\text{-}p}$, vs. increasing PMMA doping level for $[C_4mpyrr][NTf_2]$ is due to an increasing contact resistance between electrolyte and the WE surface (due to increasingly poorer wetting of the electrode

surface by the electrolyte). This can be investigated by conducting EIS characterization of the systems. Equations of the linear regressions and their corresponding R^2 values are presented in Table 6.5 below.

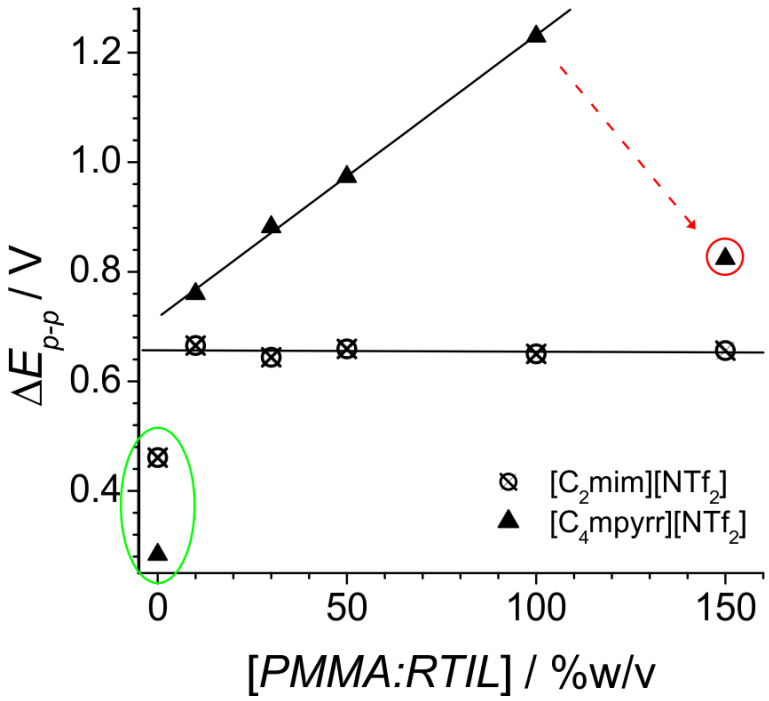

Figure 6.8. Peak-to-peak separations for the $O_2/O_2^{\bullet-}$ redox couple, $\Delta E_{p\text{-}p}$ vs. % w/v PMMA doping levels in the two RTILs on Pt macrodisk WE (vs. Ag-RE) extracted from CVs presented in Figure 6.2 and Figure 6.3, collected at a scan rate of 100 $mV \cdot s^{-1}$. The data points for 0 % w/v PMMA for both RTILs, and 150 % w/v for $[C_4mpyrr][NTf_2]$ were omitted from the linear regression performed. Corresponding equations and R^2 values of the linear fits are presented in Table 6.5.

Table 6.5. Equations of linear best-fits and R^2 values for the plots of peak-to-peak separations for the $O_2/O_2^{\bullet-}$ redox couple, $\Delta E_{p\text{-}p}$ vs. % w/v PMMA doping levels in the two RTILs on Pt macrodisk WE (vs. Ag-RE) presented in Figure 6.8.

RTIL	**Equation of linear regressions (where *I* / A and [*PMMA:RTIL*] / % w/v)**	R^2
$[C_2mim][NTf_2]$	$\Delta E_{p\text{-}p} = -2.46\times10^{-5}$ [*PMMA:RTIL*] $+ 6.57\times10^{-1}$	0.0288
$[C_4mpyrr][NTf_2]$	$\Delta E_{p\text{-}p} = 5.16\times10^{-3}$ [*PMMA:RTIL*] $+ 7.16\times10^{-1}$	0.9984

The background corrected oxygen reduction peak currents were analysed from the CVs, and plotted with respect to scan rates, v, and also square-roots of scan rates, $v^{½}$, as presented respectively in Figure 6.9 (a) and (b), as were the superoxide oxidation peak currents from the reverse CV cycle respectively in Figure 6.10 (a) and (b). Strong linear correlations between peak currents with $v^{½}$ for both oxygen reduction and the oxidation of the electrogenerated superoxide were generally observed (see R^2 values summarized in Table 6.6). This suggests that the mechanism of O_2 reduction on Pt-WE in the presence of PMMA added to both RTILs remains predominantly diffusion controlled. For $[C_4mpyrr][NTf_2]$ however, an appreciable deviation from a linear trend can been seen from Figure 6.10 (b) at 150 % w/v PMMA doping.

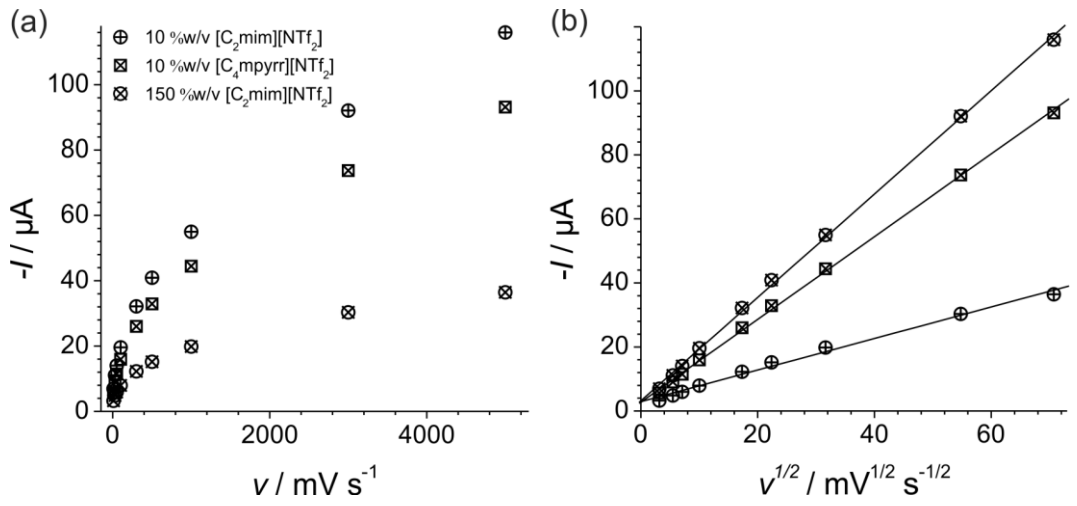

Figure 6.9. Background corrected oxygen reduction peak currents analysed from CVs obtained at different scan rates for three O_2 saturated PMMA-doped RTIL systems (10 and 150 % w/v PMMA for $[C_2mim][NTf_2]$, and 10 % w/v PMMA for $[C_4mpyrr][NTf_2]$), plotted with respect to **(a)** scan rates, v and also **(b)** square-root of scan rates, $v^{½}$. The latter plots were then fitted with linear regression, and the corresponding equations and R^2 values were presented in Table 6.6 below.

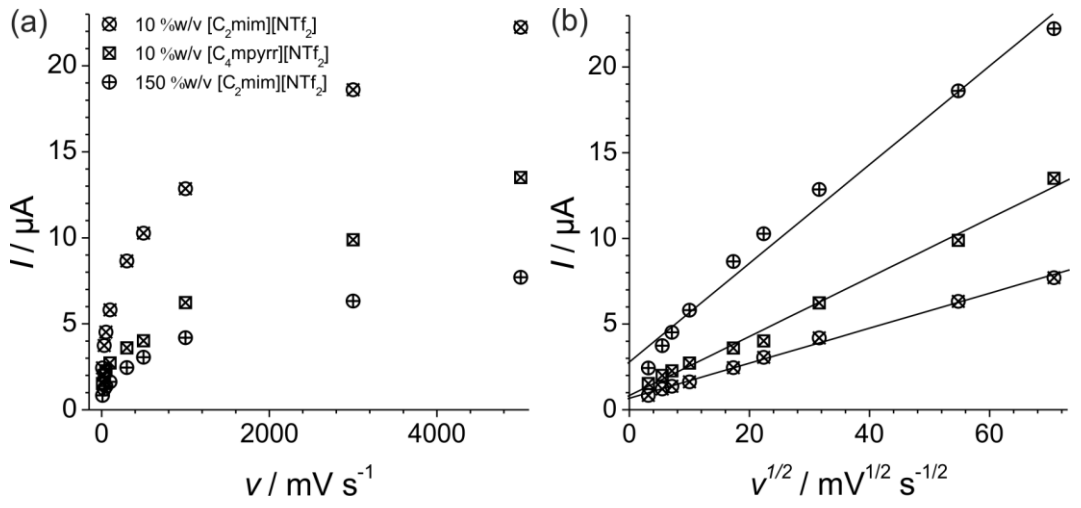

Figure 6.10. Background corrected superoxide oxidation peak currents (from the reverse CV cycles) analysed from CVs obtained at different scan rates for three O_2 saturated PMMA-doped RTIL systems (10 and 150 % w/v PMMA for $[C_2mim][NTf_2]$, and 10 % w/v PMMA for $[C_4mpyrr][NTf_2]$), plotted with respect to **(a)** scan rates, v and also **(b)** square-root of scan rates, $v^{½}$. The latter plots were then fitted with linear regression, and the corresponding equations and R^2 values were presented in Table 6.6 below.

Table 6.6. Equations of linear best-fits and R^2 values for the plots of background corrected peak currents vs. square root of scan rates, $v^{½}$, for the $O_2/O_2^{\bullet-}$ redox couple, analysed from CVs obtained at different scan rates for three O_2 saturated PMMA-doped RTIL systems (10 and 150 % w/v PMMA for $[C_2mim][NTf_2]$, and 10 % w/v PMMA for $[C_4mpyrr][NTf_2]$) on Pt macrodisk WE (vs. Ag-RE) presented in Figure 6.9 and Figure 6.10.

RTIL	**Peak**	***PMMA:RTIL* / % w/v**	**Equation of linear regressions (where *I* / A and [Scan Rates]^{½}, $v^{½}$ / mV^{½}·s$^{-½}$)**	R^2
$[C_2mim][NTf_2]$	Oxygen Reduction	10	$-I = 1.61\times10^{-6}\, v^{½} + 3.19\times10^{-6}$	0.9992
$[C_4mpyrr][NTf_2]$		10	$-I = 1.29\times10^{-6}\, v^{½} + 2.75\times10^{-6}$	0.9991
$[C_2mim][NTf_2]$		150	$-I = 4.92\times10^{-7}\, v^{½} + 2.94\times10^{-6}$	0.9925
$[C_2mim][NTf_2]$	Superoxide Oxidation	10	$I = 2.88\times10^{-7}\, v^{½} + 2.79\times10^{-6}$	0.9849
$[C_4mpyrr][NTf_2]$		10	$I = 1.72\times10^{-7}\, v^{½} + 8.28\times10^{-7}$	0.9923
$[C_2mim][NTf_2]$		150	$I = 1.02\times10^{-7}\, v^{½} + 6.72\times10^{-7}$	0.9966

6.3.1.3. Blank CVs of 150 % w/v PMMA doped RTILs on macrodisk platinum electrode

Figure 6.11 (a) and (b) shows the blank CVs of PMMA doped $[C_2mim][NTf_2]$ and $[C_4mpyrr][NTf_2]$ at 0-150 % w/v PMMA in the respective RTILs. The PMMA/RTIL mixture, setup as depicted in Figure 6.1, were left in the N_2-purged cell overnight (for > 12 hrs) before commencing CV measurements (see Section 6.2.3). Figure 6.11 (c) and (d) shows the impact of insufficiently dried 150 % w/v PMMA doped RTILs on the CV compared to one that have been left to dry under N_2 overnight. For the neat RTILs (i.e. with 0 % w/v PMMA), irreversible reduction peaks in (a) $[C_2mim][NTf_2]$ and a reversible redox couple in (b) $[C_4mpyrr][NTf_2]$ in the N_2-purged blank CVs were present. It is interesting to note that the reduction peaks in the blank CVs of both neat RTILs occur at the similar potential of ca. -1 V. This has suggested that the reduction peaks present in the blank CVs of both neat RTILs may possibly be the result of the same species that could be naturally present in both RTILs (also noting that both RTILs shares the same $[NTf_2]^-$ anion). Impurities such as water, and residual species or by-products (commonly halides) from the synthesis of the RTILs (see Section 1.3.2.4) [89] are likely suspect for the reduction peaks observed in the blank CVs. These peaks could also be observed in the blank CVs of most of the other RTILs collected on macrodisk Pt electrodes that were previously shown in Figure 3.1.

Contaminant (i.e. moisture) in the N_2-gas reticulation line have been ruled out by the persistence of the contaminant peaks from the CVs of the RTILs, purged using cylinders of high-purity N_2 gas, Argon gas, and insertion of a spare T-cell along the gas-mixing line, that was packed with activated 4 Å molecular sieves, to dry the N_2-gas that was flowing through. The proticity of the $[C_2mim]^+$ cation may explain the lack of a reverse oxidation peak observed in the N_2-purged blank CVs of neat $[C_2mim][NTf_2]$. To investigate the possibility of

trace water as the cause of the reduction peak currents observed in the blank CVs of the neat RTILs, the N_2-gas that was used to purge the cell of oxygen and other gases could be humidified by insertion of a segment of glass-cell packed with wet-cotton along the gas-mixing line. CVs of the electrolyte spiked with moisture could then be collected and be compared. Spiking of the two neat RTILs with salts containing halides (e.g. $[C_2mim][Cl]$ and $[C_4mpyrr][Cl]$) as their anions (in place of $[NTf_2]^-$) could also be investigated.

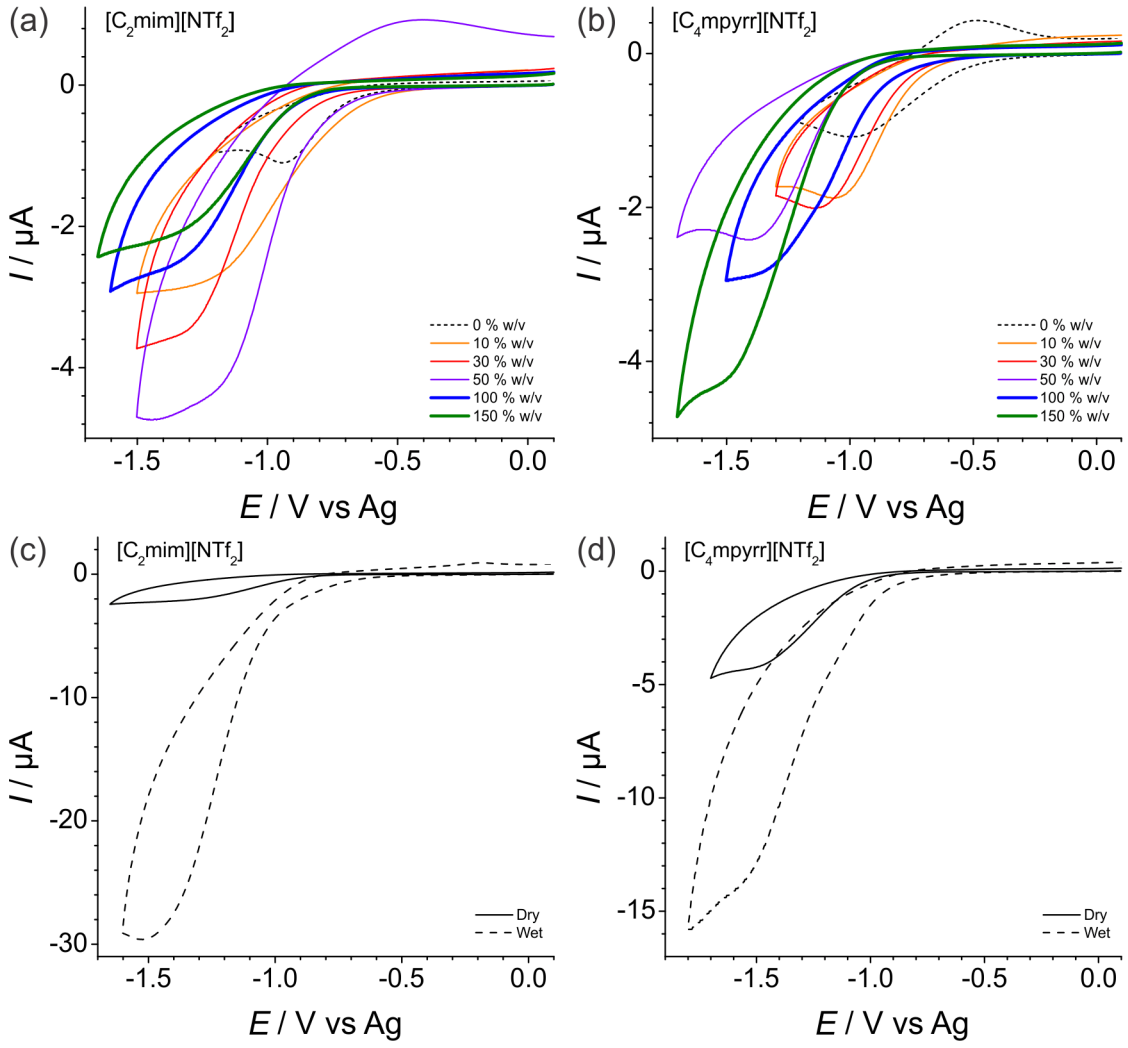

Figure 6.11. Cyclic voltammograms of N_2-purged PMMA doped **(a)** $[C_2mim][NTf_2]$ and **(b)** $[C_4mpyrr][NTf_2]$ at varying % w/v doping levels. Acetone was used as the casting solvent. The N_2-purged CVs in 150 % w/v PMMA doped **(c)** $[C_2mim][NTf_2]$ and **(d)** $[C_4mpyrr][NTf_2]$, (–) allowed to 'dry' overnight (for > 12 hrs) and (--) still 'wet' with acetone, with only ca. 1 hr of N_2-purging after casting.

It was expected that diffusion of impurities within the electrolyte would be retarded with increasing PMMA doping. This is due to an increased fluid-viscosities, and hence lower diffusion coefficients especially of charged or polar species, as the result of the ionic nature of RTILs. This would be expected to lead to a decrease in peak currents associated with the impurity peak in the neat RTILs. However, a significantly larger and irreversible (except for the 50 % w/v PMMA doped [C_2mim][NTf_2]) peak is present from 10 % w/v PMMA doping, with its peak current increasing with PMMA doping for the two subsequent data points at 30 and 50 % w/v. For [C_2mim][NTf_2], the reduction peak current subsequently decreased at 100 and 150 % w/v, while for [C_4mpyrr][NTf_2], an initial drop in peak current occurred at 100 % w/v before showing significant increase at 150 % w/v PMMA doping. The synthesized PMMA was characterized with Raman spectroscopy, Fourier transform infrared-red (FT-IR) spectroscopy, nuclear magnetic resonance (NMR) spectroscopy, and CHN elemental analysis (see Appendix A). No significant levels of impurity in the PMMA were found with those techniques that may explain the behaviour shown in Figure 6.11, for the N_2-purged blank CVs of the two RTILs doped with varying concentrations of PMMA.

One suspected possibility to explain the consistent initial increase in the reduction peak currents found in the blank CVs was the retention of trace levels of acetone, which PMMA has a strong polar affinity with. [261] It is to be noted that the neat RTILs were not exposed to acetone. Figure 6.11 (c) and (d) showed drastically bigger currents in 150 % w/v PMMA doped RTILs that still 'wet' with significant amounts of acetone, compared to that which have been allowed to dry overnight. However, the substantial increases in currents in both of the 'wet' GPEs could simply be due to greater diffusion coefficients of the impurity species due to significant lowering of the electrolyte viscosities. This, as discussed, would not explain the initial increase in reduction peak currents after addition of 10, 30, and 50 % w/v PMMA into the two RTILs, which visibly have increased their fluid viscosities. Alternatively,

acetone may also chemically and/or electrochemically interact with the existing contaminant present in the neat RTIL (for example, via an ECE mechanism, resulting in an overall > 1 electron transfer), and hence the higher currents observed. Higher doping levels resulting in a more viscous media may also inhibit efficient evaporation of acetone, thus leading to the initial increase in the contaminant peak current. This could be further investigated by preparing the PMMA/RTILs using THF (which has a known reduction potential window of < -3 V, vs. SCE) [20] instead of acetone (which is known to reduce in aqueous media, at ca. -1.3 V, on a mercury electrode vs. SCE [262], into isopropanol with the evolution of oxygen, and where on platinum surfaces, hydrogenation of acetone into propane can also occur). [262-265].

Alternatively, perhaps in the presence of PMMA, the tendency of the GPEs to retain moisture from ambient air might be enhanced. Humidification of the nitrogen gas by insertion of wetted cotton in the gas-mixing segment along the gas-mixing line could be carried out to investigate this. Further, comparisons of neat and PMMA doped RTILs, in the presence of dry and humidified N_2 gases, could also verify if the increase in peak currents of the blank CVs at increasing PMMA doping were due to an increased retention of water at higher concentrations of PMMA. Trace amounts of water may be present in the dried N_2 gas from the reticulation line, and perhaps, the gas partitioning coefficient of the polar water molecules into the GPEs were enhanced with respect to N_2 due to presence of PMMA in the RTILs. Further, different concentrations of humidified O_2 (in N_2 carrier gas) could be introduced, at a fixed level of humidification, for different PMMA doping concentrations in the RTILs to verify if an enhancement of the partitioning coefficient of moisture (vs. O_2 and N_2) exists with increasing PMMA doping.

The mechanism of the reduction of acetone on platinum was presented in a paper by Green et al. [263], where acetone is reduced by reacting with either H_2O or H_2. Trace amount of

water are typically present in RTILs even after purging in dry gases or vacuum (see Table 1.5). Further, H_2 could also be electrogenerated from the decomposition of H_2O or H^+. The reduction of residual acetone which may be present may explain the significant increase in the reduction peak currents observed in the blank CVs (see Figure 6.11). However, the reduction of acetone on platinum involves a prior adsorption step, where formation of isopropanol or propane is dependent on the two possible modes of adsorption. [264] The adsorption of acetone was also said to be a slow, irreversible process. [265] This may indicate a significantly surface confined process which is not observed in the CVs presented in Figure 6.11.

As mentioned in Section 6.3.1, the PMMA/RTIL mixture appeared to have fully gellified for the 100 and 150 % w/v PMMA doped samples. The significantly lower diffusion coefficient of species within these solid gellified electrolytes, compared to the electrolytes at lower PMMA doping levels (which remains as liquids that progressively becomes more viscous with increasing PMMA doping), may explain the change in behaviour of the observed reduction peak current. For the 150 % w/v PMMA doped $[C_4mpyrr][NTf_2]$, a morphological change, as suggested in Section 6.3.1.1, leading to a meso-porous scaffold holding RTIL ionic-conductive percolation channels within, may explain an increase in the reduction peak current after the drop at 100 % w/v. Techniques which could be used to look into this possible morphological change in future work were proposed in Section 6.3.1.1. However, most crucially, the reproducibility of these experimental results would first have to be established before these other possibilities that are discussed could be considered. Finally, the reduction peak observed in the blank CVs of the PMMA doped RTILs appeared to diminish with repeated CV cycles at fixed (10 mins) time-intervals, and eventually stabilized. However, partial recovery of this reduction peak current was observed after allowing the system to sit for a period (e.g. 1 hr). Thus, during the monitoring of O_2

concentrations with the CV technique, consecutive CV cycling at a fixed time-interval (e.g. 10 mins) would be necessary to circumvent instability of the background currents.

6.3.2. Cyclic voltammetric O_2 responses of PMMA gelified RTILs on polished platinum screen printed electrode.

Analytical utilities for oxygen sensing of gelified $[C_2mim][NTf_2]$ and $[C_4mpyrr][NTf_2]$, at 150 % w/v PMMA doping, were measured on polished Pt-SPEs by cyclic voltammetry over 3 orders of magnitude in oxygen gas concentrations, from 0.1 up to 100 % vol. O_2, as presented respectively in Figures 6.12 and 6.13 for the two RTILs. The CVs were collected at increasing O_2 concentrations starting from their blank at 0 % vol. O_2 of the N_2-purged samples (indicated by dashed lines in the figures). The voltammograms differ significantly from those collected on the macrodisk Pt-WE setup shown in Figure 6.2 and 6.3. Here, the O_2 current response decreased gradually until the edge of the available electrochemical window. No well defined peaks relating to $O_2/O_2^{\bullet-}$ redox can be observe even after having scanned down to more than -2 V (beyond the potential windows as determined by the blank CVs in Figures 6.12 and 6.13) for both GPEs on the polished platinum screen printed surfaces. This behaviour is comparable to the voltammograms observed from $[P_{14,6,6,6}]^+$-based RTIL on Pt-SPE (presented in Figure 3.2), which was attributed to sluggish electron transfer kinetics (see Sections 3.3.2, and also Figure 4.7 in Section 4.3.4) in those RTILs.

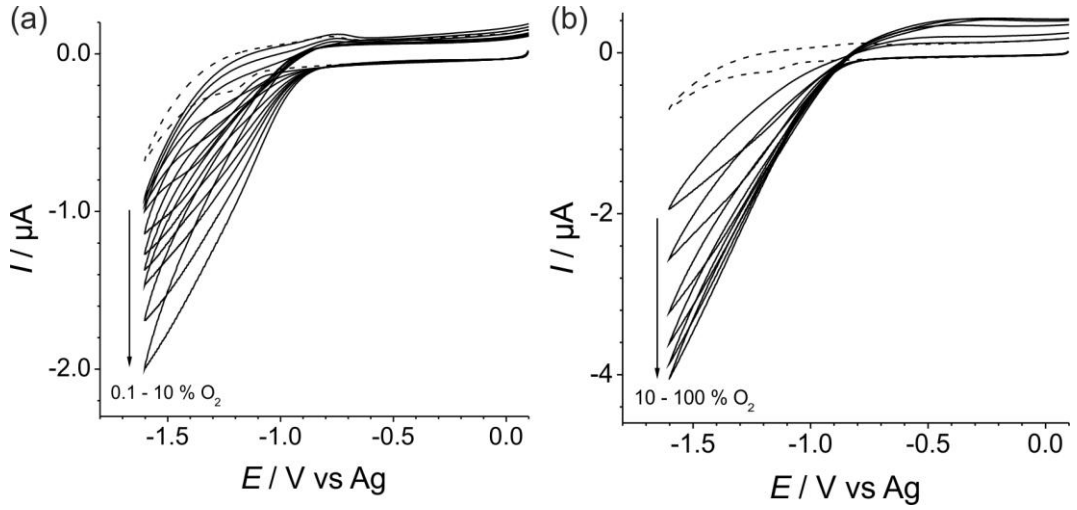

Figure 6.12. Cyclic voltammograms of $O_2/O_2^{\bullet-}$ in 150 % w/v PMMA doped $[C_2mim][NTf_2]$ GPE on polished Pt-SPE vs. screen printed Ag-RE, at cell oxygen concentrations of **(a)** 0.1, 0.5, 1, 2, 3, 4, 5, 7, 10 % vol. and **(b)** 10, 20, 40, 60, 80, 100 % vol., where blank CVs collected for N_2-purged GPEs were represented by dotted lines.

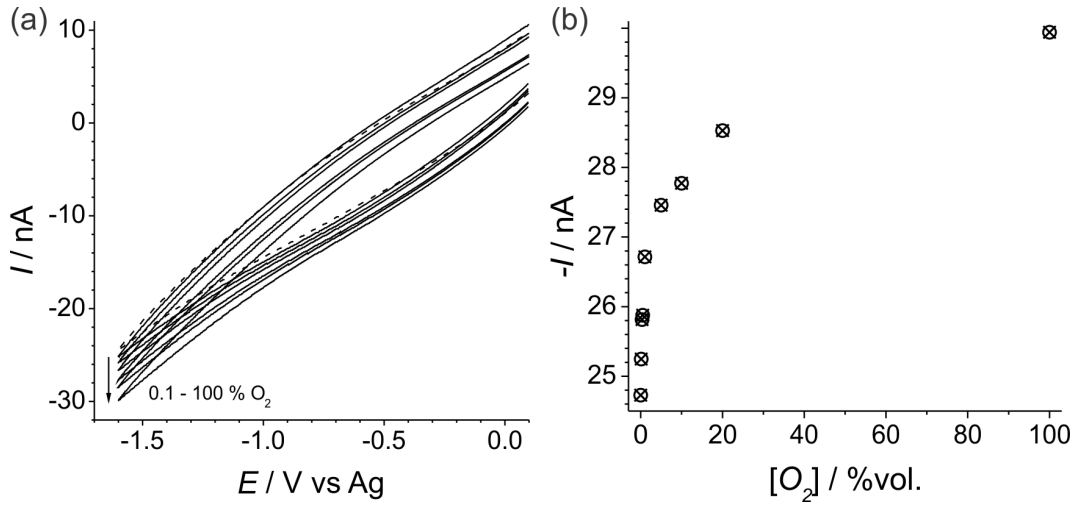

Figure 6.13. (a) Cyclic voltammograms of $O_2/O_2^{\bullet-}$ redox in 150 % w/v PMMA doped $[C_4mpyrr][NTf_2]$ GPE on polished Pt-SPE vs. screen printed Ag-RE, at selected oxygen concentrations of 0.1, 0.5, 1, 10, 20, 100 % vol., where blank CVs collected for N_2-purged GPEs were represented by dotted lines. **(b)** Plot of CV currents measured at -1.6 V from the CVs for the full O_2 concentrations measured at 0.1, 0.3, 0.5, 1, 5, 10, 20, 100 % vol.

It was further noted that sensitivity of the current response on independently prepared samples of polished Pt-SPE, towards the same concentration of O_2, varies considerably (see

Figure 6.17) and this was especially significantly for the more viscous [C_4mpyrr][NTf_2] based GPE). It is also observed that the viscosities of the RTILs was increased as the result of the addition of PMMA, with the PMMA/RTIL becoming a solid material at 100 and 150 % w/v PMMA doping. These observations hinted that the unusual voltammetry on measurements conducted on Pt-SPEs (setup as shown on Figure 2.2), compared to the macrodisk-WE setup (Figure 6.1), was more likely to do with an IR-drop effect rather than an induced sluggish electron transfer kinetics. The cause of this becomes obvious from comparison between the setup of the two experiments (e.g. macrodisk Pt-WE vs. Pt-SPE). For the macrodisk-WE setup, the WE and CE were immersed within a thicker bulk aliquot of GPE within the reservoir. However, for the Pt-SPE setup, the viscous GPE/acetone mixture was drop-casted and spread onto the polished Pt-SPE. A thin film (of micro metre scale thickness) was set up, connecting the printed electrodes after volatilization of the acetone solvent. This thus drastically increased the resistance of the μm thin-layer GPE between the integrated electrodes (e.g. WE and CE). Both the CE and RE are separated from the WE on the Pt-SPEs by a distance of 1 mm. Casting of a substantially thicker film of [C_2mim][NTf_2]-based GPE (of mm thickness) was found to result in CVs which resembles that shown in Figure 6.2, confirming the hypothesis that the CVs observed in Figures 6.12 and 6.13 are due to an IR-drop effect resulting from the use of drop-casted GPEs with μm-thicknesses. One of the primarily aims for utilizing integrated electrodes (i.e. SPEs) in this work was that it allows for improvement of gas-sensing response time by enabling a significant reduction of the electrolyte layer. Utilizing substantially thicker (mm-thick) films of the GPEs would consequently not be a practical solution to the IR-drop characteristic in the CVs. Instead, custom-made screen printed electrodes with WE and CE in an inter-digitated configuration could be explored in further studies.

The actual thicknesses of each of the deposited GPE films were not characterized, since impact of film thicknesses was not the focus of the current preliminary study. However they were expected to vary between samples, depending on the spread of the aliquots drop-casted onto each of the substrates. This would thus result in varying sensitivity of O_2 response as observed in Figure 6.17, and further confirmed the idea that the change in voltammetric response behaviour has more to do with an IR-drop effect (rather than a change in electron transfer kinetics on polished Pt-SPEs). The time from N_2-purged until O_2 saturation of the GPE would also vary with variations in film thicknesses. However, effort were made to keep the spread of the drop-casted GPE relatively consistent between samples, and the oxygen response time was experimentally assessed to be typically less than 20 mins on Pt-SPEs. The response time could potentially be greatly improved with spin-casted GPEs of sub-μm to nm thicknesses, which could be explored in future work. In spite of the lack of a distinct peak current, current response between scans on a single sensing device appeared to be relatively stable, and exhibited sensitivity to different concentrations of O_2. An initial drop in response currents was typically observed, before eventually stabilizing within the initial ~30 consecutive CV scans in the presence of 100 % vol. O_2. This was believed to be due primarily to initial instability of the background currents, which was observed to reduce in magnitude, and eventually stabilised after multiple scans.

Figure 6.12 shows the voltammograms of $O_2/O_2^{\bullet-}$ redox in 150 % w/v PMMA doped $[C_2mim][NTf_2]$, presented separately in two O_2 concentration ranges for clarity. For $[C_2mim][NTf_2]$ based GPE on polished Pt-SPEs, the currents started decreasing gradually from -0.9 V (as shown in Figure 6.12). In contrast to $[C_2mim][NTf_2]$ based GPE, voltammograms of $O_2/O_2^{\bullet-}$ redox in 150 % w/v PMMA doped $[C_4mpyrr][NTf_2]$, in Figure 6.13 (a), shows a highly slanted voltammetric characteristic. The $[C_4mpyrr][NTf_2]$ based GPE also showed very poor (nA) current response to (up to 100 % vol.) oxygen compared to that

of [C_2mim][NTf_2] (μA). Only selected CVs were presented in Figure 6.13 (a) to prevent clutter, due to the poor O_2 response currents vs. background currents. The observed voltammetric behaviour could perhaps be attributed additionally to a high contact resistance due to poor adhesion between the GPE materials with the screen printed surface (also discussed in Section 6.3.1.2). This is also supported by widening of the $O_2/O_2^{\bullet-}$ $\Delta E_{p\text{-}p}$ with increasing PMMA doping, particularly for [C_4mpyrr][NTf_2] (and not [C_2mim][NTf_2]) from macro Pt-WE experiments as shown in Figure 6.8. This could be investigated via the EIS technique in further studies. These non-ideal O_2 CV responses on polished Pt-SPEs were in stark contrast compared to oxygen reduction voltammetries similarly obtained with standard Pt macrodisk working electrode, respectively shown in Figure 6.2 and Figure 6.3.

Despite the non-ideal voltammetries, significant current response (above background) to varying concentrations of O_2 is apparent in the measured voltammetries for both RTIL-based GPEs, with [C_2mim][NTf_2] exhibiting substantially greater sensitivity towards oxygen concentrations compared to [C_4mpyrr][NTf_2]. Since there were no obvious peaks present in the voltammograms, to construct O_2 gas response calibration plots, currents were instead consistently measured at a fixed potential of -1.6 V from the voltammograms. The values were plotted with respect to their % vol. O_2 concentrations, as presented in Figure 6.14 (a) and Figure 6.13 (b). Under 100 % vol. O_2, [C_4mpyrr][NTf_2]-based GPEs were found to be relatively irresponsive to the presence of oxygen on polished Pt-SPE, with only an increase of 5 nA (see Figure 6.13 (b)) above background. Whereas, [C_2mim][NTf_2]-based GPEs produced a response signal of almost 4 μA (see Figure 6.14 (a)) above background.

Calibration data obtained for both RTIL-based GPEs (as plotted in Figure 6.12 (b) and 6.13 (b)) showed non-linear responses to varying concentrations of oxygen gas. The responses could however be reasonably fitted by power functions within suitable O_2 concentration ranges. The data were thus transformed into the linear domain by the model,

$$y = mx^n + c \quad \textbf{(6.1a)}$$

or alternatively by,

$$y^{\frac{1}{n'}} = m'x + c' \quad \textbf{(6.1b)}$$

where y is the measured current responses at -1.6 V, $I_{-1.6V}$, x is the corresponding % vol. O_2 concentrations flowing, [O_2], and m, m', n, n', c and c' are the parameters of the fit model. Linear-transformations of the experimentally measured datasets were accomplished by applying linear regression to the transformed data while varying n (*or n'*), until Chi-square, χ^2 between the linear models and the datasets were minimized. Due to significant shift in sensitivity between higher and lower O_2 concentration ranges, the measured CV currents at -1.6 V were separately fitted (i.e. segmented or piecewise regression) for low (0.1-10 % vol., see Figure 6.14 (b)), and high (10-100 % vol., see Figure 6.14 (c)) O_2 ranges for the [C_2mim][NTf_2]-based GPE sample, using equation (6.1b).

Equation (6.1a) was instead used for the [C_4mpyrr][NTf_2]-based GPE sample due to the required size of n' (at 41.3) if fitted with Equation (6.1b). The linear regression was able to fit the full O_2 concentration range for this GPE (Figure 6.15) after the transformation. In all linearly transformed calibration plots, a significant jump in current response from 0 % vol. O_2 to the lowest O_2 concentration measured (at 0.1 % vol.) were observed. LODs for [C_2mim][NTf_2]-based GPE calibration data (transformed using Equation (6.1b)) at the two concentration ranges were derive as according to equation (D.1) in the appendix, while equation (D.2) was used to estimate the LOD value for the transformed calibration data of [C_4mpyrr][NTf_2]-based GPE. The value of y_0 for the [C_4mpyrr][NTf_2]-based GPE calibration plot, and the corresponding x_0 value derived via the equation from the line of best fit from y_0, were indicate in (x, y) brackets, and marked by the red crossed-circle point in Figure 6.15.

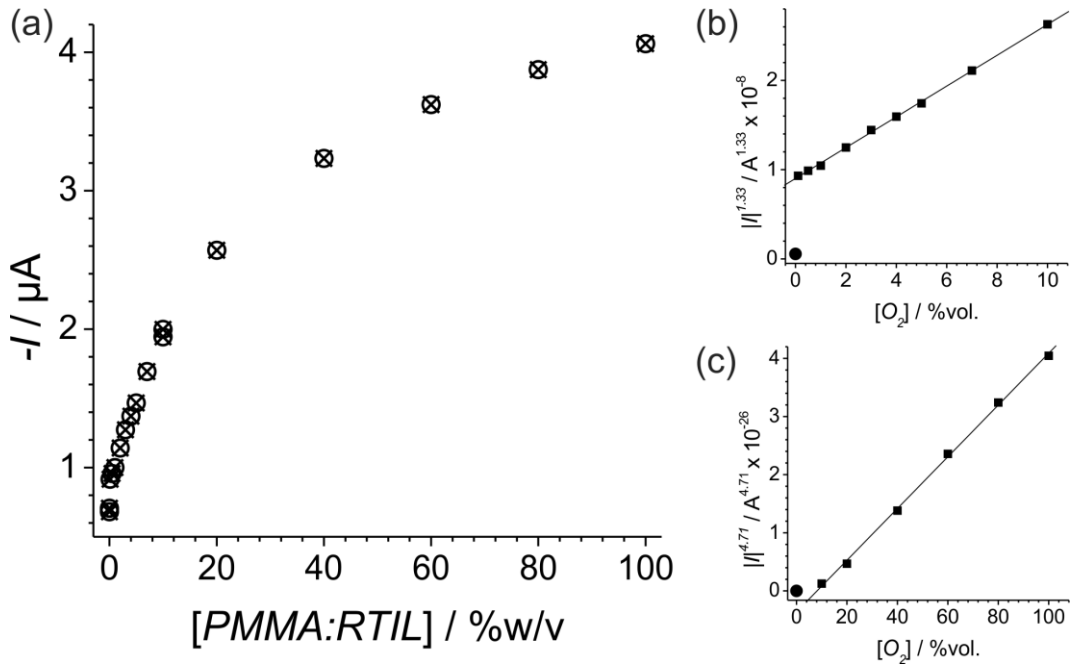

Figure 6.14. (a) O_2 calibration plot (via CV) for 150 % w/v PMMA doped $[C_2mim][NTf_2]$ GPE conducted on polished Pt-SPE (vs. Ag-RE). The CV currents, $I_{-1.6V}$, consistently measured from the CVs presented in Figure 6.12 (a) and (b) at -1.6 V, were plotted over the full O_2 concentration range (from 0.1 to 100 % vol.). The linear transformation of the CV response **(b)** for the lower O_2 concentration range (measure between 0.1-10 % vol., as shown in Figure 6.12 (a)) by raising $I_{-1.6V}$ to the power of 1.33, **(c)** for the higher O_2 concentration range (measure between 10-100 % vol., as shown in Figure 6.12 (b)) by raising $I_{-1.6V}$ to the power of 4.71. The round dot in (b) and (c) indicates the blank current measured at 0 % vol. O_2, which were omitted from the linear regression. Equations from the respective linear regressions, R^2 and estimated LOD values were listed under Table 6.7.

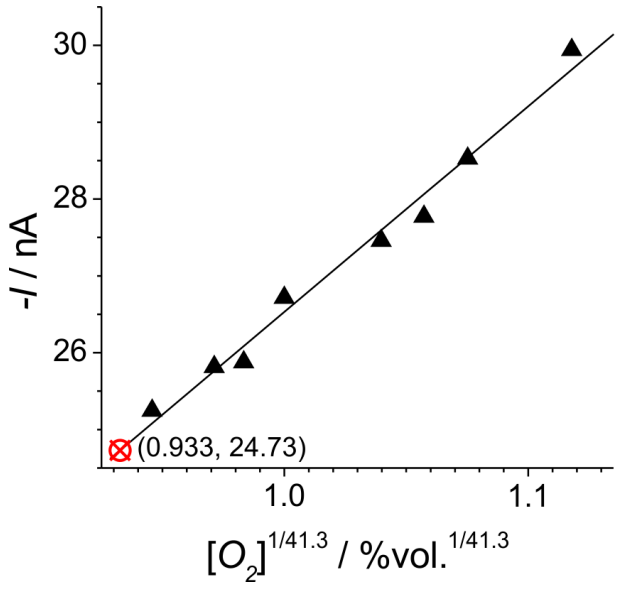

Figure 6.15. O_2 calibration plot (via CV) for 150 % w/v PMMA doped [C_4mpyrr][NTf_2] GPE conducted on polished Pt-SPE (vs. Ag-RE), linearized via power-transform by plotting the CV current response measure at -1.6 V vs. O_2-concentrations raised to the power of 1/41.3. Linear regression (indicated by the straight solid line) was performed on data points between 0.1-100 % vol. O_2. The measured blank CV current response for 0 % vol. is represented by the red crossed-circle point, and positioned on its expected position along the x-axis based on the equation of the regression fit (instead of the origin), where the (x, y) coordinates are as indicated. The equation from the linear regressions, R^2 and estimated LOD value were listed under Table 6.7. below.

It was noted that log-log transformation of a power function gives a linear line, with its slope being equivalent to the power, n, to which x is raised in Equation (Table 6.1a). Thus, common (base-10) linear-log plots in Figure 6.16 (a) and (b), together with base-10 log-log plots in Figure 6.16 (c) and (d), of the calibration data were also performed, showing linear response between: (a) 7-100 % vol. O_2 concentration range for the linear-log plot, (c) 2-60 % vol. O_2 concentration range for the log-log plot of [C_2mim][NTf_2]-based GPE calibration data, and the full (0.1-100 % vol.) concentration range for the [C_4mpyrr][NTf_2]-based GPE calibration data in (b) and (d). The equations of linear regressions, R^2, and estimated LOD values are listed in Table 6.7 below.

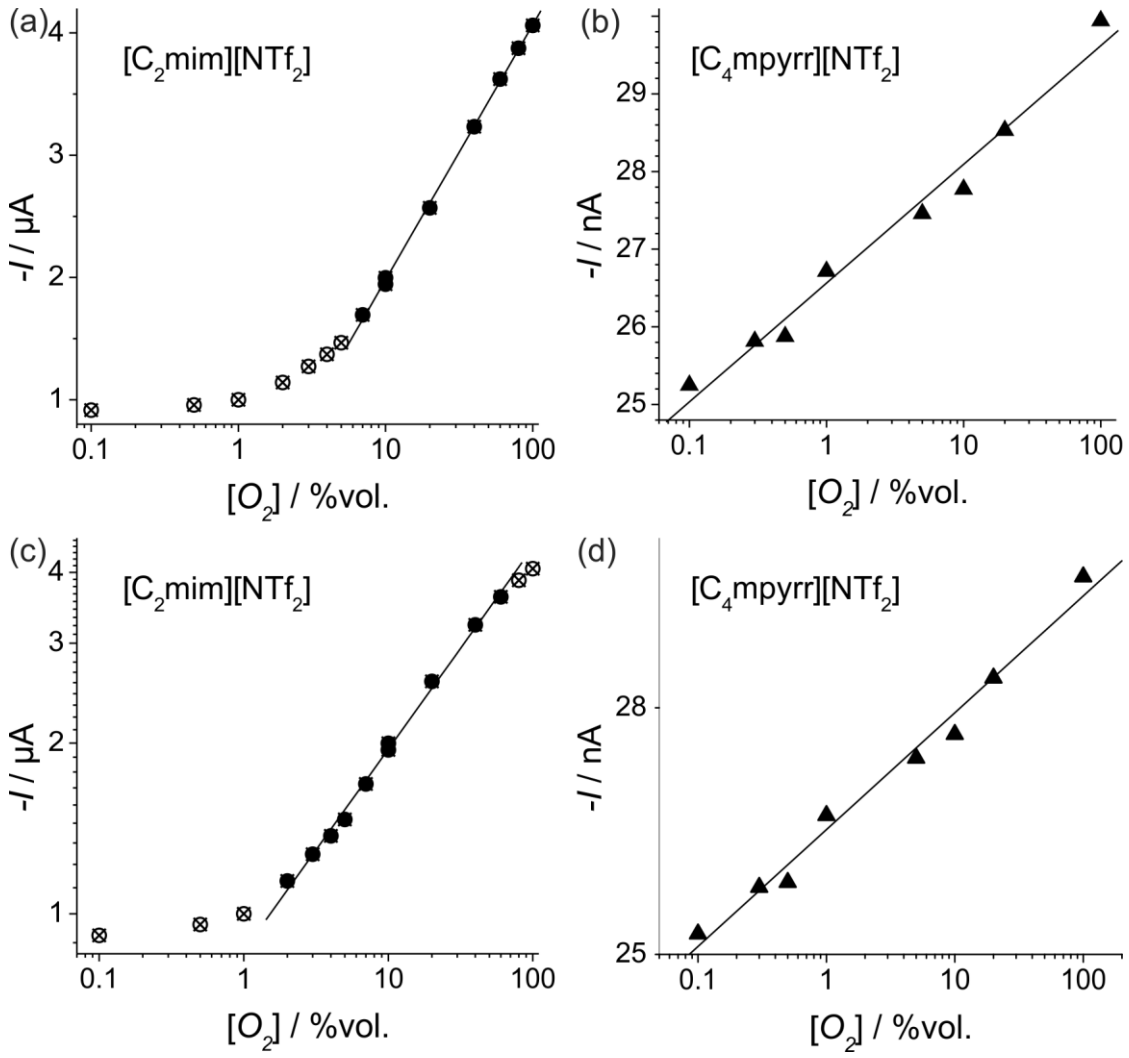

Figure 6.16. O_2 calibration plots (via CV) for 150 % w/v PMMA doped [C_2mim][NTf_2] and [C_4mpyrr][NTf_2] GPEs conducted on polished Pt-SPE (vs. Ag-RE). The CV current responses measured at -1.6 V vs. O2-concentrations were respectively linearized with $\log_{10}$-linear transformations for **(a)** and **(b)**, and log-log transformations for **(c)** and **(d)**. For [C_2mim][NTf_2]-based GPEs, only data points within (a) 7-100 % vol. and (c) 2-60 % vol. O_2 concentration ranges, as indicated by the solid-round dots, were fitted by linear regression, while the full O_2 concentration data range were linearly fitted for [C_4mpyrr][NTf_2]-based GPEs in (b) and (d). Equations from the respective linear regressions, R^2 and estimated LOD values were listed under Table 6.7.

The LOD values of these linearized linear-log and log-log transformed calibration data were estimated using equation (D.2), where $y_0 = \log|I_{0,-1.6V}|$ for the case of log-log plots (F and G). The respective low O_2 concentration divergence of the log-transformed [C_2mim][NTf_2]-based GPE calibration data were accounted for in estimations of their

associated LODs according to appendix D, with $I_{\text{linear-min}}$ values at 0.1, 7, 0.1, 2 and 0.1 % vol. respectively for the regressions, C, D, E, F and G listed in Table 6.7. Despite the non-ideal voltammograms produced by the PMMA doped RTILs measured on polished Pt-SPEs, the close to unity of R^2, coupled with low estimated LOD values from the various linear regressions, down to 0.294 % vol. for the $[C_2mim][NTf_2]$-based and 0.338 % vol. for the $[C_4mpyrr][NTf_2]$-based GPE samples, suggests that these GPEs/Pt-SPE systems may be suitable for the voltametric sensing of oxygen gas. Comparing the different transformations, it appears that log-log plots of the calibration data would be the most suitable for fitting CV O_2 concentration current responses for drop-casted films of PMMA doped $[C_4mpyrr][NTf_2]$ GPEs on polished Pt-SPEs. Whereas for $[C_2mim][NTf_2]$, a log-log transformation could be used if a wide (e.g. 0.1-100 % vol.) O_2 concentration sensitivity is required, while a $|y|^n$ power transformation would be more suitable for the monitoring of lower (ca. 10 % vol. down to ca. 0.3 % vol.) O_2 concentrations.

Table 6.7. Equations for the linear best-fit for the calibration graphs (obtained via CV on polished Pt-SPEs) presented in Figure 6.14, Figure 6.15 and Figure 6.16 for varying % vol. O_2 concentrations in 150 % w/v PMMA doped RTIL GPEs. The two $|y|^n$ power-transformed segmented linear regressions (A and B) from Figure 6.14 (b) (for 0.1-10 % vol. O_2) and (c) (for 10-100 % vol. O_2), were as labelled. Linear regressions of the calibration plot from Figure 6.16 (a), after linear-log transformed, (D) was fitted between 7-100 % vol. O_2, while the log-log transformed plot (F) was fitted between 2-60 % vol. O_2, and the remaining transformed data (C, E, and G) were fitted across the whole (0.1-100 % vol.) O_2 concentration range. The alternative LOD values specified in brackets were derived by setting y_0 in equation (Table 6.2) to the response measured at the lowest oxygen concentration, and before the onset of divergence from linearity.

	RTIL	Fit Type	Equation of calibration graph (where I / A and $[O_2]$ / % vol.)	R^2	LOD / % vol.
A	$[C_2mim][NTf_2]$	$\|y\|^n$	(b) $\|I\|^{1.33} = 1.73\times10^{-9}\,[O_2] + 9.01\times10^{-9}$	0.9989	0.294
B	$[C_2mim][NTf_2]$		(c) $\|I\|^{4.71} = 4.45\times10^{-28}\,[O_2] - 3.63\times10^{-27}$	0.9992	3.82
C	$[C_4mpyrr][NTf_2]$	$x^{\frac{1}{41.3}}$	$-I = 2.67\times10^{-8}\,[O_2]^{\frac{1}{41.3}} - 2.12\times10^{-10}$	0.9840	0.369
D	$[C_2mim][NTf_2]$	linear-log	$-I = 2.14\times10^{-6}\log_{10}[O_2] - 1.96\times10^{-7}$	0.9992	8.01
E	$[C_4mpyrr][NTf_2]$		$-I = 1.53\times10^{-9}\log_{10}[O_2] + 2.66\times10^{-8}$	0.9793	0.417
F	$[C_2mim][NTf_2]$	log-log	$\log_{10}\|I\| = 3.63\times10^{-1}\log_{10}[O_2] - 6.07$	0.9967	2.77
G	$[C_4mpyrr][NTf_2]$		$\log_{10}\|I\| = 2.42\times10^{-2}\log_{10}[O_2] - 7.58$	0.9840	0.338

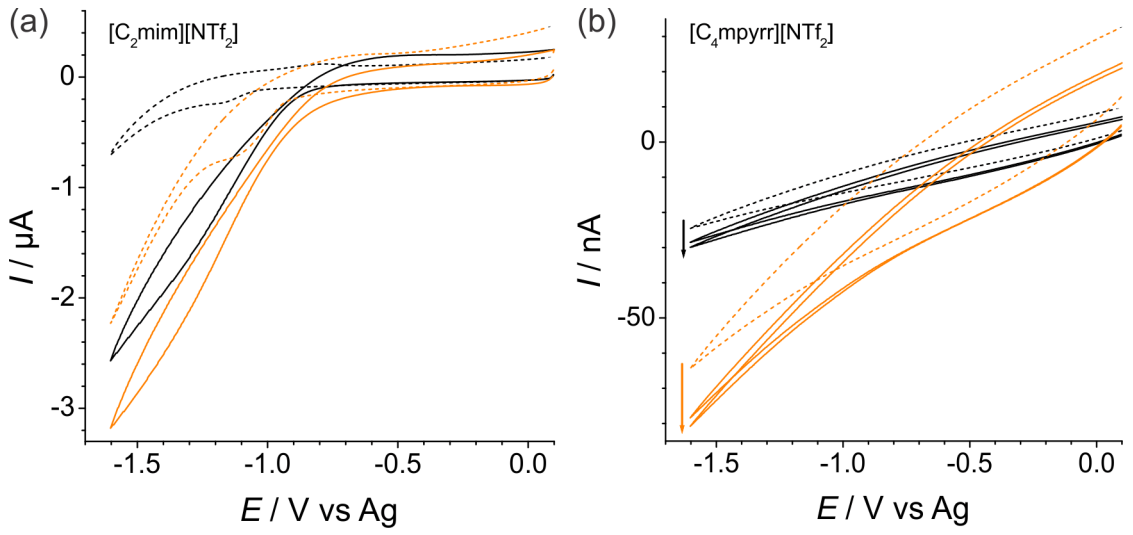

Figure 6.17. Cyclic voltammograms of duplicate samples (distinguished in black and orange) of 150 % w/v PMMA doped **(a)** [C_2mim][NTf_2] at 20 % vol. O_2, and **(b)** [C_4mpyrr][NTf_2] at 20 and 100 % vol. O_2 (with the arrows indicating direction of increasing concentrations) indicated by the solid lines, on polished Pt-SPEs. The short-dashed lines indicate the respective N_2-purged blank CVs.

6.3.3. Amperometric O_2 concentration responses of PMMA gelified RTILs on polished platinum screen printed electrode.

Amperometric O_2 concentration responses were also investigated for PMMA-gelified [C_2mim][NTf_2] and [C_4mpyrr][NTf_2] (at 150 % w/v PMMA doping) on polished Pt-SPEs, to access their analytical utility potentials as amperometric O_2 gas sensors. The measurements were concomitantly carried out for the two RTIL based GPEs, with the two different RTIL-based GPE/Pt-SPE samples inserted into each end of the same glass cell (which is shown in Figure 2.2). The experiments were conducted for over 3 orders of magnitude (from 0.1 up to 100 % vol.) of oxygen gas concentration as presented in Figure 6.18, and was repeated within a lower and narrower concentration range (between 0.1 to 5 % vol.) presented in Figure 6.20. These will be respectively referred to as the *wide* and *low* concentration ranges from here-on.

Significant amperometric responses (above background currents and noise) were obtainable down to 0.1 % vol. O_2 for both GPE/Pt-SPE systems. The overall O_2 current responses for [C_2mim][NTf_2]-based GPE on polished Pt-SPEs showed similar amperometric response behaviour to that obtained from neat [C_2mim][NTf_2] presented in Figure 5.3 (a). However, the amperometric response differs substantially for the case of [C_4mpyrr][NTf_2] between the neat RTIL shown in Figure 5.3 (b), and the PMMA doped RTIL shown in Figure 6.18 (b)). From the amperometry, it is visibly apparent that the response at higher concentrations of O_2 appears to be severely suppressed in the presence of 150 % w/v PMMA, diverging from the linear response observed for the un-doped RTIL that was shown in Figure 5.5 (b). Features of the amperometric responses presented in Figure 5.3 were discussed in greater details under Section 5.3.4.2.

Response times (from the time O_2 was first introduced to the N_2-purged GPE, until the response signal reached a maximum) for 100 % vol. O_2 were found to be less than 15 mins for [C_2mim][NTf_2], and only 3.5 mins for the [C_4mpyrr][NTf_2]-based GPE. What appears to be a fast O_2-saturation response time for the [C_4mpyrr][NTf_2]-based GPE could possibly be, instead, due to a more significant build up of passivating reactant on the WE surface as the result of much slower diffusion rates of any reaction product(s) (involving superoxide interaction with the Pt-SPE's binding material, impurities, and RTIL). Faster accumulation of passivating material on the WE surface would lead to an earlier onset where the signal response starts to diminish after reaching a peak (as discussed under Section 5.3.4.2). The N_2-purging response for both RTIL-based GPEs were also found to be significantly asymmetrical, where about 50 mins was necessary for the [C_2mim][NTf_2]-based GPE, while more than 1 hr 40 mins for the [C_4mpyrr][NTf_2]-based GPE, were necessary to recover a stable N_2-purged blank from an O_2-saturated GPE (at 150 % w/v PMMA doping). This

asymmetry too may be explained by a longer time necessarily for the accumulated passivating products to gradually desorb and diffuse away from the WE surface.

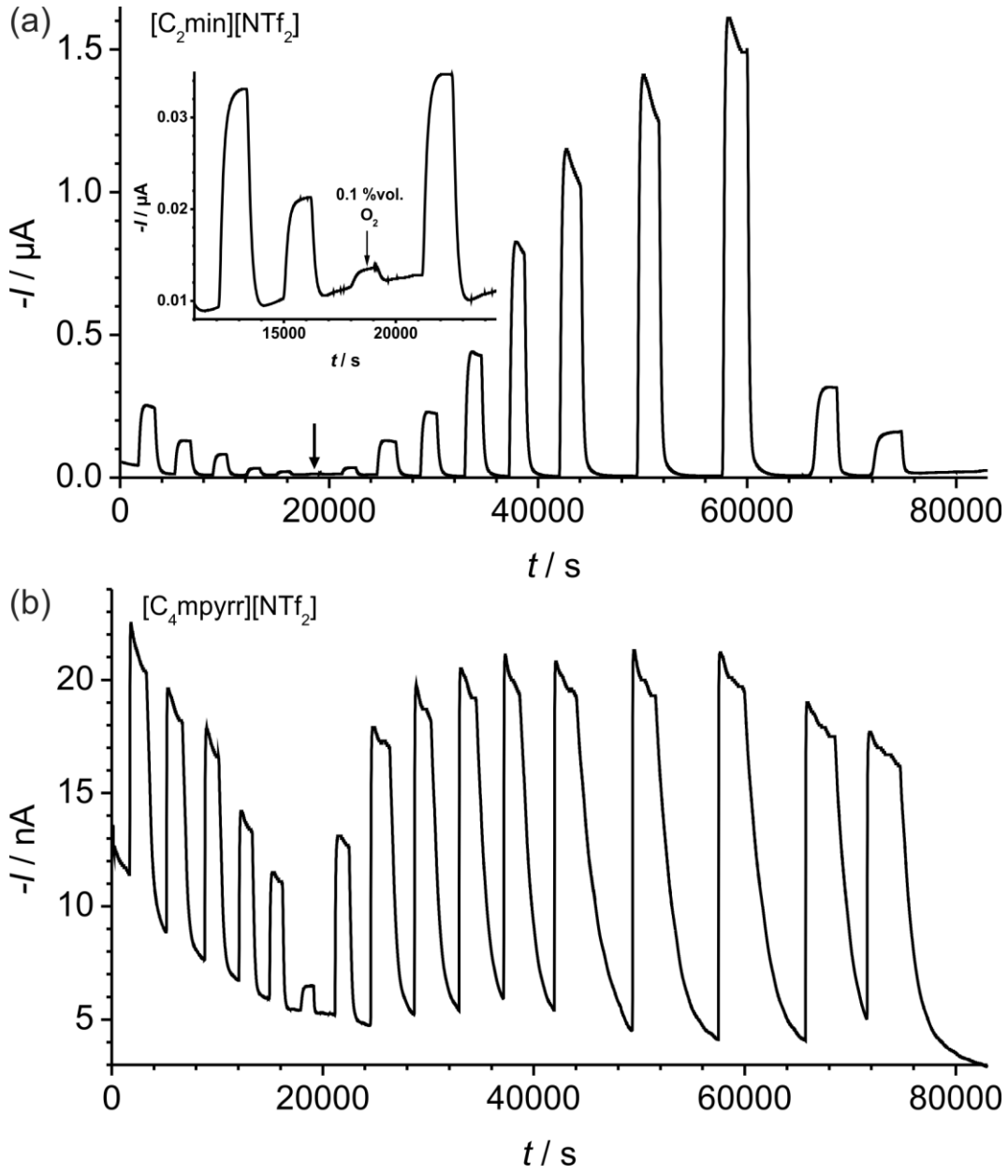

Figure 6.18. Amperometric responses of 150 % w/v PMMA doped **(a)** [C_2mim][NTf_2] and **(b)** [C_4mpyrr][NTf_2] drop casted on polished Pt-SPEs, and measured at a constant bias of -1.6 V vs. screen printed Ag-RE across the *wide* concentration range between 0.1 to 100 % vol. O_2. The gas flow was alternated between 0 % vol. O_2 (i.e. 100 % vol. N_2) and the sequential order of concentrations at: 10, 5, 3, 1, 0.5, 0.1, 1, 5, 10, 20, 40, 60, 80, 100, 20, 10 % vol. O_2. The inset of (a) shows that a significant response above noise was obtainable even at 0.1 % vol. O_2 for the [C_2mim][NTf_2]-based GPE.

Background corrected amperometric response currents in Figure 6.18 (a) and (b) were extracted following the steps described in Section 5.3.4.2 and presented in Figure 6.19 below. Significant variability of the $[C_4mpyrr][NTf_2]$-based GPE calibration data plotted in Figure 6.19, especially towards higher O_2-concentrations, were likely due to incomplete recovery of the blank signals. This is coupled with the fact that currents measured with the $[C_4mpyrr][NTf_2]$-based GPE sample was roughly 2 orders of magnitude smaller than that observed from the $[C_2mim][NTf_2]$-based GPE sample. The calibration plots were regression fitted by appropriate models (indicated under Figure 6.19), and the equations of best fit, R^2 and estimated LOD values are listed in Table 6.8.

Since the corresponding background currents (during N_2-purging) were subtracted from all the O_2 current response data points, the LOD of the linearly fitted linear-log transformed calibration plot was obtained using equation (D.2) setting $y_0 = 0$. For the $[C_2mim][NTf_2]$-based GPE, the response below 20 % vol. O_2 was found to be approximately linear (with $R^2 = 0.9988$, LOD = 0.697 % vol. O_2), but diverged from linearity above 20 % vol. O_2 (as can be seen in Figure 6.19 (a)). A 2nd order polynomial model was found to produce a better fit ($R^2 = 0.9957$) compared to a linear model ($R^2 = 0.9879$) for the full 0.1-100 % vol. O_2 range measured. A significantly further improved 2nd order polynomial fit is obtained (with $R^2 = 0.9999$) by omitting the last two sequence of responses, at 20 and 10 % vol. O_2. This indicates a significant drift (which is also apparent from Figure 6.19 (a)) of the O_2 response after being exposed up to 100 % vol. O_2 concentrations. The LOD derived from the linear regression was 10.6 % vol., while the 2nd order polynomial fit gave an improved LOD value at 4.98 % vol. As with the R^2 values, a further improved LOD is obtained (at 0.660 % vol.) by omission of the last two sequences of O_2 concentration responses (measured at 20 and 10 % vol.).

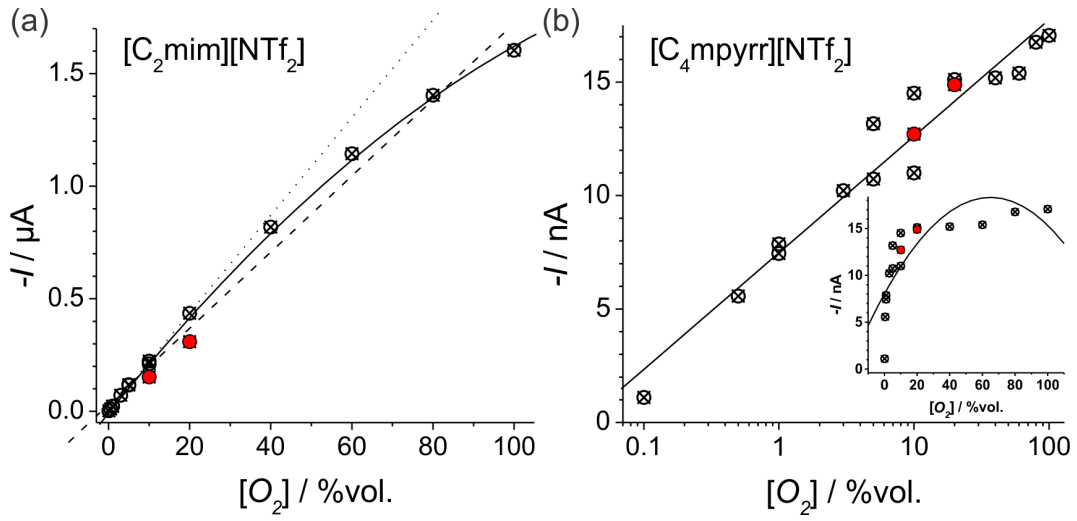

Figure 6.19. O_2 calibration plot via (amperometry) for 150 % w/v PMMA doped **(a)** [C_2mim][NTf_2] and **(b)** [C_4mpyrr][NTf_2] GPEs conducted on polished Pt-SPE (vs. Ag-RE) across the *wide* concentration range between 0.1 to 100 % vol. O_2. The data points in (a) were regression fitted by linear (dashed) and 2nd order polynomial (solid) functions, and an extrapolated linear line (dotted) fitted to only the 0.1-20 % vol. O_2 data points were also included, showing deviation from the approximately linear behaviour between 0 and 20 % vol. O_2. In (b), a linear-log transformation of the data points were performed, and shows strong linear correlation between the amperometric current response, I, and $\log_{10}[O_2]$. The inset demonstrates that a 2nd order polynomial function fails to fit the level-level plot of the [C_4mpyrr][NTf_2] based GPE calibration data. Data points shaded in red marks the corresponding final two sequences of O_2 current responses taken (at 20 and 10 % vol.) after being exposed up to 100 % vol. O_2 concentrations, as shown in Figure 6.18.

A 2nd order polynomial function failed to fit the [C_4mpyrr][NTf_2]-based GPE calibration data (with R^2 = 0.6384), as shown in the inset of Figure 6.19 (b) (which resembles the shape of an adsorption isotherm). The same was the case for log-log transformation (not presented). However, a linear-log transformation of the calibration data points (in Figure 6.19 (b)) demonstrated strong linear correlations between the amperometric current response, I, and $\log_{10}[O_2]$ for this GPE's O_2 response (with R^2 = 0.9446). Omitting the last two sequences of O_2 concentration responses did not improve the goodness of fit. The LOD of the linearly fitted linear-log transformed calibration plot was estimated to be at a low value of 0.151 % vol. O_2.

Table 6.8. Equations for the linear best-fit for the calibration graphs (obtained by amperometry on polished Pt-SPEs) measured across the *wide* concentration range between 0.1 to 100 % vol. O_2) presented in Figure 6.18 and the O_2 concentration response plotted in Figure 6.19, for varying % vol. O_2 concentrations in 150 % w/v PMMA doped RTIL GPEs.

RTIL	Plot	Equation of calibration graph (where I / A and $[O_2]$ / % vol.)	R^2	LOD / % vol.
$[C_2mim][NTf_2]$	Linear	$-I = 1.69\times10^{-8}\,[O_2] + 3.00\times10^{-8}$	0.9879	10.6
	Linear	$-I = 2.17\times10^{-8}\,[O_2] + 3.18\times10^{-9}$ †	0.9988	0.697
	2nd Order Polynomial	$-I = -6.10\times10^{-11}\,[O_2]^2 + 2.24\times10^{-8}\,[O_2] - 8.19\times10^{-9}$	0.9957	4.98
		$-I = -7.37\times10^{-11}\,[O_2]^2 + 2.34\times10^{-8}\,[O_2] - 1.49\times10^{-9}$ ‡	0.9999	0.660
$[C_4mpyrr][NTf_2]$	Linear-log	$-I = 5.14\times10^{-6}\log_{10}[O_2] + 7.47\times10^{-6}$	0.9446	0.151
		$-I = 5.10\times10^{-6}\log_{10}[O_2] + 7.44\times10^{-6}$ ‡	0.9445	0.165
	2nd Order Polynomial	$-I = -2.44\times10^{-9}\,[O_2]^2 + 3.17\times10^{-7}\,[O_2] + 8.03\times10^{-6}$	0.6384	27.3

The equations labelled † were only fitted between 0-20 % vol. O_2, while data labelled ‡ were fitted with the last two data points (after the amperometric monitoring of high levels of O_2 gas) omitted.

From the amperometric response shapes (and times) in Figure 6.18 (and also with neat RTILs as discussed in the previous chapter, Section 5.3.4.2), it has been observed that O_2 amperometric current responses tend to have better stability at lower O_2 concentrations. Furthermore, slow response especially towards decreasing and larger concentration changes, and poor stability at high O_2 concentrations in these PMMA/RTIL GPEs, makes these O_2 sensors more practically suited towards amperometric monitoring of O_2 at *low*er and within narrower concentration ranges. Thus, investigation of the amperometric response of these GPE/Pt-SPE devices were repeated in the narrower and *low*er O_2 concentration range of between 0.1 to 5 % vol. as shown in Figure 6.20. This would also allow for a more precise

assessment of the LOD values of these devices, while making apparent any divergent behaviour which may be present at lower concentrations.

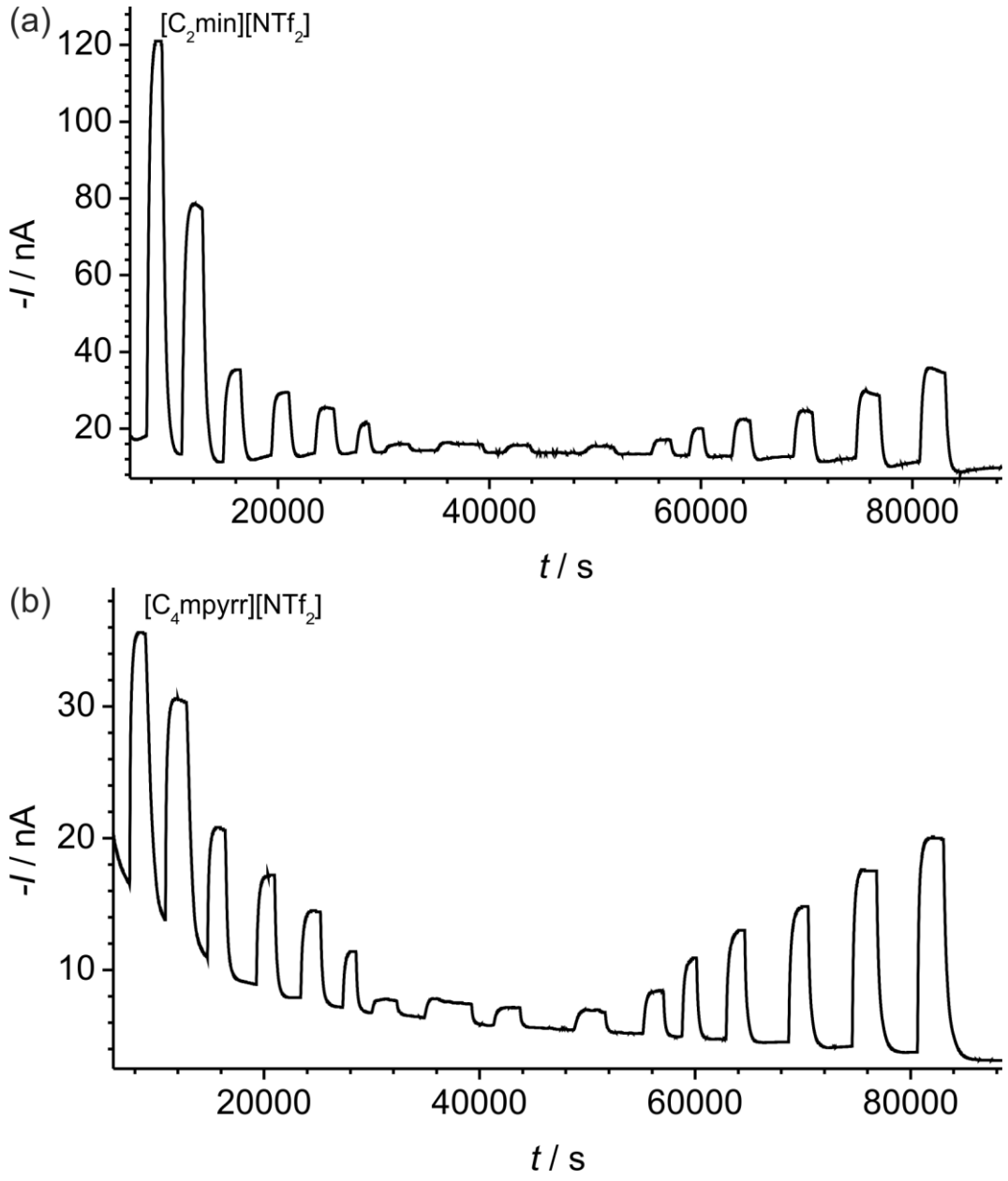

Figure 6.20. Amperometric responses of 150 % w/v PMMA doped **(a)** $[C_2mim][NTf_2]$ and **(b)** $[C_4mpyrr][NTf_2]$ drop casted on polished Pt-SPEs, and measured at a constant bias of -1.6 V vs. screen printed Ag-RE across the *low* concentration range between 0.1 to 5 % vol. O_2. The gas flow was alternated between 0 % vol. O_2 (i.e. 100 % vol. N_2) and the sequential order of concentrations at: 5, 3, 1, 0.7, 0.5, 0.3, 0.1, 0.1, 0.1, 0.1, 0.2, 0.3, 0.4, 0.5, 0.7, 1 % vol. O_2.

From Figure 6.20, it can be observed that the background current for [C_4mpyrr][NTf_2] have not yet completely stabilized, even though it was subjected to the same preliminary biasing duration as the concomitantly ran [C_2mim][NTf_2]-based sample. The observably significant initial change in background signal is also partially due to the much smaller response from the [C_4mpyrr][NTf_2]-based sample compared with [C_2mim][NTf_2]-based sample. Background-corrected amperometric response currents in Figure 6.20 (a) and (b) were extracted following the steps described in Section 5.3.4.2 and presented in Figure 6.21 below. For both RTILs, the amperometric current response shapes were significantly more steady state convergent and stable compared to those exposed to higher O_2 concentrations shown in Figure 6.18. This improvement in response characteristic is especially substantial for the [C_4mpyrr][NTf_2]-based GPE. The response current measured at 5 % vol. O_2 for [C_4mpyrr][NTf_2]-based GPE sample is only about 5.5 times smaller compared to that observed from the [C_2mim][NTf_2]-based GPE sample (in contrast with the 2 orders of magnitude difference at 100 % vol. O_2).

As with Figure 6.18 (b), the initial change in background currents is significant for the [C_4mpyrr][NTf_2]-based GPE sample compared to [C_2mim][NTf_2]-based GPE, where an overnight (i.e. > 12 hrs) condition by biasing (at -1.6 V) under N_2 environment (instead of ~1 hr) would be recommended in future studies for similarly prepared [C_4mpyrr][NTf_2]-based GPE films. The initially falling background current magnitude was the likely cause of the significant difference in O_2 concentration response-time between ascending and descending O_2 concentrations for the [C_4mpyrr][NTf_2]-based GPE sample. As a consequence of the shift in response, the calibration data were separately fitted, divided into **A** (the first 6 data points) and **B** (the last 6 data points). The calibration plots were regression fitted by appropriate models (as indicated under Figure 6.21), and their equations of best fit, R^2 and estimated LOD values obtained are listed in Table 6.9. The 0.1 % vol. O_2 data points

were omitted from the regression analysis of the [C_4mpyrr][NTf_2]-based GPE data, due to obvious and significant divergence in trends from the higher concentration data points.

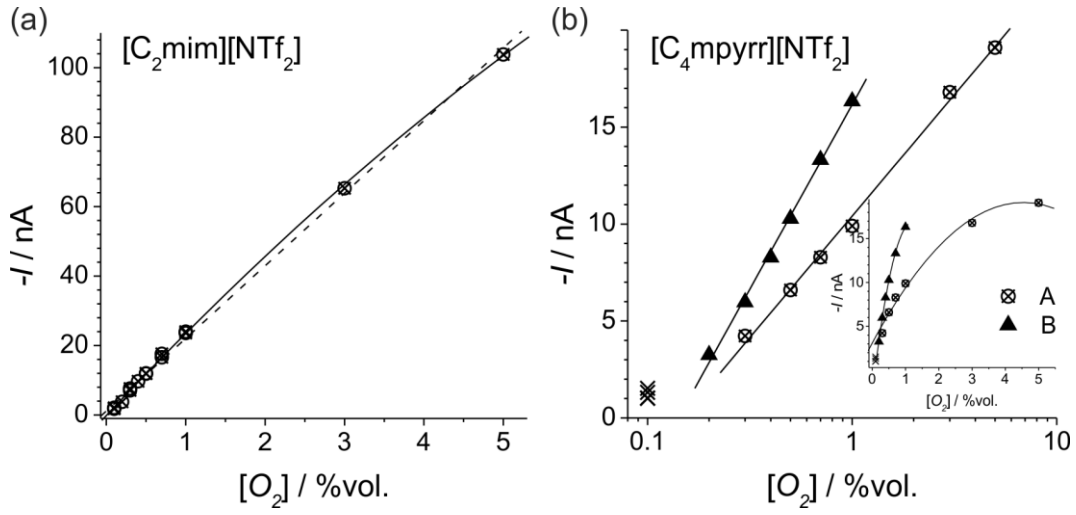

Figure 6.21. O_2 calibration plot via (amperometry) for 150 % w/v PMMA doped **(a)** [C_2mim][NTf_2] and **(b)** [C_4mpyrr][NTf_2] GPEs conducted on polished Pt-SPE (vs. Ag-RE) across the *low* concentration range between 0.1 to 5 % vol. O_2. The data points in (a) were regression fitted by linear (dashed) and 2nd order polynomial (solid) functions. In (b), the calibration data were divided into **A** (the first 6 data points) and **B** (the last 6 data points) to be separately regression fitted due to an obvious and significant shift in O_2 concentration response between ascending and descending O_2 concentrations. The 0.1 % vol. O_2 data points were omitted from the linear regression. The inset in (b) shows the level-level plot for the [C_4mpyrr][NTf_2]-based GPE, similarly separately fitted with 2nd order polynomials, and with the 0.1 % vol. O_2 data points included.

For both RTILs, the best R^2 and LOD values were obtained by fitting the calibration data using 2nd order polynomial functions, with the R^2 values obtained at 0.9996 and 0.9992 from the regression, and LODs estimated to be at 0.071 % vol. and 0.011 % vol. O_2 for [C_2mim][NTf_2]-based and [C_4mpyrr][NTf_2]-based GPEs respectively. In the linear-log transformation, significant divergence was however observed, between 0.2 and 0.1 % vol. O_2 for the [C_4mpyrr][NTf_2]-based GPE. Linear regression of the linear-log transformed calibration data, while accounting for this lower-limit divergence, gave the LOD of 0.234 % vol. O_2 for the [C_4mpyrr][NTf_2]-based GPE.

Table 6.9. Equations for the linear best-fit for the calibration graphs (obtained by amperometry on polished Pt-SPEs) measured across the *low* concentration range between 0.1 to 100 % vol. O_2) presented in Figure 6.20 and the O_2 concentration plotted in Figure 6.21, for varying % vol. O_2 concentrations in 150 % w/v PMMA doped RTIL GPEs.

RTIL	Plot	Equation of calibration graph (where I / A and $[O_2]$ / % vol.)	R^2	LOD / % vol.
$[C_2mim][NTf_2]$	Linear	$-I = 2.09\times10^{-5}\,[O_2] + 1.12\times10^{-6}$	0.9977	0.193
	2nd Order Polynomial	$-I = -7.30\times10^{-7}\,[O_2]^2 + 2.44\times10^{-5}\,[O_2] - 1.85\times10^{-7}$	0.9996	0.071
$[C_4mpyrr][NTf_2]$	2nd Order Polynomial	(A) $-I = -7.77\times10^{-10}\,[O_2]^2 + 7.05\times10^{-9}\,[O_2] + 3.12\times10^{-9}$	0.9795	0.328
		(B) $-I = -1.35\times10^{-8}\,[O_2]^2 + 3.24\times10^{-8}\,[O_2] - 2.60\times10^{-9}$	0.9992	0.011
	linear-log	(A) $-I = 1.25\times10^{-8}\log_{10}[O_2] + 1.04\times10^{-8}$	0.9965	0.398
		(B) $-I = 1.90\times10^{-8}\log_{10}[O_2] + 1.62\times10^{-8}$	0.9968	0.234

6.4. Conclusion

In an attempt to improve the robustness of SPE/RTIL systems for portable amperometric oxygen sensing applications, two gellified RTILs were characterized for their long-term electrochemical stability. Two polymers (PVC and PMMA) were preliminarily explored as potential polymers for the gelification of eight different RTILs. However with PVC, all the RTILs with the exception of two phosphonium-based RTILs (namely $[P_{14,6,6,6}][NTf_2]$ and $[P_{14,6,6,6}][FAP]$) visibly leached out of the composite material over time. Gradual leaching of the RTIL in the GPE may cause instability in the sensing response. This present work focused on the use of PMMA to gellify the two selected RTILs ($[C_2mim][NTf_2]$ and $[C_4mpyrr][NTf_2]$). Cyclic voltammetric studies of the $O_2/O_2^{\bullet-}$ redox couple in $[C_2mim][NTf_2]$ and $[C_4mpyrr][NTf_2]$ doped with varying concentrations of the PMMA polymer was conducted on a standard platinum macrodisk working electrode. O_2 reduction peak current linearly decreased with increasing PMMA concentrations in both RTILs. Both reduction of O_2 during the forward scan and oxidation of the electrogenerated superoxide in the reverse scan were found to be diffusion controlled, with scan rates of up to 5 $V \cdot s^{-1}$. For $[C_2mim][NTf_2]$, addition of PMMA from the lowest investigated concentration of 10 % w/v, resulted in a significant jump in ΔE_{p-p} of the $O_2/O_2^{\bullet-}$ redox couple, but remained constant with further addition of PMMA. For $[C_4mpyrr][NTf_2]$ however, the ΔE_{p-p} appears to be linearly dependant on PMMA concentrations. Voltammetric and amperometric responses to varying O_2 concentrations for the two RTILs, doped with 150 % w/v PMMA, were investigated on polished Pt-SPE surfaces. Due to significant resistance of the GPEs when deposited as a thin film onto the Pt-SPE, substantial IR-drop effect was present in the CVs. Although non-ideal cyclic voltammograms were observed in both RTIL-based GPEs, reasonable LOD values for O_2 gas were obtained from both CV and amperometry techniques. These thus have demonstrated the potential analytical utility for O_2 sensing with these new PMMA/RTIL

based GPE/Pt-SPE gas-sensing devices. Better stability and response characteristics at lower O_2 concentrations suggested that these PMMA/RTIL-based GPEs studied may be more suited for monitoring of lower (< 5 % vol.) range of O_2 gas concentrations. $[C_2mim][NTf_2]$-based GPEs gave better sensor response and overall performance compared to $[C_4mpyrr][NTf_2]$-based GPEs at similar PMMA doping level on polished Pt-SPEs. For improved and a more practical response rate for O_2 sensing applications, a much thinner (nm) GPE films thicknesses may be necessary, where spin casting could be a viable method to achieve this in further studies.

7. Overall Conclusions of this Thesis

7.1. General summary of findings

The body of work presented in this thesis aimed to look into the feasibility of utilizing low-cost and commercially available SPEs, used together with non-volatile RTIL electrolytes, for amperometric gas-sensing. O_2 was selected as the model gas to assess the analytical utility and overall performance of these RTIL/SPE sensing systems. The cathodic current resulting from the electroreduction of O_2 was utilised as the sensing response for different concentrations of oxygen gas. CV and amperometry techniques were employed for these investigations. For the present fundamental studies of these systems, experiments were conducted with an inert background atmosphere of N_2 gas.

The general conclusion reached was that RTIL/SPE systems provide promising platform for the amperometric sensing of O_2 and other electrochemically active gases. However, the binding material of these screen printed electrodes was found to interact with the electrogenerated superoxide during cathodic reduction of O_2 gas. This was especially significant within appreciably protic environments such as in the presence of mildly protic imidazolium-cation based RTILs. However, trace amounts of protic contaminants present (such as water) may also interfere during amperometric oxygen sensing with the more aprotic RTILs. Interactions between superoxide and the binding material in the presence of protic species resulted in irreversible and non-typical cyclic voltammetric behaviours, where a cross-over (or narrowing) behaviour of the currents during forward and reverse scans were observed in the voltammograms measured on Pt-, Au-, and Ag-SPEs. In contrast, this cross-over characteristic was not observed in the significantly more aprotic pyrrolidinium-cation based RTIL tested (i.e. $[C_4mpyrr][NTf_2]$, and the reaction was reversible. Substantial

background charging currents were observed in RTILs on C-SPEs, with the appearances of additional voltammetric waves during scans. Further, the screen printed carbon material tends to disintegrate and leech into the electrolyte over time, and this suggests that RTILs may not be a suitable electrolyte to be used on C-SPEs. However, despite of atypical voltammetric behaviours compared to ideal surfaces (of solid micro- or macro- electrodes) on the four SPEs studied, plots of peak current vs. % vol. concentration O_2 were obtainable, providing reasonable limits of detection. The results suggested that fresh-out-of-the-box SPEs with RTILs may indeed be viable sensing systems for oxygen, but are limited to short-term monitor and 'single-use'.

Subsequently, in an attempt to improve their performance and extend reusability of these devices, generally regarded as for 'single-use', five surface pre-treatment protocols (namely, sonication in THF, mechanical polishing, UV-ozone cleaning, soaking in DMF, soaking followed by anodizing in aqueous NaOH solution), were investigated. Pt-SPEs were picked, out of the four SPEs available, in this study since they were found to give the best overall shape in CVs collected within the more protic $[C_4mpyrr][NTf_2]$ RTIL. Treated and untreated Pt-SPEs were characterized for their effective active surface areas in aqueous solutions of H_2SO_4, hexaammineruthenium(III) chloride, and potassium hexacyanoferrate(III), using CV and CA techniques. The shapes of their voltammograms obtained from these experiments were also compared. Of all the pre-treatment protocols that were tested, mechanical polishing was found to be the most promising. Results showed not only that Pt-SPEs could withstand significant mechanical polishing without structurally disintegrating, the electrochemical active surface areas (normalized with respect to their topographical surface areas) of polished Pt-SPEs significantly increased after it was polished. It was proposed that polishing results in effective removal of the residual binding material residing on the surfaces of fresh-out-of-the-box Pt-SPEs, and exposing a fresh surface of active material (i.e. the platinum particles)

underneath. Mechanical polishing as a pre-treatment protocol can potentially also be extended to Ag-SPEs (i.e. the RE material on Pt-SPE), and Au-SPEs before the conduct of electrochemical experiments. The common electrochemical activation of platinum electrodes in H_2SO_4(aq) solution was found to be ineffective for the removal of contaminants, substantially passivating the screen printed surfaces, preventing the adsorption of hydrogen. Furthermore, tests conducted on Pt-, Au-, Ag-, and C-SPEs suggest that the screen printed materials are highly susceptible to degradation by exposure to strong acidic or caustic solutions. This could potentially lead to instability in the long-term due to continual etching of the binding materials. A more dilute solution was recommended if acidic/alkaline conditions are necessary in experiments utilising SPEs.

The long-term performances of unpolished and mechanically polished Pt-SPEs, used in conjunction with two selected RTILs, namely $[C_2mim][NTf_2]$ (where the $O_2/O_2^{\bullet-}$ redox cross-over voltammetric characteristic is present) and $[C_4mpyrr][NTf_2]$ (found to be comparatively more stable during short-term O_2 monitoring), were compared. The experiments were carried out by running consecutive CVs for more than 120 cycles (in the presence of 100 % vol. O_2). This would allow the effectiveness, which polishing has on improving the O_2 sensing performance of Pt-SPEs with RTILs, to be assessed. Polishing of the Pt-SPE showed substantial improvements in the voltammetry shapes and stability of the CVs over prolonged repeated scanning in the presence of O_2. Most notably, on polished Pt-SPEs, the cross-over characteristic present in O_2 saturated $[C_2mim][NTf_2]$ quickly disappeared after an initial ca. 15 scans, and eventually evolved after ca. 80 cycles into voltammograms which resembled that collected on a typical platinum macrodisk electrode. On unpolished Pt-SPE surfaces, the cross-over characteristic was (again) present during the initial scans, with additional peaks (associated with an accumulation of reaction by-products) developing gradually during consecutive scanning. Due to the high aproticity of the $[C_4mpyrr][NTf_2]$ RTIL, O_2 redox

voltammetry was substantially more stable over repeated scanning even without polishing. However, a pre-peak gradually developed on the unpolished Pt-SPEs, but were absent on polished Pt-SPEs. In contrast, subjecting Pt-SPEs to the standard electrochemical pre-treatment protocols in aqueous solutions resulted in unusual voltammetric behaviour for O_2 sensing in the two RTILs. Analytical utilities for unpolished and polished Pt-SPEs were compared from the voltammetries of different O_2 concentration collected. Calibration plots from O_2 reduction CVs peak currents on Pt-SPEs showed significantly improved sensitivities and limits of detection in both RTILs after polishing. O_2 responses on unpolished Pt-SPEs in both RTILs rapidly degenerated during amperometric monitoring of O_2, while remarkable improvements in current response were achieved on polished Pt-SPEs. Recovery of a fouled Pt-SPE surface by polishing has also been demonstrated, and could be repeated multiple times, depending on the aggressiveness and duration of each re-polishing.

Finally, in an attempt to improve the robustness of these SPE/RTIL systems for portable amperometric oxygen sensing applications, gellification of the two RTIL electrolytes with a polymer additive was characterized for their long-term electrochemical stability. PVC and PMMA were explored as potential host polymers for the gelification of RTILs. However with PVC, all the RTILs with the exception of the two (with the most hydrophobic cationic group) phosphonium-based RTILs (namely $[P_{14,6,6,6}][NTf_2]$ and $[P_{14,6,6,6}][FAP]$) eventually visibly leached out of the composite material. Cyclic voltammetric studies of the $O_2/O_2^{\bullet-}$ redox couple in $[C_2mim][NTf_2]$ and $[C_4mpyrr][NTf_2]$ doped with varying concentrations of the PMMA polymer was conducted on a standard platinum macrodisk working electrode. O_2 reduction peak current linearly decreases with increasing PMMA doping concentrations in both RTILs. Voltammetric and amperometric responses to varying O_2 concentrations for the two RTILs, doped with 150 % w/v PMMA, were investigated on polished Pt-SPE surfaces. Due to significant resistance of the GPEs when deposited as a thin film onto the Pt-SPE,

substantial IR-drop effect was present in the CVs. Although non-ideal cyclic voltammograms were observed in both RTIL-based GPEs, reasonable LOD values for O_2 gas were obtained from both CV and amperometry techniques. These thus have demonstrated the potential analytical utility for O_2 sensing with these new PMMA/RTIL based GPE/Pt-SPE gas-sensing devices. Better stability and response characteristics at lower O_2 concentrations suggested that the PMMA/RTIL-based GPEs studied may be more suited for the monitoring of lower (< 5 % vol.) range of O_2 gas concentrations. $[C_2mim][NTf_2]$-based GPEs gave better sensor response and overall performance compared to $[C_4mpyrr][NTf_2]$-based GPEs at similar PMMA doping level on polished Pt-SPEs.

7.2. Suggestions for future work

- It was suggested in Section 6.3.1.2 that a stronger interaction between $[C_4mpyrr][NTf_2]$ and PMMA, compared to $[C_2min][NTf_2]$, may exist. These could be further studied by EIS and NMR techniques.

- For the PMMA/RTIL studies in Chapter 6, repeats of existing measurements and measurements of intermediate data points, with the Pt macrodisk electrode setup (shown in Figure 6.1), are needed to verify the preliminary observations.

- To investigate the possibility of trace water as the cause of the reduction currents observed in the blank CVs of the neat RTILs, the N_2-gas that was used to purge the cell of oxygen and other gases could be humidified by insertion of a segment of glass-cell packed with wet-cotton along the gas-mixing line. CVs of the electrolyte spiked with addition of moisture could then be collected and be compared. Spiking of the two neat RTILs with salts containing halides (known by-products from the synthesis of the RTILs [89]), such as $[C_2mim][Cl]$ and $[C_4mpyrr][Cl]$, as their anions (in place of $[NTf_2]^-$) could also be investigated.

- The PMMA/RTIL mixtures could be prepared with THF instead of acetone as the mixing and casting solvent to investigate if acetone was the cause of the significant reduction peaks observed in the blank CVs collected in PMMA/RTIL GPEs.

- X-ray photoelectron spectroscopy (XPS) and near edge X-ray absorption fine structure (NEXAFS) spectroscopy could be conducted on SPEs to help identify surface compositions of the material. Contrasting the differences between XPS and NEXAFS spectrums collected from fresh-out-of-the-box and polished Pt-SPEs could further assist with the identification of impurities that may affect the

electrochemistry of oxygen reduction on its surface. Furthermore, SPE surfaces that were fouled after O_2 sensing experiments in RTILs could also be characterized with these surface-sensitive techniques to identify the adsorbed species. The results could be compared with chemical analysis of NMR spectrums of products generated during cathodic bulk electrolysis of O_2 in RTILs.

- Cross-sensitivity studies of O_2 reduction in the presence of other gases present in air (such as H_2 and CO_2), could also be conducted. Viability of the PMMA/RTIL GPEs for the sensing of other electrochemically active gases could also be pursued in future work.

- Doping of PMMA/RTIL GPEs with gas receptor molecules (such as calixarenes and porphyrins) known to selectively interact with certain gaseous or vapour species could be investigated to improve gas selectivity to the GPE/SPE sensors. The host-guest chemistries of various gases with these supra-molecules could be further investigated.

Appendices

A. Characterization of O_2 reduction potential shift in $[C_2mim][NTf_2]$ on untreated Pt-SPE by ferrocene as the internal reference.

In order to determine if the potential shift observed from the 1st and 2nd scans for O_2 reduction on SPEs (see Figure 3.2 and Figure 5.1) were merely due to a reference electrode potential shift, or due to changes in the working electrode surface, an internal redox couple potential reference was added to the system, and consecutive CVs were performed.

Figure A.1 shows the plots of various analysed quantities from consecutively ran CVs in O_2 saturated $[C_2mim][NTf_2]$ on unpolished Pt-SPE (i.e. where the most significant shift in O_2 reduction peak potentials were observed in the initial scans, i.e. see Figure 5.1), with ferrocene, dissolved in acetonitrile to make up a 0.1 M solution, before adding the appropriate aliquots with a micropipette to the (50 μL) neat $[C_2mim][NTf_2]$ electrolyte. The acetonitrile was allowed at least 1 hour to volatilise under dry N_2-flow (1000 sccm) before experiments were commenced.

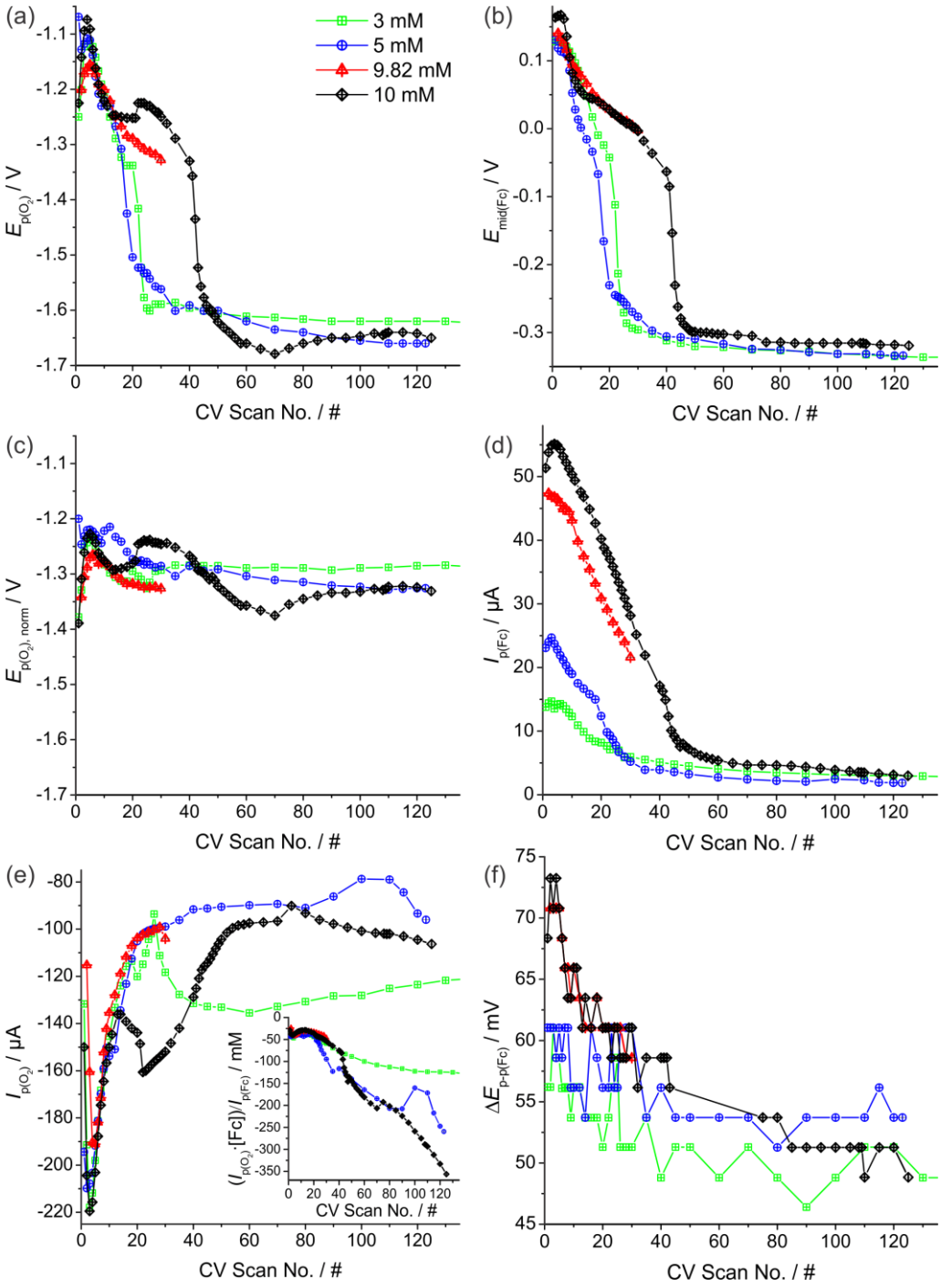

Figure A.1. Monitoring of the change in repeated CV cycles in $[C_2mim][NTf_2]$ on unpolished Pt-SPE of **(a)** O_2 reduction peak potentials, $E_{p(O_2)}$, **(b)** the mid-point potentials of the ferrocene/ferrocenium redox couple, $E_{mid(Fc)}$, **(c)** O_2 reduction peak potentials normalized by shifting the mid-point ferrocene/ferrocenium redox couple potential to zero (i.e. $E_{p(O_2)} - E_{mid(Fc)}$), **(d)** ferrocene oxidation peak currents, $I_{p(Fc)}$, **(e)** O_2 reduction peak currents, $I_{p(O_2)}$, and **(f)** peak-to-peak potential separation of the ferrocene/ferrocenium redox couple, $\Delta E_{p\text{-}p(Fc)}$. The inset of (e) shows the oxygen reduction currents, normalized by dividing it by $(I_{p(Fc)}/[Fc])$, where [Fc] is the concentrations of ferrocene (in mM) added. The CVs were conducted under 100 % vol. O_2 flow, at a scan rate of 0.1 $V \cdot s^{-1}$, and with a recovery time interval of 8 minutes between each CV cycle. Different colours of the plot indicate different ferrocene concentrations added to the $[C_2mim][NTf_2]$ electrolyte.

Figure A.1 (a) shows the oxygen reduction peak potentials, $E_{p(O_2)}$, and how they vary with repeat CV scanning. The reduction peak potential was measured (instead of the half wave potentials) since the reverse (superoxide oxidation) peak was not present on unpolished SPEs. The mid-point potential, $E_{mid(Fc)}$, (Figure A.1 (b)) of the ferrocene internal reference was determined from averaging the ferrocene oxidation and ferrocenium (Fc^+) reduction peak potentials. The large potential jump in $E_{p(O_2)}$ could be accounted for by the concomitant jump in $E_{mid(Fc)}$ (with a total of ca. 0.5 V from the first to the last CV cycle). This result demonstrates that the shift in $E_{p(O_2)}$ was due mainly to the unstable Ag pseudo-reference electrode on the Pt-SPE, and could be attributed to the counter electrode reaction product (e.g. from $[NTf_2]^-$ oxidation discussed in Section 5.4) diffusing to the Ag-RE. Figure A.1 (c) shows the normalized O_2 peak potentials, $E_{p(O_2),norm}$, by setting $E_{mid(Fc)}$ to 0 V (e.g. $E_{p(O_2),norm} = E_{p(O_2)} - E_{mid(Fc)}$), which ranged approximately between -1.22 V to -1.38 V (i.e. $E_{p(O_2),norm}$ varies within 0.16 V throughout the consecutive CV cycles). Although there is still some variability in the peak potentials, it is clear that the majority of the potential shift can be attributed to the unstable Ag quasi-reference electrode.

The oxidation peak currents of Fc, $I_{p(Fc)}$, decrease on subsequent scans as shown in Figure A.1 (d), and this was assumed to be the result of the dissolved Fc gradually volatilizing from the electrolyte. [266] Linearly fitting $I_{p(Fc)}$ of the first CV cycles at varying concentrations of Fc, [Fc], (where $[Fc] = 1.94 \cdot I_{p(Fc)} + 0.325$, $R^2 = 0.9995$) the concentration of Fc remaining in the electrolyte converges to a value equivalent to < 0.9 mM by the 120th cycle and appears to be stable past the 180th CV cycle (i.e. > 24 hours since the Fc was introduced into the electrolyte).

10 mM of Fc was initially selected to ensure that the Fc/Fc^+ redox couple peaks are visible (with respect to the O_2 reduction peak). However, it was observed that the presence of Fc appears to have a short-term stabilizing effect on $E_{mid(Fc)}$ (i.e. the potential on the

quasi-reference electrode), compared to the neat $[C_2mim][NTf_2]$, as presented in Figure 5.1. The experiment was thus repeated with lower concentrations (5 mM and 3 mM) of Fc, and an earlier onset of a shift in on $E_{mid(Fc)}$ was observed (while on $E_{mid(Fc)}$ shifts in neat $[C_2mim][NTf_2]$ typically occurs on the second or third scan in the presence of 100 % vol. O_2 flow). This may be due primarily to the presence of Fc (which could reversibly oxidize as the counter electrode reaction), thus suppressing the irreversible oxidation of the $[NTf_2]^-$ anion during each scan. Furthermore, Fc could also act as a free-radical scavenger [267, 268], due to the electronic resonance in the two cyclopentadienyl groups, and may partially quench the electrogenerated superoxide radical from reacting with the binding material in the presence of the mildly protic $[C_2mim]^+$ cation. The comparison of the voltammetries obtained with and without the presence of Fc (as shown in Figure A.2) further supports this. The CV in the neat $[C_2mim][NTf_2]$ has considerably degenerated after the 120th scan, compared to the CV in $[C_2mim][NTf_2]$ with 10 mM Fc added to it, which shows substantially improved voltammetry on the 120th cycle, and even the 300th scan.

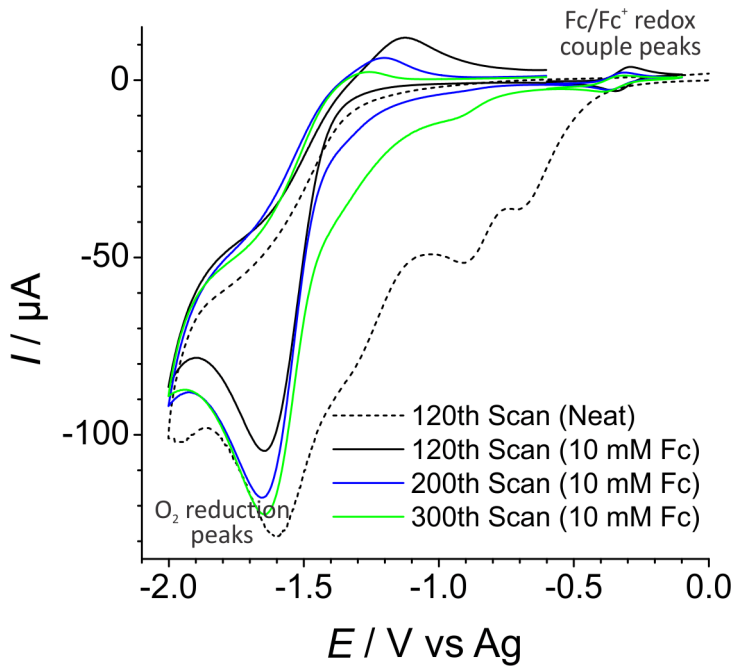

Figure A.2. Cyclic voltammetry of O_2 saturated [C_2mim][NTf_2] on unpolished Pt-SPEs carried out in the neat RTIL (at the 120th scan cycle), and with 10 mM of ferrocene (Fc) added (at the 120th, 200th, and 300th scan cycle).

The substantial initial (i.e. < 50 cycles) variations of the O_2 reduction peak currents in [C_2mim][NTf_2], $I_{p(O_2)}$, (as shown in Figure A.1 (e)) indicates that the O_2 reduction peak (scanning at 100 % vol. O_2 flow) in [C_2mim][NTf_2]/unpolished Pt-SPE system is highly unstable in the initial scans. This instability is much smaller but still significantly persists past ca. 50th CV cycle and beyond which could reduce the limits of detection and lead to drift in the response of the sensor. However, assuming that the falling $I_{p(Fc)}$ in consecutive CV scans as shown in Figure A.1 (d) was due instead to a gradual passivation of the Pt-SPE working electrode surface (e.g. due to adsorption of RTIL/binding material decomposition products), $I_{p(O_2)}$, was normalized with respect to the Fc oxidation peak currents, $(I_{p(O_2)}\cdot[Fc])/I_{p(Fc)}$ (as shown in the inset of Figure A.1 (e)). This was carried out by dividing $I_{p(O_2)}$ by $(I_{p(Fc)}/[Fc])$, assuming $I_{p(Fc)}$ correlates with the 'un-passivated' working electrode surface area in progressive scans. It was found that $(I_{p(O_2)}\cdot[Fc])/I_{p(Fc)}$ appears to remain relatively stable up to 20 CV cycles before significantly declining with further CV cycles. From a sensing

application point of view, if this decline of the sensor response is largely reproducible (i.e. for up to ~40th scans with the exception of the 5 mM Fc sample, see inset of Figure A.1 (e)), it could then be taken into account in the calibration algorithm of an actual gas-sensor device. In the absence of Fc (i.e. in neat [C_2mim][NTf_2]) it was previously noted (in Chapter 3) that the peak current reaches relative stability (as compared to the initial cycles) much more quickly (i.e. typically ca. 12 conditioning CV cycles in the presence of 100 % vol. is sufficient before a more stable response in short-term subsequent scans is attained).

Finally, Figure A.1 (f) shows the peak-to-peak potentials of the Fc/Fc^+ redox couple in the presence of O_2 in [C_2mim][NTf_2], which appeared to decrease and stabilizes after 50 CV cycles. This shows that the kinetics are improving and may indicate an improvement in the surface condition of the Pt-SPE working electrode after > 50 consecutive CV cycles in the presence of 100 % vol. O_2 flow.

B. Characterizations of synthesized poly(methyl methacrylate) purity.

The PMMA that was synthesized (as detailed Section 6.2.1) was characterized for its purity. Raman spectroscopy (Horiba, LabRam model 1B, New Jersey, USA) (Figure B.1) and fourier transform infrared spectroscopy (FT-IR; PerkinElmer Spectrum 100, Melbourne, Australia) (Figure B.2) were carried out on powdered samples. The Raman spectroscopy was collected with integrated signals from 16 accumulations of 60 s collection intervals, with an excitation line of 632.817 cm^{-1} at 2 mV at the 150 μm slit, 600 lines per mm grating and x 50 objective lense, and was pre-calibrated with Silicon (with an expected peak at 520.7 cm^{-1}). Comparing with the respective spectrums in the literature, no significant impurity peaks were observed in the Raman [269] and FT-IR spectrums [270, 271].

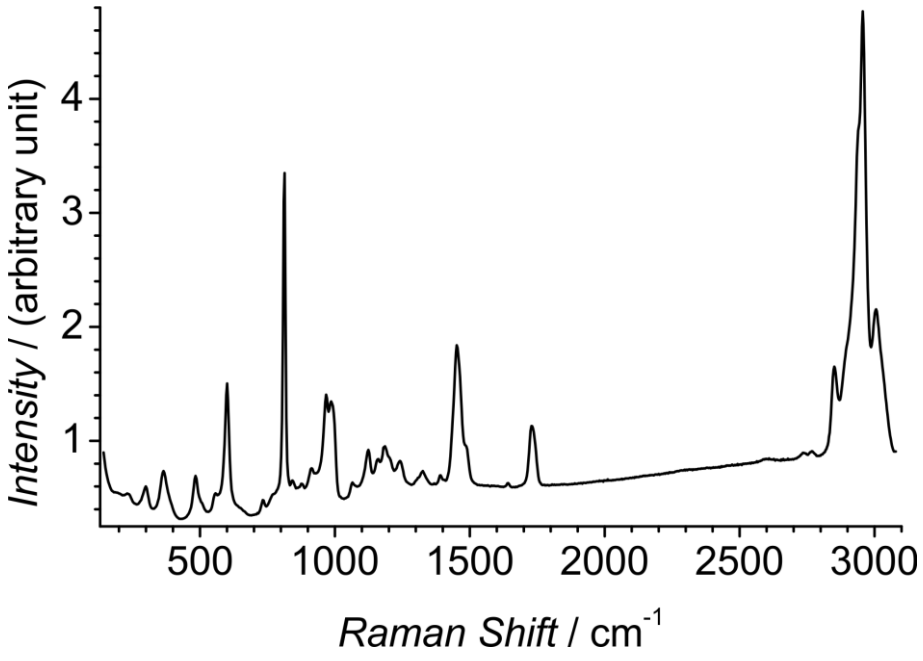

Figure B.1. Raman spectra of powdered samples of the PMMA synthesized.

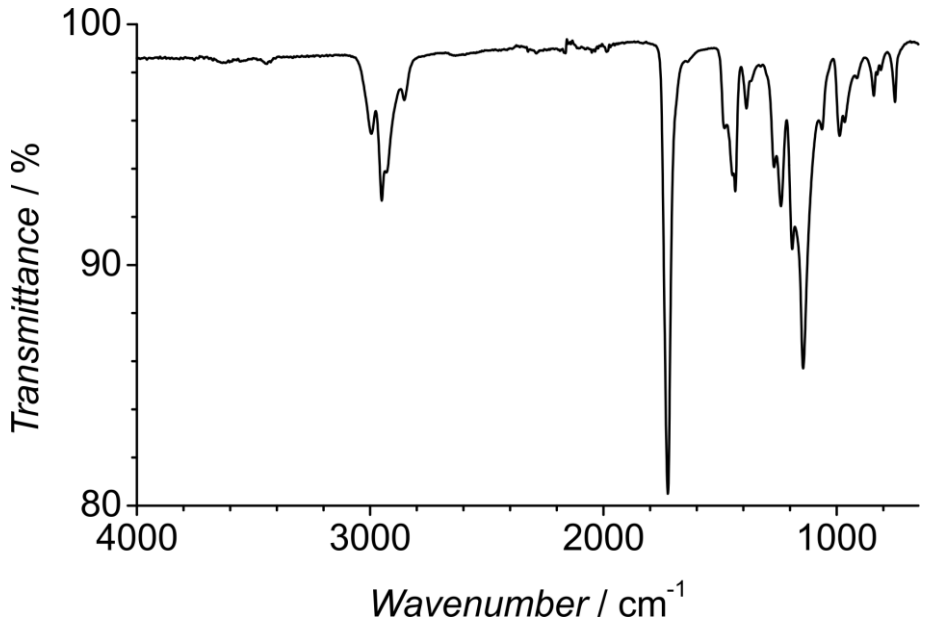

Figure B.2. FT-IR spectra of powdered samples of the PMMA synthesized.

Nuclear magnetic resonance (NMR; Bruker, Ultrashield 400, Conventry, England) spectroscopy was also conducted on the synthesized PMMA, dissolved in deuterated chloroform ($CDCl_3$), at 400.14 MHz, as shown in Figure B.3. Comparing with various literatures [272-274], the polymer synthesized is likely atactic in nature. This is expected for a random solution polymerization process. The $CDCl_3$ peak is located at the 7.26 ppm position, and small amounts of THF (at 3.75 ppm) and water (at 1.62 ppm) impurities were also present. [275] The water was likely from absorbed moisture in the $CDCl_3$ solvent, while THF was probably from the preparation of the PMMA powder (see Section 6.2.1). THF has a wide reduction potential window of < 3 V, vs. SCE, and thus its presence in the electrolyte would not be expected to have a direct impact on the cathodic CV scans measured.

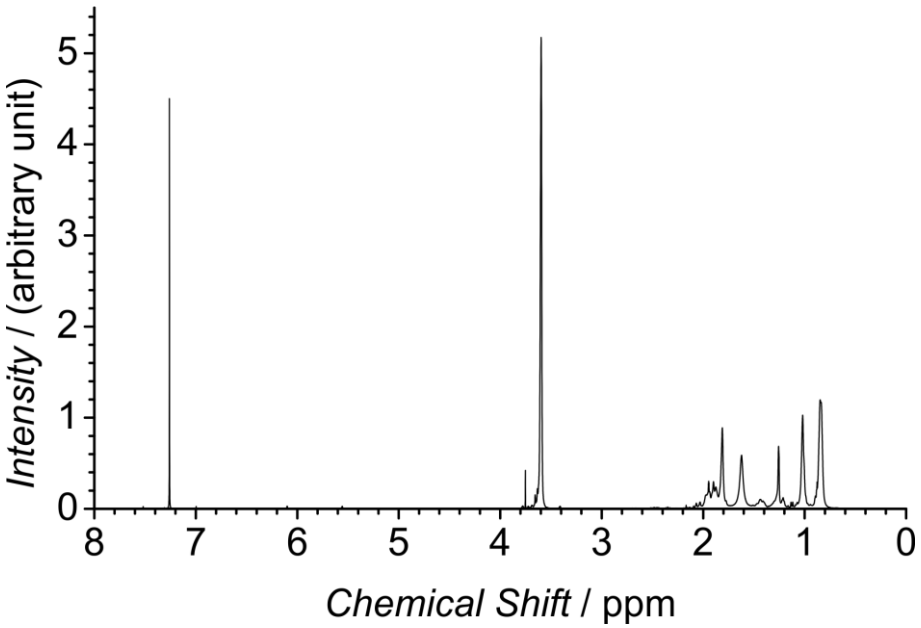

Figure B.3. NMR spectra of the PMMA synthesized, dissolved in $CDCl_3$ and collected at 400.13 MHz.

CHN elemental analysis (PerkinElmer, CHNS/O Analyzer 2400, Series II, Melbourne, Australia) was performed on powdered samples of the PMMA synthesized. The results were summarized in Table A.1.Table B.1. The average values of the triplicate measurements, and differences from the respective expected values (in $g \cdot mol^{-1}$ and %) for PMMA were also presented. For carbon, the average of the measured value only differed by 0.61 %, from the expected value for PMMA. The measured value for hydrogen defers from the expected value for PMMA by 2.82 %, and this difference is accounted for based on the range of the spread of values obtained in the triplicate measurements.

Table B.1. CHN elemental analysis of powdered samples of the PMMA synthesized. The average values of the triplicate measurements, and differences from the respective expected values (in g·mol^{-1} and %) were derived.

Sample	***Carbon* / g·mol^{-1}**	***Hydrogen* / g·mol^{-1}**	***Nitrogen* / g·mol^{-1}**
1	60.34	8.21	-0.06
2	60.42	8.18	-0.09
3	60.27	8.44	-0.03
Average	60.34	8.28	-0.06
Expected	59.98	8.05	0
Difference	0.36	0.23	-0.06
***%-Difference* / %**	0.61	2.82	-

C. Molecular weight and glass transitioning temperature of the synthesized PMMA.

The glass transition temperatures, T_g, were determined by differential scanning calorimetry (DSC; TA Instrument 2910 MDSC V4.4E, Shin, Osaka, Japan) following the procedure set out in ASTM standard E1356-08 (reapproved 2014) [276]. The DSC temperature was calibrated using the extrapolated onset of melting of indium (156.5985 °C, standard), tin (321.93 °C), and zinc (419.53 °C). The cell constant of the DSC was calibrated with the indium standard sample. 3.27 mg sample drop casted into the aluminium cell to form a clear uniform film, using acetone as the casting solvent, and left over the weekend to dry. The solution was sonicated for 15 mins to degas before drop casting. DSC measurements were carried out under nitrogen atmosphere. A total of 3 scans were carried out from 24 to 180 °C, at a heating rate of 10 °C per minute, allowing it to cool to room temperature between each scan. A preliminary thermal cycle is typically conducted during DSC measurements to allow for the volatilization of solvents or stabilizing contact of the sample with the cell (especially for powdered samples). Thus, the 1st (preliminary) thermal cycle was not analysed, and only the values obtained from the final (i.e. 3rd) thermal cycle was used for the estimation of the molecular weight.

The DSC curves collected are presented in Figure C.1. From the DSC curves, the various glass transitioning temperatures (extrapolated onset temperature, T_f, midpoint temperature, T_m, inflection temperature, T_i, extrapolated end-temperature, T_e) [276] were analysed using Universal Analysis 2000 (TA Instruments, Version 4.5A, Build 4.5.0.5) and presented in Table C.1. T_m and T_i both are commonly reported as the T_g of a material in the literature. Although, accordingly to ASTM standard E1356-08 [276], T_m is the recommended value to be

reported as the T_g of a material. Peaks likely corresponding to the evaporation of residual acetone were observed at 40.99 and 44.01 °C on the 1st thermal cycle.

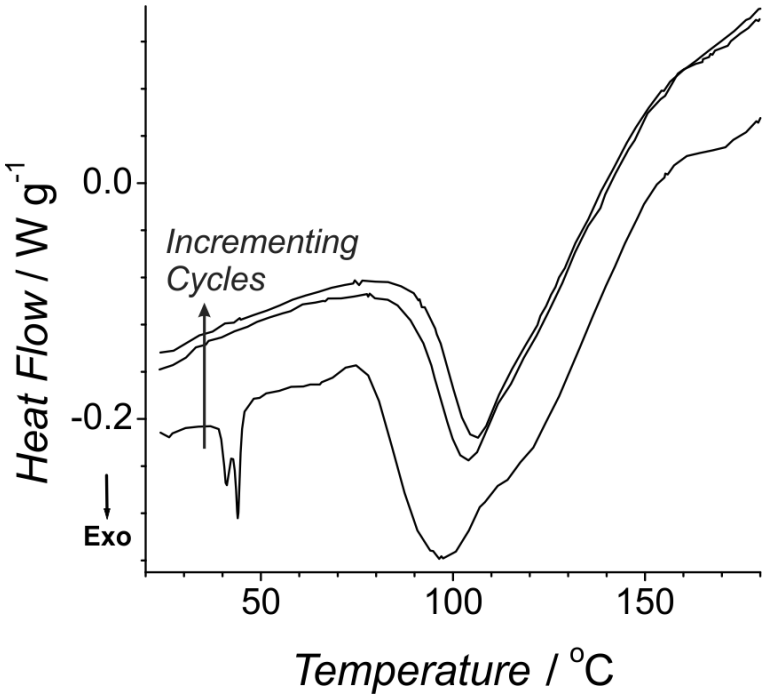

Figure C.1. DSC curves of 3.27 mg sample of the PMMA synthesized, drop casted with acetone as a film in the aluminium cell. A total of 3 thermal cycles were performed to allow complete volatilization of any residual acetone.

A reproducible shift in gradient was observed in the DSC curves at ca. 150 °C, and the onset temperature, $T_{m,f}$, analysed for the 3rd cycle at that thermal region, was found to be at 153.26 °C. This $T_{m,f}$ value is close to the melting point of 160 °C for high molecular weight ($M_w > \times 10^5$) PMMA [277]. One paper listed the T_g of PMMA synthesized (at 60 °C) by free-radical polymerization method to be at 106 °C. [258] However, the T_g value of PMMA is heavily dependent on its tacticity [278, 279] and molecular weight [278, 280]. Based on the expected tacticity mentioned in Section 6.2.1 (i.e. $s : i : h$ of ca. 0.45 : 0.14 : 0.41) for the PMMA synthesized, the T_g value of a high molecular weight polymer (weight average molecular weight, M_w, = 1.8×10^5; number average molecular weight, M_n, = 1.0×10^5), purified via. a

similar method, was given to be at 109.5 °C. [279] Beevers and White obtained an expression for the T_g of PMMA synthesized by free-radical polymerization in their 1960 paper [281],

$$T_g = (114 \pm 1) - (2.1 \pm 0.2) \times 10^5 / M_n \qquad \textbf{(C.1)}$$

Rearranging Equation (A.1) and taking the 3rd DSC cycle value of T_g for the presently synthesized PMMA from Table C.1, its M_n was estimated to be at (9.5±1.0)×10^3 based on T_m, and (13.5±1.4)×10^3 based on T_i. Polydispersity index of PMMA sample was not available, but could be estimated by dynamic light scattering (DLS) technique, to enable conversion of M_n to M_w.

Table C.1. Various T_g values extracted from the 2nd and 3rd DSC thermal cycles, presented in Figure C.1. onset temperature, T_f, midpoint temperature, T_m, inflection temperature, T_i, extrapolated end-temperature, T_e

Cycle	T_f	T_m*	T_i	T_e
		/ °C		
2nd	89.12	88.88	94.79	102.44
3rd	91.44	91.96	98.50	105.03

** Recommended as the "preferred" value to be reported according to ASTM (Designation: E1356-08).*

D. Estimating limits of detection from calibration data subjected to linearizing transformations.

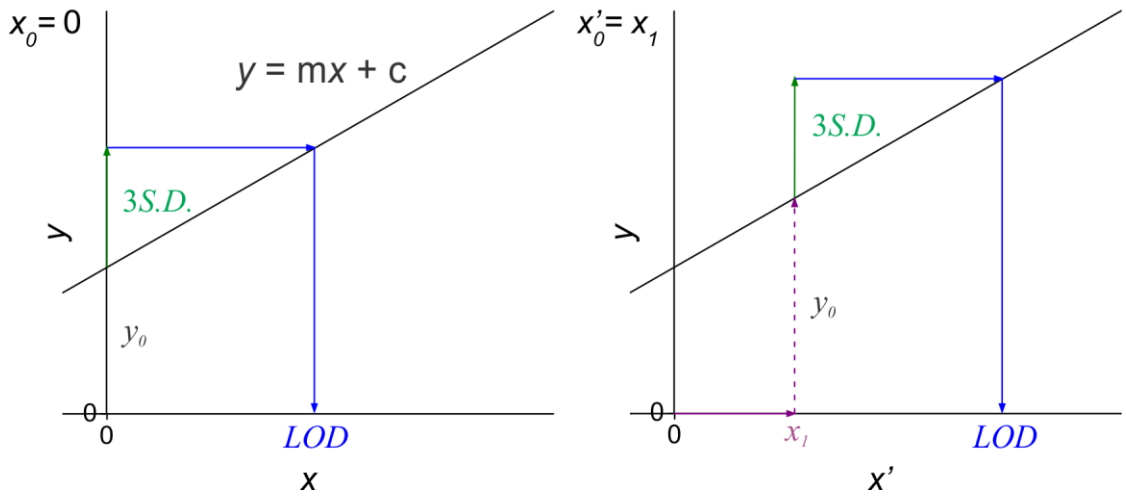

Figure D.1. (Left) Illustration of how LODs are estimated from linear regression of a calibration data. **(Right)** Calculating LOD for a calibration data subjected to linearizing transformation such that the blank position is shifted from the origin of the transformed plot-x-axis by x_1.

From linear regression of a calibration plot, the limits of detection, LOD, can be derived based on the standard criterion of *three times the standard deviation, S.D., at the y-intercept value obtained from the linear fit*, i.e.

$$\text{LOD} = \frac{3 \times S.D.}{m} \qquad \textbf{(D.1)}$$

where m is the slope of the line of linear fit. This can be easily understood from the illustration in Figure D.1 (left).

However for some cases of calibration plots subjected to linearizing transformations of the x-axis to an x'-axis (see Figure D.1) where the origin becomes undefined (i.e. linear-log plots, log-log plots, or plots where x-axis values are transformed by rising to a negative power),

applying equation (D.1) would lead to an inaccurate evaluation of its LOD. Since x_0 is undefined, while an actual measured blank response is available, by examining Figure D.1 (right), it becomes conceptually apparent that applying equation (D.2) would provide a better way to estimate LODs from these transformed calibration data,

$$\text{LOD} = \frac{(3 \times S.D. + y_o) - c}{m} \qquad \textbf{(D.2)}$$

where y_0 is taken as the measured current response, *I*, for 0 % vol. O_2.

y_0 normally is the theoretical value of the response at $x = 0$, however since its associated x_0 value is undefined along the line of linear fit, it is proposed here that a more representative and defined value for x_0' (along the *x'*-axis) can be found by redefining it based on the *actual* measured y_0 value, then calculating for the value of x_0' from it by applying the linear equation of the fit. If the uncertainty of y_0 is known, then the magnitude of the uncertainty should be added to y_0 for the derivation of LOD. A more precise value measured for y_0 is thus desired for a lower LOD value. It is also to be noted that equation (D.1) is simply a special case of equation D.2: where the defined theoretical $y_0 = c$, since the response at 0 % vol. O_2 lies exactly at the origin along the x-axis, and thus those two terms naturally cancels out.

Finally, for calibration data which exhibits clear divergence from linearity closer to the origin, equation (D.2) could too be employed, where y_0 is instead substituted with the measured current response value corresponding to the lowest O_2 concentration still residing reasonably close along the linear fit, $y_0 = I_{\text{linear-min}}$. While for the cases of calibration data fitted by polynomial functions, since as $[O_2] \rightarrow 0$ % vol. the higher degree terms $\rightarrow 0$ much quicker compared to the first degree term, the function would thus reduce to a linear equation. Consequently, the LOD could be thus simply be estimated using equation (D.1), where *m* is taken to be the coefficient of the first degree term of the 2nd order polynomial function.

References

1. Barb, A. J.; Faulkner, L. R., *Electrochemical Methods - Fundamentals and Applications*. 2nd Edition ed.; John Wiley & Sons, Inc.: Hoboken, 2001.
2. Atkins, P. W., *Physical Chemistry*. 5th Edition ed.; Oxford University Press: Oxford, 1995.
3. Fisher, A. C., *Electrode Dynamics*. Oxford University Press Inc.: New York, 1996.
4. Compton, R. G.; Banks, C. E., *Understanding Voltammetry*. World Scientific Publishing Co. Pte. Ltd.: Singapore, 2007.
5. O'Sullivan, S.; Alvarez de Eulate, E.; Yuen, Y. H.; Helmerhorst, E.; Arrigan, D. W. M. *Analyst* **2013,** 138, (20), 6192-6196.
6. Alvarez de Eulate, E.; Serls, L.; Arrigan, D. M. *Anal Bioanal Chem* **2013,** 405, (11), 3801-3806.
7. Alvarez de Eulate, E.; Silvester, D. S.; Arrigan, D. W. M. *Chemistry – An Asian Journal* **2012,** 7, (11), 2559-2561.
8. O'Mahony, A. M.; Scanlon, M. D.; Berduque, A.; Beni, V.; Arrigan, D. W. M.; Faggi, E.; Bencini, A. *Electrochemistry Communications* **2005,** 7, (10), 976-982.
9. Shul, G.; Opallo, M.; Marken, F. *Electrochimica Acta* **2005,** 50, (11), 2315-2322.
10. Shaw, D. J., *Introduction to Colloid & Surface Chemistry*. 4th Edition ed.; Butterworth-Heinemann Ltd: 1993.
11. von Helmholtz, H. L. F. *Ann. Phys.* **1879,** 243, 337-382.
12. Gouy, G. *J. Phys. Theor. Appl.* **1910,** 9, 457-468.
13. Chapman, D. *Philos. Mag., Ser. 6* **1913,** 25, 475-581.
14. Stern, O. *Elektrochem. Angew. Phys. Chem.* **1924,** 30, 508-516.
15. Grahame, D. C. *Chemical Reviews* **1947,** 41, (3), 441-501.
16. Bockris, J. O. M.; Devanathan, M. A. V.; Muller, K. *Proceedings of the Royal Society of London. Series A. Mathematical and Physical Sciences* **1963,** 274, (1356), 55-79.
17. Kornyshev, A. A. *The Journal of Physical Chemistry B* **2007,** 111, (20), 5545-5557.
18. Fedorov, M. V.; Kornyshev, A. A. *The Journal of Physical Chemistry B* **2008,** 112, (38), 11868-11872.
19. Fedorov, M. V.; Kornyshev, A. A. *Chemical Reviews* **2014,** 114, (5), 2978-3036.
20. Bard, A. J.; Faulkner, L. R., *Electrochemical Methods. Fundamentals and Applications*. 2001.
21. Wang, J., *Analytical Electrochemistry*. 2nd Edition ed.; Wiley-VCH: Brisbane, 2001.
22. Cottrell, F. F. *Zeitschrift fur Physikalische Chemie-Stochiometrie und Verwandtschaftslehre* **1903,** 42, 385-431.
23. Randles, J. E. B. *Discussions of the Faraday Society* **1947,** 1, (0), 11-19.
24. Sevcik, A. *Collect. Czech. Chem. Commun.* **1948,** 13, 348-377.
25. Grundler, P., *Chemical Sensors - An Introduction for Scientists and Engineers*. Springer: Berlin Heidelberg, 2007.
26. Knake, R.; Jacquinot, P.; Hodgson, A. W. E.; Hauser, P. C. *Analytica Chimica Acta* **2005,** 549, (1–2), 1-9.
27. Stetter, J. R.; Li, J. *Chem. Rev.* **2008,** 108, (2), 352-366.
28. Chang, S. C.; Stetter, J. R.; Cha, C. S. *Talanta* **1993,** 40, (4), 461-477.
29. Li, H.; Mu, X.; Wang, Z.; Guo, M.; Zeng, X.; Mason, A. J. In *Room Temperature Ionic-Liquid Electrochemical Gas Sensor Array System for Real-Time Mine Safety Monitoring*, Sensors, 2013 IEEE, Baltimore, MD, 2013; Baltimore, MD, pp 1-4.
30. Holm, T. *Journal of Chromatography A* **1999,** 842, (1–2), 221-227.
31. Lovelock, J. E. *Nature* **1960,** 188, (4748), 401-401.
32. Ando, M.; Kobayashi, T.; Haruta, M. *Catalysis Today* **1997,** 36, (1), 135-141.
33. Dakin, J.; Chambers, P., REVIEW OF METHODS OF OPTICAL GAS Detection by Direct Optical Spectroscopy, with Emphasis on Correlation Spectroscopy. In *Optical Chemical Sensors*,

Baldini, F.; Chester, A. N.; Homola, J.; Martellucci, S., Eds. Springer Netherlands: 2006; Vol. 224, pp 457-477.
34. Vyas, J. C.; Katti, V. R.; Gupta, S. K.; Yakhmi, J. V. *Sensors and Actuators B: Chemical* **2006,** 115, (1), 28-32.
35. Su, P.-G.; Lin, L.-G.; Tzou, W.-H. *Sensors and Actuators B: Chemical* **2013,** 181, (0), 795-801.
36. Koshets, I. A.; Kazantseva, Z. I.; Shirshov, Y. M.; Cherenok, S. A.; Kalchenko, V. I. *Sensors and Actuators B* **2005,** 106, 177-181.
37. Shi, B. C.; Wolf, M. O.; Jarvis, D.; Young, J. F. *J. Appl. Phys.* **2005,** 98, (114314), 1-4.
38. Maskell, W. C. *Journal of Physics E: Scientific Instruments* **1987,** 20, (10), 1156-1168.
39. Pravdová, V.; Pravda, M.; Guilbault, G. G. *Analytical Letters* **2002,** 35, (15), 2389-2419.
40. Barbri, N. E.; Mirhisse, J.; Ionescu, R.; Bari, N. E.; Correig, X.; Bouchikhi, B.; Llobet, E. *Sensors and Actuators B* **2009,** 141, 538-543.
41. Kwon, C. H.; Yun, D. H.; Hong, H.-K.; Kim, S.-R.; Lee, K.; Lim, H. Y.; Yoon, K. H. *Sensors and Actuators B* **2000,** 65, 327-330.
42. Lange, U.; Roznyatovskaya, N. V.; Mirsky, V. M. *Analytica Chimica Acta* **2008,** 614, (1), 1-26.
43. Dai, L.; Soundarrajan, P.; Kim, T. *Pure Appl. Chem.* **2002,** 74, (9), 1753-1772.
44. Ertl, P.; Wagner, M.; Corton, E.; Mikkelsen, S. R. *Biosensors and Bioelectronics* **2003,** 18, 907.
45. Huang, X.-J.; Aldous, L.; O'Mahony, A. M.; del Campo, F. J.; Compton, R. G. *Analytical Chemistry* **2010,** 82, (12), 5238-5245.
46. Yun, M.; Myung, N. V.; Vasquez, R. P.; Wang, J., Nanowire Growth for Sensor Arrays. In *Nanofabrication Technologies*, 2003; Vol. 5220, pp 1-9.
47. Ertl, G.; Küppers, J., *Low Energy Electrons and Surface Chemistry*. Verlag Chemie: Weinheim, 1974; Vol. 4.
48. Nonnenmacher, M.; O'Boyle, M. P.; Wickramasinghe, H. K. *Applied Physics Letters* **1991,** 58, (25), 2921-2923.
49. Barsan, N.; Weimar, U. *Journal of Electroceramics* **2001,** 7, (3), 143-167.
50. Yamazoe, N. *Sensors and Actuators B: Chemical* **1991,** 5, (1–4), 7-19.
51. Yamazoe, N.; Kurokawa, Y.; Seiyama, T. *Sensors and Actuators* **1983,** 4, (0), 283-289.
52. Jin, Y. Toxic Gas Sensors using Thin Film Transistor Platform at Low Temperature. Massachusetts Institute of Technology, Massachusetts, 2009.
53. Liao, F.; Chen, C.; Subramanian, V. *Sensors and Actuators B* **2005,** 107, 849-855.
54. Bartlett, P. N.; Archer, P. B. M.; Ling-Chung, S. K. *Sensors and Actuators* **1989,** 19, (2), 125-140.
55. Miasik, J. J.; Hooper, A.; Tofield, B. C. *Journal of the Chemical Society, Faraday Transactions 1: Physical Chemistry in Condensed Phases* **1986,** 82, (4), 1117-1126.
56. Bartlett, P. N.; Ling-Chung, S. K. *Sensors and Actuators* **1989,** 19, (2), 141-150.
57. Bai, H.; Shi, G. *Sensors* **2007,** 7, 267-307.
58. Kemp, N. T.; McGrouther, D.; Cochrane, J. W.; Newbury, R. *Advance Materials* **2007,** 19, 2634-2638.
59. Thapa, P. S.; Ackerson, B. J.; Grischkowsky, D. R.; Flanders, B. N. *Nanotechnology* **2009,** 20, (235307), 1-10.
60. Pandey, S.; Goswami, G. K.; Nanda, K. K. *Sci. Rep.* **2013,** 3.
61. Zavickis, J.; Linarts, A.; Knite, M. *Energetika* **2011,** 57, (1), 44-49.
62. Di Francia, G.; Alfano, B.; La Ferrara, V. *Journal of Sensors* **2009,** 2009.
63. Ramamoorthy, R.; Dutta, P. K.; Akbar, S. A. *Journal of Materials Science* **2003,** 38, 4271-4282.
64. Shuk, P.; Jantz, R. In *Advanced Oxygen Sensor with Oxide Electrode Materials*, Fifth International Conference on Sensing Technology, 2011; IEEE.
65. Peters, H. M., H.H Procedure for the gas analysis at elevated temperatures using galvanic solid electrolyte elements. DD-Patent 21673, 1961.
66. Weissbart, J.; Ruka, R. *Review of Scientific Instruments* **1961,** 32, (5), 593-595.
67. Toniolo, R.; Dossi, N.; Pizzariello, A.; Doherty, A. P.; Susmel, S.; Bontempelli, G. *Journal of Electroanalytical Chemistry* **2012,** 670, (0), 23-29.
68. Yap, C. M.; Xu, G. Q.; Ang, S. G. *Analytical Chemistry* **2012,** 85, (1), 107-113.

69. Shim, J. H.; Lee, Y. *Analytical Chemistry* **2009,** 81, (20), 8571-8576.
70. Dai, M.; Maxwell, S.; Vogt, B. D.; La Belle, J. T. *Analytica Chimica Acta* **2012,** 738, (0), 27-34.
71. Lang, X.-Y.; Fu, H.-Y.; Hou, C.; Han, G.-F.; Yang, P.; Liu, Y.-B.; Jiang, Q. *Nat Commun* **2013,** 4.
72. EC08, A. A. N. Autolab Application Note EC08.
73. Silvester, D. S. *Analyst* **2011,** 136, 4871-4882.
74. Bakker, E. *Anal. Chem.* **2004,** 76, 3285-3298.
75. Cao, Z.; Buttner, W. J.; Stetter, J. R. *Electroanalysis* **1992,** 4, (3), 253-266.
76. Clark, L. C.; Wolf, R.; Granger, D.; Taylor, Z. *Journal of Applied Physiology* **1953,** 6, (3), 189-193.
77. Sawyer, D. T.; George, R. S.; Rhodes, R. C. *Analytical Chemistry* **1959,** 31, (1), 2-5.
78. City Technology Ltd. http://www.citytech.com/
79. Wang, R.; Okajima, T.; Kitamura, F.; Ohsaka, T. *Electroanalysis* **2004,** 16, (1-2), 66-72.
80. Hrnčiřová, P.; Opekar, F. *Sensors and Actuators B: Chemical* **2002,** 81, (2–3), 329-333.
81. Nádherná, M.; Opekar, F.; Reiter, J.; Štulík, K. *Sensors and Actuators B: Chemical* **2012,** 161, (1), 811-817.
82. Ostermann, R.; Smarsly, B. *Nanoscale* **2009,** 1, (2), 266-270.
83. Buzzeo, M. C.; Evans, R. G.; Compton, R. G. *ChemPhysChem* **2004,** 5, (8), 1106-1120.
84. Huang, X.-J.; Rogers, E. I.; Hardacre, C.; Compton, R. G. *The Journal of Physical Chemistry B* **2009,** 113, (26), 8953-8959.
85. Buzzeo, M. C.; Klymenko, O. V.; Wadhawan, J. D.; Hardacre, C.; Seddon, K. R.; Compton, R. G. *The Journal of Physical Chemistry A* **2003,** 107, (42), 8872-8878.
86. Niedrach, L. W.; Alford, H. R. *Journal of Electrochemical Society* **1965,** 112, (2), 117-124.
87. Shoup, D.; Szabo, A. *Journal of Electroanalytical Chemistry and Interfacial Electrochemistry* **1982,** 140, (2), 237-245.
88. Aoki, K.; Osteryoung, J. *Journal of Electroanalytical Chemistry and Interfacial Electrochemistry* **1981,** 122, (0), 19-35.
89. Barrosse-Antle, L. E.; Bond, A. M.; Compton, R. G.; O'Mahony, A. M.; Rogers, E. I.; Silvester, D. S. *Chemistry – An Asian Journal* **2010,** 5, (2), 202-230.
90. Rogers, E. I.; O'Mahony, A. M.; Aldous, L.; Compton, R. G. *ECS Transactions* **2010,** 33, (7), 473-502.
91. Song, C.; Zhang, J., Electrocatalytic Oxygen Reduction Reaction. In *PEM Fuel Cell Electrocatalysts and Catalyst Layers*, Zhang, J., Ed. Springer London: 2008; pp 89-134.
92. Göpel, W.; Reinhardt, G.; Rösch, M. *Solid State Ionics* **2000,** 136–137, (0), 519-531.
93. Mills, A.; Tommons, C.; Bailey, R. T.; Crilly, P.; Tedford, M. C. *Analytica Chimica Acta* **2011,** 702, (2), 269-273.
94. Xiang, L.; Yu, P.; Zhang, M.; Hao, J.; Wang, Y.; Zhu, L.; Dai, L.; Mao, L. *Analytical Chemistry* **2014,** 86, (10), 5017-5023.
95. GreeleyJ; Stephens, I. E. L.; Bondarenko, A. S.; Johansson, T. P.; Hansen, H. A.; Jaramillo, T. F.; RossmeislJ; ChorkendorffI; Nørskov, J. K. *Nat Chem* **2009,** 1, (7), 552-556.
96. Chen, Z.; Waje, M.; Li, W.; Yan, Y. *Angewandte Chemie International Edition* **2007,** 46, (22), 4060-4063.
97. Wang, C.; Daimon, H.; Onodera, T.; Koda, T.; Sun, S. *Angewandte Chemie International Edition* **2008,** 47, (19), 3588-3591.
98. Gębicki, J.; Kloskowski, A.; Chrzanowski, W. *Electrochimica Acta* **2011,** 56, (27), 9910-9915.
99. AlNashef, I. M.; Leonard, M. L.; Kittle, M. C.; Matthews, M. A.; Weidner, J. W. *Electrochem. Solid-State Lett.* **2001,** 4, D16-D18.
100. Buzzeo, M. C.; Klymenko, O. V.; Wadhawan, J. D.; Hardacre, C.; Seddon, K. R.; Compton, R. G. *J. Phys. Chem. A* **2003,** 107, 8872-8878.
101. Sawyer, D. T.; Chiericato, G., Jr.; Angelis, C. T.; Nanni, E. J., Jr.; Tsuchiya, T. *Anal. Chem.* **1982,** 54, 1720-1724.
102. René, A.; Abasq, M.-L.; Hauchard, D.; Hapiot, P. *Analytical Chemistry* **2010,** 82, (20), 8703-8710.

103. Baltes, N.; Beyle, F.; Freiner, S.; Geier, F.; Joos, M.; Pinkwart, K.; Rabenecker, P. *Talanta* **2013,** 116, 474-481.
104. Hutton, L.; Newton, M. E.; Unwin, P. R.; Macpherson, J. V. *Analytical Chemistry* **2008,** 81, (3), 1023-1032.
105. Xiong, L.; Barnes, E. O.; Compton, R. G. *Sensors and Actuators B: Chemical* **2014,** 200, (0), 157-166.
106. AlNashef, I. M.; Leonard, M. L.; Kittle, M. C.; Matthews, M. A.; Weidner, J. W. *Electrochem Solid State Letters* **2001,** 4, (11), D16-D18.
107. Buzzeo, M. C.; Klymenko, O. V.; Wadhawan, J. D.; Hardacre, C.; Seddon, K. R.; Compton, R. G. *J Phys Chem A* **2003,** 107, (42), 8872-8878.
108. Sawyer, D. T. *Analytical Chemistry* **1982,** 54, (11), 1720-1724.
109. Hapiot, P.; Lagrost, C. *Chemical Reviews* **2008,** 108, (7), 2238-2264.
110. AlNashef, I. M.; Hashim, M. A.; Mjalli, F. S.; Ali, M. Q. A. h.; Hayyan, M. *Tetrahedron Letters* **2010,** 51, (15), 1976-1978.
111. Metters, J. P.; Kadara, R. O.; Banks, C. E. *Analyst* **2011,** 136, 1067-1076.
112. Washe, A. P.; Lozano-Sanchez, P.; Bejarano-Nosas, D.; Katakis, I. *Electrochemica Acta* **2013,** 91, 166-172.
113. Mata, D.; Bejarano, D.; Botero, M. L.; Lozano, P.; Constanti, M.; Katakis, I. *Electrochimica Acta* **2010,** 55, 4261.
114. Pravda, M.; O'Meara, C.; Guilbault, G. G. *Talanta* **2001,** 54, 887-892.
115. Wang, J.; Xu, D. K.; Kawade, A. N.; Polsky, R. *Analytical Chemistry* **2001,** 73, 5576.
116. Hart, J. P.; Wering, S. A. *Trends in Analytical Chemistry* **1997,** 16, (2), 89.
117. Nagata, R.; Clark, S. A.; Yokoyama, K.; Tamiya, E.; Karube, I. *Analytica Chimica Acta* **1995,** 304, 157.
118. Galán-Vidal, C. A.; Muñoz, J.; Domínguez, C.; Alegret, S. *TrAC Trends in Analytical Chemistry* **1995,** 14, (5), 225-231.
119. Choudhry, N. A.; Kampouris, D. K.; Kadara, R. O.; Jenkinson, N.; Banks, C. E. *Analytical Methods* **2009,** 1, (3), 183-187.
120. Honeychurch, K. C.; Hart, J. P. *TrAC Trends in Analytical Chemistry* **2003,** 22, (7), 456-469.
121. Bilitewski, U.; Chemnitius, G. C.; Ruger, P.; Schmid, R. D. *Sensors and Actuators B* **1992,** 7, 351-355.
122. Fanjul-Bolado, P.; Hernández-Santos, D.; Lamas-Ardisana, P. J.; Martín-Pernía, A.; Costa-García, A. *Electrocheimica Acta* **2008,** 53, 3635.
123. Kadara, R. O.; Jenkinson, N.; Banks, C. E. *Sensors and Actuators B* **2009,** 138, 556-562.
124. Parsek, J.; Trnkova, L.; Gablech, I.; Businova, P.; Drbohlavova, J.; Chomoucka, J.; Adam, V.; Kizek, R.; Hubalek, J. *International Journal of Electrochemical Science* **2012,** 7, 1785.
125. Prasek, J.; Trnkova, L.; Gablech, I.; Businova, P.; Drbohlavova, J.; Chomoucka, J.; Adam, V.; Kizek, R.; Hubalek, J. *Int. J. Electrochem. Sci.* **2012,** 7, 1785-1801.
126. García-González, R.; Fernández-Abedul, M. T.; Pernía, A.; Costa-García, A. *Electrochim. Acta* **2008,** 53, 3242-3249.
127. Gebicki, J.; Kloskowski, A.; Chrzanowski, W. *Electrochim. Acta* **2011,** 56, 9910-9915.
128. Chou, C.-H.; Chang, J.-L.; Zen, J.-M. *Electroanalysis* **2009,** 21, (2), 206-209.
129. Metters, J. P.; Tan, F.; Kadara, R. O.; Banks, C. E. *Anal. Methods* **2012,** 4, 1272-1277.
130. Rogers, R. D.; Seddon, K. R., *Ionic Liquids as Green Solvents. Progress and Prospects*. 2003.
131. Lee, S.-Y.; Ogawa, A.; Kanno, M.; Nakamoto, H.; Yasuda, T.; Watanabe, M. *Journal of the American Chemical Society* **2010,** 132, (28), 9764-9773.
132. Liu, S.; Zhou, L.; Wang, P.; Zhang, F.; Yu, S.; Shao, Z.; Yi, B. *ACS Applied Materials & Interfaces* **2014,** 6, (5), 3195-3200.
133. Chang, Y.-H.; Lin, P.-Y.; Huang, S.-R.; Liu, K.-Y.; Lin, K.-F. *Journal of Materials Chemistry* **2012,** 22, (31), 15592-15598.
134. Cheng, P.; Wang, W.; Lan, T.; Chen, R.; Wang, J.; Yu, J.; Wu, H.; Yang, H.; Deng, C.; Guo, S. *Journal of Photochemistry and Photobiology A: Chemistry* **2010,** 212, (2–3), 147-152.

135. Mikoshiba, S.; Murai, S.; Sumino, H.; Kado, T.; Kosugi, D.; Hayase, S. *Current Applied Physics* **2005,** 5, (2), 152-158.
136. Hirotake, K.; Daisuke, K.; Yutaka, O. *Japanese Journal of Applied Physics* **2008,** 47, (4S), 3152.
137. Lee, J.; Panzer, M. J.; He, Y.; Lodge, T. P.; Frisbie, C. D. *Journal of the American Chemical Society* **2007,** 129, (15), 4532-4533.
138. Cho, J. H.; Lee, J.; Xia, Y.; Kim, B.; He, Y.; Renn, M. J.; Lodge, T. P.; Daniel Frisbie, C. *Nat Mater* **2008,** 7, (11), 900-906.
139. Shvedene, N. V.; Chernyshov, D. V.; Khrenova, M. G.; Formanovsky, A. A.; Baulin, V. E. *Electroanalysis* **2006,** 18, (13-14), 1416-1421.
140. Mu, X.; Wang, Z.; Zeng, X.; Mason, A. J. *Sensors Journal, IEEE* **2013,** 13, (10), 3976-3981.
141. Lee, J.; Murugappan, K.; Arrigan, D. W. M.; Silvester, D. S. *Electrochimica Acta* **2013,** 101, 158-168.
142. Murugappan, K.; Lee, J.; Silvester, D. S. *Electrochemistry Communications* **2011,** 13, 1435-1438.
143. Bonhôte, P. A. D.; Papageorgiou, N.; Kalyanasundaram, K.; Grätzel, M. *Inorg. Chem.* **1996,** 35, 1168.
144. Buzzeo, M. C.; Evans, R. G.; Compton, R. G. *ChemPhysChem* **2004,** 5, 1106-1120.
145. Silvester, D. S.; Compton, R. G. *Z. Phys. Chem.* **2006,** 220, 1247-1274.
146. Bonhôte, P.; Dias, A.-P.; Papageorgiou, N.; Kalyanasundaram, K.; Grätzel, M. *Inorganic Chemistry* **1996,** 35, (5), 1168-1178.
147. O'Mahony, A. M.; Silvester, D. S.; Aldous, L.; Hardacre, C.; Compton, R. G. *Journal of Chemical & Engineering Data* **2008,** 53, (12), 2884-2891.
148. Buzzeo, M. C.; Hardacre, C.; Compton, R. G. *Anal. Chem.* **2004,** 76, 4583-4588.
149. Murugappan, K.; Lee, J.; Silvester, D. S. *Electrochem. Commun.* **2011,** 13, 1435-1438.
150. Islam, M. M.; Ohsaka, T. *The Journal of Physical Chemistry C* **2008,** 112, (4), 1269-1275.
151. Zhang, D.; Okajima, T.; Matsumoto, F.; Ohsaka, T. *Journal of The Electrochemical Society* **2004,** 151, (4), D31-D37.
152. Katayama, Y.; Onodera, H.; Yamagata, M.; Miura, T. *Journal of The Electrochemical Society* **2004,** 151, (1), A59-A63.
153. Wang, Z.; Lin, P.; Baker, G. A.; Stetter, J.; Zeng, X. *Analytical Chemistry* **2011,** 83, (18), 7066-7073.
154. Xiong, S.-Q.; Wei, Y.; Guo, Z.; Chen, X.; Wang, J.; Liu, J.-H.; Huang, X.-J. *The Journal of Physical Chemistry C* **2011,** 115, (35), 17471-17478.
155. Ghilane, J.; Lagrost, C.; Hapiot, P. *Analytical Chemistry* **2007,** 79, (19), 7383-7391.
156. Barrosse-Antle, L. E.; Bond, A. M.; Compton, R. G.; O'Mahony, A. M.; Rogers, E. I.; Silvester, D. S. *Chem. Asian J.* **2010,** 5, 202-230.
157. Endres, F.; Hofft, O.; Borisenko, N.; Gasparotto, L. H.; Prowald, A.; Al-Salman, R.; Carstens, T.; Atkin, R.; Bund, A.; Zein El Abedin, S. *Physical Chemistry Chemical Physics* **2010,** 12, (8), 1724-1732.
158. Schroder, U.; Wadhawan, J. D.; Compton, R. G.; Marken, F.; Suarez, P. A. Z.; Consorti, C. S.; de Souza, R. F.; Dupont, J. *New Journal of Chemistry* **2000,** 24, (12), 1009-1015.
159. Evans, R. G.; Klymenko, O. V.; Hardacre, C.; Seddon, K. R.; Compton, R. G. *Journal of Electroanalytical Chemistry* **2003,** 556, 179-188.
160. Liu, H.; Liu, Y.; Li, J. *Physical Chemistry Chemical Physics* **2010,** 12, (8), 1685-1697.
161. Migliorini, M. V.; Donato, R. K.; Benvegnú, M. A.; Dupont, J.; Gonçalves, R. S.; Schrekker, H. S. *Catalysis Communications* **2008,** 9, (6), 971-975.
162. Sobota, M.; Schmid, M.; Happel, M.; Amende, M.; Maier, F.; Steinrück, H. P.; Paape, N.; Wasserscheid, P.; Laurin, M.; Gottfried, J. M.; Libuda, J. *Physical Chemistry Chemical Physics* **2010,** 12, (35), 10610-10621.
163. De Vos, N.; Maton, C.; Stevens, C. V. *ChemElectroChem* **2014**, n/a-n/a.
164. Smith, R. C.; Reeves, J. C. *Biochemical Pharmacology* **1987,** 36, (9), 1457-1460.
165. Lin, S. C., Diazalactones with primary diamine, dehydration. Google Patents: 1988.

166. Cheng, J.-F.; Kaiho, C.; Chen, M.; Arrhenius, T.; Nadzan, A. *Tetrahedron Letters* **2002,** 43, (26), 4571-4573.
167. Hausler, M. J.; Hayes, M. H. B., *Sorption of Imidazolinone Herbicides by Humic Acid Preparations*. Woodhead Publishing: Cambridge, England, 1997.
168. Köddermann, T.; Ludwig, R.; Paschek, D. *ChemPhysChem* **2008,** 9, (13), 1851-1858.
169. Vorotyntsev, M. A.; Zinovyeva, V. A.; Picquet, M. *Electrochimica Acta* **2010,** 55, (18), 5063-5070.
170. Zevenbergen, M. A. G.; Wouters, D.; Dam, V.-A. T.; Brongersma, S. H.; Crego-Calama, M. *Analytical Chemistry* **2011,** 83, (16), 6300-6307.
171. Nádherná, M.; Opekar, F.; Reiter, J. *Electrochimica Acta* **2011,** 56, (16), 5650-5655.
172. Li, Z.; Jiang, J.; Lei, G.; Gao, D. *Polymers for Advanced Technologies* **2006,** 17, (7-8), 604-607.
173. Ramesh, S.; Liew, C.-W.; Ramesh, K. *Journal of Non-Crystalline Solids* **2011,** 357, (10), 2132-2138.
174. Fenton, D.; Parker, J.; Wright, P. *Polymer* **1973,** 14, (11), 589-589.
175. Wright, P. V. *British Polymer Journal* **1975,** 7, (5), 319-327.
176. Song, J. Y.; Wang, Y. Y.; Wan, C. C. *Journal of Power Sources* **1999,** 77, (2), 183-197.
177. Appetecchi, G. B.; Croce, F.; Scrosati, B. *Electrochimica Acta* **1995,** 40, (8), 991-997.
178. Bohnke, O.; Frand, G.; Rezrazi, M.; Rousselot, C.; Truche, C. *Solid State Ionics* **1993,** 66, (1–2), 97-104.
179. Bohnke, O.; Frand, G.; Rezrazi, M.; Rousselot, C.; Truche, C. *Solid State Ionics* **1993,** 66, (1–2), 105-112.
180. Feuillade, G.; Perche, P. *J Appl Electrochem* **1975,** 5, (1), 63-69.
181. Iijima, T.; Toyoguchi, Y.; Eda, N. *Denki Kagaku* **1985,** 53, 619-623.
182. Stallworth, P. E.; Greenbaum, S. G.; Croce, F.; Slane, S.; Salomon, M. *Electrochimica Acta* **1995,** 40, (13–14), 2137-2141.
183. Stephan, A. M.; Renganathan, N. G.; Kumar, T. P.; Thirunakaran, R.; Pitchumani, S.; Shrisudersan, J.; Muniyandi, N. *Solid State Ionics* **2000,** 130, (1–2), 123-132.
184. Sirisopanaporn, C.; Fernicola, A.; Scrosati, B. *Journal of Power Sources* **2009,** 186, (2), 490-495.
185. Seki, S.; Kobayashi, Y.; Miyashiro, H.; Ohno, Y.; Usami, A.; Mita, Y.; Kihira, N.; Watanabe, M.; Terada, N. *The Journal of Physical Chemistry B* **2006,** 110, (21), 10228-10230.
186. Appetecchi, G. B.; Scaccia, S.; Tizzani, C. *J. Electrochem. Soc.* **2006,** 153, (9), A1685-A1691.
187. Salminen, J.; Papaiconomou, N.; Kumar, R. A.; Lee, J. M.; Kerr, J.; Newman, J.; Prausnitz, J. M. *Fluid Phase Equilibria* **2007,** 261, (1-2), 421-426.
188. Sydam, R.; Deepa, M.; Srivastava, A. K. *RSC Advances* **2012,** 2, (24), 9011-9021.
189. Bohnke, O.; Rousselot, C. G. P. A.; Truche, C. *J. Electrochem. Soc.* **1992,** 139, (7), 1962-1965.
190. Singh, P. K.; Kim, K.-W.; Park, N.-G.; Rhee, H.-W. *Synthetic Metals* **2008,** 158, (14), 590-593.
191. Fernicola, A.; Panero, S.; Scrosati, B.; Tamada, M.; Ohno, H. *ChemPhysChem* **2007,** 8, (7), 1103-1107.
192. Pandey, G. P.; Yogesh, K.; Hashmi, S. A. *Indian Journal of Chemistry* **2010,** 49A, 743-751.
193. Pandey, G. P.; Hashmi, S. A. *Journal of Power Sources* **2009,** 187, (2), 627-634.
194. Coll, C.; Labrador, R. H.; Manez, R. M.; Soto, J.; Sancenon, F.; Segui, M.-J.; Sanchez, E. *Chemical Communications* **2005**, (24), 3033-3035.
195. Chiou, C.-Y.; Chou, T.-C. *Sensors and Actuators B: Chemical* **2002,** 87, (1), 1-7.
196. Do, J.-S.; Shieh, R.-Y. *Sensors and Actuators B: Chemical* **1996,** 37, (1–2), 19-26.
197. Fort, A.; Lotti, C.; Mugnaini, M.; Palombari, R.; Rocchi, S.; Vignoli, V. *Microelectronics Journal* **2009,** 40, (9), 1308-1312.
198. He-Qing, Y.; Jun-Tao, L. *Sensors and Actuators* **1989,** 19, (1), 33-40.
199. Ho, K.-C.; Hung, W.-T.; Yang, J.-C. *Sensors* **2003,** 3, (8), 290-303.
200. Kim, K.-S.; Park, S.-Y.; Choi, S.; Lee, H. *Journal of Power Sources* **2006,** 155, (2), 385-390.
201. Liew, C.-W.; Ramesh, S. *J. Mater. Res.* **2012,** 27, (23), 2996-3004.
202. Noda, A.; Watanabe, M. *Electrochimica Acta* **2000,** 45, (8–9), 1265-1270.
203. Pyati, R.; Murray, R. W. *Journal of The Electrochemical Society* **1996,** 143, (2), 401-405.

204. Watanabe, M.; Mizumura, T. *Solid State Ionics* **1996,** 86–88, Part 1, (0), 353-356.
205. Missan, H. P. S.; Lalia, B. S.; Karan, K.; Maxwell, A. *Materials Science and Engineering: B* **2010,** 175, (2), 143-149.
206. Rhoo, H.-J.; Kim, H.-T.; Park, J.-K.; Hwang, T.-S. *Electrochimica Acta* **1997,** 42, (10), 1571-1579.
207. Stephan, A. M.; Kumar, T. P.; Renganathan, N. G.; Pitchumani, S.; Thirunakaran, R.; Muniyandi, N. *Journal of Power Sources* **2000,** 89, (1), 80-87.
208. Kim, K. M.; Park, N. G.; Ryu, K. S.; Chang, S. H. *Polymer* **2002,** 43, (14), 3951-3957.
209. MacFarlane, D. R.; Meakin, P.; Sun, J.; Amini, N.; Forsyth, M. *The Journal of Physical Chemistry B* **1999,** 103, (20), 4164-4170.
210. Ayesh, A. I.; Mohsin, M. A.; Haik, M. Y.; Haik, Y. *Current Applied Physics* **2012,** 12, (4), 1223-1228.
211. Haik, Y. *Applied Mechanical Engineering* **2012,** 2, (1), 1-2.
212. Singh, B.; Sekhon, S. S. *Chemical Physics Letters* **2005,** 414, (1–3), 34-39.
213. Singh, B.; Hundal, M. S.; Park, G.-G.; Park, J.-S.; Lee, W.-Y.; Kim, C.-S.; Yamada, K.; Sekhon, S. S. *Solid State Ionics* **2007,** 178, (23–24), 1404-1410.
214. Ohno, H.; Yoshizawa, M.; Ogihara, W. *Electrochimica Acta* **2004,** 50, (2–3), 255-261.
215. Fuller, J.; Breda, A. C.; Carlin, R. T. *J. Electrochem. Soc.* **1997,** 144, (4), L67-L70.
216. Fuller, J.; Breda, A. C.; Carlin, R. T. *Journal of Electroanalytical Chemistry* **1998,** 459, (1), 29-34.
217. Rahman, M.; Shoff Hugh, W.; Brazel Christopher, S., Ionic Liquids as Alternative Plasticizers for Poly(vinyl chloride): Flexibility and Stability in Thermal, Leaching, and UV Environments. In *Ionic Liquids in Polymer Systems*, American Chemical Society: 2005; Vol. 913, pp 103-118.
218. Ohno, H. *Electrochimica Acta* **2001,** 46, (10-11), 1407-1411.
219. Ohno, H.; Ito, K. *Chemistry Letters* **1998,** 27, (8), 751-752.
220. DropSens. http://www.dropsens.com/ (20th June),
221. MacFarlane, D. R.; Meakin, P.; Sun, J.; Amini, N. *J. Phys Chem. B* **1999,** 103, 4164-4170.
222. Schröder, U.; Wadhawan, J. D.; Compton, R. G.; Marken, F.; Suarez, P. A. Z.; Consorti, C. S.; de Souza, R. F.; Dupont, J. *New J. Chem.* **2000,** 24, 1009-1015.
223. Silvester, D. S.; Wain, A. J.; Aldous, L.; Hardacre, C.; Compton, R. G. *J. Electroanal. Chem.* **2006,** 596, 131-140.
224. Toniolo, R.; Dossi, N.; Pizzariello, A.; Doherty, A. P.; Susmel, S.; Bontempelli, G. *J. Electroanal. Chem.* **2012,** 670, 23-29.
225. Wang, Z.; Lin, P.; Baker, G. A.; Stetter, J.; Zeng, X. *Anal. Chem.* **2011,** 83, 7066-7073.
226. Evans, R. G.; Klymenko, O. V.; Saddoughi, S. A.; Hardacre, C.; Compton, R. G. *J. Phys. Chem. B* **2004,** 107, 7878-7886.
227. Huang, X.-J.; Rogers, E. I.; Hardacre, C.; Compton, R. G. *J. Phys. Chem. B* **2009,** 113, 8953-8959.
228. Huang, X.-J.; Aldous, L.; O'Mahony, A. O.; del Campo, F. J.; Compton, R. G. *Anal. Chem.* **2010,** 82, 5238–5245.
229. Wibowo, R.; Aldous, L.; Rogers, E. I.; Ward Jones, S. E.; Compton, R. G. *J. Phys. Chem. C* **2010,** 114, (8), 3618-3626.
230. Lancaster, N. L.; Salter, P. A.; Welton, T.; Young, G. B. *The Journal of Organic Chemistry* **2002,** 67, (25), 8855-8861.
231. Wiberg, G. K. H.; Mayrhofer, K. J. J.; Arenz, M. *Fuel Cells* **2010,** 10, (4), 575-581.
232. Wang, S. C.; Chang, K. S.; Yuan, C. J. *Electrochimica Acta* **2009,** 54, 4937-4943.
233. Wei, H.; Sun, J.-J.; Xie, Y.; Lin, C.-G.; Wang, Y.-M.; Yin, W.-H.; Chen, G.-N. *Analytical Chimica Acta* **2007,** 588, 297-303.
234. Hook, D. A.; Olhausen, J. A.; Krim, J.; Dugger, M. T. *Microelectromechanical Systems, Journal of* **2010,** 19, (6), 1292-1298.
235. Vig, J. R. *Ultraviolet-Ozone Cleaning of Semiconductor Surfaces*; Army Research Laboratory - Electronics and Power Sources Directorate: Fort Monmouth, U.S.A., 1992.
236. Lange, D. A.; Jennings, H. M.; Shah, S. P. *Journal of Materials Science* **1993,** 28, 3879-3884.
237. EPFL EDF v11.07.2011 (Plugin for ImageJ). http://bigwww.epfl.ch/demo/edf/index.html

238. Forster, B.; Ville, D. V. D.; Berent, J.; Sage, D.; Unser, M. *Microscopy Research and Technique* **2004,** 65, (1-2), 33-42.
239. Zhan, D.; Velmurugan, J.; Mirkin, M. V. *Journal of the American Chemical Society* **2009,** 131, (41), 14756-14760.
240. Bio-Logic Science Instruments, Calculation of the platinum's active surface, Application note #11. www.bio-logic.info
241. Jerkiewicz, G.; Vatankhah, G.; Lessard, J.; Soriaga, M. P.; Park, Y.-S. *Electrochimica Acta* **2004,** 49, 1451-1459.
242. Chatenet, M.; Aurousseau, M.; Durand, R.; Andolfatto, F. *Journal of The Electrochemical Society* **2003,** 150, (3), D47-D55.
243. Rodger, D. C.; Li, W.; Weiland, J. D.; Humayun, M. S.; Tai, Y.-C., Flexible Circuit Technologies for Biomedical Applications. Chapter 1. Advances in Micro/Nano Electromechanical Systems and Fabrication Technologies: 2013; p 25.
244. Zevenbergen, M. A. G.; Wouters, D.; Dam, V.-A. T.; Brongersma, S. H.; Crego-Calama, M. *Analytical Chemistry* **2011,** 83, (16), 6300-6307.
245. Angerstein-Kozlowska, H.; Conway, B. E.; Sharp, W. B. A. *Journal of Electroanalytical Chemistry and Interfacial Electrochemistry* **1973,** 43, (1), 9-36.
246. Conway, B. E. *Progress in Surface Science* **1995,** 49, (4), 331-452.
247. Blumberger, J.; Sprik, M. *The Journal of Physical Chemistry B* **2005,** 109, (14), 6793-6804.
248. Mbadcam, J. K.; Wouaha, G. F. T.; Gomdje, V. H. *E-Journal of Chemistry* **2010,** 7, (3), 721-726.
249. Granger, M. C.; Swain, G. M. *Journal of the Electrochemical Society* **1999,** 146, (12), 4551-4558.
250. Sheppard, S.-A.; A. Campbell, S.; R. Smith, J.; W. Lloyd, G.; C. Walsh, F.; R. Ralph, T. *The Analyst* **1998,** 123, (10), 1923-1929.
251. Wang, Y.; Limon-Petersen, J. G.; Compton, R. G. *Journal of Electroanalytical Chemistry* **2011,** 652, 13-17.
252. Konopka, S. J.; McDuffie, B. *Analytical Chemistry* **1970,** 42, (14), 1741-1746.
253. An Wong, C. H.; Ambrosi, A.; Pumera, M. *Nanoscale* **2012,** 4, (16), 4972-4977.
254. Torriero, A. A. J.; Sunarso, J.; Howlett, P. C. *Electrochimica Acta* **2012,** 82, (0), 60-68.
255. Ležaić, A. J.; Pašti, I.; Vukomanović, M.; Ćirić-Marjanović, G. *Electrochimica Acta*, (0).
256. Lee, J.; Arrigan, D. W. M.; Silvester, D. S. **2014**.
257. Qin, Y.; Peper, S.; Bakker, E. *Electroanalysis* **2002,** 14, (19-20), 1375-1381.
258. Graham, R. K.; Dunkelberger, D. L.; Panchak, J. R. *Journal of Polymer Science* **1962,** 59, (168), S43-S45.
259. Rudolph, M. *Journal of Electroanalytical Chemistry and Interfacial Electrochemistry* **1991,** 314, (1–2), 13-22.
260. Rudolph, M.; Reddy, D. P.; Feldberg, S. W. *Analytical Chemistry* **1994,** 66, (10), 589A-600A.
261. Olejnik, R.; Slobodian, P.; Riha, P.; Machovsky, M. *Journal of Applied Polymer Science* **2012,** 126, (1), 21-29.
262. Brown, O. R.; Lister, K. *Discussions of the Faraday Society* **1968,** 45, (0), 106-115.
263. Green, S. K.; Tompsett, G. A.; Kim, H. J.; Kim, W. B.; Huber, G. W. *ChemSusChem* **2012,** 5, (12), 2410-2420.
264. de Hemptinne, X.; Schunck, K. *Transactions of the Faraday Society* **1969,** 65, (0), 591-597.
265. Bänsch, B.; Härtung, T.; Baltruschat, H.; Heitbaum, J. *Journal of Electroanalytical Chemistry and Interfacial Electrochemistry* **1989,** 259, (1–2), 207-215.
266. Fu, C.; Aldous, L.; Dickinson, E. J. F.; Manan, N. S. A.; Compton, R. G. *Chemical Communications* **2011,** 47, (25), 7083-7085.
267. Collinson, E.; Dainton, F. S.; Gillis, H. *The Journal of Physical Chemistry* **1961,** 65, (4), 695-696.
268. Mayeda, E. A.; Bard, A. J. *Journal of the American Chemical Society* **1973,** 95, (19), 6223-6226.
269. Thakur, V. K.; Vennerberg, D.; Madbouly, S. A.; Kessler, M. R. *RSC Advances* **2014,** 4, (13), 6677-6684.
270. Otsuka, T.; Chujo, Y. *Polym J* **2010,** 42, (1), 58-65.
271. Pereira, N. S.; Sales, M. J. A.; Ceschin, A. M. *Polímeros* **2012,** 22, 384-389.

272. Xie, L.; Huang, X.; Wu, C.; Jiang, P. *Journal of Materials Chemistry* **2011,** 21, (16), 5897-5906.
273. Tamboli, M. S.; Palei, P. K.; Patil, S. S.; Kulkarni, M. V.; Maldar, N. N.; Kale, B. B. *Dalton Transactions* **2014,** 43, (35), 13232-13241.
274. Maegawa, M.; Ajiro, H.; Kamei, D.; Akashi, M. *Polym J* **2013,** 45, (9), 898-903.
275. Gottlieb, H. E.; Kotlyar, V.; Nudelman, A. *The Journal of Organic Chemistry* **1997,** 62, (21), 7512-7515.
276. ASTM Standard E1356 - 08, 2014, "Standard Test Method for Assignment of the Glass Transition Temperatures by Differential Scanning Calorimetry", West Conshohocken, PA 19428-2959, United States, DOI: 10.1520/E1356, www.astm.org.
277. Smith, W. F.; Hashemi, J., *Foundations of materials science and engineering*. 4th Edition ed.; McGraw-Hill: 2006.
278. Thompson, E. V. *Journal of Polymer Science Part A-2: Polymer Physics* **1966,** 4, (2), 199-208.
279. Jiang, W.; Yang, W.; Zeng, X.; Fu, S. *Journal of Polymer Science Part A: Polymer Chemistry* **2004,** 42, (3), 733-741.
280. Roth, C. B.; Pound, A.; Kamp, S. W.; Murray, C. A.; Dutcher, J. R. *Eur. Phys. J. E* **2006,** 20, (4), 441-448.
281. Beevers, R. B.; White, E. F. T. *Transactions of the Faraday Society* **1960,** 56, (0), 744-752.

This marks the completion of an infliction of

Permanent Head Damage